SCUOLA DI DOTTORATO
UNIVERSITÀ DEGLI STUDI DI MILANO-BICOCCA

Department of
Earth and Environmental Sciences

PhD program in Chemical, Geological and Environmental Sciences
Cycle XXXII

Geological Sciences Curriculum

From outcrop to fracture model: a multidisciplinary approach to characterize fracture networks from outcrop analogues in carbonates affected by extensional tectonics

Martinelli Mattia

Registration number: 823020

Tutor: Prof. Andrea Bistacchi
Co-tutor: Prof. Riccardo Castellanza
Dott. Francois Bonneau

Coordinator: Professoressa Maria Luce Frezzotti

ACADEMIC YEAR 2018/2019

From outcrop to fracture model: a multidisciplinary approach to characterize fracture networks from outcrop analogues in carbonates affected by extensional tectonics

PhD student: Mattia Martinelli

This thesis has been funded by ENI S.p.a. in the framework of the SEFRAC project. The aim of the project was to improve fracture characterization and modeling in fractured carbonate hydrocarbon reservoirs in different tectonic environments using outcrop analogues.

A Giulia…

Table of contents

Abstract

Fracture networks exert a primary role in the control of permeability and flow of geo-fluids (e.g hydrocarbons, ground water, hydrothermal fluids, etc.). Fracture parameters in the subsurface are usually characterized using borehole and seismic data, but these are affected by a scale gap. Well data are only sparse and partial and even the best seismic data cannot detect fractures shorter than ca. 200 m. Km-scale outcrop analogues can help to fill this gap, allowing to collect huge amounts of data at different scales.
This PhD thesis investigates the fracture networks in carbonates of the Maltese Islands, located in the Pelagian Platform in the foreland of the Sicilian-Apennine-Maghrebian fold and thrust belt, that are world-class analogues of extensional fractured and faulted hydrocarbon reservoirs. Here a Late-Oligocene – Late Miocene carbonatic sequence composed by different types of carbonates is exposed. It is cross-cut by normal faults with a vertical displacement up to 210 meters, arranged in two main sets striking ENE-WSW and WNW-ESE. Moreover, Neptunian dykes associated with small normal faults (less than 5 meters of displacement) are present in the lower units. We applied a multidisciplinary approach that allowed us to carry out the following studies that are presented in the four chapters of this thesis.

i) we characterized the tectonic and geodynamic evolution of the Maltese Islands and Pelagian Platform from the Late Oligocene to the Pliocene also to understand the timing of the formation and kinematics of the different fault and joint sets.
ii) we investigated the fault zone architecture, the fracture parameters and their impact on hydraulic connectivity in the damage of the Qala fault (Gozo). The study was performed applying a new workflow that combines linear scan-lines and scan-areas analysis applied on a large Digital Outcrop Model also using automatic methods for the extraction of fracture parameters.
iii) we investigated the control of the mechanical stratigraphy and in particular of the elastic properties of the rocks on the damage zone thickness combining petrographical, petrophysical, geomechanical and numerical modeling analyses.
iv) we characterized the Representative Elementary Volume of fracture parameters of a DFN model built using outcrop data derived from the DOM study of chapter ii to drive Discrete Fracture Network modeling. Results show that the REV can be used to model DFN on a smaller scale with respect to the reservoir scale solving many numerical problems.

Riassunto

I network di fratture hanno un ruolo fondamentale nel controllo della permeabilità e del flusso dei geo-fluidi (e.g. idrocarburi, acqua, fluidi idrotermali ecc.). Nel sottosuolo i parametri delle fratture vengono solitamente caratterizzati utilizzando dati di pozzo e dati sismici, i quali però sono divisi da un salto di scala. Infatti, i dati di pozzo sono sparsi e parziali mentre anche la sismica migliore non è in grado di identificare fratture con dimensione minori di 200 metri. Gli analoghi esumati di reservoir possono aiutare a colmare questo divario permettendo di raccogliere una grande quantità di dati a scale differenti.

In questa tesi di dottorato abbiamo caratterizzato il network di fratture nei carbonati delle isole di Malta e Gozo, che si trovano all'interno della Piattaforma Pelagica nel foreland della catena Appeninico-Magrebide e sono degli spettacolari analoghi esumati di reservoir di idrocarburi fratturati sviluppatisi in ambienti tettonici estensionali. La stratigrafia delle isole maltesi è caratterizzata dalla presenza di differenti tipi di carbonati di età compresa tra il tardo Oligocene e il Miocene superiore, tagliati da due set di faglie normali (ENE-WSW e WNW-ESE) con rigetti verticali che possono raggiungere i 210 metri. Dicchi nettuniani associati a faglie normali con rigetto limitato (meno di 5 metri) sono inoltre presenti nelle unità più antiche. In questa tesi abbiamo utilizzato un approccio multidisciplinare che ci ha permesso di effettuare diversi tipi di studi che sono presentati nei quattro capitoli della tesi.

i) Nel primo capitolo abbiamo ricostruito l'evoluzione tettonica e geodinamica delle isole di Malta e Gozo e della Piattaforma Pelagica a partire dal tardo Oligocene fino al Pliocene. Questo ci ha permesso inoltre di ricostruire l'età di formazione e la cinematica dei diversi set di faglie e fratture.
ii) Nel secondo capitolo abbiamo caratterizzato l'architettura della zona di faglia, i parametri delle fratture e il loro impatto sulla connettività idraulica nella zona di danneggiamento legata alla faglia di Qala (Gozo). Per fare questo abbiamo applicato un nuovo workflow che combina scan-line lineari con scan-area applicate su modelli di affioramento digitali di dimensioni chilometriche utilizzando inoltre metodi automatici per il calcolo dei parametri della fratturazione.
iii) Nel terzo capitolo, abbiamo mostrato come la meccanica stratigrafica e in particolare le proprietà elastiche delle rocce giochino un ruolo fondamentale nel controllo dello spessore della damage zone. I risultati sono stati ottenuti combinando osservazioni di terreno con analisi petrofisiche, petrografiche, geo-meccaniche e modelli numerici.
iv) Nel quarto capitolo abbiamo caratterizzato il Volume Elementare Rappresentativo (REV) delle proprietà delle fratture in un DFN realizzato con i parametri di fratture ottenuti dallo studio dell'affioramento effettuato nel capitolo ii. Abbiamo inoltre mostrato che la dimensione del REV può essere utilizzata per modellare i DFN ad una scala più piccola rispetto a quella del reservoir. Questo permette di risolvere alcuni problemi legati alla modellazione della fratturazione alla scala del reservoir.

1

Late Oligocene to Pliocene Extension in the Maltese Islands and Implications for Geodynamics of the Pantelleria Rift and Pelagian Platform

This chapter is presented in the form of a paper published in the Journal Tectonics.

Published article

Martinelli, M., Bistacchi, A., Balsamo,F., & Meda, M. (2019). Late Oligocene to Pliocene extension in the Maltese Islands and implications for geodynamics of the Pantelleria Rift and Pelagian Platform. Tectonics, 38, 3394–3415. https://doi.org/10.1029/2019TC005627

Late Oligocene to Pliocene extension in the Maltese Islands and implications for geodynamics of the Pantelleria Rift and Pelagian Platform

Mattia Martinelli[1]*, Andrea Bistacchi[1], Fabrizio Balsamo[2] and Marco Meda[3].

[1] Dipartimento di Scienze dell'Ambiente e della Terra, Università degli Studi di Milano Bicocca, Piazza della Scienza 4, 20126 Milano, Italy

[2] NEXT- Natural and Experimental Tectonics research group, Dipartimento Scienze Chimiche, della Vita e della Sostenibilità Ambientale, Università degli Studi di Parma, Padiglione 7 - Scienze della Terra, Campus Universitario, Parco Area delle Scienze 157/A, 43124 Parma, Italy

[3] ENI Spa, Upstream and Technical Services, 5° Palazzo Uffici, Via Emilia, 1 20097 San Donato Milanese, Italy.

* Corresponding author: Mattia Martinelli (m.martinelli34@campus.unimib.it)

Key Points:

- Two independent extensional tectonic events, separated by a quiescence stage, are reconstructed in the Maltese Islands.
- Both events were caused by the stress regime imposed in the Pelagian Platform by the roll-back of the subducting slab.
- The switch in main extension direction between the two events is a result of the varying orientation of the trench.

1.1 Abstract

The tectonic and geodynamic evolution of the Pelagian platform and of the Pantelleria Rift System, located in the foreland of the Apennine-Sicilian-Maghrebian Belt, from the Late Oligocene onwards, is still debated. Here we present a new interpretation based on structural data collected in the Malta and Gozo islands. With a tectonic back-stripping approach, we recognized two main extensional events separated by a period of tectonic quiescence: (D1) Early Miocene WNW-ESE extension; (D2) Late Miocene to Pliocene N-S extension that led to the opening of the Pantelleria Rift System. During both extensional events the Maltese Islands and the Pelagian Platform were located in the foreland of the Apennine-Sicilian-Maghrebian Belt (Western Mediterranean Arc), in a period of slab roll-back. We suggest that both tectonic events are an evidence of the extensional regime imposed on the foreland area by the roll-back of the subducting slab. The switch in the main extension axis between D1 and D2 (WNW-ESE vs. N-S) can be interpreted as a result of the varying orientation and distance of the trench due to the progressive development of the Western Mediterranean Arc, and provides an independent tool to "monitor" the slab roll-back. Results obtained in this study allowed, for the first time, to bind the tectonic evolution of the area with the geodynamic evolution of the Western and Central Mediterranean.

Keywords

Maltese Islands, Pelagian Platform, Pantelleria rift system, Tectonic evolution, Geodynamic evolution, Slab roll-back

1.2 Introduction

Fold and thrust belts developed along subduction zones are characterized by complex deformation patterns and their influence is felt in foreland areas well ahead the trench and/or the front of contractional tectonics. Flexure of the foreland due to the load imposed by the advancing convergent margin results in extensional tectonics, which can be interpreted also as the effect of slab pull (Bradley & Kidd, 1991; Doglioni, 1995; Forsyth & Uyeda, 1975; Langhi et al., 2011; Tavani et al., 2015a, 2015b, 2019; Turcotte & Schubert, 1982). Hence, forelands are characterized by extensional faults, veins and joints parallel to the trench axis (Beaudoin et al., 2012; Billi and Salvini, 2003; Mazzoli et al., 2005; Quinta & Tavani, 2012; Ranero et al., 2003; Scisciani et al., 2001; Tavani et al., 2015a, 2015b, 2019) and from structures perpendicular to the fold and thrust belt, like cross-joints and release faults (Bai et al., 2002; Gross, 1993; Tavani et al., 2019).

The Islands of Malta and Gozo are located in the Pelagian platform, which extends from Tunisia to the Ionian Basin (Burollet et. al. 1978) and represents the foreland of the Apennine-Sicilian-Maghrebian Belt (Argnani, 1990; Hill & Hayward, 1988) (Figure 1a). The Pelagian platform is

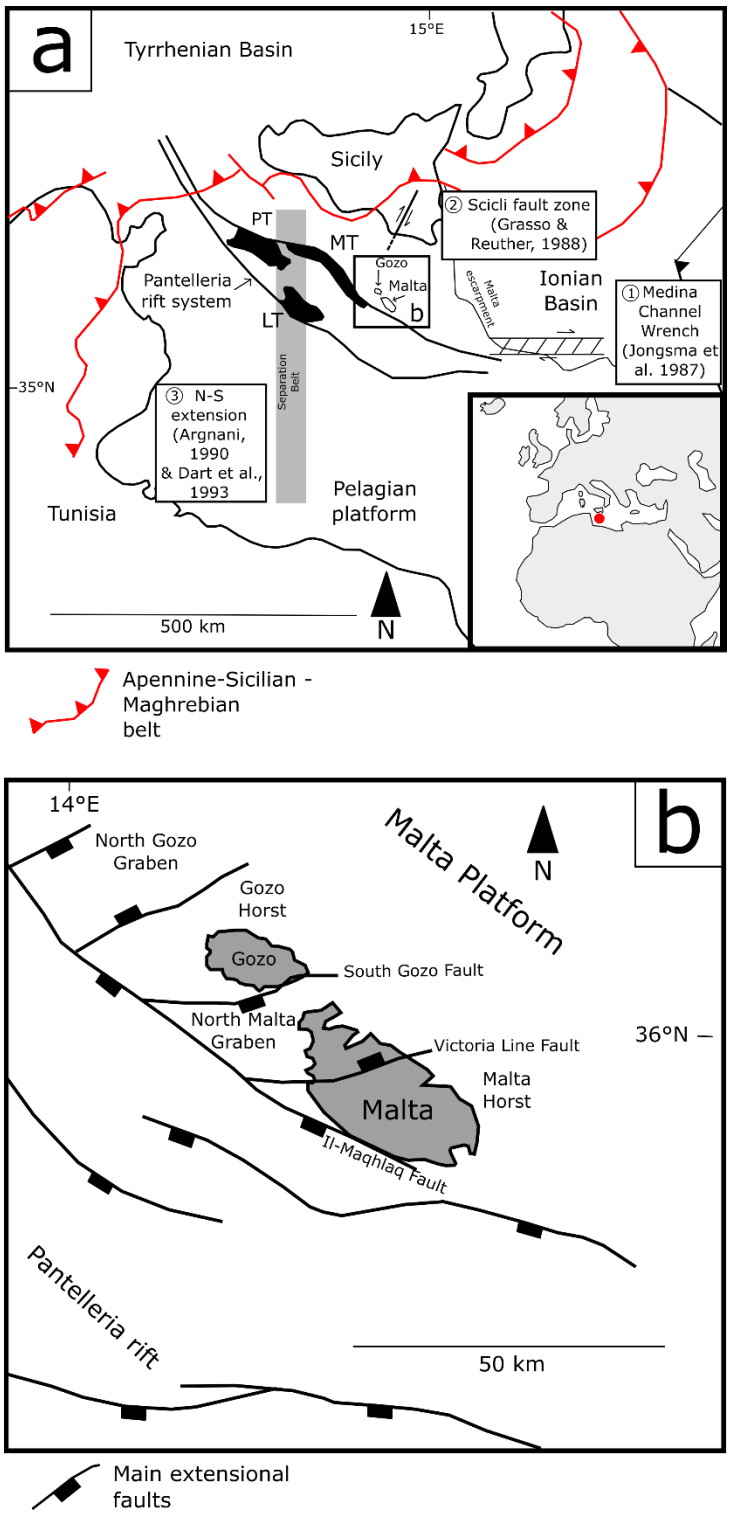

Figure 1. (a) Position of the Maltese Islands in the foreland of the Apennine-Sicilian-Maghrebian Belt (PT = Pantelleria Trough; LT = Linosa Trough; MT= Malta Trough). Numbered rectangles highlight key areas for the three main interpretations proposed for the evolution of the Pantelleria Rift **S**ystem by the cited authors; (b) Main tectonic features of the Maltese Graben System. (modified after Dart, 1993).

crosscut by the Pantelleria Rift System (Finetti 1982; Finetti, 1984; Reuther & Eisbacher, 1985) which started opening in the Late Miocene (Dart et al., 1993) and it is composed by three main NW-SE trending depressions: the Pantelleria, Linosa and Malta troughs (Reuther and Eisbacher, 1985; Figure 1a). To the E of the Malta Trough, on the shoulder of the rift system, there is the 2nd order Maltese Graben System, composed by the Malta and Gozo horsts and by two ENE-WSW trending grabens: the North Malta Graben and the North Gozo Graben (Dart et al., 1993); (Figure 1b).

Different authors agree on the general statement that the Late-Miocene to Present tectonic evolution of the Pantelleria Rift and related minor structures (like the Maltese Graben System) results from the stress field imposed by the advancing Apennine-Sicilian-Maghrebian Belt (Argnani, 1990; Dart et al., 1993). However, the timing and kinematic details of this evolution are still debated (Argnani, 1990; Ben-Avraham et al., 1987; Boccaletti et al., 1987; Catalano et al., 2009; Cello, 1987; Dart et al., 1993; Finetti, 1984; Grasso and Reuther, 1988, Jongsma et al., 1985; Reuther & Eisbacher, 1985). Most kinematic models proposed so far fall in three categories that can be summarized as follows (Figure 1a):

(1) Some authors see the Pantelleria Rift System as a pull-apart basin developed along a dextral wrench zone - the Medina Channel Wrench, which is the SE boundary of the rift system (Ben-Avraham et al., 1987; Boccaletti et al. 1987; Catalano et al., 2009; Cello, 1987; Finetti, 1984; Jongsma et al., 1985; Reuther & Eisbacher, 1985).

(2) Alternatively, Grasso and Reuther (1988) suggested that the Pantelleria Rift System might be a pull-apart structure associated with the NNE-SSW Scicli Wrench Zone. This zone is interpreted as a large wrench zone, mostly developed offshore in the Malta Plateau (the shallow-water domain between Sicily and the Maltese Islands), and outcropping onshore in SE Sicily (Iblei Mountains).

(3) The last interpretation was proposed by Argnani (1990) and Dart et al. (1993). According to these authors, the Pantelleria Rift system is a direct consequence of a N-S foreland extension, ahead of the retreating trench. Moreover, the authors recognized a N-S transfer fault (the Separation Belt) between the Pantelleria and Linosa Troughs, associated with Neogene volcanic centres (Argnani, 1990).

Within this geodynamic framework, different interpretations have been proposed for the tectonic evolution of the Maltese Islands, that are characterized by Oligocene-Miocene carbonates crosscut by two sets of ENE-WSW and WNW-ESE normal faults, and by roughly N-S Neptunian dykes confined in the lower units (Dart et al., 1993; Illies, 1981; Pedley et al., 1976; Reuther & Eisbacher, 1985). Neptunian dykes are particularly interesting for dating deformation, since they are bodies of younger sediments infilling fissures in rocks exposed on the sea floor (Bates & Jackson, 1980;

Cozzi, 2000; Crne et al., 2007; Smart et al., 1988; Visser, 1980). They form due to fracturing of the lithified host rocks and they are almost immediately filled by the overlying unconsolidated sediments (Lehner, 1991; Wendt, 1971), hence they have almost the same age of the infilling sediments.

Reuther and Eisbacher (1985) and Illies (1981) divided the evolution of the graben system in three phases: (1) formation of the ENE-WSW faults, (2) formation of the WNW-ESE set, and (3) reactivation of the ENE-WSW faults in dextral strike slip. Reuther and Eisbacher (1985) did not consider the Neptunian dykes in their reconstruction, while Illies (1981) associated them to an independent movement before rifting. On the other hand, Dart et al. (1993) suggested that both ENE-WSW and WNW-ESE fault sets are coeval and developed in response to N-S extension during the Miocene, and interpreted the Neptunian dykes as marking the onset of the extension.

In this contribution, we present a new evolutionary model for the Maltese Graben System based on detailed structural analysis performed on different stratigraphic units in the Maltese islands. Our model consists of two different extensional events: a WNW-ESE extension during the Early Miocene (D1), and a later N-S extension from the Late Miocene onwards (D2). This scenario is consistent with the model of Cenozoic geodynamic evolution of the Western and Central Mediterranean proposed by Faccenna et al. (2001) and Faccenna et al. (2004a, 2004b).

1.3 Geology of the Maltese Islands

The stratigraphic sequence exposed in the Maltese Islands starts with the Upper Oligocene and ends with the Late Miocene. It is characterized by shallow-water marine carbonates arranged in five formations (from oldest to youngest): (i) the Lower Coralline Limestone (Chattian), (ii) the Globigerina Limestone (Late Oligocene to Langhian), (iii) the Blue Clay Formation (Serravalian to Early Tortonian), (iv) the Greensand Formation (Tortonian), and (v) the Upper Coralline Limestone (Late Tortonian to Early Messinian) (Figure 2a; Dart et al., 1993; Felix, 1973; Murray, 1890; Pedley et al., 1976).

The Lower Coralline Limestone (Chattian) is composed by four members (Pedley, 1978). The oldest is the Maghlaq Member: a biomicrite characterized by the presence of benthonic foraminifera. It passes transitionally up to the Attard Member: a coralline algal limestone (wackestones and packstones) containing algal rhodoliths, gastropods and bryozoan. After the deposition of the Attard Member, depositional conditions became unfavourable to rhodolitic growth and this lead to the deposition of the planar to cross-stratified, coarse-grained limestones of the Xlendi Member. The top of the Xlendi Member is characterized by the presence of the characteristic Scutella Beds, very rich in these echinoids. The last member of the Lower

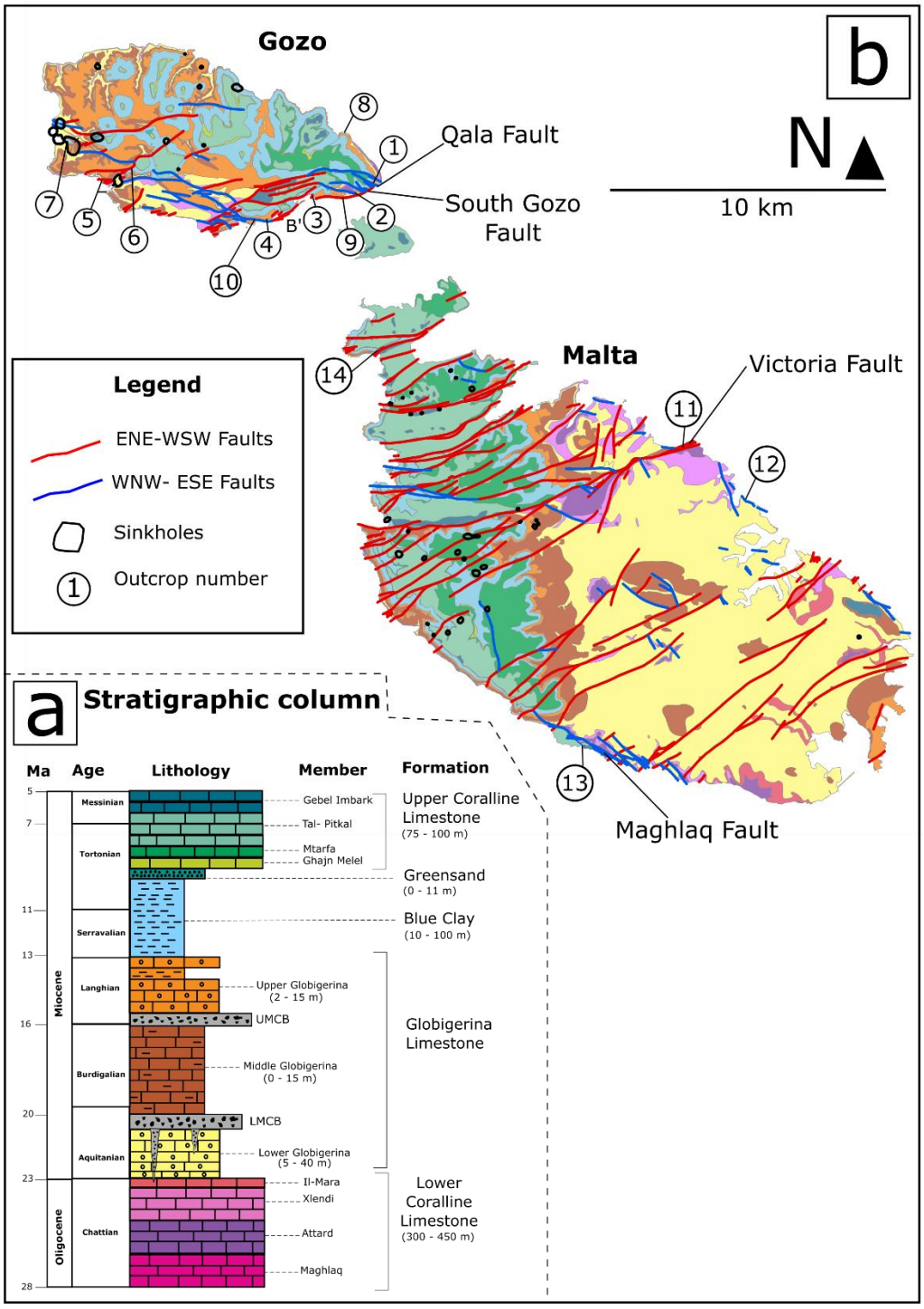

Figure 2. (a) Stratigraphic column of the Maltese Islands redrawn after Pedley (1976) and Dart (1993); (b) Geological map of the Maltese Islands redrawn with updates from the 1: 25.000 Geological map of the Oil Exploration Directorate, Office of the Prime Minister, Malta, (1993). A more detailed geological map with the outcropping area of the Neptunian dykes, cross sections and area where kinematic data have been collected is available in the supporting data (Supplementary data in this thesis, Figure S1).

Coralline Limestone is the Il-Mara Member, characterized by mudstones, wackestones and packstones with abundant bryozoan fragments. The depositional environment has been interpreted (Felix, 1973; Pedley et al., 1976) as a shallow gulf-type area (Maghlaq Member) followed by open-marine conditions that brought to the deposition of abundant algal rhodoliths (Attard and Xlendi Member), and finally as a shallow marine shoal environment (Il-Mara Member).

The Globigerina Limestone Formation was deposited between the Aquitanian and the Langhian in a marine environment with depths of 40-150 m (Dart et al., 1993; Felix, 1973; Pedley et al., 1976). It is composed by three members, bounded by unconformities marked by hardgrounds and glauconitic conglomerates: (i) Lower Globigerina, (ii) Middle Globigerina, and (iii) Upper Globigerina (Rizzo, 1932). The Lower Globigerina Member (Aquitanian) is composed by pale-cream to yellow planktonic foraminiferal packstones and wackestones. It has a minimum thickness of 5 meters, but it reaches 100 m in the Valletta Basin of Malta. In Gozo, it reaches a maximum thickness of 40 m (Pedley, 1975; Pedley et al., 1976). The top is characterized by a hardground overlaid by the Lower Main Conglomerate Bed (LMCB) (Pedley et al., 1976): a marker very useful when mapping fault offset, less than 1 meter thick. Moreover, the Lower Globigerina Member is characterized by the presence of Neptunian dykes (Illies, 1981; Pratt, 1990) and small normal faults (throw <5m) with the same attitude of the Neptunian dykes (Gatt, 2005). Above the LMCB we find the Middle Globigerina Member (Aquitanian-Burdigalian), characterized by pale-grey and white marly mudstones and poorly cemented mudstones. This member shows thickness variations similar to those of the Lower Globigerina, which are particularly evident in Gozo, where the unit reaches a thickness up to 15 meters in the western part of the Island, whereas it is absent in the eastern part (Pedley et al., 1976). Also the top of the Middle Globigerina Member is marked by a conglomerate bed: the Upper Main Conglomerate Bed (UMCB) (Pedley et al., 1976). It is 0.5m thick and it is present both in Malta and in Gozo. The last member of the Globigerina Limestone is the Upper Globigerina Member. It is a tripartite unit with a lower and upper pale-yellow biomicrite, intercalated by a pale-grey marly biomicrite (Morris, 1952). In Gozo, it shows a thickness of ~15 m (Pedley et al., 1976).

The Blue Clay Formation (Serravallian to Early Tortonian) testifies an abrupt change in the depositional environment. It is characterized by blue-gray marly clays with less than 30% carbonate component (Murray, 1890; Pedley et al., 1976) deposited in an open marine environment with water depths from 100 m up to 150 m. This unit shows important thickness variations in the range 18 to 65m (Pedley et al., 1976).

The Greensand Formation (Tortonian) was deposited above an erosional surface affecting the Blue Clay. It is composed by a thin and discontinuous layer of glauconitic sandstones (Pedley et al., 1976).

The Upper Coralline Limestone (Late Tortonian to Messinian) is the youngest formation of the Maltese Arcipelago (Bianucci et al., 2011; Giannelli & Salvatorini, 1975; Mazzei, 1985; Russo & Bossio, 1975). It is composed by four members: from oldest to younger they are (1) the foraminiferal packstones of the Ghajn Melel Member; (2) the Mtarfa Member, composed by massive to thickly-bedded mudstones and wackestones (Bosence & Pedley, 1982); (3) the Tal-Pitkal Member, composed by coarse-grained wackestones and packstones with abundant rodholithes in the lower part and patch reefs and biostrome in the upper part; (4) the Gebel Imbark Member, composed by basal beds of cross stratified ooidal and peloidal grainstones overlied by carbonate mudstones associated with grey marls.

From a structural point of view, the Malta and Gozo islands are cut by two main sets of normal faults trending WNW-ESE and ENE-WSW (Dart et al 1993; Illies, 1981; Pedley et al., 1976; Reuther & Eisbacher, 1985) forming a horst and graben structure that dissects the Oligo-Miocene series of the Islands (Figure 2b). In particular, four regional structural features can be identified: the Malta and Gozo horsts, and the North Gozo and North Malta grabens (Figure 1b). The main faults outcropping in the islands are the ENE-WSW Victoria Fault and South Gozo Fault (bordering the North Malta Graben), and the WNW-ESE Maghlaq Fault (Bonson et al., 2007; Pedley et al., 1976) (Figure 2b). The Victoria Fault has a vertical separation of 120 m and, according to Villani et al. (2018) had its maximum activity during the Pliocene-Early Pleistocene. The Maghlaq Fault is located in the SE part of Malta and with 210 m of vertical separation is the most important fault of the WNW-ESE set (Bonson et al, 2007). (Figure 2b). On the Gozo Island the two main faults are the South Gozo Fault and the Qala Fault. The South Gozo Fault is an ENE-WSW normal fault with a dip of 65° toward SE (Cooke et al., 2018) that border the southern part of the island. It juxtaposed the Upper Coralline Limestone with the Lower Globigerina Formation with a vertical displacement of at least 80 meters. The South Qala fault is a WNW-ESE normal faults with a minimum vertical displacement of 50 meters (Cooke et al, 2018) and an average dip of 61° toward SSW (Figure 2b).

1.4 Structural data

The Maltese islands allow carrying out detailed structural and geological surveys on exceptionally continuous outcrops, particularly along the coast, where they can extend for several kilometres. In the islands interior, the best outcrops are represented by hilltops, gullies, and quarries. Data for the structural analysis were collected in 14 different sites characterized by almost horizontal bedding

(10 in Gozo and 4 in Malta; Figure 2b). Structural data include attitude measurement of fault surfaces (306 data), mode I joints (265 data) and Neptunian dykes (96 data), fault kinematic indicators (382 measurements including 12 shear fractures), and cross-cutting and abutting relationships among the structures. We choose to characterize more outcrops in Gozo because here the Lower Globigerina Limestone is better exposed then in Malta, hence the best outcrops to observe Neptunian dykes and the small normal faults in the Lower Globigerina are on this island (Figure 2b and Figure S1 in the supporting data). As a base for our structural survey, we used the 1:25.000 geological map of the Oil Exploration Directorate, Office of the Prime Minister of Malta published in 1993 and provided by the Malta Planning Authority and the Malta Resources Authority. The map is generally very detailed, and only in a few places we have carried out detailed surveys to improve it and allow a better structural and kinematic analysis (Figure 2b and Figure S1 in the supporting data, Supplementary material in this thesis).

1.4.1 Fault and fracture sets

The islands of Malta and Gozo are dissected by two sets of normal faults striking N70°E (ENE-WSW) and N286°E (WNW-ESE). The ENE-WSW set has an average dip of 80° either toward NNW or SSE. WNW–ESE set has an average dip of 80° both toward NNE or SSW (Figure 3). The two fault sets have vertical displacements ranging from several to hundreds of meters as demonstrated by stratigraphic separation. Several attitude data were taken also on the major faults of Malta and Gozo (e.g.Victoria Fault, South Gozo Fault, Qala Fault, Maghalq Fault showing that they are part of these two sets (Figure 2b and Figure 3). Moreover, four fracture sets were recognized: i) strike N73°E (ENE-WSW) and dip 88° toward NNW or SSE; ii) N287°E (WNW-ESE) and dip 86° toward NE or SW; iii) strike N0°E (N-S) and dip 87° toward E or W; and iv) N45°E (NE-SW) and dip 81° toward NW or SE (Figure 3). In some cases, joints are filled by calcite, hence they are veins. Finally, different sets of Neptunian dykes (N-S, NE-SW and WNW-ESE) with an average dip angle of 85° are present in the Lower Globigerina Member and in the upper part of the Lower Coralline Limestone (Figure 3). Neptunian dykes have apertures ranging from 1 mm to several centimetres and they are filled with material coming from the Lower Main Conglomerate Bed (LMCB), composed by mm- to cm-size brown pebbles absorbed inside a whitish to yellow matrix. The contact between the Neptunian dykes and the calcarenites of the Lower Globigerina Member is marked by a characteristics white-coloured alteration halo. The walls of the Neptunian dykes are sharp and almost planar, indicating that they were not formed as consequence of dissolution processes. The Lower Globigerina Member is also characterized by the presence of small normal faults showing the same strike as the Neptunian dykes (N-S, NE-SW and WNW-ESE) and an average dip of 60°, with less than 5 m of displacement (Figure 3). Since

in terms of stratigraphic position and strike these faults are similar to the Neptunian dykes, we will call them “normal faults associated with the Neptunian dykes”.

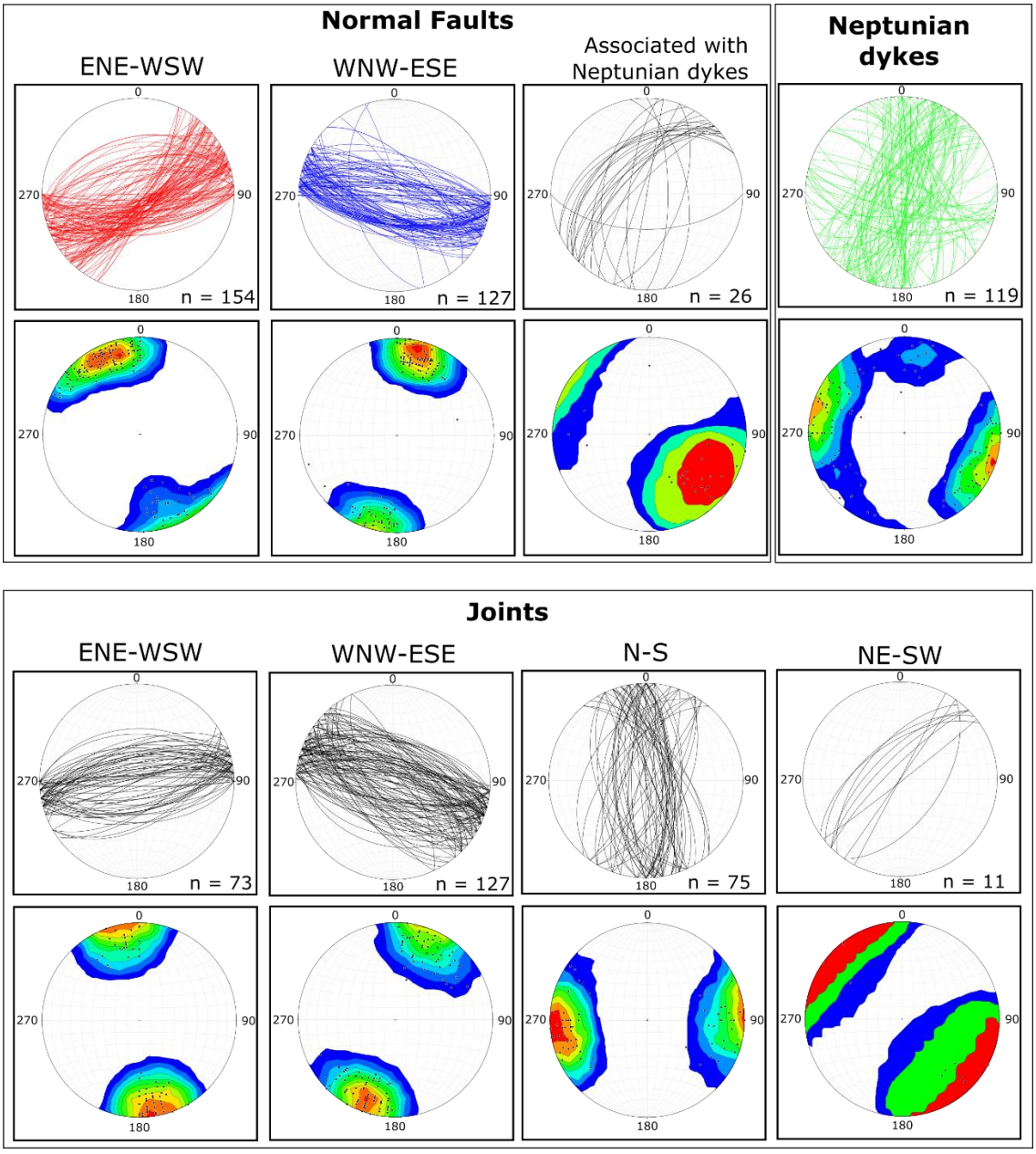

Figure 3. Lower hemisphere equal-area plots and density contour of poles representing attitude of normal faults, Neptunian dykes and joints in the investigated outcrops. Attitude data can be found in table S1 in the supporting information (supplementary material in this thesis).

1.4.2 Relative chronology

Relationships between structures and stratigraphy are summarized in Figure 4. ENE-WSW and WNW-ESE normal faults cross-cut all the stratigraphic units (Figure 4 a, b, e). This behaviour is also confirmed by joint sets associated to faults (ENE-WSW, WNW-ESE; N-S; NE-SW), that are present in all stratigraphic units. These joints are not common in the Middle Globigerina Limestone member and in the Blue Clay because they are composed by marls and clays not prone to brittle deformation (Figure 4e). On the other hand, Neptunian dykes and associated small normal faults are present only in the Lower Globigerina Member (Aquitanian) and in the upper part of the Lower Coralline Limestone (Figure 4 c, d, e). Neptunian dykes are sealed by the Lower Main Conglomerate Bed (LMCB), which is also the source of the infilling sediments (Figure 4c, e), whereas the faults cut the conglomerate and are sealed by the overlying units (Middle or Upper Globigerina) (Figure 4d, e). ENE-WSW and WNW-ESE faults show mutual cross-cutting and/or abutting relationships, suggesting that they are coeval. Also fracture sets with ENE-WSW and WNW-ESE strike mutually crosscut and abut each other (Figure 5a); they are the most important ones both in terms of frequency and continuity (master joints), and they are parallel to the larger faults (e.g South Gozo Fault, Qala Fault, Victoria Fault, Maghlaq Fault). On the other hand, fractures of sets N-S and NE-SW are less frequent and less continuous (cross joints) and usually terminate against the master joints (Figure 5a). All joints and ESE-WSW and WNW-ESE fault sets crosscut the Neptunian dykes (Figure 5b, c, d, e).

1.4.3 Kinematic indicators

The kinematic indicators collected in the 14 different sites are summarized in Figure 6. The stratigraphic offset of the small faults associated with the Neptunian dykes can be inferred from the offset in the Lower Main Conglomerate Bed (LMCB) (Figure 7a) suggesting a normal movement. More detailed kinematic indicators consist in slickensides showing dip-slip kinematics. Unfortunately, these structures are not common, probably due to the limited displacements (< 5 m), but when they are present, the kinematics is very consistent (Figure 7b). We carefully searched for evidences of larger displacements or reactivation, both for Neptunian dykes and associated normal faults but these were not detected and, given the high quality and continuity of the outcrops, we are confident that these structures were not reactivated in later deformation stages. In addition, Neptunian dykes were interpreted as hybrid fractures and they have been used as kinematic indicators in the same way as joints, hybrid tensional/shear fractures and fissures are commonly used (e.g. Davis et al., 2011; Twiss & Moores, 2007). On the other hand, both the ENE-WSW and WNW-ESE normal fault sets are very suitable for kinematic analysis since they provide common and consistent kinematic indicators (Figure 6 and Figure 7 c, d, e, f, g, h).

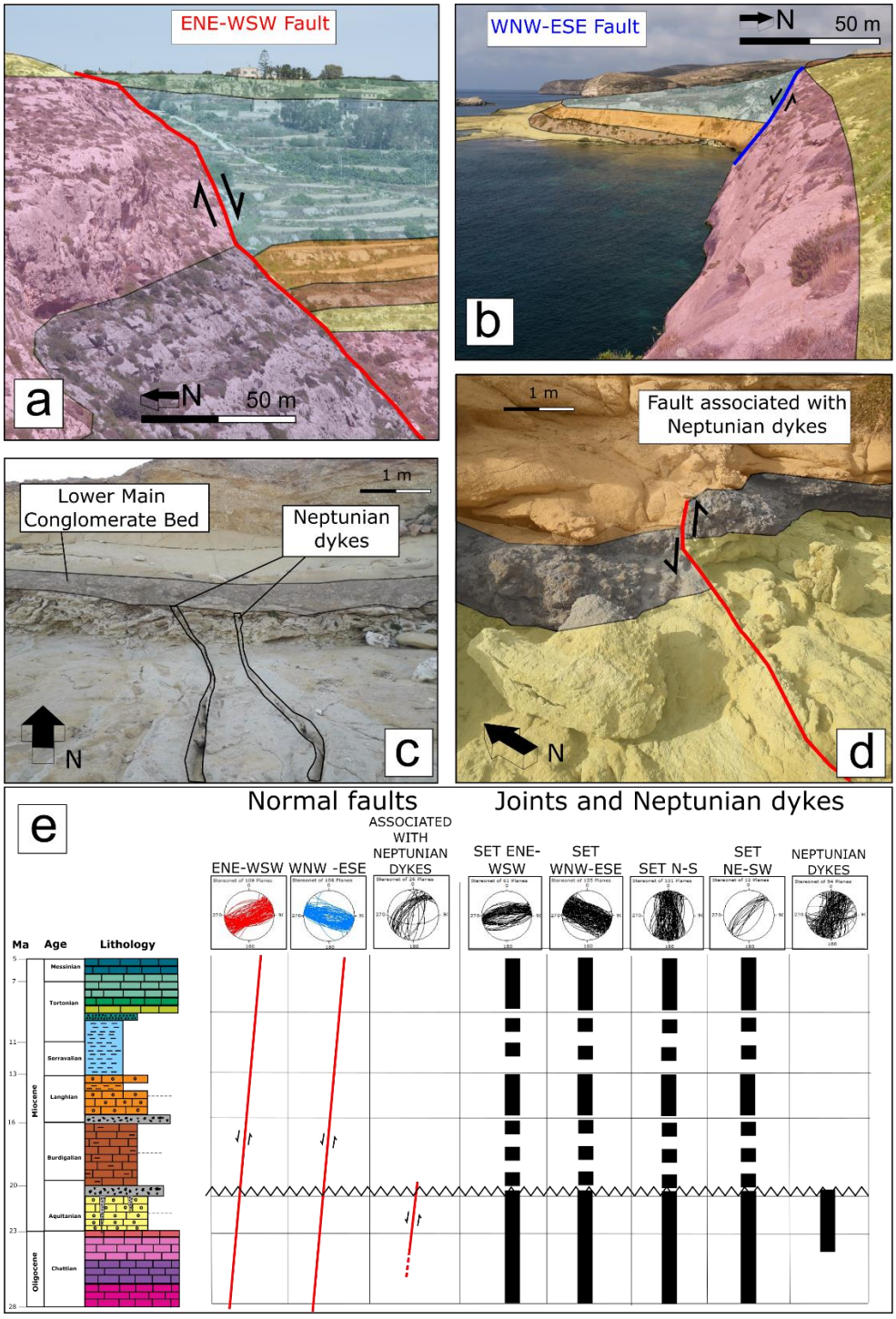

Figure 4. Relative chronology and relationship with the stratigraphy of normal faults, Neptunian dykes and joints. Colour-coding as in stratigraphic column. (a,b) ENE-WSW normal fault and WNW-ESE normal faults both cross-cut all the stratigraphy (c): Neptunian dykes and the overlying conglomerate that infills and seal them. (d) The small normal faults associated with Neptunian dykes. It is possible to see that they cut the conglomerate but are sealed by the overlying unit. (e) Summary of the relative chronology and relationship with the stratigraphy of the structural features.

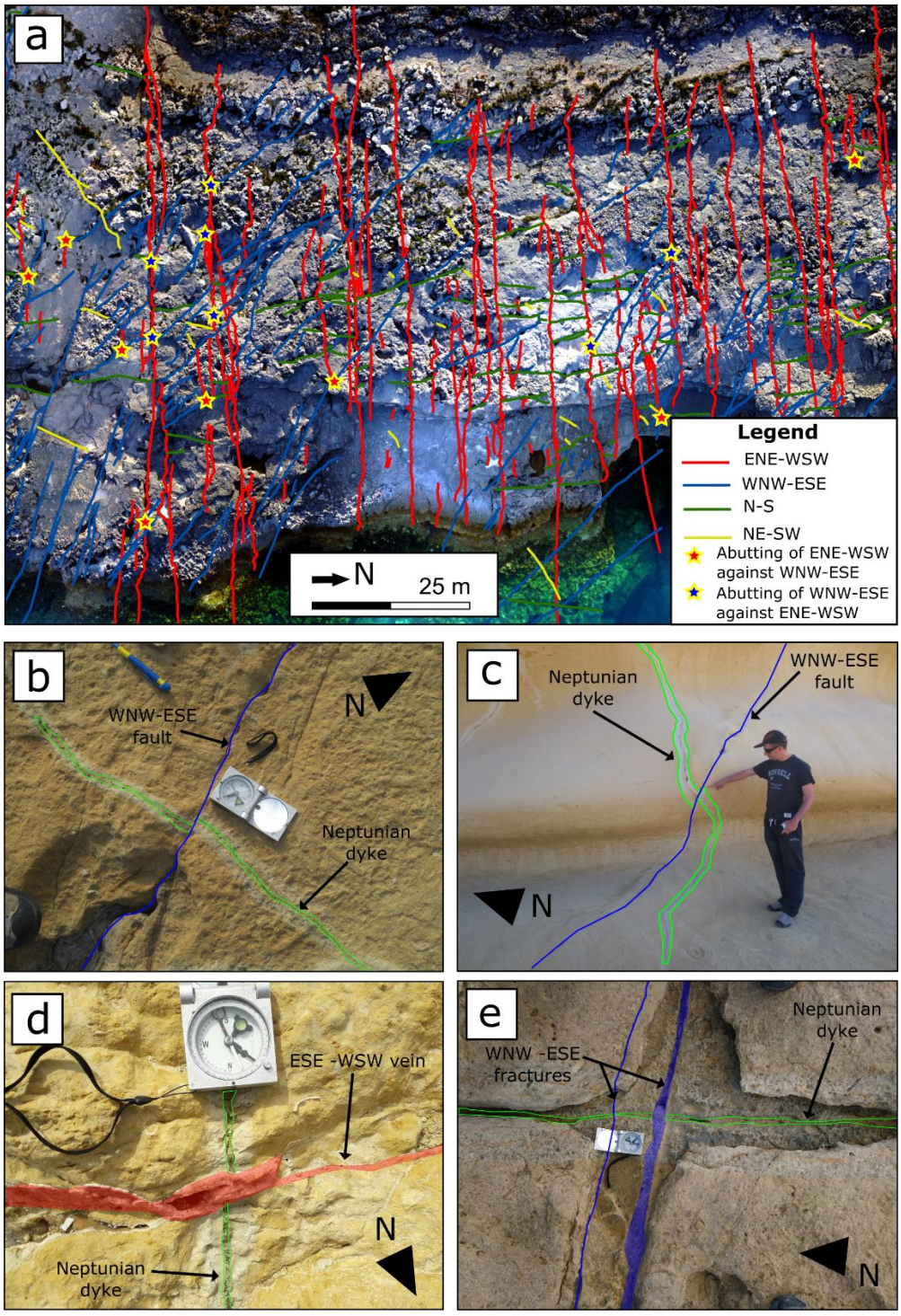

Figure 5. Cross-cutting relationships. (a) Drone picture showing a plan view of the mutual abutting and cross-cutting relationships of ENE-WSW and WNW-ESE joint sets (master joints). Moreover, it is possible to see that N-S and NE-SW joints terminate against the master joints. (b) plan view of a WNW-ESE normal fault that cross-cut a Neptunian dyke. (c) side view of a WNW-ESE normal fault that cross-cuts a Neptunian dyke. (d) plan view of a ENE-WSW veins that cross-cuts a Neptunian dyke. (e) plan view of a WNW-ESE joint that cross-cuts a Neptunian dyke.

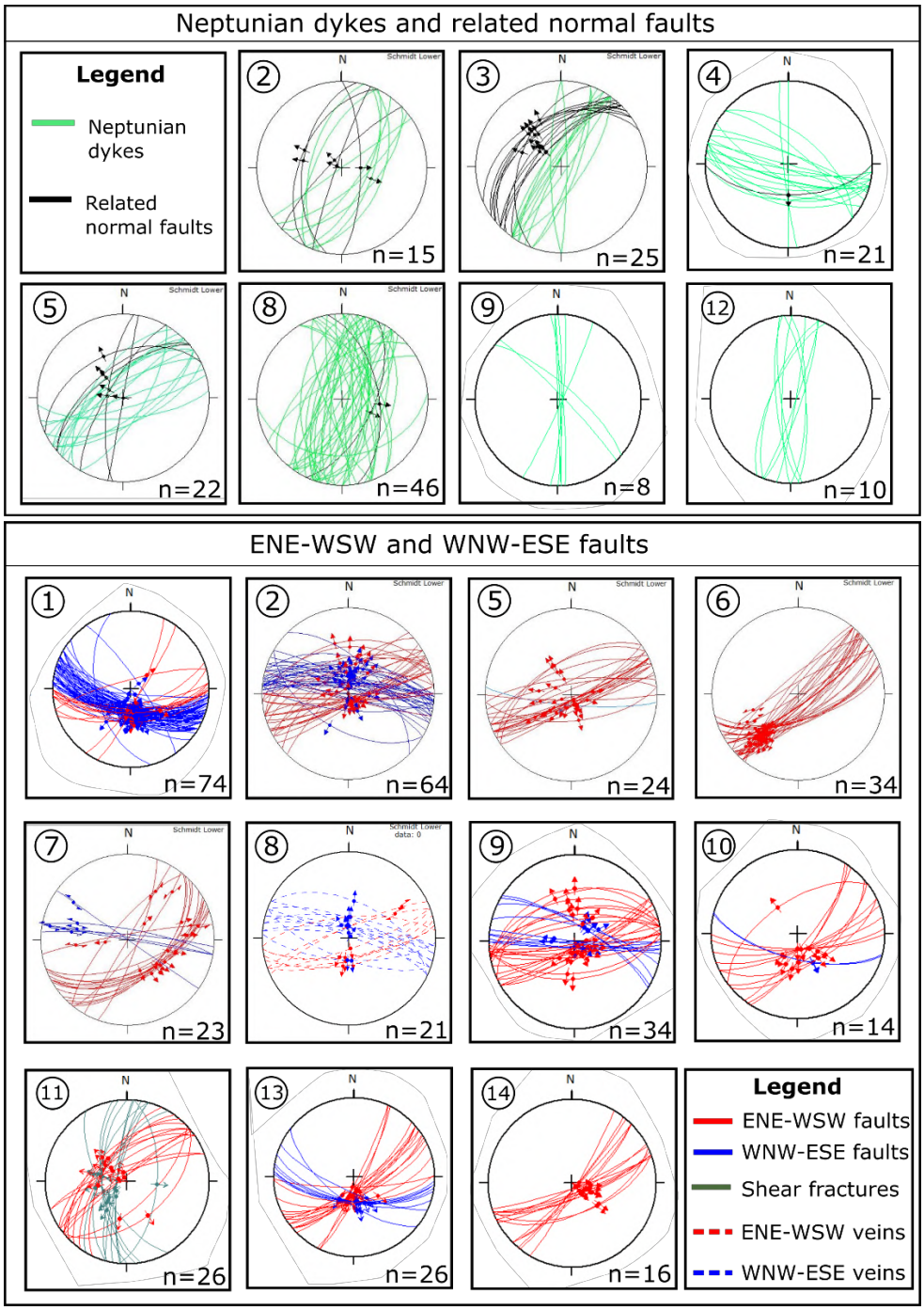

Figure 6. Lower hemisphere equal-area plots of kinematic data. Numbers of the outcrops are referred to those in Figure 2. Attitude data and pitches are available in table S2 and table S3 in the supporting data.

These are generally slickensides displaying grooves and/or calcite fibres testifying a normal to trans-tensional kinematics. ENE-WSW faults generally show dip-slip to slightly dextral-normal

movements, whereas WNW-ESE faults show dip-slip to normal-sinistral movements (Figure 6

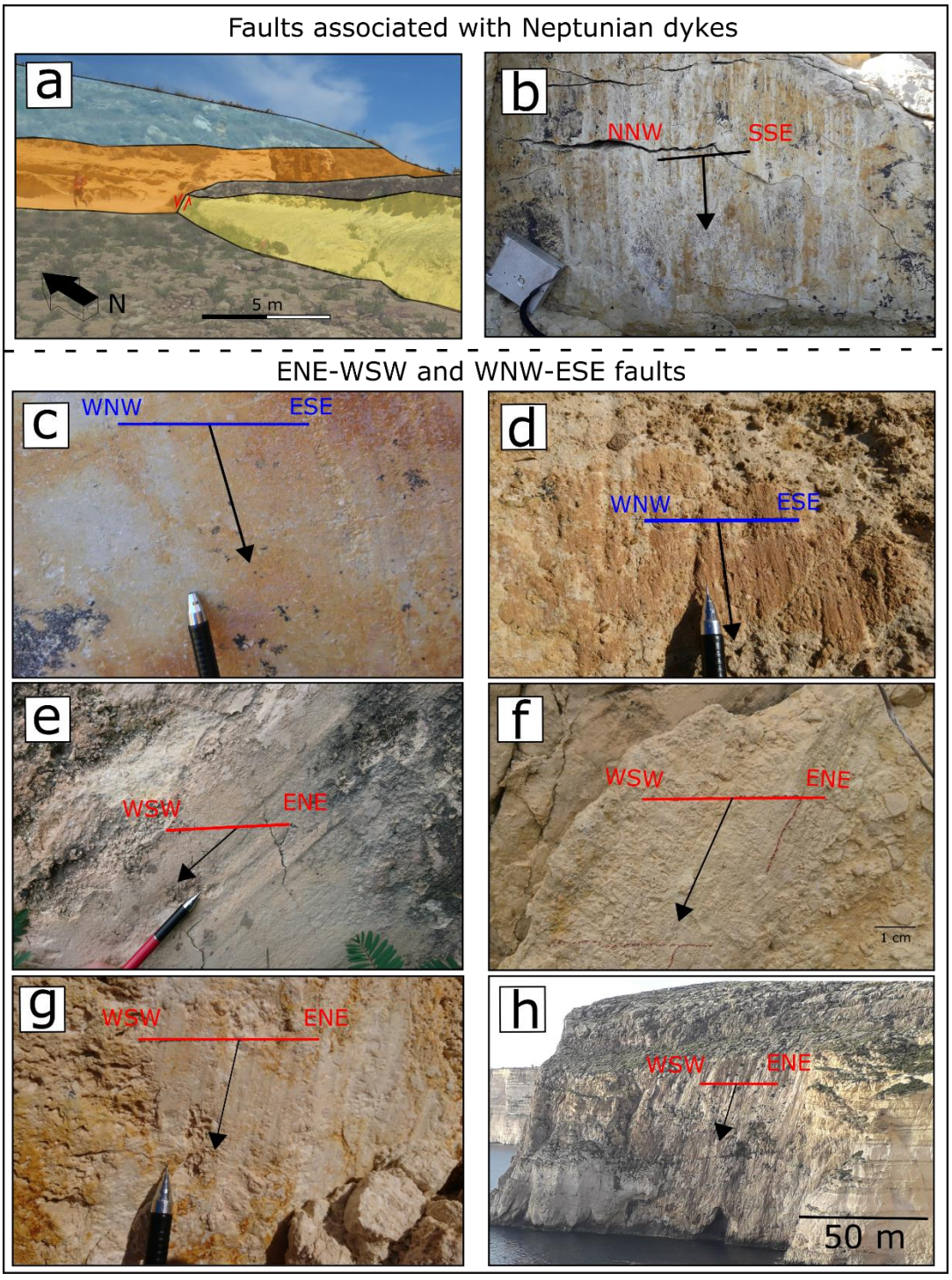

Figure 7. Kinematic indicators. (a) Stratigraphic off-set of the Lower Main Conglomerate Bed. (b) Kinematic indicators of normal faults associated with Neptunian dykes. (c, d) Kinematic indicators associated with WNW-ESE normal faults show a dip-slip to slightly sinistral movement. (e, f, g, h) ENE-WSW faults show dip-slip to normal-dextral movement. Colour-coding as in stratigraphic column of Figure 2a.

and Figure 7, c, d, e, f, g, h). In site 8, different calcite-filled hybrid opening/shear fibrous veins striking ENE-WSW and WNW–ESE have been found (Figure 6). The direction of the fibres usually shows a dip-slip to slightly dextral-normal movement for ENE-WSW veins and a dip-slip to normal-sinistral movement for WNW-ESE veins, in agreement with kinematic indicators observed on faults. Only in site 7, some strike-slip kinematic indicators have been found at the margin of a sinkhole (Figure 6). In site number 11, N-S striking shear-fractures, associated to the main fault plane (ENE-WSW), show dip-slip to slightly trans-tensional movements (Figure 6). Sites number 1, 2, 9, 11 and 13 are located on the major faults of Malta and Gozo. In particular site number 1 is on the Qala Fault, sites number 2 and 9 are on the South Gozo Fault, site number 11 is on the Victoria Fault and site number 13 is on the Maghlaq Fault (Figure 2b).

1.5 Structural analysis

1.5.1 Tectonic evolution

Field observations, kinematic indicators and cross-cutting or abutting relationships suggest that Neptunian dykes and associated normal faults (N-S, NE-SW and WNW-ESE) developed during a different and older tectonic event respect to WNW-ESE and ENE-WSW larger-scale normal faults (e.g Victoria Fault, South Gozo Fault, Maghlaq Fault, Qala Fault). Neptunian dykes are coeval to the Lower Main Conglomerate Bed (LMCB) since they are infilled by the material that forms the Conglomerate. Moreover, Neptunian dykes and related normal faults are interpreted as coeval because they have the same attitude, the same stratigraphic position (coeval to the Lower Main Conglomerate Bed (LMCB)) and they are all sealed by the Middle Globigerina Member, suggesting that they formed between the Late Aquitanian and the Early Burdigalian (22 – 17 Ma).

Conversely, WNW-ESE and ENE-WSW faults cut all the stratigraphic sequence, mutually cross cut and abut each other, and are not associated to any evidence of syn-sedimentary deformation. This suggests that they are coeval and that they formed after the deposition of the Upper Coralline Limestone.

Hence, our interpretation is that, from the Oligocene onward, the Maltese Islands underwent two main extensional tectonic events. The first (D1) between the Late Aquitanian and the Early Burdigalian (22 – 17 Ma) led to the formation of the Neptunian dykes and associated normal faults. The second (D2) led to the formation of ENE-WSW and WNW-ESE faults (e.g.Victoria Fault, South Gozo Fault, Maghlaq Fault, Qala Fault) and related fracture sets. D2 could have started during the Messinian (7-5 Ma), with an increased activity after 5 Ma, so after deposition of the Upper Coralline Limestone, which is cut by these faults and does not show evidence of syn-sedimentary deformation. This hypothesis is supported by the observation made by Dart et al. (1993), who found growth strata related to ENE-WSW and WNW-ESE faults in the offshore Plio-

Quaternary succession of the North Gozo Graben, and date their maximum activity to the Pliocene. Unfortunately, it is not possible to make hypotheses on post-Pliocene deformations since younger units do not outcrop in Malta or Gozo.

It is worth noting that the few strike-slip kinematic indicators, found only in site number 7, near some large sinkholes, are not related to a different regional tectonic phase (as suggested by Illies, 1981; Reuther & Eisbacher, 1985), but to the formation of the collapse structures (as already pointed out by Dart et al., 1993; Illies, 1980; Pedley, 1974). For this reason, this site has been excluded from the paleostress modelling.

1.5.2 Paleostress modelling

We have used paleostress modelling, with stress inversion techniques, to infer the paleostress regime that can be associated with deformation stages D1 and D2. We have subdivided fault slip data in subsets for stress inversion based on the tectonic evolution described in previous chapters. Hence we have not used automatic separation procedures (as suggested by e.g. Liesa & Lisle, 2004; Lisle & Srivastava, 2004; Simon, 2019; Sperner & Zweigel, 2010), but in every outcrop we have separated the Neptunian dykes and associated normal faults (D1 subset, Figure 8) from the ENE-WSW and WNW-ESE faults and associated veins and shear fractures (D2 subset, figure 9).

The fundamental assumption in stress inversion is that slip vectors measured on fault surfaces can be directly related to the underlying (paleo-) stress field, according to the Wallace-Bott hypothesis (Bott, 1959; Wallace, 1951) that the observed slip vector should be parallel to the tangential component of traction (the stress vector acting on a fault with a particular orientation; the angle α between these vectors is called deviation angle). Also the opening direction of tensional veins and dikes can be used as a constraint in stress inversion since it is assumed to be parallel to the least compressive stress axis σ_3 (e.g. Hubbert & Rubey, 1959). All stress inversion techniques rely on some sort of statistical procedure aimed at minimizing the difference between the set of observations and the predictions issued from a model stress field (e.g. Angelier, 1990). This means solving an inverse problem and explains the collective name of "stress inversion" techniques. Differences between these techniques, which will not be addressed here, regard mainly (i) the way the difference between the model and observables is calculated (target function), and (ii) the procedure used to perform the minimization (see Celerier et al., 2012; Delvaux and Sperner, 2003; Lacombe, 2012; Simon, 2019; Sperner and Zweigel, 2010 for extensive reviews).

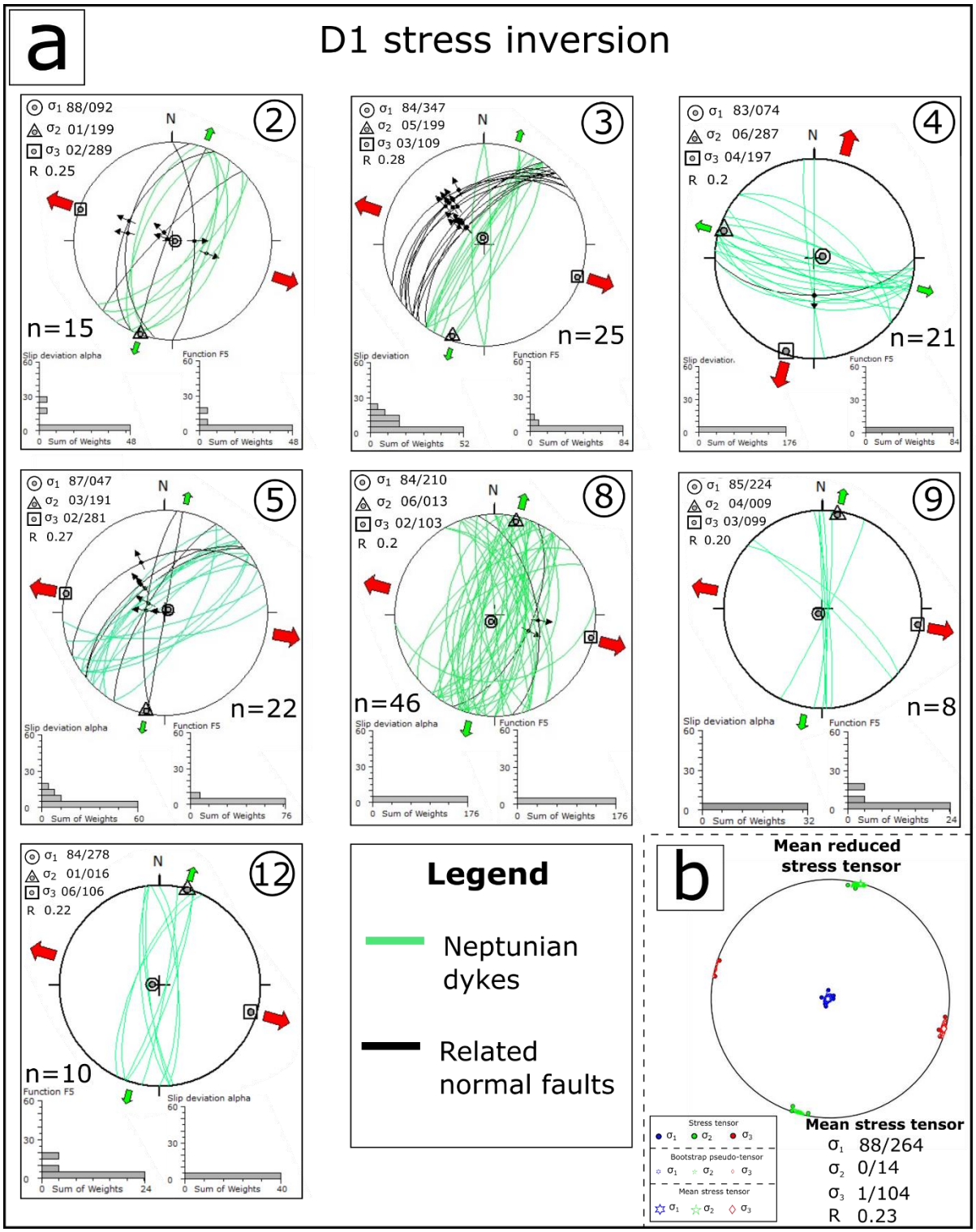

Figure 8. Stress inversion performed for D1 extension. (a) Results of the stress inversion. See text for explanation. Histograms show the values of F5 functions and of the slip deviation angle alpha. Outcrop numbers refer to those in Figure 2b. Kinematic data can be found in table S2 in the supporting information (Supplementary material in this thesis). (b) Mean stress tensor extracted from the bootstrapping analysis.

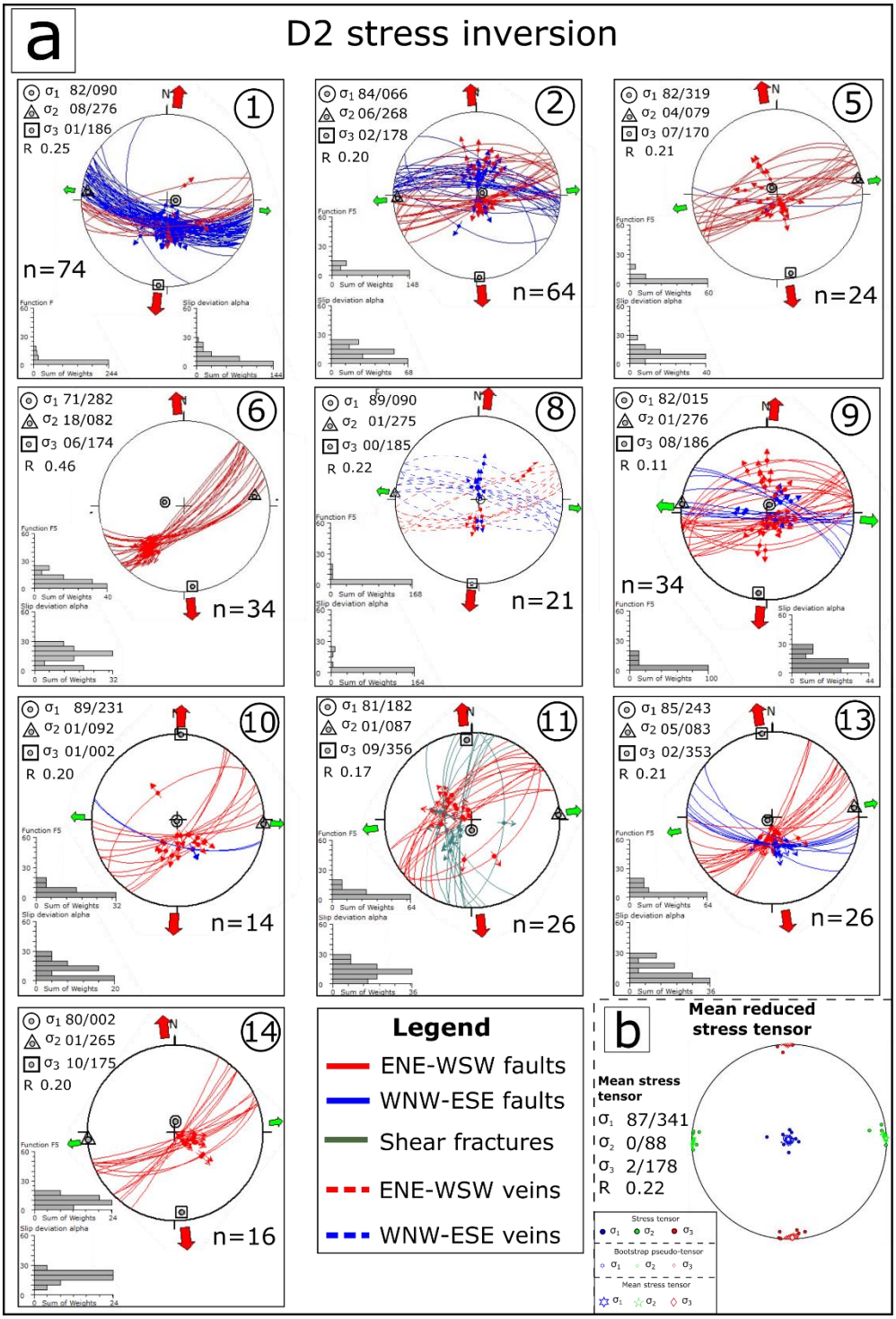

Figure 9. Stress inversion performed for D2 extension. (a) Results of the stress inversion. See text for explanation. Histograms show the values of F5 functions and of the slip deviation angle alpha. Outcrop numbers refer to those in Figure 2b. Kinematic data can be found in table S3 in the supporting information (Supplementary material in this thesis). (b) Mean stress tensor extracted from the bootstrapping analysis.

The assumptions implied in stress inversion techniques are generally considered reasonable if (e.g. Ramsay & Lisle, 2002, p. 785): (i) rocks can be considered isotropic or transversely isotropic (i.e. with anisotropy axes approximately parallel to stress axes), and (ii) displacements are small at the scale of the analysis (infinitesimal strain and rotation). Both conditions are met in Malta and Gozo, where faults show generally limited slip and bedding is always sub-horizontal (transverse isotropy condition) thus providing an ideal area for paleostress modelling.

In this work, we used the F5 target function (Delvaux and Sperner, 2003) in the implementation provided by WinTensor (www.damiendelvaux.be/Tensor/tensor-index.html). This target function is particularly well suited for the case at hand because it allows for the simultaneous inversion of slip-vectors and opening directions. As suggested by Delvaux and Sperner (2003) and Angelier (1990), we consider as reliable a paleostress tensor solution if in the fluctuation histograms we do not observe values of the target function F5 > 20 and of the deviation angle $\alpha > 30$.

The solution to stress inversion problems is given in terms of a reduced stress tensor (e.g. Angelier, 1990), defined in an adimensional way by the orientations of the principal stress axes and the shape ratio defining the relative magnitude of σ2 with respect to σ1 and σ3 as $\varphi = (\sigma2 - \sigma3)/(\sigma1 - \sigma3)$ (Angelier, 1990).

Since the unknowns are four (three orientations and the shape ratio), in order to obtain a robust numeric solution at least four statistically independent structure sets are needed (e.g. Angelier, 1990). In our study this condition is met in all considered outcrops (Figure 8 and Figure 9).

Finally, we obtain the mean stress at the scale of the islands of Gozo and Malta for each deformation stage by summation of the stress tensors, normalization, and calculation of the eigenvectors and eigenvalues of the mean tensor (Jelinek, 1981; Traforti et al., 2018). To test the reliability and homogeneity of means stress tensor solutions, we applied a bootstrap modelling (Constable and Tauxe, 1990; Efron, 1979;) implemented in a custom Matlab script (Traforti et al., 2018) (Figure 8b and 9b).

1.5.2.1 D1 extension

Stress inversion for D1 extension (Figure 8a) indicates that kinematic data collected in all outcrops are consistent with a WNW-ESE extension with a sub-vertical σ_1, σ_3 sub-horizontal trending WNW-ESE, and σ_2 sub- horizontal NNE-SSW, with σ_2 very close in magnitude to σ_3 (Bai et al., 2002) and a shape ratio $\varphi \approx 0.23$. Moreover, in all outcrops the value of the F5 function remains under 20 and the angle α is always less than 30°, confirming that all the fault slip data are compatible with the stress tensor model. Only site number 4 differs from the others (Figure 8a) since σ_2 and σ_3 show a permutation with respect to the other sites. This can be justified as just a

local perturbation, owing to the fact that also in the other sites σ_2 and σ_3 are very close in magnitude. The average reduced stress tensor, calculated excluding site number 4, has principal stress axes (trend/plunge) σ_1 = 264/88, σ_2 = 14/00, σ_3 = 104/01, and shape ratio $\varphi = (\sigma_2 - \sigma_3)/(\sigma_1 - \sigma_3)$ = 0.23. Bootstrapping analysis indicates a high degree of homogeneity within the different outcrops (Figure 8b).

1.5.2.2 D2 extension

Stress inversion for D2 extension (Figure 9a) indicates that kinematic data collected in all outcrops are consistent with a N-S extension with σ_1 sub-vertical, σ_3 sub-horizontal directed N-S, and σ_2 sub-horizontal E-W, with σ_2 very close in magnitude to σ_3 and a shape ratio $\varphi \approx 0.28$. Moreover, in all outcrops the value of the F5 function remains under 20 and the angle α is always less than 30°, confirming that all the fault slip data are compatible with the stress tensor model. The average reduced stress tensor has principal stress axes (trend/plunge) σ_1 = 341/87, σ_2 = 88/00, σ_3 = 178/02, and shape ratio $\varphi = (\sigma_2 - \sigma_3)/(\sigma_1 - \sigma_3)$ = 0.22. Bootstrapping analysis indicates a high degree of homogeneity within the different outcrops (Figure 9b).

1.6 Implications for the geodynamic evolution of the Pelagian Platform and Pantelleria Rift System

We can summarize the tectonic evolution of the Maltese Islands from the Late Oligocene to the Pliocene by defining the following deformation phases:

D1) Oblate WNW-ESE extension (σ_2 close in magnitude to σ_3) developed during the Late Aquitanian-Early Burdigalian (20 -17 Ma), resulting in small normal faults (separation < 5m) with associated Neptunian dykes

D2) Oblate N-S extension (σ_2 close in magnitude to σ_3) developed from the Late Miocene to Pliocene (7 – 1.5 Ma), leading to nucleation and propagation of two coeval fault sets, striking WNW-ESE and ENE-WSW, with separation of up to 200 meters. These fault sets include the major regional faults in Malta and Gozo (e.g.Victoria Fault, South Gozo Fault, Maghlaq Fault, Qala Fault).

The fact that the ENE-WSW and WNW-ESE faults and fracture sets are coeval is demonstrated by mutual cross-cutting and abutting relationships, and by the absence of a progressive rotation of fault and fracture systems going upwards in the stratigraphy.

The formation of two coeval fault sets oblique to the main extension direction can be explained with a three-dimensional deformation where all the principal strain axes are different from zero (Krantz, 1988; Reches, 1978, 1983; Reches & Dieterich, 1983). These kind of fault systems,

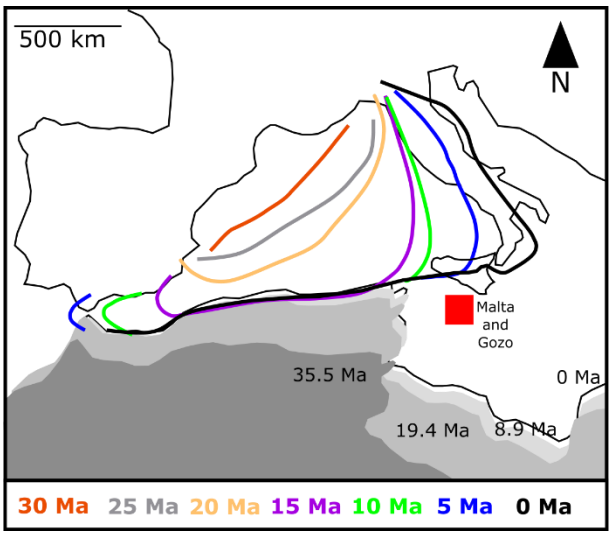

Figure 10. Position of the thrust front in the Western and Central Mediterranean from 30 to 0 Ma and motion of Africa with respect to fixed Eurasia as calculated by Dewey et al. (1989). Movement of the trench was redrawn after Royden and Faccenna, (2018) while African motion was redrawn after Faccenna et al. (2001). The Maltese Islands are highlighted in red.

sometimes called orthorhombic systems (Krantz, 1988; Reches, 1978, 1983; Reches & Dieterich, 1983), have been already described in different areas of the world in extensional tectonic settings (Aydin & Reches, 1982; Bistacchi & Massironi, 2000; Carvell et al., 2014; Collanega et al., 2017; Franceschi et al., 2014; Krantz, 1988; Miller et al., 2007).

While structures associated to D1 were considered only in a few previous studies (Dart et al., 1993; Gatt, 2005; Illies, 1981; Reuther & Eisbacher, 1985), and never associated with a regional-scale tectonic event, the larger faults associated to D2 are well known and in the past have been associated with different and contrasting deformation phases (Argnani, 1990; Ben-Avraham et al., 1987; Boccaletti et al., 1987; Catalano et al., 2009; Cello, 1987; Dart et al., 1993; Finetti, 1984; Grasso & Reuther, 1988; Jongsma et al., 1985; Reuther & Eisbacher, 1985). Our approach, combining stress inversion modelling and dating of deformation structures using crosscutting and abutting relationships and relationships with stratigraphy, allowed clarifying the tectonic evolution of the Maltese Islands.

In the following we show how the tectonic evolution of the Maltese Islands fits in the geodynamic evolution of the Central and Western Mediterranean, from the Oligocene onward, as proposed by Faccenna et al., (2001, 2004a, 2004b). Noteworthy, the structures discussed in this contribution represent the only outcropping record of the stress regime in the Pelagian Platform (a large marine area) and the only opportunity to constrain the geodynamic evolution of this area, from the Late Oligocene to the Pliocene, with structural data collected in the field.

1.6.1 Cenozoic Evolution of the Western and Central Mediterranean

In the Late Eocene (35 Ma) the area from Iberia to the Present Ligurian region was characterized by a wide SE trending subduction zone more than 1500 km long called the Western Mediterranean Subduction Zone (WMSZ; Faccenna et al., 2004a, 2004b). The movement of the trench and position of Africa with respect to Eurasia between 30 Ma and present is summarized in Figure 10. The slab was dipping towards NW consuming an oceanic domain, now completely subducted if we exclude slices tectonically accreted in the Apennine-Sicilian-Maghrebian Belt (Le Pichon et

al., 1988). At 30 Ma the slab started a retrograde SE motion (Cherchi & Montandert, 1982; Facenna et al.2004a, 2004b; Gorini et al., 1994; Jolivet et al., 1999; Jolivet and Facenna, 2000; Serranne, 1999) that propagated southward between 30 and 23 Ma, with extension both in the back-arc region and in the orogenic wedge (Caby et al., 2001; Garcia-Duenas et al., 1986; Jabaloy et al., 1993; Rossetti et al., 2001; Saadallah & Caby, 1996). Between 23 and 15 Ma the extension reached its maximum velocity with the counter-clockwise rotation of the Sardinia-Corsica block (Burrus, 1984; Van der Voo, 1993). During all this evolution, the position of the Maltese Islands remained more or less constant as demonstrated by paleomagnetic data (Brandano et al., 2008; Dewey et al., 1989). Extension continued up to 17 - 16 Ma, when the retrograde movement of the slab ended and with it the extension in the Central and Western Mediterranean. Between 15 and 10 Ma no important extension was observed in the region. The tectonic activity started again at c. 10 Ma in the Tyrrhenian region (Faccenna et al., 2001) with an increase of the extension rate at 5 Ma due to the roll back of the Calabrian slab under the Appenine-Sicilian-Maghrebian Belt. (Faccena et al., 2004a).

1.6.2 Early Miocene extension (D1)

During D1, in the Late Aquitanian/Early Burdigalian (20 -17 Ma), the Liguro-Provencal basin was completing its opening with the rapid counter-clockwise rotation of the Sardinia-Corsica block. The trench of the future Apennine-Sicilian-Maghrebian Belt was oriented NE-SW and was crossing all the Mediterranean in a more westerly position with respect to the present one (Figure 11 a, b, c), but it was already migrating towards the E due to slab roll back (Faccenna et al, 2001; 2004a, 2004b). Our interpretation is that this migration eventually brought the Maltese Islands and surrounding areas (Sicily, Tunisia, Pelagian Platform, and the future Pantelleria Rift System) in a foreland position causing the onset of the WNW - ESE extension that led to phase D1. (Figure 11 c, 11f). Similar evidences of extensional tectonics during the Early Miocene have been found by other authors in different areas of the Central Mediterranean. Pedley & Grasso (1992) describe the presence of N-S-trending structures in the NW part of the Hyblean platform (NW Sicily) that should have been active in this period. Tavani et al. (2015b) found evidences of an Early Burdigalian extension in the Penestrini Mountains (Central Apennines) followed by a tectonic quiescence up to the Tortonian. Belguith et al. (2011) have documented a minor Lower-Middle Miocene extension in onshore Tunisia. La Bruna et al. (2017, 2018) reported several evidences of extensional tectonics associated to the foreland basin evolution in the Monte Alpi area (Southern-Appenines) during the Miocene. The conclusion of phase D1 observed in Gozo at c. 17 Ma is consistent with a quiescence in slab roll back documented between 17 and 7 Ma by Faccenna et al., (2001, 2004a, 2004b). (Figure 11d, 11f).

1.6.3 Late Miocene – Pliocene extension (D2)

The age of phase D2 (Late Miocene – Pliocene) corresponds to a renewed activity of the Apennine-Sicilian-Maghrebian Belt and migration of the trench due to roll-back of the Calabrian slab (Figure 11e-11f). In this period however, the geometry and kinematics of the slab changed with respect to the Early Miocene, and the belt assumed the present arc shape, due to a very pronounced and radial slab roll-back (Faccenna, 2004a). The increase of the slab velocity was caused by the slab break-off in the Sicily channel (Faccena et al., 2001, 2004a, 2004b). This event caused the two slabs to roll-back in different radial directions. Southwards in North Africa and in the Maltese region, and South-eastwards in Calabria (Faccena et al., 2001, 2004a, 2004b). In the region of the Pelagian Platform, this resulted in a switch from WNW-ESE extension to N-S extension, which is reflected in phase D2 (Figure 11 e-11f). In the area of the Maltese Islands, this led to the formation of the Maltese Graben System together with the related ENE-WSW and WNW-ESE faults (Victoria Fault, South Gozo Fault, Mahgalq Fault, to cite the larger ones).

This reconstruction is confirmed by data collected by other authors. Dart et al. (1993), using seismic data collected across the North Gozo Graben, recognized ENE-WSW and WNW-ESE trending faults dated to the Late Miocene and Pliocene. Villani et al. (2018) suggested that the Victoria Fault started its activity during the Late Miocene, with a maximum slip-rate during the Pliocene. Reuther & Eisbacher (1985) proposed the same evolution for the South Gozo Fault.

At the regional scale, the D2 extension caused the opening of the Pantelleria Rift System that is Late Miocene to Pliocene in age (Civile et al., 2008; Dart, 1993; Finetti & Morelli, 1972; Illies, 1981; Reuther and Eisbacher, 1985). Even if the Pantelleria Rift System is mainly bounded by WNW-ESE trending faults, which accommodate most of the displacement (Civile et al., 2010; Finetti, 1984; Reuther & Eisbacher, 1985), also ENE-WSW trending faults have been observed in seismic data (Argnani, 1990; Boccaletti et al, 1987; Finetti, 1984), confirming that the fault pattern recognized in the Maltese Islands is representative of the regional scale fault system of the rift. Dart et al. (1993) have shown that the stratigraphic sequence of the Maltese Islands is the same of the Pantelleria Rift, and they demonstrated that the two areas underwent the same tectonic history. All these data confirm our interpretation that the Pantelleria Rift System and the Maltese Graben System are coeval and they were formed in response to a N-S extension started from the Late Miocene, and mainly in the Pliocene, in agreement with the hypothesis proposed from Argnani (1990) and Dart et al. (1993).

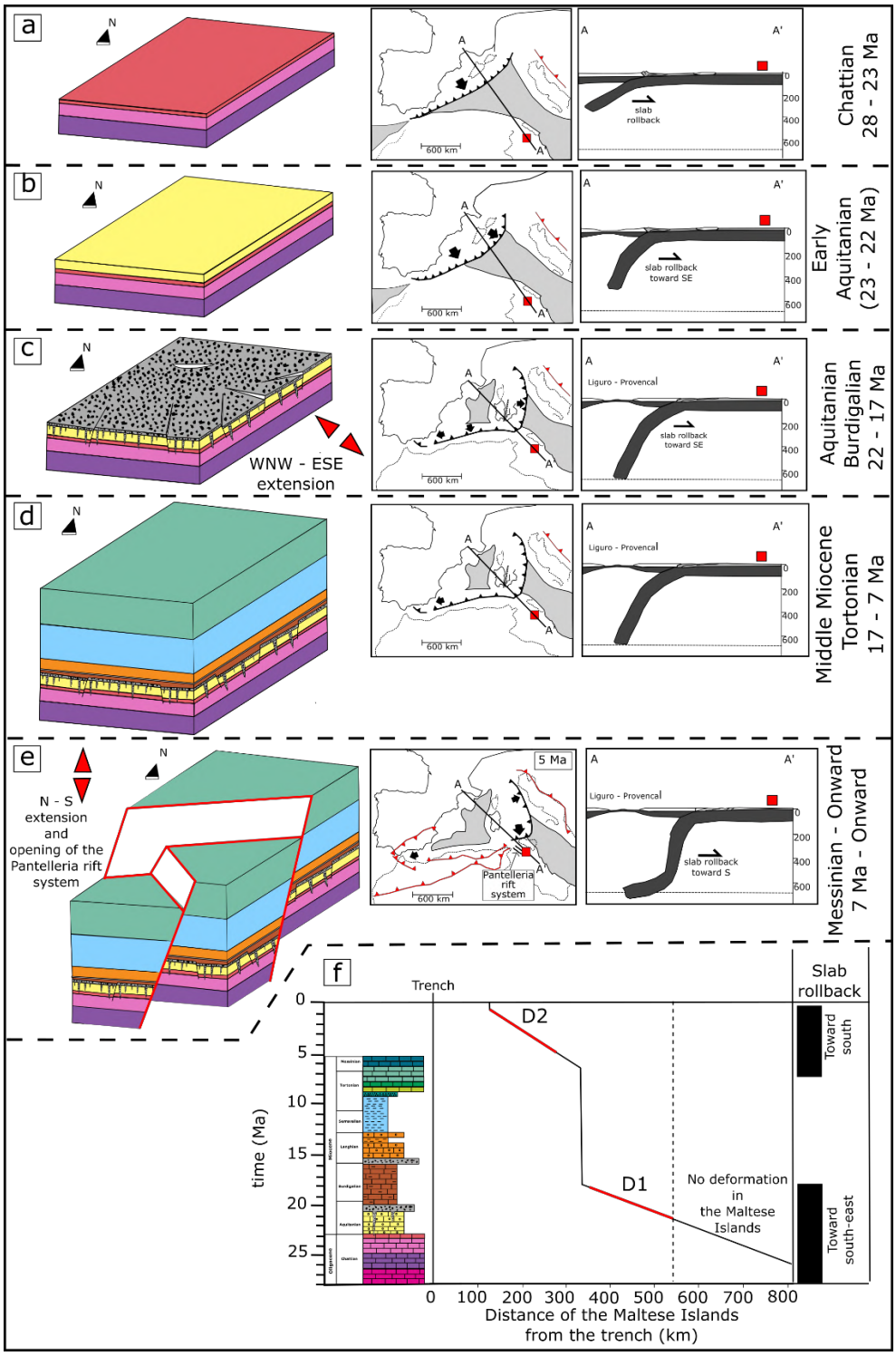

Figure 11. (a, b, c, d, e) Tectonostratigraphic evolution of the Maltese Islands in the framework of the geodynamic evolution of the Western and Central Mediterranean (see text for explanation). Colours refer to the stratigraphic column of Figure 2a. Sketches of trench and slab migration modified after Faccenna et al. (2001; 2004a; 2004b), with section A-A' translated in order to reach the Maltese Islands. Red square highlights the position of the Maltese Islands. (f) Position of the Maltese Islands with respect to the trench.

Extensional activity in others part of the foreland of the Apennine-Sicilian-Maghrebian Belt have been documented by other authors. Scisciani et al., (2002) and Scisciani and Monfalcone, (2006) described Pliocene and Messinian extensional faults in central Apennine. Belguith et al., (2011) recognized different NW-SE trending rifts in Tunisia formed in response to an extensional event that took place between the latest Miocene and the Early Quaternary. Barrier (1992) documented the presence of ENE-WSW and NW-SE normal faults in the Ragusa Platform (SE Sicily) formed during the Late Miocene-Early Pliocene in response to the flexure of the foreland.

1.7 Conclusions

1) From the Late Oligocene to the Pliocene the Maltese Islands underwent two main deformation events divided by a period of tectonic quiescence:
    - The D1 oblate WNW - ESE extension (σ_2 close in magnitude to σ_3) developed during the Late Aquitanian-Early Burdigalian (20 -17 Ma), resulting in small normal faults (separation < 5m) with associated Neptunian dykes.
    - The D2 oblate N-S extension (σ_2 close in magnitude to σ_3) developed from the Late Miocene to the Pliocene (7 – 1.5 Ma), leading to nucleation and propagation of two coeval sets of regional-scale faults, striking WNW-ESE and ENE-WSW, with separations of up to 200 meters and to the opening of the Pantelleria Rift System.
2) We interpret both the extensional events as caused by the foreland flexure and slab roll-back. Indeed, both tectonic events took place during periods of slab-retreat, while the tectonic quiescence between D1 and D2 corresponds to a stasis of the slab roll-back.
3) In this context, fault-slip data can be used as an independent tool to "monitor" the slab roll-back evolution.

Acknowledgments

Fieldwork and structural analysis was carried out by Martinelli, Bistacchi and Balsamo. Meda participated in important discussions after field work. This paper was written by Martinelli with contributions from all co-authors. We thank Eni Spa for funding, reviewing and allowing us to publish the results of the study. Damien Delvaux is thanked for making available the WinTensor software for stress inversion. The bootstrapping analysis was performed with a Matlab code written by Bistacchi. The Malta Planning Authority and the Malta Resources Authority are acknowledged for providing topographic data and base geological maps. Aaron Micallef and Martin Pedley are warmly acknowledged for fruitful discussions and a very useful introduction to the geology of Malta and Gozo. Fabrizio Storti and Silvia Mittempergher are warmly thanked for continuing and fruitful discussions during this project. Student Anna Losa is thanked for field

assistance. All structural and kinematic data can be found in the supporting information (Tables S1, S2, S3) together with a detailed 1:25000 geological map (Figure S1). Moreover, structural and kinematic data are stored in the B2 SHARE repository (https:// b2share.eudat.eu/) with the following record number 2f4930d68315451684908985b5c68f3aWe also thank the Editor Laurent Jolivet, the anonymous associated editor, two anonymous reviewers and Vincenzo La Bruna for their comments that helped us to improve the manuscript.

References

Angelier, J. (1990). Inversion of field data in fault tectonics to obtain the regional stress. III—a new rapid direct inversion method by analytical means. Geophysical Journal International 103, 363–376.

Argnani, A. (1990). The strait of sicily rift zone: Foreland deformation related to the evolution of a back-arc basin. Journal of Geodynamics, 12(2–4), 311–331. https://doi.org/10.1016/0264-3707(90)90028-S

Aydin, A., & Reches, Z. (1982). Number and orientation of fault sets in the field and in experiments. Geology 10:107–112. http://dx.doi.org/10.1130/0091-7613(1982)10b107: NAOOFSN2.0.CO;2.

Bai, T., Maerten, L., Gross, M.R., & Aydin, A. (2002). Orthogonal cross joints: do they imply a regional stress rotation? J. Struct. Geol. 24 (1), 77–88.

Bates, R.L., & Jackson, J.A. (1980). 2nd. Glossary of Geology, vol. 751 Am. Geol. Inst.

Barrier, E. (1992). Tectonic analysis of a flexed foreland: the Ragusa Platform. Tectonophysics, 206: 91-111.

Beaudoin, N., Leprêtre, R., Bellahsen, N., Lacombe, O., Amrouch, K., Callot, J.P., Emmanuel, L., & Daniel, J.M. (2012). Structural and microstructural evolution of the Rattlesnake Mountain Anticline (Wyoming, USA): new insights into the Sevier and Laramide orogenic stress build-up in the Bighorn Basin. Tectonophysics 576, 20–45

Belguith, Y., Geoffroy, L., Rigane, A., Gourmelen, C., & Ben, H. (2011). Tectonophysics Neogene extensional deformation and related stress regimes in central Tunisia. Tectonophysics, 509(3–4), 198–207. https://doi.org/10.1016/j.tecto.2011.06.009

Ben-Avraham, Z., Nur, A., & Giuseppe, C. (1987). Active transcurrent fault system along the north African passive margin. Tectonophysics, 141(1–3), 249–260. https://doi.org/10.1016/0040-1951(87)90189-2

Bianucci, G., Gatt, M., Catanzariti, R., Sorbi, S., Bonavia, C. G., Curmi, R., & Varola, A. (2011). Systematics, biostratigraphy and evolutionary pattern of the Oligo-Miocene marine mammals from the Maltese Islands. Geobios, 44(6), 549–585. https://doi.org/10.1016/j.geobios.2011.02.009

Billi, A., & Salvini, F. (2003). Development of systematic joints in response to flexure-related fibre stress in flexed foreland plates: The Apulian forebulge case history, Italy. Journal of Geodynamics, 36 (4), 523–536

Bistacchi, A., & Massironi, M. (2000). Post-nappe brittle tectonics and kinematic evolution of the north-western Alps: an integrated approach. Tectonophysics, vol. 327; p. 267-292, ISSN: 0040-1951.

Boccaletti, M., Cello, G., & Tortorici, L.(1987). Transtensional tectonics in the Sicily Channel. Journal of Structural Geology, Vol. 9, No.7, pp. 869–876.

Bonson, C. G., Childs, C., Walsh, J. J., Scho, M. P. J., & Carboni, V. (2007). Geometric and kinematic controls on the internal structure of a large normal fault in massive limestones : The Maghlaq Fault , Malta. Journal of Structural Geology 29, 336–354. https://doi.org/10.1016/j.jsg.2006.06.016

Bosence, D. W. J., & Pedley, H. M. (1982). Sedimentology and palaeoecology of a miocene coralline algal biostrome from the Maltese Islands. Paleogeography, Paleoclimatology, Paleoecology 38, 9–43.

Bott, M. H. P. (1959). The mechanics of oblique-slip faulting. Geological Magazine, 96,109-117.

Bradley, D.C., & Kidd, W.S.F. (1991). Flexural extension of the upper continental crust in collisional foredeeps. GSA Bulletin 103 (11), 1416–1438.

Brandano, M., Frezza, V., Tomassetti, L., Pedley, M., Cuffaro, M., & Matteucci, R. (2008). The controlling factors of an Upper Oligocene carbonate ramp (Attard Member, Lower Coralline Lms. Fm., Malta): from facies to paleolatitude. Rendiconti online Società Geologica Italiana, 45-50.

Burrolet, P. F., Mugniot, J., & Sweeney, P. (1978). The geology of the Pelagian Block. The Margins and Basins of Southern Tunisia and Tripolitania. In: The Ocean Basins and Margins, 4B, A. Nairn & W. Kanes, eds., 331-359.

Burrus, J. (1984). Contribution to a geodynamic synthesis of the Provencal basin (north-western Mediterranean), Marine Geology, 55, 247 – 269.

Caby, R., Hammor, D., & Delor, C. (2001). Metamorphic evolution, partial melting and Miocene exhumation of lower crust in the Edough metamorphic core complex, west Mediterranean orogen, eastern Algeria. Tectonophysics, 342: 239–273.

Carvell, J., Blenkinsop, T., Clarke, G., & Tonelli, M. (2014). Scaling, kinematics and evolution of a polymodal fault system: Hail Creek Mine, NE Australia. Tectonophysics, 632: 138–150. http://dx.doi.org/10.1016/j.tecto.2014.06.003.

Catalano, S., Guidi, G., De, Lanzafame, G., & Tortorici, L. (2009). Late Quaternary deformation on the island on Pantelleria: New constraints for the recent tectonic evolution of the Sicily Channel Rift (southern Italy). Journal of Geodynamics, 48, 75–82. https://doi.org/10.1016/j.jog.2009.06.005

Célérier, B., Etchecopar, A., Bergerat, F., Vergely, P., Arthaud, F., & Laurent, P. (2012). Inferring stress from faulting: From early concepts to inverse methods. Tectonophysics, 581, 206–219. https://doi.org/10.1016/j.tecto.2012.02.009

Cello, G. (1987). Structure and deformation processes in the Strait of Sicily "rift zone". Tectonophysics, 141, 237–247.

Civile, D., Lodolo, E., Tortorici, L., Lanzafame, G., & Brancolini, G. (2008). Relationships between magmatism and tectonics in a continental rift: The Pantelleria Island region (Sicily Channel, Italy). Marine Geology, 251, 32–46.

Civile, D., Lodolo, E., Accettella, D., Geletti, R., Ben-Avraham, Z., Deponte, M., Facchin, L., Ramella, R., & Romeo, R. (2010). The Pantelleria graben (Sicily Channel, Central Mediterranean): An example of intraplate 'passive' rift. Tectonophysics, 490, 173–183.

Cherchi, A., & Montandert, L. (1982). Oligo-Miocene rift of Sardinia and the early history of the Western Mediterranean Basin, Nature, vol. 298, 736–739.

Constable, C., & Tauxe, L. (1990). The bootstrap for magnetic susceptibility tensors. Journal of Geophysical Research, 95(B6), 8383. https://doi.org/10.1029/JB095iB06p08383

Cooke, A. P., Fisher, Q. J., Michie, E. A. H., & Yielding, G. (2018). Investigating the controls on fault rock distribution in normal faulted shallow burial limestones , Malta , and the implications for fluid flow. Journal of Structural Geology, 114, 22–42. https://doi.org/10.1016/j.jsg.2018.05.024

Collanega, L., Massironi, M., Breda. A., & Kiølhamar B. E. (2017). Onset of N-Atlantic rifting in the Hoop Fault Complex (SW Barents Sea): An orthorhombic dominated faulting?. Tectonophysics 706-707, 59-70. http://dx.doi.org/10.1016/j.tecto.2017.04.003

Cozzi, A. (2000). Synsedimentary tensional features in Upper Triassic shallow-water platform carbonates of the Carnian Prealps (northern Italy) and their importance as palaeostress indicators. Basin Research. 12, 133–146. https://doi.org/10.1046/j.1365-2117.2000.00117.x.

Črne, A.E., Šmuc, A., & Skaberne, D. (2007). Jurassic neptunian dikes at Mt Mangart (Julian Alps, NW Slovenia). Facies 53 (2), 249–265. https://doi.org/10.1007/s10347-007-0102-8.

Dart, C. J., Bosence, D. W. J., & Mccay, K. R. (1993). Stratigraphy and structure of the Maltese graben system. Journal of the Geological Society, 150(6), 1153–1166. https://doi.org/10.1144/gsjgs.150.6.1153

Davis, G. H, Reynolds S.J., & Kluth C.F. (2011). Structural Geology of Rocks and Regions, 3rd edition, ISBN: 0471152315, 839 pages. New York Jhon Wiley and Sons Inc.

Delvaux, D., & Sperner, B. (2003). Stress tensor inversion from fault kinematic indicators and focal mechanism data: the TENSOR program. In: New Insights into Structural Interpretation and Modelling (D. Nieuwland Ed.). Geological Society, London, Special Publications, 212: 75-100.

Dewey, J.F., Helman, M.L., Turco, E., Hutton, D.H.W., & Knott, S.D. (1989). Kinematics of the western Mediterranean. In Alpine Tectonics, ed.MP Coward,D Dietrich, R G Park, pp. 265–83. Geological Society Special Publication 45. London: Geol. Soc. Lond.

Doglioni, C. (1995). Geological remarks on the relationships between extension and convergentgeodynamic settings. Tectonophysics 252 (1), 253–267.

Efron, B. (1979). Bootstrap methods: another look at the jackknife. The Annals of Statistics, Vol. 7, No. 1, 1-26.

Faccenna, C., Becker, T.W., Lucente, F.P., Jolivet, L., Rossetti, F. (2001). History of subduction and back arc extension in the Central Mediterranean. Geophysical Journal International 145, 809–820.

Faccenna, C., Piromallo, C., Crespo-Blanc, A., Jolivet, L., Rossetti, F. (2004a). Lateral slab deformation and the origin of the western Mediterranean arcs. Tectonics 23 (TC1012). doi:10.1029/2002TC001488.

Faccenna, C., Funicello, F., Piromallo, C., Rossetti, F., Giardini, D., & Funiciello, R. (2004b). Subduction and back –arc extension in the Tyrrhenian Sea. Mem. Descr. Carta Geol.d'It. XLIV, pp.165-184

Felix, R. (1973). Oligo--Miocene stratigraphy of Malta and Gozo. Mededelingen. Landbouwhogeschool Wageningen, 73-20.

Finetti, I. (1982). Structure, stratigraphy and evolution of the central Mediterranean. Bollettino di geofisica Teorica ed Applicata, 24, 247-312

Finetti, I. (1984). Geophysical study of the Sicily Channel rift zone. Bollettino di geofisica Teorica ed Applicata, 26, 3-28

Finetti, I., & Morelli, C. (1972). Wide scale digital seismic exploration of the Mediterranean Sea. Bolletino di Geofisica Teorica ed Applicata, 14, 291–342.

Forsyth, D., & Uyeda, S. (1975). Geophysical Journal International, Volume 43, Issue 1, October 1975, Pages 163–200, https://doi.org/10.1111/j.1365-246X.1975.tb00631.x

Franceschi, M., Massironi, M., Franceschi, P., & Picotti, V. (2014). Spatial analysis of thickness variability applied to an Early Jurassic carbonate platform in the central Southern Alps (Italy): a tool to unravel syn-sedimentary faulting. Terra Nova, 26, 239–246. http://dx.doi.org/10.1111/ter.12092

Garcıa-Duenas, V., Martìnez, J.M., & Navarro, F. (1986). La zona de falla de Torres Cartas, conjunto de fallas normales de bajo ángulo entre Nevado-Filábrides y Alpujárrides (Sierra Al-hamilla, Béticas orientales), Geogaceta, 1, 17–19.

Gatt, P. A. (2005). Syntectonic Deposition of an Oligo-Miocene Phosphorite Conglomerate Bed in Malta. The Central Mediterranean Naturalist, 4(2), 109–118.

Giannelli, L., & Salvatorini, G. (1975). I foraminifera planctonici dei sedimenti Teziari dell'Archipelago Maltese. Atti della Società Toscana di Scienze Naturali, Memorie Serie A, 83 ,1-24.

Gorini, C., Mauffret, A., Guennoc, P., & Le Marrec, A. (1994). Structure of the Gulf of Lions (northwestern Mediterranean Sea): A rewiev, in Hydrocarbon and Petroleum geology of France, edited by A. Mascle, pp. 223-243, Eur. Assoc. of Pet. Geol., Houten, Netherlands.

Grasso, M., & Reuther, C.D. (1988). The western margin of the Hyblean plateau: a neotectonic transform system on the SE Sicilian foreland Annales Tectonicae, 2, 107-120.

Gross, M.R. (1993). The origin and spacing of cross joints: examples from the Monterey Formation, Santa Barbara Coastline, California. Journal of Structural Geology. 15 (6), 737–751.

Hill, K.V., & Hayward, A.B. (1988). Structural constraints of the Tertiary plate tectonic evolution of Italy. Marine and Petroleum Geology, 5, 2-15.

Hubbert, M. K., & Rubey, W. W. (1959). Role of fluid pressure in the mechanics of overthrust faulting. Bulletin of the Geological Society of America, 70, 115-205.

Illies, J. H.(1981). Graben Formation – the Maltese Island – a case history. Tectonophysics 73, 151–168.

Jabaloy, A., Galindo-Saldivar, J., & Gonzales-Lodeiro, F. (1993). The Alpujarride-Nevado-Filabride extensional shear zone, Betic Cordillera, SE Spain. Journal of Structural Geology, 15, 555 – 569.

Jelinek, V. (1981). Characterization of the magnetic fabric of rocks. Tectonophysics, 79(3–4), T63–T67. https://doi.org/10.1016/0040-1951(81)90110-4

Jolivet, L., Faccenna, C., D'Agostino, N.,Fournier, M., & Worrall, D. (1999). The kinematics of back-arc basins, examples from the Tyrrhenian, Aegean and Japan Seas, in The Mediterranean Basins: Tertiary Extension Within the Alpine Orogen, edited by B. Durand et al., Geological society of London, Special Publications, 156, 21–53.

Jolivet, L., & Faccenna, C. (2000), Mediterranean extension and the Africa-Eurasia collision. Tectonics, 19(6), 1095–1106.

Jongsma, D., van Hinte, J. E., & Woodside, J. M. (1985). Geologic structure and neotectonics of the North African Continental Margin south of Sicily. Marine and Petroleum Geology, 2(2), 156–179. https://doi.org/10.1016/0264-8172(85)90005-4

Krantz, R.W. (1988). Multiple fault sets and three-dimensional strain: theory and application. Journal of Structural Geology, 10:225–237. http://dx.doi.org/10.1016/0191-8141(88)90056-9.

La Bruna, V., Agosta, F., & Prosser, G. (2017). New insights on the structural setting of the Monte Alpi area, Basilicata. Italy. Italian Journal of Geosciences, 132, 220-237.

La Bruna, V., Agosta, F., Lamarche, J., Viseur, S., & Prosser, G. (2018). Fault growth mechanisms and scaling properties in foreland basin system: The case study of Monte Alpi, Southern Apennines, Italy. Journal of Structural Geology, 116, 94-113.

Lacombe, O. (2012). Do fault slip data inversions actually yield "paleostresses" that can be compared with contemporary stresses? A critical discussion. Comptes Rendus Geoscience, 344(3–4), 159–173. https://doi.org/10.1016/j.crte.2012.01.006

Langhi, L., Ciftci, N.B., & Borel, G.D. (2011). Impact of lithospheric flexure on the evolution of shallow faults in the Timor foreland system. Marine Geology, 284 (1), 40–54.

Lehner, B.L. (1991). Neptunian dykes along a drowned carbonate platform margin: an indication for recurrent extensional tectonic activity?. Terra. Nova 3, 593–602.

Le Pichon, X., Bergerat., F., & Roulet, M. (1988). Plate kinematics and tectonics leading to Alpine belt formation; A new analysis. Geological Society of America, Special Publications, 218, 111-131.

Liesa, C.L., & Lisle, R.J. (2004). Reliability of methods to separate stress tensors from heterogeneous fault–slip data. Journal of Structural Geology, 26, 559–572.

Lisle, R.J., and Srivastava, D.C. (2004). Test of the frictional reactivation theory for faults and validity of fault-slip analysis. Geology, 32 (7), 569-572.

Mazzei, R. (1985). The Miocene sequence of the Maltese Islands: Biostratigraphic and chronostratigraphic references based on nannofossils. Atti Società Toscana di Scienze Naturali, Memorie serie A, 92, 165-197.

Mazzoli, S., Pierantoni, P.P., Borraccini, F., Paltrinieri,W., & Deiana, G. (2005). Geometry, segmentation pattern and displacement variations along a major Apennine thrust zone, central Italy. Journal of Structural Geology. 27 (11), 1940–1953

Miller, J.M., Nelson, E.P., Hitzman, M., Muccilli, P., & Hall,W.D.M. (2007). Orthorhombic fault–fracture patterns and non-plane strain in a synthetic transfer zone during rifting: Lennard shelf, Canning basin, Western Australia. Journal of Structural Geology, 29, 1002–1021. http://dx.doi.org/10.1016/j.jsg.2007.01.004.

Morris, T.O. (1952). The Water Resources of Malta Government Printing Office, Malta

Murray, J. (1890). The Maltese Islands with special reference to their geological structure. Scottish Geographical Magazine, 6, 449-488.

Oil Exploration Directorate, Office of the Prime Minister, Malta. (1993). Geological map of the Maltese Islands, scale 1.25.000.

Pedley, H., M. (1974). Miocene sea floor subsidence and later sub aerial solution subsidence structures in the Maltese islands. Proceedings of the Geologists' Association, 11.5, 533-547.

Pedley, H., M. (1975). The Oligo-Miocene sediments of the Maltese islands. PhD thesis, University of Hull.

Pedley, H., M., House, M., & Waugh, B. (1976). The Geology of Malta and Gozo. Proceedings of the Geologist Association, 87 (3), 325-341.

Pedley, H.M. (1978). A new lithostratigraphical and palaeoenvironmental interpretation for the coralline limestone formations (Miocene) of the Maltese Islands. Overseas geology and mineral resources. 54, 1–17.

Pedley, H. M., & Grasso, M. (1992). Miocene syntectonic sedimentation along the western margins of the Hyblean-Malta platform: A guide to plate margin processes in the central Mediterranean. Journal of Geodynamics, 15(1–2), 19–37. https://doi.org/10.1016/0264-3707(92)90004-C

Pratt, S. K. (1990). Hardground genesis in pelagic carbonates from the Miocene of Malta and Cretaceus of southern England. PhD thesis, University of London

Quintà, A., & Tavani, S. (2012). The foreland deformation in the south-western Basque–Cantabrian Belt (Spain). Tectonophysics 576, 4–19.

Ramsay, J.G., & Lisle, R.J. (2000). The Techniques of Modern Structural Geology. Volume 3: Applications of Continuum Mechanics in Structural Geology 785-810. Academic Press, London.

Ranero, C.R., Morgan, J.P., McIntosh, K., & Reichert, C. (2003). Bending-related faulting and mantle serpentinization at the Middle America trench. Nature 425 (6956), 367–373. http://dx.doi.org/10.1038/nature01961.

Reches, Z. (1978). Analysis of faulting in three-dimensional strain field. Tectonophysics, 47, 109–129. http://dx.doi.org/10.1016/0040-1951(78)90154-3.

Reches, Z. (1983). Faulting of rocks in three-dimensional strain fields II. Theoretical analysis. Tectonophysics, 95, 133–156. http://dx.doi.org/10.1016/0040-1951(83)90264-0.

Reches, Z., & Dieterich, J.H. (1983). Faulting of rocks in three-dimensional strain fields I. Failure of rocks in polyaxial, servo-control experiments. Tectonophysics 95, 111–132. http://dx.doi.org/10.1016/0040-1951(83)90263-9.

Reuther, C.D., & Eisbacher, G. H. (1985). Pantelleria Rift - crustal extension in a convergent intraplate setting. Geologische Rundschau, 74(3), 585–597. https://doi.org/10.1007/BF01821214

Rizzo, C. (1932). Report on the Geology of the Maltese Islands. Government Printing Office, Malta.

Rossetti, F., Faccenna, C., Goff, B., Monié, P., Argenteri, A., Funicello, R., & Mattei, M. (2001). Alpine structural and metamorphic signature of the Sila Piccola Massif nappe stack (Calabria, ltaly): lnsights for the tectonic evolution of the Calabrian Arc. Tectonics, 20(1), 112–133.

Royden, L., & Faccenna, C. (2018). Subduction Orogeny and the Late Cenozoic Evolution of the Mediterranean Arcs. Annual Review of Earth Planetary Sciences, 46, 261–89. https://doi.org/10.1146/annurev-earth-060115-012419,

Russo, A., & Bossio, A. (1975). Prima utilizzazione degli ostracodi per la biostratigrafia e la paleoecologia del Miocene dell'Arcipelago Maltese. Bollettino della Società Paleontologica Italiana, 15, 215–227.

Saadallah, A., & Caby, R. (1996). Alpine extensional detachment tectonics in the Grande Kabylie metamorphic core complex of the Maghrebides (northern Algeria). Tectonophysics, 267, 257–273.

Scisciani, V., Calamita, F., Tavarnelli, E., Rusciadelli, G., Ori, G.G., & Paltrinieri, W. (2001). Foreland-dipping normal faults in the inner edges of syn-orogenic basins: a case from the Central Apennines, Italy. Tectonophysics, 330 (3), 211–224.

Scisciani, V., Tavarnelli, E., & Calamita, F. (2002). The interaction of extensional and contractional deformations in the outer zones of the Central Apennines, Italy. Journal of Structural Geology, 24, 1647–1658.

Scisciani, V., & Montefalcone, R. (2006). Coexistence of thin-and thick-skinned tectonics: An example from the Central Apennines, Italy. Geological society of America, Special Papers, 414, 33–54.

Serranne, G. T. (1999). The Gulf of Lion continental margin (NW Mediterranean) revisited by IBS: an overview. In Durand, B., Jolivet, L., Horváth, F., & Seranne, M. The Mediterranean Basins: Tertiary Extension within the Alpine Orogen, Geological society of London, Special Publications, 156, 15–36.

Simón, J. L. (2019). Forty years of paleostress analysis: has it attained maturity? Journal of Structural Geology, 125, 124–133. https://doi.org/10.1016/j.jsg.2018.02.011

Smart, P.L., Palmer, R.J., Whitaker, F., & Wright, V.P. (1988). Neptunian Dikes and Fissure Fills: An Overview and. In: Paleokarst. Springer, 149–162.

Sperner, B., & Zweigel, P. (2010). A plea for more caution in fault-slip analysis. Tectonophysics, 482(1–4), 29–41.

Tavani, S., Storti, F., Lacombe, O., Corradetti, A., Muñoz, J. A., & Mazzoli, S. (2015a). A review of deformation pattern templates in foreland basin systems and fold-and-thrust belts: Implications for the state of stress in the frontal regions of thrust wedges. Earth-Science Reviews, 141, 82–104. https://doi.org/10.1016/j.earscirev.2014.11.013

Tavani, S., Vignaroli, G., & Parente, M. (2015b). Transverse versus longitudinal extension in the foredeep-peripheral bulge system: Role of Cretaceous structural inheritances during early Miocene extensional faulting in inner central Apennines belt. Tectonics, 34, 1412–1430, doi:10.1002/2015TC003836.

Tavani, S., Corradetti, A., De Matteis, M., Iannace, A., Mazzoli, S., Castelluccio, A., & Spanos, D. (2019). Early-orogenic deformation in the Ionian zone of the Hellenides: Effects of slab retreat and arching on syn-orogenic stress evolution. Journal of Structural Geology 124, 168-181. https://doi.org/10.1016/j.jsg.2019.04.012

Traforti, A., Massironi, M., Bistacchi, A., Zampieri, D., & Viola, G. (2018). Slip-tendency analysis as a tool to constrain the mechanical properties of anisotropic rocks. Journal of Structural Geology, 117, 136–147. https://doi.org/10.1016/j.jsg.2018.09.001

Turcotte, D., & Schubert, G. (1982). Geodynamics. Wiley, New York.

Twiss, R.J., & Moores, E. M. (2007). Structural Geology, 2nd edition. ISBN 9780 7167 4951 6, 736 pages.

Van der Voo, R. (1993). Paleomagnetism of the Atlantic Thethys and Iapetus Oceans, Cambridge University Press, New York.

Villani, F., Amico, S. D., Panzera, F., Vassallo, M., Bozionelos, G., Farrugia, D., & Galea, P. (2018). Shallow high-resolution geophysical investigation along the western segment of the Victoria Lines Fault (island of Malta). Tectonophysics, 220–233. https://doi.org/10.1016/j.tecto.2018.01.010

Visser, W.A. (1980). Geological nomenclature: Royal Geological and Mining Society of the Netherlands, The Hague, Martinus Nijoss, 540 pp.

Wallace, R.E. (1951). Geometry of shearing stress and relation to faulting. Journal of Structural Geology, 59, 118-130.

Wendt, J. (1971). Genese und Fauna submariner und sedimentarer Spaltenfüllungen im mediterranen Jura. Paleontographica Abteilung, 136, 122-192.

2

Damage zone characterization combining scan-line and scan-area analysis on a km-scale Digital Outcrop Model: the Qala Fault (Gozo).

This chapter is presented in the form of a paper that is currently under review in the Journal of Structural Geology.

The scripts used for scan-line and scan-area analysis are available in the supplementary materials.

NOTE FOR THE READER

In this chapter, we refer to a method presented in Bistacchi et al., 2019. This method introduces a statistical method to analyze the spatial distribution of fractures belonging to a given fracture set and sampled along a linear scanline. Indeed, fracture sets having the same fracture density (P10) might have very different spatial distribution that needs to be characterized. In this paper we suggest to apply non parametric statistic to characterize the spatial distribution of fracture sets, by evaluating if on a scanline of length L a correlation exists between the fracture position along the scanline (X) and the fracture spacing (S) (Figure 1).

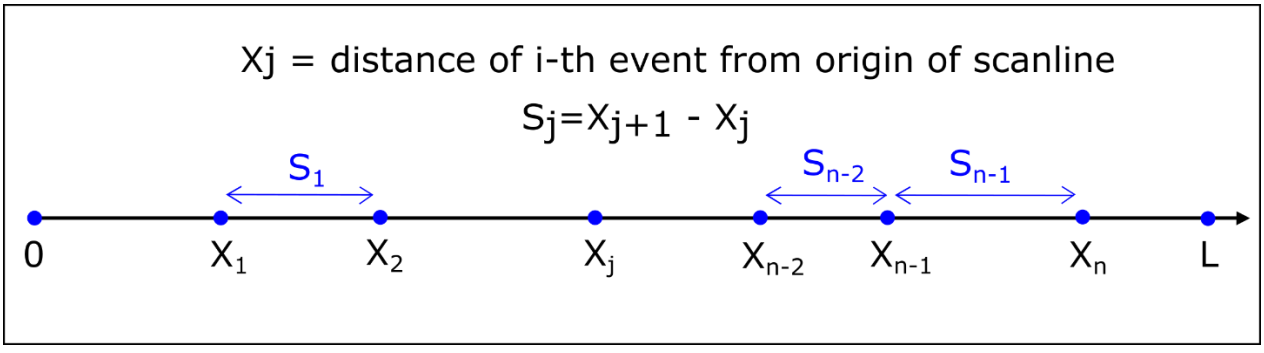

Figure 1: Given a scanline of length L, we can define the position X of n fractures occurring along it, and the spacing S between them

In particular, it is possible to:

i) test if fracture spacing is correlated with fracture position (fracture spacing increases or decreases along the scan line defining a trend, Figure 2) by applying the Spearman rank correlation coefficient for trend between fracture spacing (S_n) and fracture position (X_n).

ii) test if fracture are clustered defining a pattern (Figure 2) by applying the Spearman rank correlation coefficient between fracture spacing (S_{n-1}) and the spacing of neighbour fractures (S_{n-2})

If no trend or pattern are found, fractures can be randomly or uniformly distributed (Figure 2). Random distribution is tested using a χ^2 test for Poisson distribution. To test if fractures are uniformly distributed, we compare the cumulative frequency curve of the fractures along the scanline (with fracture position as horizontal axis) with the cumulative frequency curve of a uniform distribution using the Kolgorov-Smirnov test.

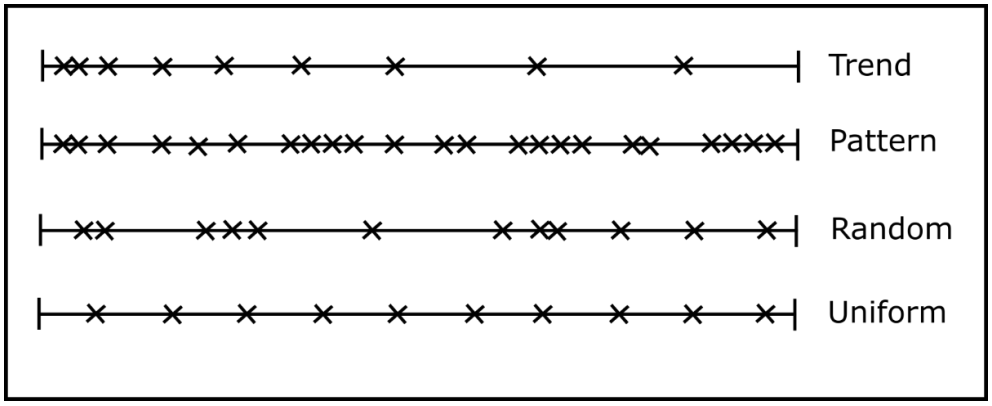

Figure 2: The possible spatial distributions of fractures along a scanline. Figure modified from Swan and Sandilands , 1995

For a complete explanation of the non parametric statistical tests we refer the reader to the book "Introduction to Geological Data Analysis" written by A.R.H. Swan and M. Sandilands, 1995 pages 221-233.

Chapter 2

Damage zone characterization combining scan-line and scan-area analysis on a km-scale Digital Outcrop Model: the Qala Fault (Gozo)

M. Martinelli[1*], A. Bistacchi[1], S. Mittempergher[1,2], F. Bonneau[3], F. Balsamo[4], G. Caumon[3] and M. Meda[5].

[1]Dipartimento di Scienze dell'Ambiente e della Terra, Universita' degli Studi di Milano Bicocca, Piazza della Scienza 4, 20126 Milano

[2]Dipartimento di Scienze Chimiche e Geologiche, Università degli Studi di Modena e Reggio Emilia, via Campi 103, 41125 Modena

[3]Université de Lorraine, CNRS / ENSG, GeoRessources, F-54000 Nancy, France

[4] NEXT- Natural and Experimental Tectonics research group, Dipartimento Scienze Chimiche, della Vita e della Sostenibilità Ambientale, Università degli Studi di Parma, Padiglione 7 - Scienze della Terra, Campus Universitario, Parco Area delle Scienze 157/A, 43124 Parma, Italy

[5] ENI Spa, Upstream and Technical Services - San Donato Milanese – Italy

*corresponding author: m.martinelli34@campus.unimib.it; Phone number: +393281157446

Authors e-mail addresses: Mattia Martinelli: m.martinelli34@campus.unimib.it; Andrea Bistacchi: andrea.bistacchi@unimib.it; Silvia Mittempergher: silvia.mittempergher@unimore.it; Francois Bonneau: francois.bonneau@univ-lorraine.fr; Fabrizio Balsamo: fabrizio.balsamo@unipr.it; Guillaume Caumon: guillaume.caumon@univ-lorraine.fr; Marco Meda: marco.meda@eni.com

Keywords: Fracture network characterization; Fracture parameters; Outcrop analogues; Digital Outcrop Model; Fault damage zone; Maltese islands

2.1 Abstract

Fault damage zones can act as a preferential corridor for the fluid flow in the subsurface, and for this reason the characterization of their structure, including the attributes of the associated fracture network, is fundamental. However, defining these attributes from subsurface data is difficult because of limited resolution (seismic data) or of limited spatial coverage (borehole data). Outcrop analogues can help filling this observation gap, allowing an almost continuous investigation of the fault damage zone from the master slip surface to the background fractures. In this work we characterized the damage zone of the Qala fault, a normal fault developed in platform carbonates of the Gozo Island (Maltese Islands), combining field analysis and a high resolution photogrammetric Digital Outcrop Model (DOM). We demonstrate that by combining scanline and scan-area analysis applied on a DOM, it is possible to characterize the damage zone width and the spatial organization, geometrical parameters and connectivity of the associated fracture network. Moreover, we showed that even faults with limited displacement (i.e., 50-100 m) can be characterized by a thick damage zone that forms a large connected and permeable area which extends for several hundreds of meters far away from the master slip surface.

2.2 Introduction

Fracture networks exert a primary role in the control of permeability and fluid flow in fractured reservoirs of geo-fluids (e.g. hydrocarbons, groundwater, hydrothermal fluids, CO_2, etc.), but unfortunately, the full characterization of fracture parameters from borehole and/or seismic data is

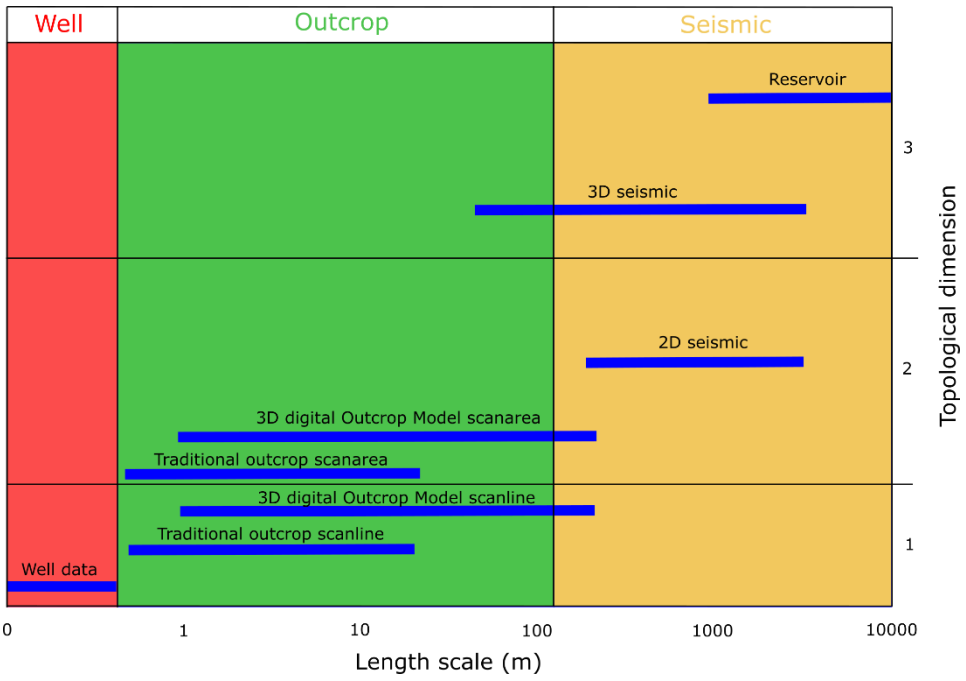

Figure 1: Length scale of Well, Outcrop and Seismic data.

difficult. In fact, a critical gap in data exists at scales between a few meters and several hundred meters, since fractures at length scale of less than ~200 m cannot be detected even in the best seismic datasets, and, on the other hand, borehole data are sparse and give only local information on small–scale fractures (Figure 1). Outcrop analogue studies may fill this gap, and particularly km-scale outcrop analogues allow collecting very large multi-scale datasets to characterize fracture network parameters and their variability (Basa et al., 2019; Bertrand et al., 2015; Bistacchi et al., 2015; Jacquemyn et al., 2015) (Figure 1).

However, even if a large continuous outcrop is available, collecting all fracture parameters directly in the field is impossible and only small areas (less than a few hundreds of m^2) can be studied with traditional surveying methods. For this reason, modern structural analysis projects require a photogrammetric or laser scanning survey to be carried out, in order to provide a high-resolution topographic and imagery base model for the structural analysis, called Digital Outcrop Model (DOM) or Virtual Outcrop Model (Bellian et al., 2005; McCaffrey et al., 2005; Buckley et al., 2008; Haneberg, 2008; Hodgetts, 2013; Tavani et al., 2014; Vasuki et al., 2014; Bistacchi et al., 2015; Franceschi et al., 2015; Martinelli et al., 2017). Depending on the outcrop morphology (cliff vs. pavement) and size, the DOM can be rendered as a point cloud, a textured surface, or a 2.5D dataset composed by orthophoto and a digital elevation model (DEM) (Bistacchi et al., 2015). Fracture networks mapped on a DOM can be analyzed with virtual scan-lines and scan-areas allowing extracting very large datasets that can never be equaled in size or quality with traditional surveys. Some authors hold that the DOM approach allows collecting large datasets in a small time, but what is important for us is that the analysis of DOM provide big data sets useful for a robust statistic characterization of most parameters of a fracture network.

In this contribution, we show that the detection and statistical analysis of the fracture network from km-long DOM allows also to define the Representative Elementary Volume (REV), that is the volume above which the study parameter or properties is homogenous and statistically stationary (Bear, 1972), of the fracture density, intensity and topology. REV of fractured media has been widely used to characterize the hydraulic behavior and the hydraulic properties of rock masses with the help of DFN models and numerical modelling (Long et al., 1982; Oda, 1986; Li et al., 2009; Rong et al., 2013; Azizmohammadi and Matthäi, 2017;) or to investigate mechanical and geometrical properties (Esmaieli et al., 2010; Müller et al., 2010).

The need to have a complete characterization of the fracture network is particularly important for fault-related fractures where the fault zone structure has a crucial role on the permeability (Smith, 1980; Smith et al., 1990; Taylor and Dietvorst, 1991; Evans et al., 1997; Knai, T.A. and Knipe, 1998; Wiprut and Zoback, 2000; Fisher and Knipe, 2001; Jolley et al., 2007). A widely used and accepted conceptual model for fault zone architecture requires the presence of a thin fault core, where most of the deformation is localised, enclosed into a wider damage zone with an exponential

decrease of "fracturing" (various parameters are used by different authors) towards the undeformed (or less deformed) host rock (Aydin and Johnson, 1978; Chester and Logan, 1986; Caine et al., 1996; Shipton and Cowie, 2001; Mitchell and Faulkner, 2009; Bistacchi et al., 2010; Riley et al., 2010, Smith et al., 2013, Balsamo et al., 2019). Quite often fault cores have a low permeability and can act as barriers for fluid flow perpendicular to the fault zone (Knipe, 1992; Antonellini and Aydin, 1994; Caine et al., 1996; Evans et al., 1997; Fulljames et al., 1997; Yielding et al., 1997; Fisher and Knipe, 2001; Flodin et al., 2005; Færseth et al., 2007; Cooke et al., 2018; Rempe et al., 2018). On the contrary, highly fractured damage zones are believed to represent preferential conduits for fluid flow, and sometimes reservoirs by themselves (Chester and Logan, 1986; Chester et al., 1993; Antonellini and Aydin, 1994; Wibberley and Shimamoto, 2003; Micarelli et al., 2006; Agosta et al., 2007; Agosta, 2008; Mitchell and Faulkner, 2009). Many authors hold that one of the main factors controlling the width of the damage zone is the amount of displacement accommodated by the fault. In many papers from the '80s and '90s a simple power-law correlation is proposed between displacement and some fracturing parameters. (Schulz and Evans, 1998; Vermilye and Scholz, 1998; Schulz and Evans, 2000; Mitchell and Faulkner, 2009; Savage and Brodsky, 2011) , but more recent works highlight that the uncertainty on this kind of correlation can span over two orders of magnitude, and by the fact that the power-law must be limited by a cut-off after some large displacement has been accumulated (Mitchell and Faulkner, 2009; Bistacchi et al., 2010; Savage and Brodsky, 2011; Faulkner et al., 2011, Smith et al., 2013; Choi et al., 2016; Mayolle et al., 2019).

In this work, we analyze the fracture network parameters within the footwall damage zone of the Qala Fault, a normal fault exposed in the Gozo Island (Maltese Archipelago). This fault is characterized by a highly fractured inner damage zone (5 m thick) directly flanking the principal slip surface, and by a wide outer damage zone extending for hundreds of meters in the footwall block. Based on accurate fracture tracing on a photogrammetric DOM, we demonstrate that by integrating linear and areal methods for fracture quantification, it is possible to (1) univocally separate the damage zone from the background, (2) identify fracture corridors, (3) collect fracture parameters, and (4) characterize the REV and topological properties of the fracture network. Our quantitative data are compared with current models for the development of fault damage zones.

2.3 Geological outline

Malta and Gozo are located in the foreland of the Apennine-Sicilian-Maghrebian fold and thrust belt, within the Pantelleria rift system. (Pedley et al., 1976; Illies et al., 1981; Reuther and Eisbacher, 1985; Dart et al., 1993; Martinelli et al., 2019) (Figure 2a). (Insert Figure 2 here). The two islands are crosscut by two sets of normal faults striking WNW-ESE and ENE-WSW (Martinelli et al., 2019 and references therein) (Figure 2b). The main faults of these two sets are

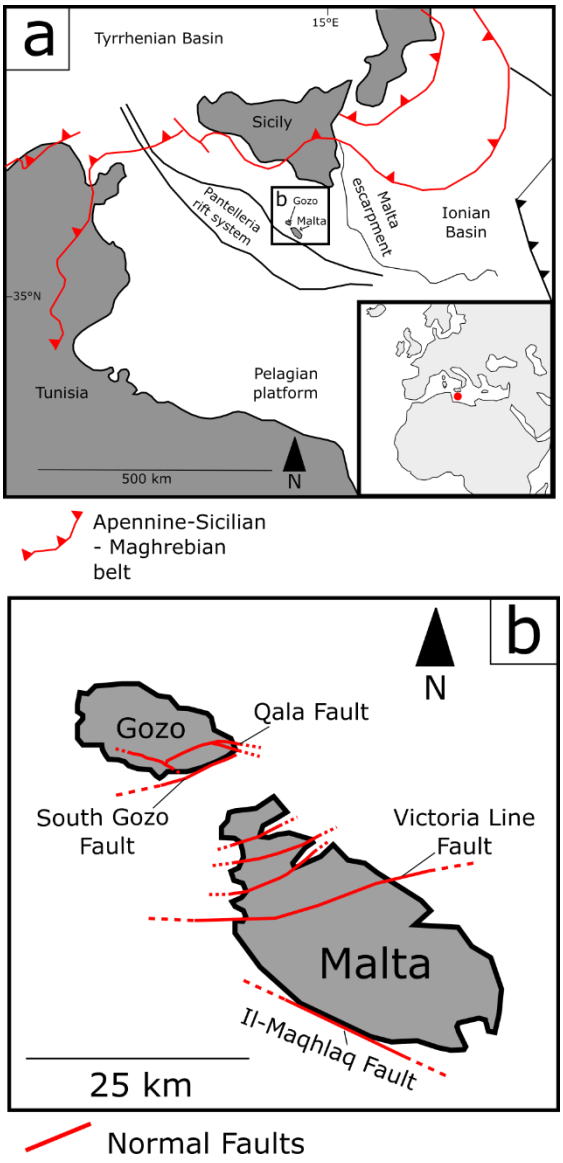

Figure 2: a) Position of the Maltese islands in the foreland of the Apennine-Sicilian-Maghrebian belt; b) Structural framework and main faults of the Maltese Islands. Modified after Martinelli et al., 2019 and Dart el al., 1993

the South Gozo Fault and the Qala Fault on Gozo and the Victoria Fault and the Maqhlaq Fault on Malta (Figure 2b). Associated with these normal faults, four sets of joints are present, striking i) ENE-WSW; ii) WNW-ESE; iii) N-S; iv) NE-SW (Martinelli et al., 2019). Both ENE-WSW and WNW-ESE fault and joint sets mutually cross-cut and abut each other, whereas N-S and NE-SW joint sets show abutting relationships with the other two sets. Martinelli et al. (2019) demonstrated that the two sets of normal faults (ENE-WSW and WNW-ESE) and the four joint sets formed together in response of a N-S extension during the Late Miocene. An earlier deformation event, evidenced by Neptunian dykes and small normal faults, is represented in the lower units, but it is not relevant for this contribution on the Qala Fault (Martinelli et al., 2019 and references therein). The Oligocene-Miocene sequence of Malta and Gozo consists of shallow marine carbonates of Oligocene to Late Messinian age composed, from bottom to top, by 5 formations: i) Lower Coralline Limestone Formation (Maghlaq Member, Attard Member, Xlendi Member and Il Mara Member) ii) Globigerina Limestone (Lower Globigerina Member, Middle Globigerina Member and Upper Globigerina Member) iii) Blue Clay Formation iv) Green Sand Formation v) Upper Coralline Limestone Formation (Murray, 1890; Felix, 1973; Pedley et al., 1976; Dart et al., 1993) (Figure 3a).

2.4 The SE Gozo outcrop

(Insert Figure 3 here) The Qala Fault is a WNW-ESE normal fault with a minimum vertical separation of 50 meters (Cooke et al, 2018) and an average dip of 70° towards SW. In the studied outcrop, it juxtaposes the lower levels of the Blue Clay Formation with the Lower Coralline Limestone (Figure 3b).

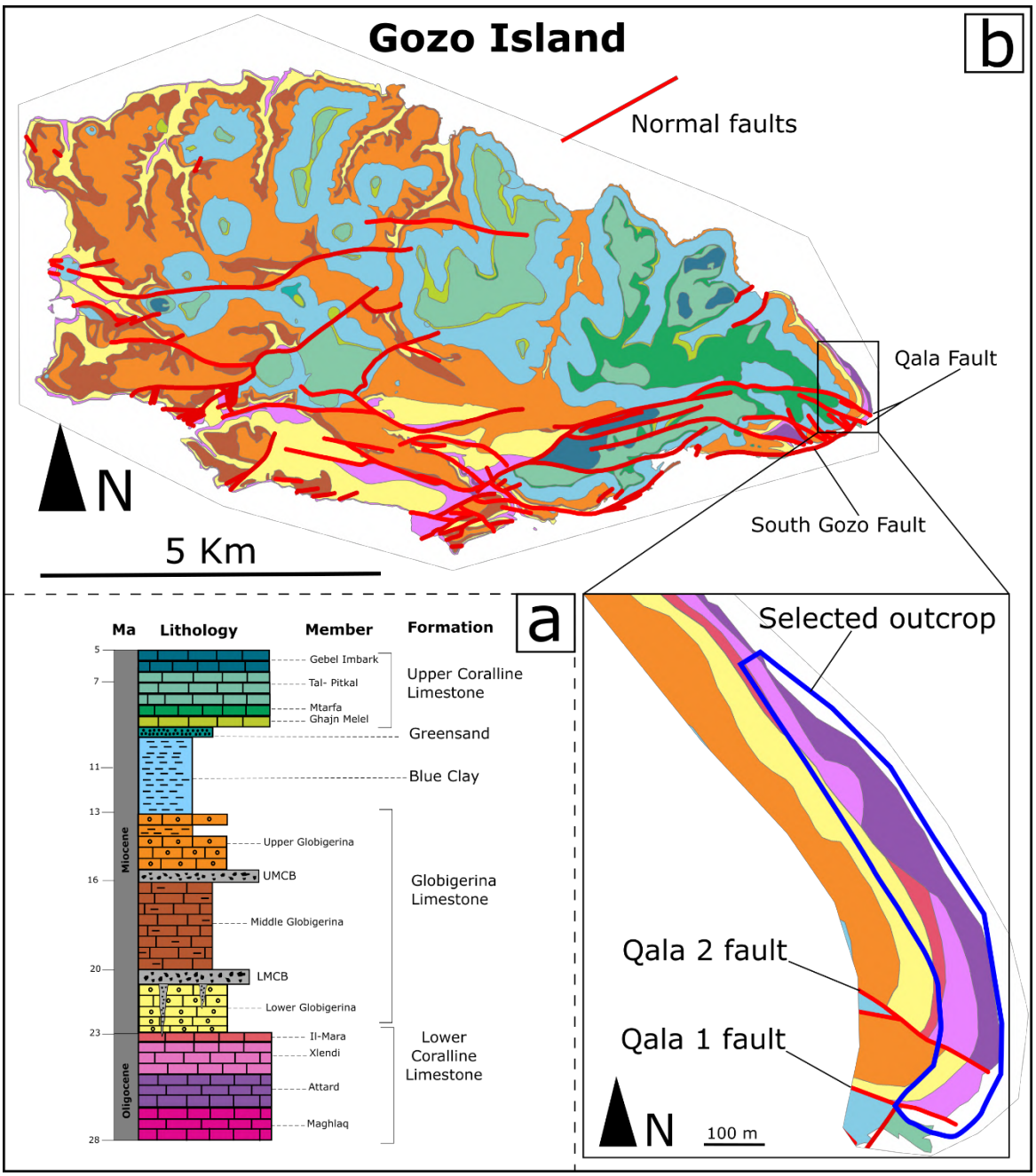

Figure 3: a) Stratigraphy of the Maltese Islands. Stratigraphic column modified after Martinelli et al., 2019; b) Geological maps of the Gozo island modified after Martinelli et al., 2019. The black rectangle highlights the outcrop selected for this study. Colours refer to those of the stratigraphic column.

The footwall of the Qala Fault crops out continuously along the eastern coast of Gozo for almost 3 km (Figure 3b), and it was chosen to characterize the architecture of the damage zone and the parameters of the fracture network in the fault damage zone. The outcrop chosen for our study is an extremely continuous coastal pavement, with no debris cover at all, extending for 2.8 km northward from the fault core of the Qala Fault, with a width between 30 and 60 meters.

For this study we concentrated our attention in the southern part of the outcrop (1 km long) (Figure 3b). There the Qala Fault is composed by two fault strands that we call Qala 1 and Qala 2 faults (Figure 3b). Qala 1 fault is a 61° SSW dipping normal fault with a minimum vertical displacement of 50 meters (Cooke et al., 2018). Qala 2 is a south-dipping (>80°) normal fault with 30 meters of vertical separation (Cooke et al., 2018). Between the Qala 1 Fault and the Qala 2 Fault, the Xlendi Member of the Lower Coralline Limestone is exposed, whereas to the north of the Qala 2 Fault the Attard Member is continuously outcropping for almost 800 meters (Figure 3b). Cooke et al., (2018), using circular scanlines along a transect perpendicular to the trace of the fault core, showed that the slip surface of Qala 2 fault is surrounded both in the hanging wall and in the footwall by about 5 m of highly fractured rocks (fracture intensity > 15 m^{-1}). Outside of these zones, fracture intensity rapidly decreases to < 5 m^{-1}.

2.5 Review of fracture parameters and methods for fracture network characterization

Following common usage, by "fractures" in the following we mean a broad class of geological structures including joints, veins, shear fractures, stylolites (Twiss and Moores, 2006). Single fractures are defined by their position in space, orientation, length, height. Fracture position is defined by the coordinates of the fracture center, but also by the relative position of a fracture with respect to the others. Fracture orientation is the orientation of the fracture surface in 3D space, defined by strike or dip-azimuth and dip. Fracture length is defined as the length of the fracture along strike, while fracture height is the length measured along dip.

Fracture sets (sets of fractures with common genesis and/or orientation) and fracture networks (all fractures in a fractured rock mass, including all sets) are characterized by cumulative properties such as density, intensity and topology (Dershowitz and Einstein, 1988). Fracture intensity and density can be measured in 3D, 2D or 1D (Dershowitz and Einstein, 1988) (Figure 4a). Intensity is expressed in m^{-1} and is given by the total fracture surface/length/number divided by the sampling volume/area/length (respectively in 3D/2D/1D). Density is expressed in m^{-3}/ m^{-2}/m^{-1} and is always given by the total number of fractures divided by the sampling volume/area/length (respectively in 3D/2D/1D). In the following, we will follow Dershowitz and Einstein, (1988) in indicating fracture intensity as P_{32}, P_{21} and P_{10}, and fracture density as P_{30}, P_{20} and P_{10} (respectively in 3D/2D/1D) (Figure 4a). Note that in 1D the definitions of fracture intensity and density converge (Figure 4a).

The topology of a fracture network in 2D (e.g. fracture traces on an outcrop surface) can be characterized by the type of fracture terminations, considered as nodes that fall in three categories: i) X nodes for fracture intersections; ii) Y nodes for fracture abutting; iii) I nodes for isolated fracture tips (Manzocchi, 2002; Sanderson and Nixon, 2015; Sævik and Nixon, 2017) (Figure 4b). Computing statistics regarding these nodes, and particularly the proportion of X, Y and I nodes in

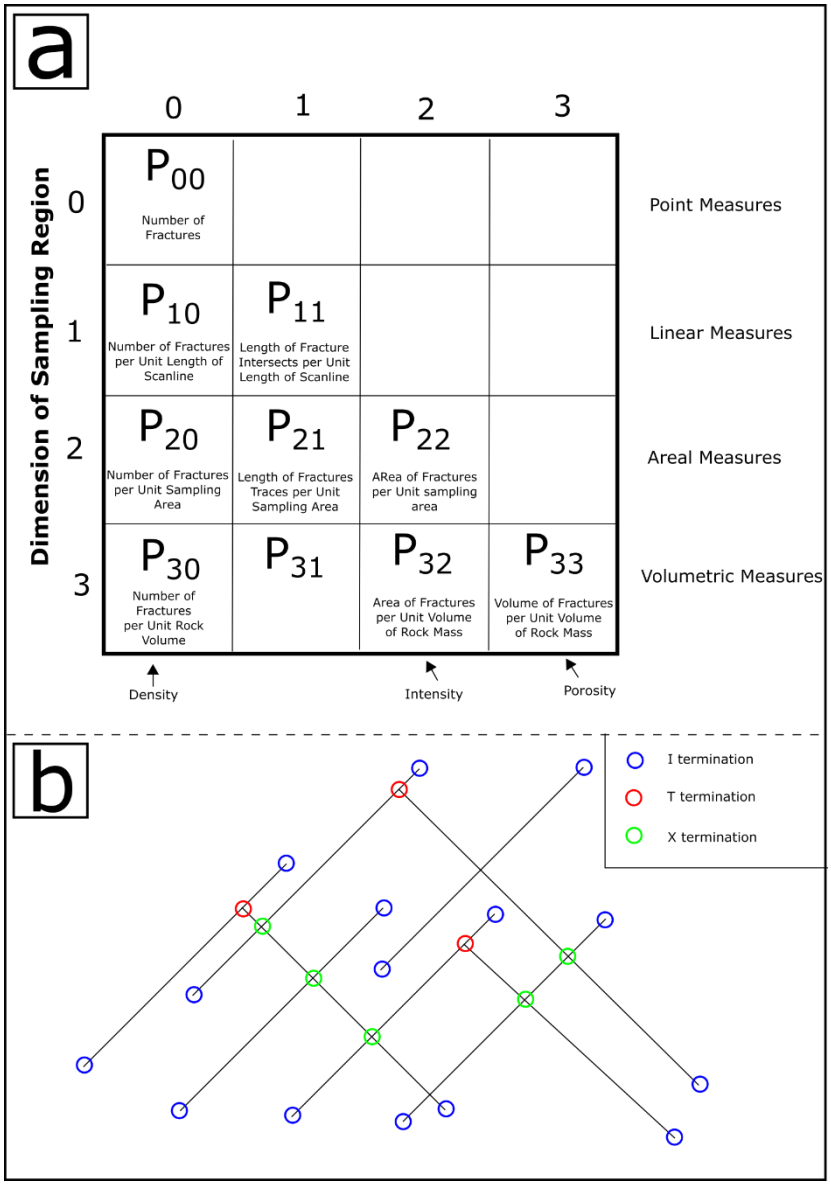

Figure 4: a) Matrix that shows the possible topological dimension for the measurements of P20 and P21. b) The three possible fracture terminations

a fracture network, can be used to measure the connectivity of the network (Sanderson and Nixon, 2015). Saevik and Nixon (2017) perform numerical modelling on fracture networks having different topologies and they propose an equation that can be used to predict the hydraulic connectivity f of a fracture network from the (normalized) equivalent number of connections per fractures using the number of n_x, n_y and n_i of X, Y and I nodes respectively:

$$f = \max(0,2.94 * n'_c - 2.13;$$

where n'_c is the equivalent number of connections per fracture and it is defined by the following equation:

$$n'_c = \frac{4n_X + 2n_Y}{4n_X + 2n_Y + 2n_I};$$

Below the percolation threshold the hydraulic connectivity is zero. (Insert Figure 4 here)

More common methods for obtaining statistically significant samples of fracture parameters are: (i) linear scan-lines (Priest and Hudson, 1981; Priest, 1993; Bons et al., 2004); (ii) areal sampling or scan-areas (Baecher and Laaney, 1978; Call et al., 1976; Cruden, 1977; Kulatilake and Wu, 1984; Pahl, 1981; Priest, 1993; Wu and Pollard, 1995), and (iii) circular scanlines (Mauldon et al., 2001; Rohrbaugh et al., 2002; Healy et al., 2017) (Figure 5a). In the following, we will briefly summarize these methods, their limitations and their applications to the analysis of fracture networks, particularly in fault damage zones.

2.5.1 Linear scanline

The linear scanline sampling method consists of marking a physical or virtual line (a scanline) on the outcrop and collecting the parameters (position, orientation, length, height, etc.) of every fracture that intersects the line (Priest and Hudson, 1981; Priest, 1993). Fracture density/intensity P_{10} (in 1D the two parameters converge) corresponds to the inverse of the average spacing of fractures along a scanline that is perpendicular to the average orientation of a fracture set (Dershowitz and Herda, 1992). Hence, an ideal scanline must be chosen perpendicular to the fracture set orientation. If this is not possible, to minimize the orientation bias the angle must be as large as possible and the Terzaghi correction must be applied (Terzaghi, 1965)

$$S_c = \frac{S_m}{sin\alpha}$$

where S_c is the corrected spacing, S_m is the measured spacing, and α is the angle between the scanline and the average orientation of the fracture set. When more than one fracture set is present, the analysis must be repeated for each set.

In addition, data collected with the scanline method are also affected by size, truncation, and censoring biases (Zeeb et al., 2013). Despite these limitations, scanlines are a valuable and relatively fast method for characterizing the fracture network, and the only available method for analyzing sub-seismic fractures in borehole log data.

Scanline data perpendicular to faults are commonly used for defining the extent and properties of the damage zone (e. g., Mitchell and Faulkner, 2009; Mitchell and Faulkner, 2012). Recently Choi et al., (2016) proposed to use the distribution of the cumulative fracture frequency for distinguishing the damage zone from the background fractures. In particular, the authors proposed to use the slope of the cumulative curve of fracture intensity against the distance to the fault core to identify different degrees of deformation across the damage zone. The damage zone width is defined at the distance where the slope of the cumulative curve change. Scanline data can also be analyzed for identifying spatial correlation in fracture parameters (e.g., Guerriero et al., 2011; Marrett et al., 2018; Bistacchi et al., 2019). Bistacchi et al., (2019) proposed a spatial statistics

method, based on the non-parametric Spearman's correlation coefficient, to establish if fracture position is correlated or not with fracture spacing. It is thus possible to discriminate trends (i.e., increase or decrease in fracture spacing with distance), or patterns (e.g. fracture corridors or clusters) from uniform or random spatial distributions. Furthermore, this method allows to define statistically homogeneous domains where properties of each fracture set (e.g. intensity, density, length spacing, topology) can be properly calculated.

2.5.2 Areal sampling

The areal sampling methods provide 2D information characterizing fracture parameters inside a given area of the outcrop. The scan-area can be a square, a rectangle or any other convex region (Pahl, 1981; Priest, 1993; Wu and Pollard, 1995). Since this method usually permits to characterize large areas, it is less affected by size, truncation, and censoring biases (Watkins et al., 2015). If the scan area is circular or square, orientation bias is also minimized. Scan-areas can be used for measuring fracture orientation, fracture intensity P_{21}, fracture density P_{20}, length distribution and to collect the topological relationships between different fracture sets (e.g. Sanderson, 2016; Peacock et al., 2018). Areal sampling can be affected by truncation and censoring bias if the dimension of the scan-areas is too small with respect to the length of fractures or if the outcrop size is limited.

2.5.3 Circular window sampling

A particular case of areal sampling method is the circular window method proposed by Mauldon, 1998, Mauldon et al. 2001, and Rohrbaugh et al., 2002. This method allows estimating indirectly fracture density, intensity and length, by counting the number of fracture intersections n with the border of the circular scan-area and the number of fracture terminations m inside the scan-area (Figure 5a). The estimates are calculated, for a circular scanline with radius r, as:

$$intensity\ estimator: \quad I = \frac{n}{4r} \quad (1)$$

$$density\ estimator: \quad \rho = \frac{m}{2\pi r^2} \quad (2)$$

$$mean\ trace\ length\ estimator: \quad \mu = \frac{\pi r m}{2n} \quad (3)$$

The main weakness of this method is that it estimates the parameters rather than directly measuring them. Some authors hold that, if a minimum of 30 nodes is sampled ($n + m \geq 30$), the estimation of the abovementioned parameters is robust (Rohrbaugh et al. 2002). However, even for large datasets the estimation can be biased as discussed in Pahl, (1981), and in general the applicability of this method is strongly dependent on the characteristics of the fracture network. In addition, this method does not allow characterizing other fracture parameters such as trend, aperture, spacing and topology (Mauldon, 1998, Mauldon et al. 2001 and Rohrbaugh et al., 2002). Watkins et al.

(2015), proposed a combination of circular window and linear scanline methods, called augmented circular scanline method. The authors used the circular scanline method to extract density, intensity and mean trace length, and calculate all the other parameters (strike, dip, length, aperture) from every fracture that intersects the circular scanline edge. In conclusion, even if this method permits a faster data collection with respect to the classical areal sampling method (Watkins et al., 2015), it provides a limited dataset with respect to the areal sampling and, as the other methods, it suffers from length censoring and it doesn't permit to characterize fracture spatial distribution (Watkins et al., 2015).

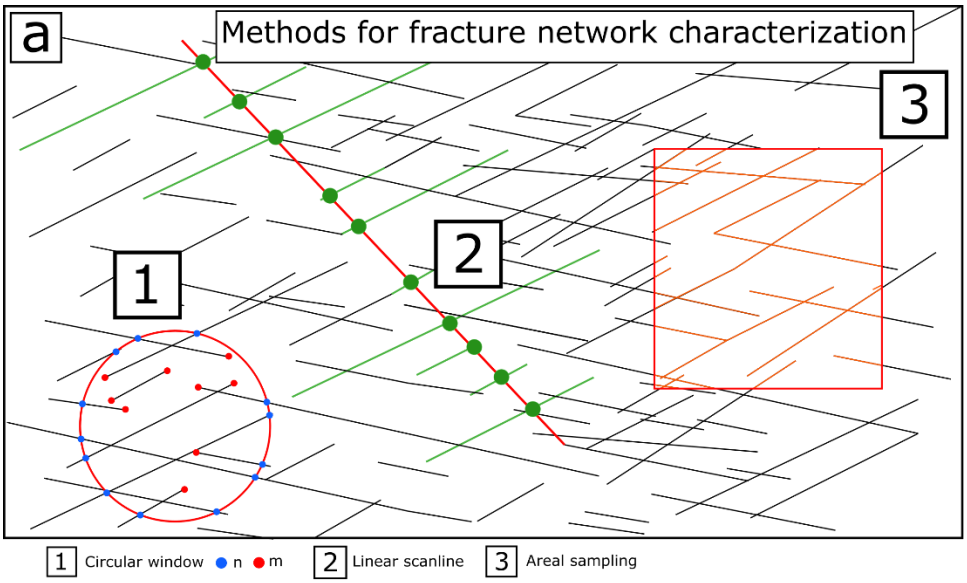

Figure 5: a) the main methods used for fracture network characterization; b,c) the integrated method (DOMstudio workflow) proposed in this study: linear scan-line analysis to investigate spatial distribution of the fracture network (b); scan-area analysis to extract fracture parameters (c).

2.6 The DOMstudio workflow

It is clear that all the methods described above have their own strengths and limitations, but, if a large continuous outcrop is available, areal sampling provides the most complete dataset, as also pointed out by Watkins et al., (2015). However, the main issue of this technique is that it does not allow characterizing the spatial organization of the fracture network. To overcome this problem, we developed the DOMstudio workflow, presented for the first time in this contribution, which combines the linear scan-line and the scan-area sampling methods with photogrammetric DOM (Figure 5b-c). As first step, a detailed photogrammetric model of the outcrop is realized in order to extract a high resolution orthophoto and then on the orthophoto the fracture network is digitized. After that, we first analyze the spatial distribution of the fracture network using scan-lines, to define domains where fracture distribution is stationary (no trend or pattern/clustering, Figure 5b). Then we apply areal sampling methods, with sampling areas matching the stationary domains (Figure 5c). Digitizing the fracture network directly on a DOM allows us to completely automatize the fracture network characterization workflow with custom Python scripts to be used in Skua-Gocad (with the GoPy plugin). These scripts allow drawing linear scanlines and scan-areas directly on the DOM and automatically extract the fracture parameters. For the linear scanline analysis, the script extracts a point at each intersection of a fracture trace with the scan-line and then it calculates the fracture position and spacing along the scanline. For scan-areas the script directly measures the fracture parameters (length, density, intensity, spacing and topology). In the next sections, the steps of this workflow will be described in detail.

2.6.1 Field analysis

An extensive field analysis was performed in the footwall of the Qala fault in order to recognize the main fracture sets and to characterize their structural and topological parameters. Moreover, field observations were used to define the proper resolution and the extension of the photogrammetric DOM.

2.6.2 Photogrammetric DOM and fracture interpretation

Pictures for the photogrammetric reconstruction were collected with a DJI Mavic Pro from different altitudes of 30 and 60 m. Collected pictures were processed with SFM (Structure from Motion) methodologies using Agisoft Photoscan. This yielded point clouds, high-resolution DEM and orthophotos with a ground resolution of 9 mm/pixel. A quality check performed in the field after DOM interpretation confirmed that this resolution is sufficient to properly map all the structures. More than 4700 fractures were manually digitized on the orthophotos and classified according to trend (Figure 6). (Insert Figure 6 here).

It is important to understand that the DOM interpretation only yields a (very large) set of lineaments that represent the intersection of some structural feature with the outcrop surface. To

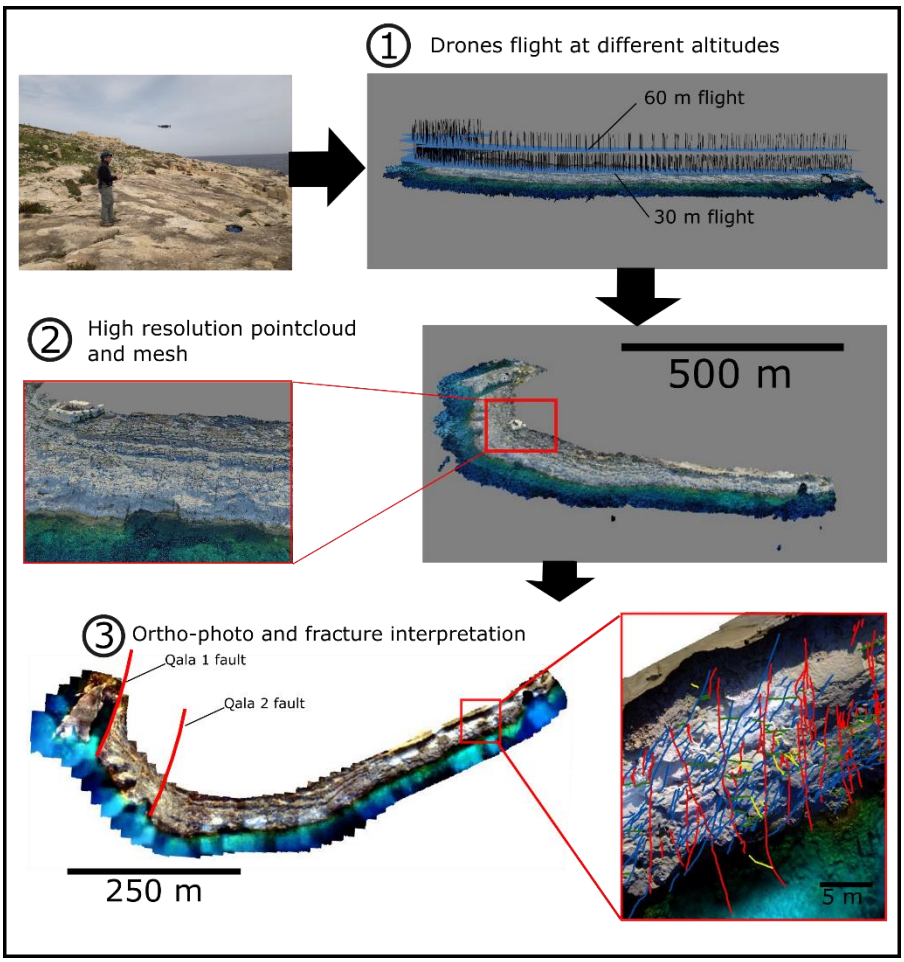

Figure 6: The workflow followed for the realization of the DOM and orthophoto for the fracture network digitization.

ensure that the structural and tectonic meaning of the lineaments (either joints, shear fractures, veins, styolites, etc.) mapped on the DOM was well understood, and that the relative chronology was properly characterized, we carried out a second traditional field survey after the DOM interpretation. This allowed us to label each lineament with structural attributes that can be characterized only in the field (e.g. dip angle, kinematic indicators, vein filling, etc.).

2.6.3 Fracture parameters characterization

The digitized fracture network and the Digital Outcrop Model were imported in Skua-Gocad. Virtual scan lines perpendicular to each fracture set and parallel to bedding (horizontal in this case) were created, and fracture intersections were extracted along the scanlines. Fracture spacing values were corrected using the Terzaghi correction. Fracture position and fracture spacing were then analyzed with custom Matlab scripts (DOMstudioLine) applying statistical tests to assess whether fracture distribution was stationary, or if fractures showed a trend or pattern/clustering (Bistacchi et al., 2019). This analysis allowed to define homogenous areas with stationary statistical distributions. Moreover, using the cumulative curve of the fracture position along the linear scanline we applied the methods proposed by Choi et al. (2016) to identify the width of the damage zone. After linear scanline analysis, we characterized the REV (Representative Elementary Volume) of the P_{20}, P_{21} and n'_c parameters. To do that using custom python scripts we applied on the DOM several square scan-areas varying the area of square scan-areas from 25 m^2 to 1600 m^2 and for every scan-area we calculated the P_{20}, P_{21} and n'_c value. The distribution obtained in the

1600 m^2 scan-areas was taken as the true value and compared with distributions obtained from smaller scan-areas, using the T- and F-tests. Following Esmaieli et al., (2010), we assume that the REV is reached for the smaller scan-area where both the statistical test fail to reject the null hypothesis of no difference with the distribution of the larger scan-area. As last step we performed the scan-area analysis, that allows measuring fracture density (P_{20}), fracture intensity (P_{21}), fracture length, fracture spacing and fracture network topology. Position and dimension of the scan-areas were chosen following the results of the linear scanline and REV analysis.

2.7 Results

2.7.1 Field analysis

Our field analysis reveals that the fault zone of the Qala 2 fault (a normal fault with ≈ 30 meters of vertical displacement) is characterized by a symmetric highly fractured zone, 5 m thick, that borders the fault core both in the hanging wall and in the footwall. We will call this zone the inner damage zone (IDZ). This observation is consistent with the findings of Cooke et al. (2018), who showed that the IDZ has a fracture density/intensity $P10 \approx 15\ m^{-1}$ that rapidly decreases to lower values within 5 m from the fault core.

We extended our analysis to larger area that was not investigated by Cooke et al. (2018) and we found that a thicker damage zone continues farther away from the fault core. We call this the outer damage zone (ODZ). Our observations show that the ODZ extends for several hundred meters both in the hanging wall and in the footwall (Figure 7a).

The hanging-wall ODZ extends to the South, from the Qala 2 fault towards the Qala 1 fault for ≈150 m in the Xlendi Member of the Lower Coralline Limestone. In this stratigraphic unit, we find mainly deformation bands with subordinated joints (Figure 7a).

On the other hand, in the footwall ODZ we find the Attard Member of the Lower Coralline Limestone for almost 800 meters. Here, the most common structures are joints with subordinate veins (Figure7a). Since the possibility to fully characterize the fracture network in the hanging wall is low due to its limited exposure, we decided to concentrate our attention in the footwall that is characterized by the same stratigraphic unit for almost 800 meters and is not disturbed by the presence of other faults (Figure 7a). Joints in the footwall are arranged in four sets striking ENE-WSW, WNW-ESE, N-S, and NE-SW (Figure 7b). Both ENE-WSW and WNW-ESE joint belong to major sets (“master joints”) and mutually cross-cut and abut, so the two sets have the same relative age. N-S and NE-SW joint sets are minor sets (“cross joints”) and systematically show abutting relationships with the major sets, so also these sets are interpreted as having the same relative age (Figure 7c) as also pointed by Martinelli et al., (2019).

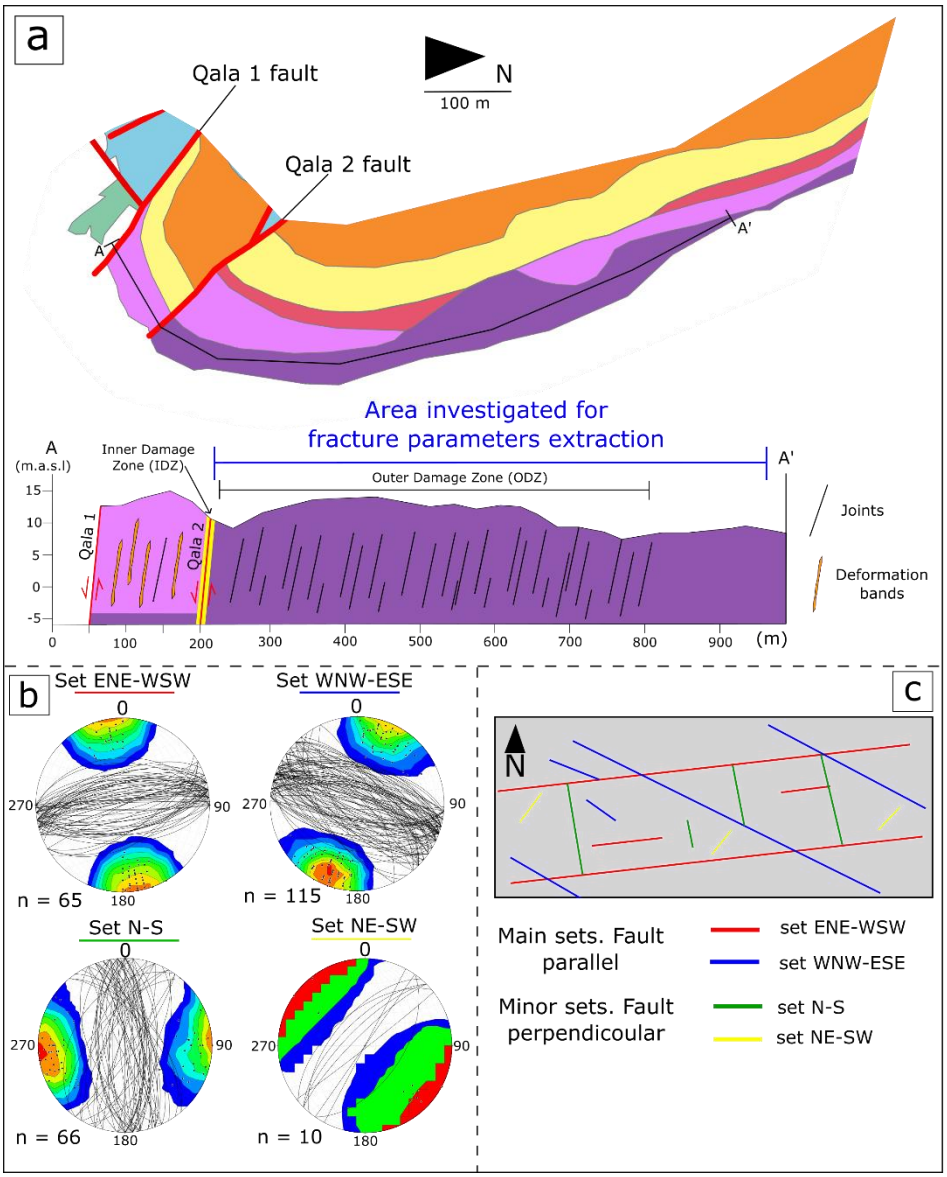

Figure 7: a) Main structural features of Qala fault zone. Colours refer to those of the stratigraphic column in Figure 3a; b) Lower hemisphere equal-area plots and density contour of poles representing attitude of the four sets of joint detected in the footwall of the Qala 2 fault; c) abutting and crosscutting relationships of the four joint sets. Attitude of the joints are available in Table S1 of the supplementary data

2.7.2 Linear scanline analysis

Fracture parameters characterization has been performed in the footwall of the Qala 2 fault, along an almost 900 m long composite scan-line spanning the whole outcrop from South to North (Figure 8a and 9a). The NE-SW set is sparse and poorly represented and for this reason it was excluded from the analysis. The N-S fracture set is parallel to the outcrop, and the resulting scanlines would be too short to give a statistically significant number of data. Therefore, the linear scanline analysis was performed only for the two main fracture sets (ENE-WSW and WNW-ESE).

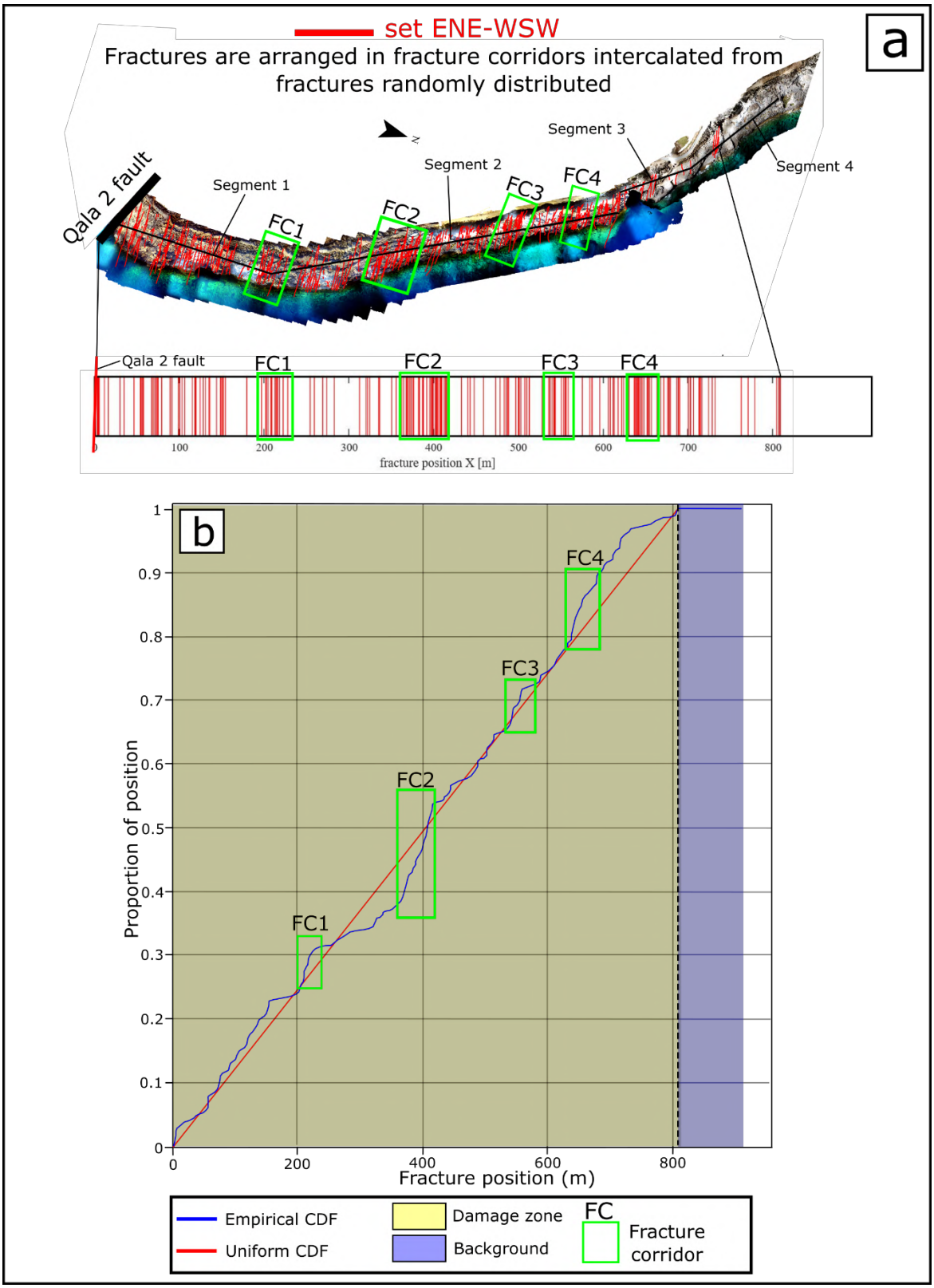

Figure 8: Results of the linear scan-line analysis for set ENE-WSW. a) Position of the linear scanline on the Digital Outcrop Model; b) cumulative curve of the fracture position along the scanline. Position of the fractures along the scanline is available in Table S2 of the supplementary data.

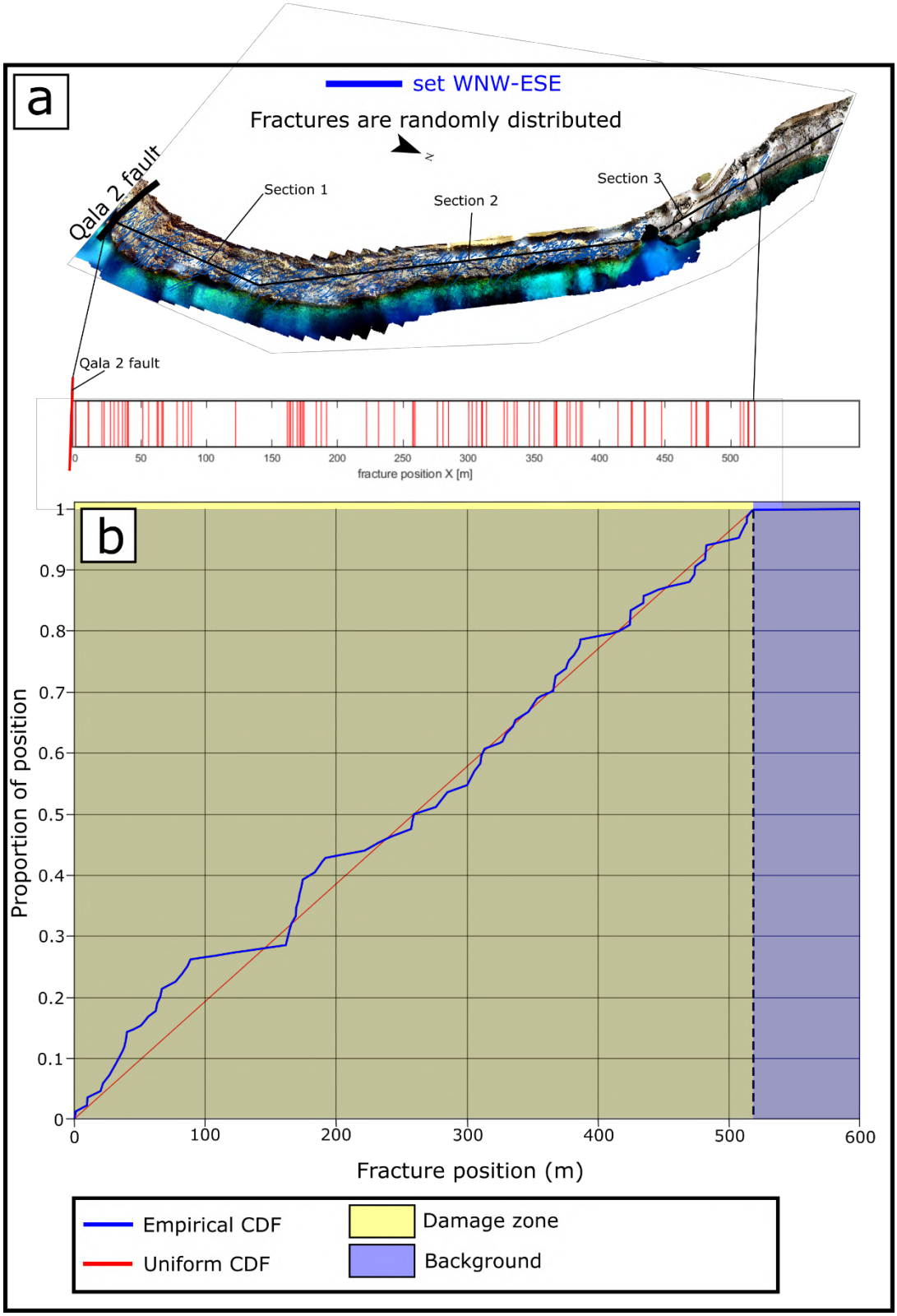

Figure 9: Results of the linear scan-line analysis of set WNW-ESE. a) position of the linear scanline on the Digital Outcrop Model; b) cumulative curve of the fracture position along the scanline. Position of the fractures along the scanline is available in Table S2 of the supplementary data.

To cover the entire length of the outcrop, four scanlines for the ENE-WSW set (Figure 8a) and

three for the WNW-ESE set (Figure 9a) were traced directly on the DOM (Digital Outcrop Model), corrected with the Terzaghi correction and combined in order to obtain a single scanline from the fault to the background (Figure 8a and 9a). The statistical analysis of Bistacchi et al., (2019) was applied on the combined scan-lines for both ENE-WSW and WNW-ESE sets.

The analysis shows that set ENE-WSW is characterized by the presence of four fracture corridors clearly identifiable also in the cumulative curve as a prolonged and almost uniform change in slope (Figure 8b). Fracture corridors are ~20-40 m wide and spaced ~100-200 m. The analysis was then repeated in smaller areas between the fracture corridors showing that, if we exclude the corridors from the dataset, fractures are randomly distributed (Figure 8b).

The linear scanline analysis performed for the WNW – ESE set reveals that it is characterized by a random spatial distribution and no fracture corridors were detected (Figure 9b).

Since the linear scanline used for the characterization of the WNW-ESE set is perpendicular to the Qala 2 fault (after Terzaghi's correction), it is possible to use its cumulative curve of the fracture position to identify the thickness of the damage zone (Choi et al., 2016; Mayolle et al., 2019). Even if local change in the slope of the curve is present, the overall inclination remains constant up to 520 meters away from the fault core (Figure 9b). Here, the slope of the cumulative curve suddenly drops to zero because no more fractures were detected until the end of the scanline (Figure 9b). For this reason, we conclude that the ODZ is 520 meters thick, and background fracturing is practically non-existent. (Insert Figures 8 and 9 here)

2.7.3 Representative Elementary Volume analysis

Since the fracture corridors all have different dimensions and parameters, looking for a fracture corridor REV is meaningless, so we excluded them from the analysis. Results summarized in Figure 10, show that the P_{20} REV is reached for scan-areas of 400 m^2 for set ENE-WSW and N-S, and for scan-areas of 900 m^2 for set WNW-ESE (Figure 10a). The P_{21} REV is reached for scan-areas of 225 m^2 for set ENE-WSW and N-S, and for scan-areas of 400 m^2 for set WNW-ESE (Figure 10b). Based on these results, we choose to perform the complete scan-area characterization using the most restrictive REV, hence with scan-areas larger than 400 m^2 for set ENE-WSW and N-S, and for scan-areas larger than 900 m^2 for set WNW-ESE. The topological REV performed on the n'_c parameter (equivalent number of connections per fracture) (Sævik and Nixon, 2017) is reached for scan-areas of 500 m^2 (Figure 10c).

2.7.4 Scan area analysis

Scan-areas were drawn covering uniformly areas identified by the scanline analysis. For the ENE-WSW set, a scan-area was placed on every fracture corridor and eight scan-areas were used in the

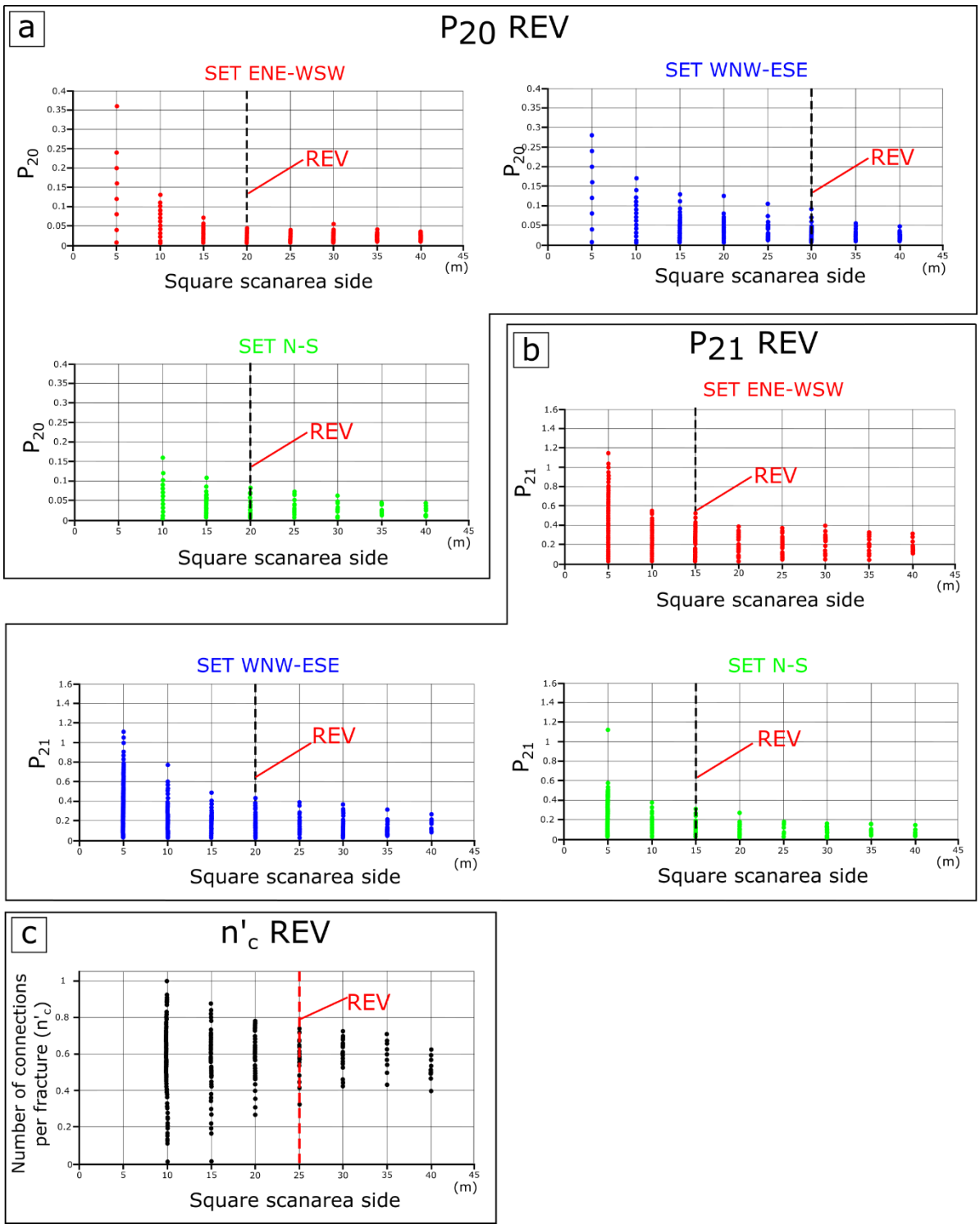

Figure 10: Results of the Representative Elementary Volume analysis of P20, P21 and n'c parameters for the ENE-WSW, WNW-ESE and N-S set. Data used for REV analysis are available in Table S3 (P20), S4 (P21) and S5 (n'c) in the supplementary data. Results of the t-test and f-test with p values are available in Figure S1 in the supplementary data

areas between the corridors characterized by randomly distributed fractures. For the WNW- ESE set, nine scan-areas were used. For the N-S set, even if we were not able to characterize the spatial distribution, we decided to use the same scan-areas as for the WNW-ESE set. Results are summarized in Figure 11. (Insert Figure 11 here)

Set ENE-WSW has mean fracture density $P20 \approx 0.03\, m^{-2}$ in the areas between fracture corridors and it reaches a maximum value of $P20 \approx 0.07\, m^{-2}$ within the fracture corridors. The mean fracture intensity is $P21 \approx 0.25\, m^{-2}$ with a maximum $P21 \approx 0.4\, m^{-2}$ inside fracture corridors and within 100 meters from the fault core. Fracture length ranges from a minimum of 0.2 m to a maximum of 30 m, with the median around 5 m, the first quartile around 2.5 m and the third quartile around 8 m both for fracture corridors and the areas with randomly distributed fractures. We observe that within 120 meters from the fault core fracture are longer with respect to the other areas as also testified from the values of P21. The maximum measured value of fracture length is controlled by the width of the outcrop and the presence of few longer fractures cannot be excluded (censoring bias). Fracture spacing ranges from a minimum of 0.15 m to a maximum of 30 m in the area between the fracture corridors where fractures are randomly distributed and show a negative exponential spacing distribution with mean and standard deviation of 5.6 m. Inside the fracture corridors, fractures are more closely spaced with a minimum of 0.1 m and a maximum of 10 m.

Set WNW – ESE has mean density value of $P20 \approx 0.03\, m^{-2}$ with a minimum of $P20 \approx 0.02\, m^{-2}$ and a maximum of $P20 \approx 0.08\, m^{-2}$. These fluctuations are compatible with a random distribution of the fracture network with areas characterized by a lower value with respect to the mean and areas characterized by higher values; the same behavior is observed for the fracture intensity, with a mean of $P20 \approx 0.15\, m^{-2}$, a minimum of $P21 \approx 0.11\, m^{-2}$ and a maximum of $P21 \approx 0.38\, m^{-2}$; Fracture length ranges from a minimum of ≈ 0.2 m to a maximum of 15 meters with the median around ≈ 4 meters, the first quartile around ≈ 2.5 and the third quartile around ≈ 7 meters. As for set ENE-WSW, fractures are slightly longer close to the slip surface. Fracture spacing ranges from a minimum of 0.15 meters to a maximum of 33 meters and show a negative exponential spacing distribution with mean and standard deviation of 5.36 m.

The N-S fracture set has mean density value of $P20 \approx 0.02\, m^{-2}$, with a minimum of $P20 \approx 0.01\, m^{-2}$ and a maximum of $P20 \approx 0.04\, m^{-2}$. As for set WNW-ESE, this oscillation is compatible with a random distribution. The mean intensity value is $P21 \approx 0.08$ with a maximum of $P21 \approx 0.12\, m^{-2}$ and a minimum of $P21 \approx 0.02\, m^{-2}$. As expected, N-S fractures are significantly shorter with respect to the ENE-WSW and WNW-ESE fracture sets; indeed they usually terminate against these two sets, the length ranges from a minimum of 0.1 m to a maximum of 13 meters with median around 2 meters, the first quartile around 1 and the third quartile around

5 meters. Fracture spacing ranges from a minimum of 0.1 meters to a maximum of 25 meters a median of 5 meters and shows a negative exponential spacing distribution with mean and standard deviation of 5.6 m.

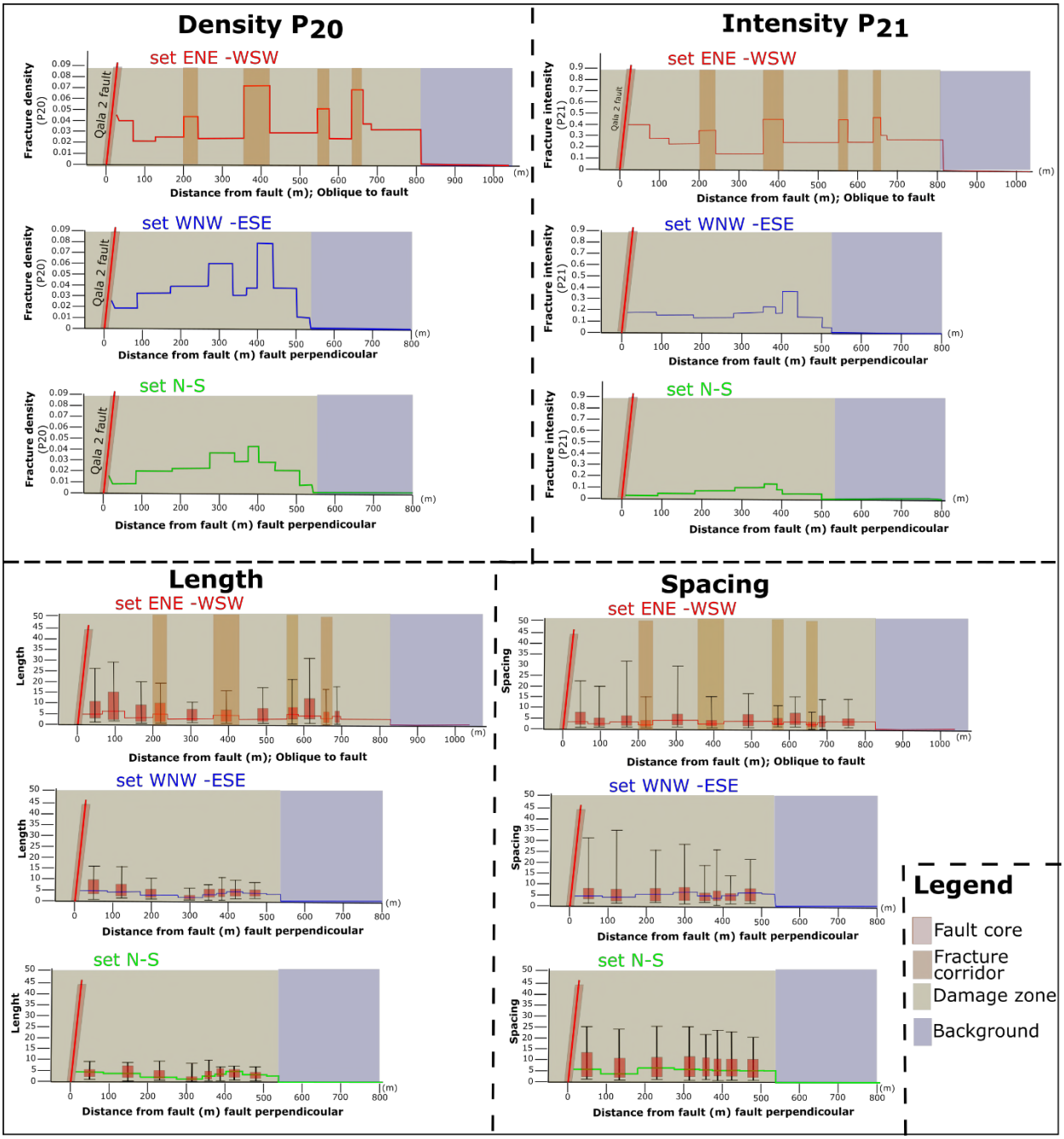

Figure 11: Results of the scan-area analysis for density (P20), intensity (P21), length and spacing of ENE-WSW, WNW-ESE and N-S fracture sets. See text for a complete explanation. Length data are available in Table S6 in the supplementary data; Spacing data are available in Table S7 in the supplementary data.

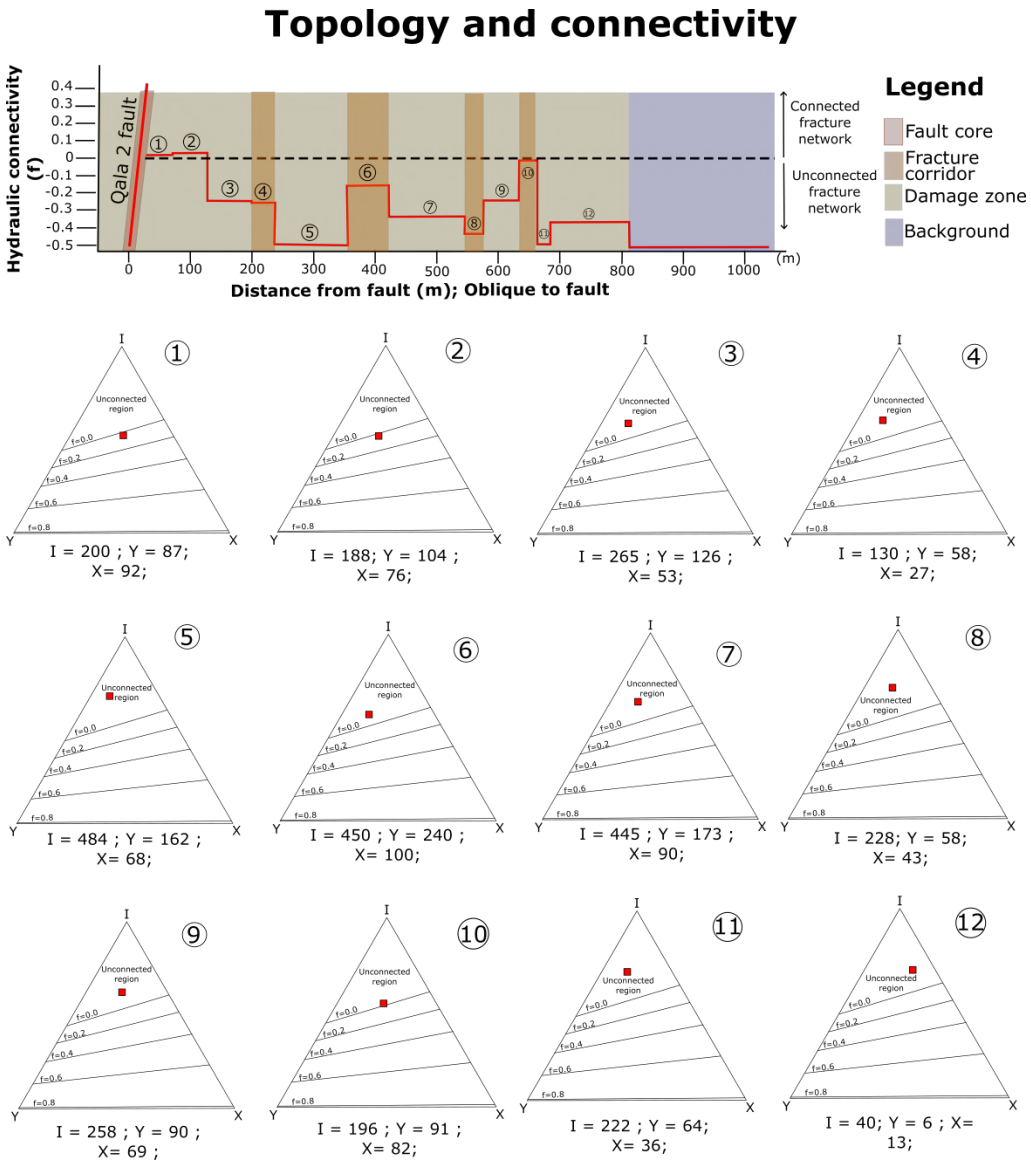

Figura 12: Results of the topological analysis and of the hydraulic connectivity using the method proposed by Saevik and Nixon, 2017. Fracture network is connected within 120 meters from the fault slip surface.

The fracture topology was characterized considering all the fracture sets. A scan-area was placed on every fracture corridor to properly consider their influence and eight scan-areas bigger than 500 m^2 were placed in the area between them. For every scan-area, the number of X, Y and I nodes was calculated and used to extract the hydraulic connectivity with the equation proposed by Saevik and Nixon, (2017). The results show that the fracture network is connected within 100-120 meters from the fault zone (Figure 12). Above this distance the hydraulic connectivity function decreases to zero, indicating that the fracture network is no more connected (Figure 12). Moreover, all the fracture corridors have a hydraulic connectivity equal to 0.

2.8 Discussion

2.8.1 The DOMstudio workflow

In this work we propose a new workflow that combines field analysis and interpretation on a high-resolution photogrammetric DOM with scan-line and scan-area analyses to study fracture parameters in the damage zone of normal faults in carbonates. The combination of field analysis with the interpretation carried out on the photogrammetric DOM was fundamental. Field data allowed discriminating the different fracture sets, labelling each lineament with structural attributes, and choosing the right resolution and extent of the photogrammetric DOM. At the same time, the photogrammetric DOM allowed us to map all fractures over the whole outcrop, from the fault core to the background domain not affected by fault-related fracturing. The same task, performed directly on the field would have required a huge amount of time and relevant errors in the position, geometry, topology and number of fractures. Moreover, the use of a digital fracture network allows us to use automatic methods to extract the fracture parameters and eventually obtain highly reliable statistics. The combination of linear scan-line and scan-area analysis permits to first characterize the spatial distribution of the fracture network in order to identify area with homogenous fracture distribution and then to extract fracture parameters from the individuated homogenous domains. Our new workflow also allowed us also to define the REV for P_{20}, P_{21} and topology. The results of this analysis bring two important advantages: i) they allow defining minimum dimension of the scan-area for a proper statistical analysis and at the same time to understand if the studied outcrop is big enough to fully characterize the fracture network; ii) they allow to map the distribution of structurally homogeneous volumes on the outcrop, as well as sub-volumes of increased fracture density (fracture corridors).

2.8.2 Comparison of the Qala 2 fault zone with current damage zone models

The analysis of the damage zone of the Qala 2 fault yields some important results: i) the damage zone is composed by a highly fractured IDZ zone, c. 5 m thick, and by an ODZ, c. 520 m thick; ii) if we exclude the fracture corridors, average fracture parameters (intensity, density, spacing) are rather constant within each zone (IDZ, ODZ, and background) with the only exception of P_{20} and P_{21} of set ENE-WSW that are slightly higher close to the fault zone; iii) fracture parameter values change abruptly at the boundaries between IDZ and ODZ, and between ODZ and background; iv) fracture length shows a substantial transition at c. 120 m within the ODZ, associated with just a slight variation of P_{21} and P_{20}, but associated to a relevant change in fracture connectivity.

These results are in contrast with some current models describing fracturing within damage zones (Mandl, 1988; Evans, 1990; Knott, 1994; Knott et al., 1996; Beach et al., 1999; Mandl, 1999;

Shipton and Cowie, 2001; Manighetti et al., 2004; Mitchell and Faulkner, 2009, 2012; Faulkner et al., 2011; Savage and Brodsky, 2011; Torabi and Berg, 2011; Choi et al., 2016; Perrin et al., 2016;). In the next paragraphs, we discuss this matter under different points of view.

2.8.3 Relationship between Damage zone width and fault displacement

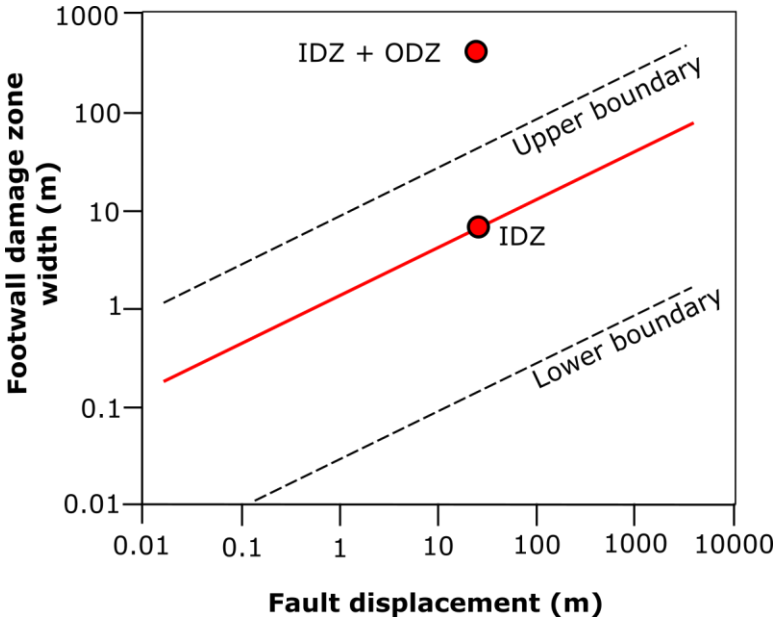

Figure 13: Comparison of the damage zone width of the Qala Fault with the dataset proposed by Choi et al., 2016 for footwall Damage Zone thickness considering both Inner Damage Zone (IDZ) and Outer Damage Zone (ODZ) and the IDZ alone;

The relationships between fault displacement and damage zone width has been investigated by several authors and many agree that the two parameters are related (Evans, 1990; Knott, 1994; Knott et al., 1996; Beach et al., 1999; Shipton and Cowie, 2001; Manighetti et al., 2004; Mitchell and Faulkner, 2009, 2012; Faulkner et al., 2011; Savage and Brodsky, 2011; Torabi and Berg, 2011; Choi et al. 2016; Perrin et al., 2016; Balsamo et al., 2019; Mayolle et al., 2019). Moreover, an asymmetry between the damage zone in the hanging wall and in the footwall of normal faults has been reported by many authors, who show more wide and intensely fractured damage zones in the hanging wall (Mandl, 1988; Knott et al., 1996; Mandl, 1999; Choi et al., 2016). Savage and Brodsky (2011), Choi et al. (2016) and Mayolle et al. (2019) provide extensive reviews about damage zone width and its relationship with displacement in normal faults using data from several sources and extracted scaling relationships for hanging wall and footwall damage zones with both deformation bands and joint/fractures, also proposing different criteria for damage zone definition.

The Qala 2 normal Fault shows c. 30 meters of slip, and its ODZ is almost 520 m wide in the footwall. If we compare this value with the dataset provided by Choi et al. (2016) for damage zone width in footwalls (Figure 13), it is clear that the damage zone of the Qala 2 Fault is characterized by an anomalously high value. An explanation can be that most of the previous studies about the relationships between the damage zone width with the fault displacement were performed directly on the field on a smaller scale with respect to the one of this study, with the fracture characterization carried out very close to the fault slip surface (usually some meters and only in

few cases for more than 200 meters). With this limitation that do not permit a complete observation of the fractures moving away from the faults, the highly fractured zone (inner damage zone) close to the slip surfaces could have been interpreted as the damage zone, whereas the surrounding outer damage zone could have been interpreted has the background fracturing. This hypothesis is supported by the fact that, if we consider only the width of the IDZ, it is consistent with the dataset provided by Choi et al., (2016) (Figure 13). This observation suggests that in the study and definition of the damage zone width there is the need to consider a volume as large as possible because faults (even with low displacement) can be surrounded by a large fractured volume with fracture density higher that the background. An alternative explanation for the high damage zone width reported in this study, is that we performed our analysis in the eastern termination of the Qala normal fault (Figure 3), where the two fault splays form a horsetail geometry. Such tip damage zones are commonly reported as sites of increased structural complexity and high fracture intensity (e.g., Choi et al., 2016, and references therein; Vermilye and Scholz, 1998). In both cases, our study indicates that greater exposures are essential for statistical analyses.

2.8.4 Fracture parameters inside the ODZ

The variation of fracture density within the damage zone has been characterized by several authors (e.g. Chester and Logan, 1986; Smith et al., 1990; Mitchell and Faulkner, 2009; Mitchell and Faulkner, 2012; Smith et al., 2013; Mayolle et al., 2019). Many studies show that fracture density in damage zones decreases exponentially moving away from fault cores, while others claim that deformation intensity unevenly decreases with fluctuations associated with secondary faults in the damage zone (e.g., Balsamo et al., 2019). However, as already seen for the relationships between damage zone width and fault displacement, for the investigated displacement range (i.e., 30-50 m), very few previous studies continuously characterized the fracture parameters for distances larger than two hundred meters from the fault core. Our observations on the Qala 2 faults confirm the exponential decrease of fracture density in the highly fractured IDZ (as already pointed by Cooke et al., 2018). However, this is not the case in the ODZ where fracture parameters (density, intensity and spacing) remain almost stable until the background is reached with the only exception of the P_{21} and P_{20} of set ENE-WSW that has slightly higher values within 100-120 meters from the fault core. On the other hand, fracture length shows a slightly different behavior with respect to the other parameters. Indeed, for ENE-WSW and WNW-ESE fracture sets, fractures are longer within 100-120 from the master slip surface. After this distance, fracture lengths decrease and oscillates around a mean value until the background value is reached abruptly. Fracture lengths of the N-S set is almost constant inside all the ODZ zone. This is due to the fact that the N-S fractures terminate against the fractures belonging to the major sets (ENE-WSW and WNW-ESE), therefore their growth and spacing is limited by the spacing of ENE and WNW fractures.

2.8.5 The structure of the Qala 2 fault and implications for fluid flow

The Qala 2 fault is composed by three distinct zones: the thin fault core (0.1 m thick), the highly fractured IDZ (5m thick), and the ODZ (520 m thick) (Figure 14).

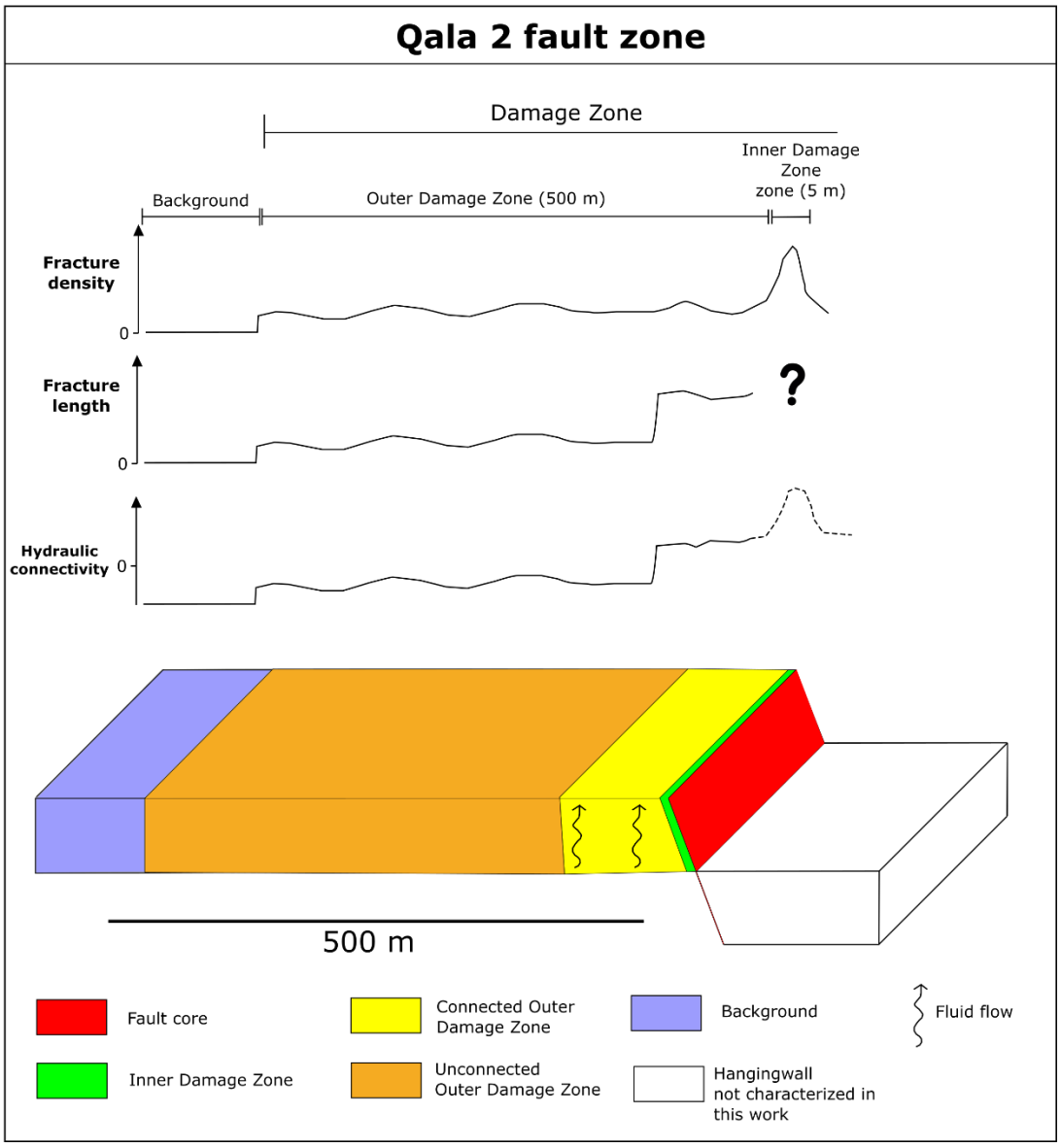

Figure 14: Conceptual model of the structure of the Qala 2 fault zone

Since the IDZ, especially in low displacement faults, is thin and confined close to the slip surface and the fault core can in some cases acts as a barrier for the fluid flow, the presence of a wide fractured zone can have an important role on the subsurface fluid flow. The analysis of the topology using the method proposed by Saevik and Nixon (2017), allowed us to characterize the hydraulic connectivity of the fracture network moving away from the faults. The results show that a connected fractured area is present in the ODZ within 100-120 meters from the fault slip surface

(Figure 14). This increase in the hydraulic connectivity is associated with an increase in the fracture length of set ENE-WSW and WNW-ESE and with a slightly increase of P_{20} and P_{21} of ENE-WSW. This result shows that fracture length seems to have a more important role then P_{20} in the control of the fracture network connectivity and that even a limited increase in the fracture length can cause an important change in the connectivity (Figure 15). The role of fracture length in controlling the fracture network connectivity is even more clear in fracture corridors, where fracture density is higher than in the other domains, but the hydraulic connectivity remains always below the percolation threshold because fracture length remains almost constant. This observation confirms once again the importance to use large outcrops to characterize fracture networks and especially fracture length distribution.

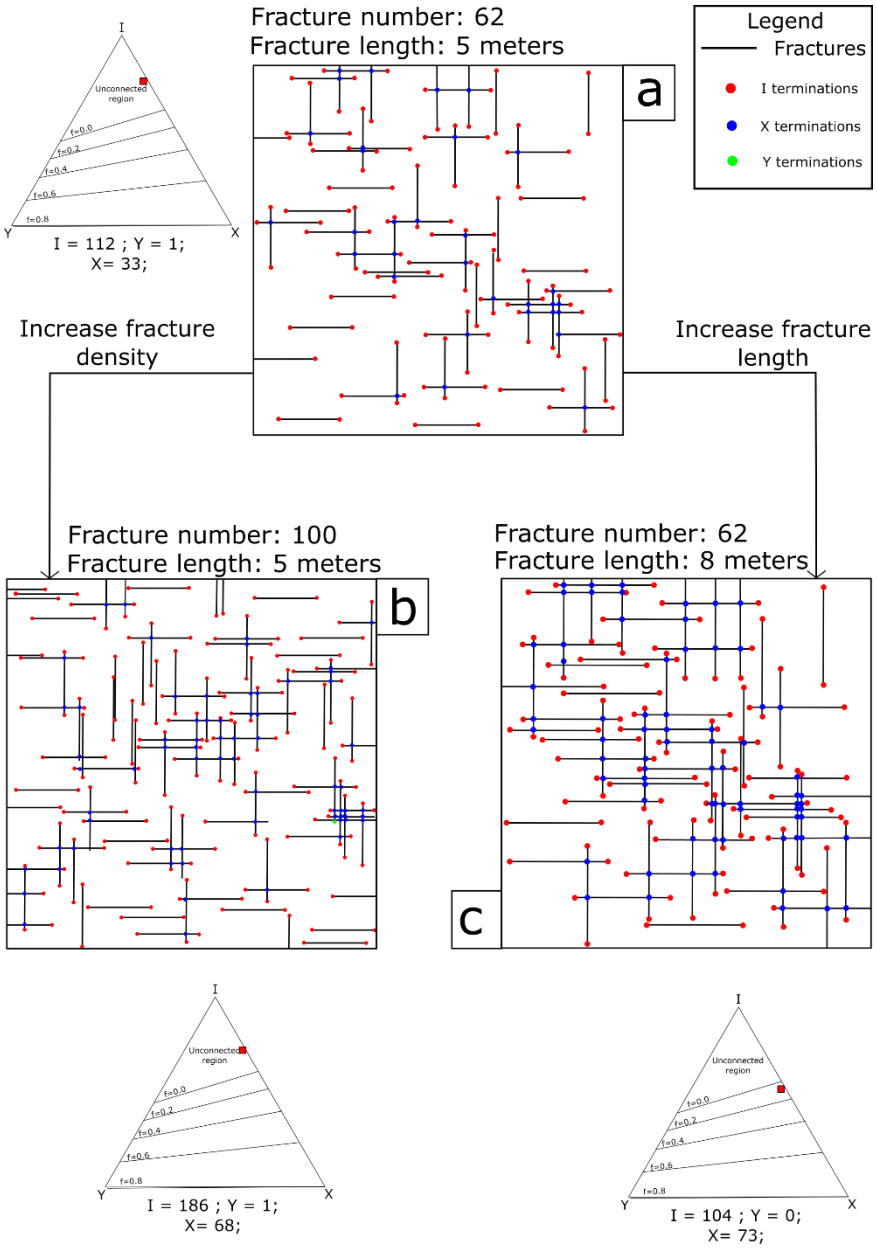

Figure 15: Scheme showing that fracture length has a crucial role in the fracture hydraulic connectivity as observed in the Qala 2 fault zone. a) unconnected fracture network composed by 62 fractures arranged in two orthogonal sets randomly distributed with fracture length of 5 meters; b) fracture network with the same characteristic of the first one but with higher density is still unconnected; c) fracture network with same characteristics of the first one but with longer fracture is connected

2.9 Conclusion

In this work we characterized spatial distribution, parameters, hydraulic connectivity and Representative Elementary Volume of a fracture network in the footwall of a normal fault affecting carbonate rocks. The results obtained combining linear scan-line and scan-area analysis with a high resolution photogrammetric model allow us to conclude that:

1) Towards the footwall, the Qala 2 fault zone is characterized by three distinct zones: the fault core, the highly fractured IDZ (Inner Damage Zone, 5 m thick) and the ODZ (Outer Damage Zone, 520 m thick).
2) The width of the Outer Damage Zone is larger than expected for normal faults with similar displacement, when compared with a compilation of field data in similar contexts (Choi et al., 2016). Therefore, in the characterization of the damage zone width there is the need to consider a volume as large as possible, in order to be sure to include the background in the analysis.
3) It is fundamental to apply the linear scan-line analysis before the scan-area analysis in order to properly characterize the spatial distribution of the fracture network.
4) Inside the ODZ, fracture parameters (density, intensity…) are more or less stable until the background is reached. According with the definition of Sanderson and Nixon (2017), the network is hydraulically connected only within the first 120 m from the fault core, where, although fracture density remains constant, fracture length increases. This result underlines that, for an effective characterization of fracture permeability, 1D information from scanline analysis needs to be integrated with areal information to fully characterize the fracture length distribution and intersections.
5) The combination of field work, detailed photogrammetry and automatic methods to extract fracture parameters allow to quickly collect and analyze a huge amount of fracture data giving statistically robust results, on a scale impossible to characterize with only field surveys.

Acknowledgments

Fieldwork and structural analysis were carried out by Martinelli, Bistacchi and Balsamo. Mittempergher, Caumon and Meda participated in important discussions after field work. The workflow for the Representative Elementary Volume Analysis was set up by Martinelli, Bonneau, Bistacchi and Caumon. Python scripts for the automatic extraction of fracture parameters from the DOM were written by Martinelli, Bistacchi and Bonneau. This paper was written by Martinelli with contributions from all co-authors. We thank Eni Spa for funding, reviewing and allowing us to publish the results of the study. The Malta Planning Authority and the Malta Resources

Authority are acknowledged for providing topographic data and base geological maps. Aaron Micallef is warmly acknowledged for fruitful discussions and a very useful introduction to the geology of Malta. We thank C. Antoine and the sponsors of the RING Consortium for the development of GoPy. All data are available in the supporting materials and moreover they are stored in the B2 share repository with the following DOI: XXXX/b2share.061f3bc873f7461c884b5ac9ea25bc52 (at the moment these data are not open access, we will convert them to open access if the article will be accepted)

References

Agosta, F., 2008. Fluid flow properties of basin-bounding normal faults in platform carbonates, Fucino Basin, central Italy. Geological Society Special Publication 299, 277–291. https://doi.org/10.1144/SP299.17

Agosta, F., Prasad, M., Aydin, A., 2007. Physical properties of carbonate fault rocks, fucino basin (Central Italy): Implications for fault seal in platform carbonates. Geofluids 7, 19–32. https://doi.org/10.1111/j.1468-8123.2006.00158.x

Antonellini, M., Aydin, A., 1994. Effect of faulting on fluid flow in porous sandstones: petrophysical properties. American Association of Petroleum Geologists Bulletin 78, 355–377.

Aydin, A., Johnson, A.M., 1978. Development of Faults as Zones of DEformation Bands and as Slip Surfaces in Sandstone. Pageoph 116.

Azizmohammadi, S., Matthäi, S.K., 2017. Is the permeability of naturally fractured rocks scale dependent? Water Resources Research 53, 8041–8063. https://doi.org/10.1002/2016WR019764

Baecher, G., Laaney, N.A., 1978. trace Length biased in joint surveys. American Rock Mechanics Association.

Balsamo, F., Clemenzi, L., Storti, F., Solum, J., Taberner, C., 2019. Tectonic control on vein attributes and deformation intensity in fault damage zones affecting Natih platform carbonates, Jabal Qusaybah, North Oman. Journal of Structural Geology 122, 38–57. https://doi.org/10.1016/j.jsg.2019.02.009

Basa, A., Ahmed, F., Bhattacharyya, K., Roy, A., 2019. Evolution and characterization of fracture patterns: Insights from multi-scale analysis of the Buxa dolomite in the Siang Valley, Arunachal Lesser Himalayan fold-thrust belt. Journal of Structural Geology 123, 54–66. https://doi.org/10.1016/j.jsg.2019.03.004

Beach, A., Welbon, A.I., Brockbank, P.J., McCallum, J.E., 1999. Reservoir damage around faults: Outcrop examples from the Suez rift. Petroleum Geoscience 5, 109–116. https://doi.org/10.1144/petgeo.5.2.109

Bear, J., 1972. Dynamics of Fluids in Porous Media. American Elsevier Publishing Company, New York, 764 p. https://doi.org/10.1097/00010694-197508000-00022

Bellian, J.A., Kerans, C., Jennette, D.C., 2005. Digital Outcrop Models: Applications of Terrestrial Scanning Lidar Technology in Stratigraphic Modeling. Journal of Sedimentary Research 75, 166–176. https://doi.org/10.2110/jsr.2005.013

Bertrand, L., Géraud, Y., Le Garzic, E., Place, J., Diraison, M., Walter, B., Haffen, S., 2015. A multiscale analysis of a fracture pattern in granite: A case study ofthe Tamariu granite, Catalunya, Spain. Journal of Structural Geology 78, 52–66. https://doi.org/10.1016/j.jsg.2015.05.013

Bistacchi, A., Balsamo, F., Storti, F., Mozafari, M., Swennen, R., Solum, J., Tueckmantel, C., Taberner, C., 2015. Photogrammetric digital outcrop reconstruction, visualization with textured surfaces, and three-dimensional structural analysis and modeling: Innovative methodologies applied to fault-related dolomitization (Vajont Limestone, Southern Alps, Italy). Geosphere 11, 2031–2048. https://doi.org/10.1130/GES01005.1

Bistacchi, A., Massironi, M., Menegon, L., 2010. Three-dimensional characterization of a crustal-scale fault zone: The Pusteria and Sprechenstein fault system (Eastern Alps). Journal of Structural Geology 32, 2022–2041. https://doi.org/10.1016/j.jsg.2010.06.003

Bistacchi, A., Mittempergher, S., Martinelli, M., 2019. A robust non-parametric statistical approach to characterize fracture spatial distribution. Geophysical Research Abstract EGU2019 12361-2 21.

Bons, P.D., Arnold, J., Elburg, M.A., Kalda, J., Soesoo, A., van Milligen, B.P., 2004. Melt extraction and accumulation from partially molten rocks. Lithos 78, 25–42. https://doi.org/10.1016/j.lithos.2004.04.041

Buckley, S.J., Howell, J.A., Enge, H.D., Kurz, T.H., 2008. Terrestrial laser scanning in geology: Data acquisition, processing and accuracy considerations. Journal of the Geological Society 165, 625–638. https://doi.org/10.1144/0016-76492007-100

Caine, J.S., Evans, J.P., Forster, C.B., 1996. Fault zone architecture and permeability structure. Geology 24, 1025–1028. https://doi.org/10.1130/0091-7613(1996)024<1025:FZAAPS>2.3.CO;2

Call, R.D., Savely, J.P., Nicholas, D.E., 1976. Estimation of Joint Set Characteristics From surface Mapping Data. The 17th U.S. Symposium on Rock Mechanics (USRMS), 25-27 August, Snow Bird, Utah.

Chester, F. M., Logan, J.M., 1986. Implications for mechanical properties of Brittle Faults from Observations of the Punchbowl Fault Zone, California. Pageoph 124. https://doi.org/10.1130/0016-7606(1988)100<1451:DOSSSF>2.3.CO;2

Chester, F.M., Evans, J.P., Biegel, R.L., 1993. Internal structure and weakening mechanisms of the San Andreas Fault. Journal of Geophysical Research 98, 771–786. https://doi.org/10.1029/92JB01866

Choi, J.H., Edwards, P., Ko, K., Kim, Y.S., 2016. Definition and classification of fault damage zones: A review and a new methodological approach. Earth-Science Reviews 152, 70–87. https://doi.org/10.1016/j.earscirev.2015.11.006

Cooke, A.P., Fisher, Q.J., Michie, E.A.H., Yielding, G., 2018. Investigating the controls on fault rock distribution in normal faulted shallow burial limestones, Malta, and the implications for fluid flow. Journal of Structural Geology 114, 22–42. https://doi.org/10.1016/j.jsg.2018.05.024

Cruden, D.M., 1977. Describing the size of discontinuities. International Journal of Rock Mechanics and Mining Sciences And 14, 133–137. https://doi.org/10.1016/0148-9062(77)90004-3

Dart, C.J., Bosence, D.W.J., McClay, K.R., 1993. Stratigraphy and structure of the Maltese Graben system. Journal - Geological Society (London) 150, 1153–1166. https://doi.org/10.1144/gsjgs.150.6.1153

Dershowitz, W., Herda, H., 1992. Interpretation of fracture spacing and intensity. In JR Tillerson & W Wawersik (Eds), Proceedings of the 33rd U.S. Rock Mechanics Symposium, Balkema, Rotterdam, 757–766.

Dershowitz, W.S., Einstein, H.H., 1988. Characterizing Rock Joint Geometry with Joint System Model. Rock Mechanics and Rock Engineering 21, 21–51.

Esmaieli, K., Hadjigeorgiou, J., Grenon, M., 2010. Estimating geometrical and mechanical REV based on synthetic rock mass models at Brunswick Mine. International Journal of Rock Mechanics and Mining Sciences 47, 915–926. https://doi.org/10.1016/j.ijrmms.2010.05.010

Evans, J.P., 1990. Brevia SHORT NOTES Thickness--displacement relationships for fault zones.

Journal of Structural Geology 12, 1061–1065.

Evans, J.P., Forster, C.B., Goddard, J. V., 1997. Permeability of fault-related rocks, and implications for hydraulic structure of fault zones. Journal of Structural Geology 19, 1393–1404.

Færseth, R.B., Johnsen, E., Sperrevik, S., 2007. Methodology for risking fault seal capacity: Implications of fault zone architecture. AAPG Bulletin 91, 1231–1246. https://doi.org/10.1306/03080706051

Faulkner, D.R., Mitchell, T.M., Jensen, E., Cembrano, J., 2011. Scaling of fault damage zones with displacement and the implications for fault growth processes. Journal of Geophysical Research: Solid Earth 116, 1–11. https://doi.org/10.1029/2010JB007788

Felix, R., 1973. Oligo-Miocene stratigraphy of Malta and Gozo. Mededelingen Landbouwhogeschool Wageningen 73, 1–103.

Fisher, Q.J., Knipe, R.J., 2001. The permeability of faults within siliciclastic petroleum reservoirs of the North Sea and Norwegian Continental Shelf. Marine and Petroleum Geology 18, 1063–1081. https://doi.org/10.1016/S0264-8172(01)00042-3

Flodin, E.A., Aydin, A., Gerdes, M., Wiggins, W.D., 2005. Petrophysical Properties and Sealing Capacity of Fault Rock, Aztec Sandstone, Nevada.

Franceschi, M., Martinelli, M., Gislimberti, L., Rizzi, A., Massironi, M., 2015. Integration of 3D modeling, aerial LiDAR and photogrammetry to study a synsedimentary structure in the Early Jurassic Calcari Grigi (Southern Alps, Italy). European Journal of Remote Sensing 48, 527–539. https://doi.org/10.5721/EuJRS20154830

Fulljames, J.R., Zijerveld, L.J.J., Franssen, R.C.M.W., 1997. Fault seal processes: systematic analysis of fault seals over geological and production time scales. Norwegian Petroleum Society Special Publications 7, 51–59. https://doi.org/10.1016/S0928-8937(97)80006-9

Guerriero, V., Vitale, S., Ciarcia, S., Mazzoli, S., 2011. Improved statistical multi-scale analysis of fractured reservoir analogues. Tectonophysics 504, 14–24. https://doi.org/10.1016/j.tecto.2011.01.003

Haneberg, W.C., 2008. Using close range terrestrial digital photogrammetry for 3-D rock slope modeling and discontinuity mapping in the United States. Bulletin of Engineering Geology and the Environment 67, 457–469. https://doi.org/10.1007/s10064-008-0157-y

Healy, D., Rizzo, R.E., Cornwell, D.G., Farrell, N.J.C., Watkins, H., Timms, N.E., Gomez-

Rivas, E., Smith, M., 2017. FracPaQ: A MATLAB™ toolbox for the quantification of fracture patterns. Journal of Structural Geology 95, 1–16. https://doi.org/10.1016/j.jsg.2016.12.003

Hodgetts, D., 2013. Laser scanning and digital outcrop geology in the petroleum industry: A review. Marine and Petroleum Geology 46, 335–354. https://doi.org/10.1016/j.marpetgeo.2013.02.014

Illies, J.H., 1981. Graben formation - the maltese islands - a case history. Tectonophysics, 73, 151–168.

Jacquemyn, C., Huysmans, M., Hunt, D., Casini, G., Swennen, R., 2015. Multi-scale three-dimensional distribution of fracture- and igneous intrusion-controlled hydrothermal dolomite from digital outcrop model, Latemar platform, Dolomites, northern Italy. AAPG Bulletin 99, 957–984. https://doi.org/10.1306/10231414089

Jolley, S.J., Dijk, H., Lamens, J.H., Fisher, Q.J., Manzocchi, T., Eikmans, H., Huang, Y., 2007. Faulting and fault sealing in production simulation models: Brent Province, northern North Sea. Petroleum Geoscience 13, 321–340. https://doi.org/10.1144/1354-079306-733

Knai, T.A. and Knipe, R.J., 1998. The impact of faults on fluid flow in the Heidrum Field. JONES, G., FISHER, Q. J. & KNIPE, R. J. (Eds) Faulting, Fault Sealing and Fluid Flow in Hydrocarbon Reservoirs. Geological Society, London, Special Publications, 147, 269–282. https://doi.org/10.1016/j.petrol.2018.11.056

Knipe, R.J., 1992. Faulting processes and fault seal. Structural and Tectonic Modelling and Its Application to Petroleum Geology. Proceedings of Norwegian Petroleum Society Workshop, 18–20 October 1989, Stavanger, Norway Norwegian Petroleum Society Special Publications 325–342.

Knott, S.D., 1994. Fault zone thickness versus displacement in the Permo-Triassic sandstones of NW England. Journal - Geological Society (London) 151, 17–25. https://doi.org/10.1144/gsjgs.151.1.0017

Knott, S.D., Beach, A., Brockbank, P.J., Lawson, J., Mccallum, J.E., Welbon, A.I., 1996. Spatial and mechanical controls on normal fault populations. Journal of Structural Geology 18, 359–372.

Kulatilake, P.H.S.W., Wu, T.H., 1984. The density of discontinuity traces in sampling windows. International Journal of Rock Mechanics and Mining Sciences And 21, 345–347. https://doi.org/10.1016/0148-9062(84)90367-X

Li, J.H., Zhang, L.M., Wang, Y., Fredlund, D.G., 2009. Permeability tensor and representative elementary volume of saturated cracked soil. Canadian Geotechnical Journal 46, 928–942. https://doi.org/10.1139/T09-037

Long, J.C.S., Remer, J.S., Wilson, C.R., Witherspoon, P.A., 1982. Porous media equivalents for networks of discontinuous fractures. Water Resources Research 18, 645–658. https://doi.org/10.1029/WR018i003p00645

Mandl, G., 1999. Faulting in brittle rocks: an introduction to the mechanism of tectonic faults. Springer Science & Business Media. https://doi.org/10.1016/S0191-8141(96)80056-3

Mandl, G., 1988. Mechanics of tectonic faulting: models and basic concepts. Amsterdam: Elsevier 408. https://doi.org/10.1016/0191-8141(89)90058-8

Manighetti, I., King, G., Sammis, C.G., 2004. The role of off-fault damage in the evolution of normal faults. Earth and Planetary Science Letters 217, 399–408. https://doi.org/10.1016/S0012-821X(03)00601-0

Manzocchi, T., 2002. The connectivity of two-dimensional networks of spatially correlated fractures. Water Resources Research 38, 1-1-1–20. https://doi.org/10.1029/2000wr000180

Marrett, R., Gale, J.F.W., Gómez, L.A., Laubach, S.E., 2018. Correlation analysis of fracture arrangement in space. Journal of Structural Geology 108, 16–33. https://doi.org/10.1016/j.jsg.2017.06.012

Martinelli, M., Bistacchi, A., Balsamo, F., Meda, M., 2019. Late Oligocene to Pliocene Extension in the Maltese Islands and Implications for Geodynamics of the Pantelleria Rift and Pelagian Platform. Tectonics. https://doi.org/10.1029/2019TC005627

Martinelli, M., Franceschi, M., Massironi, M., Rizzi, A., Salvetti, G., Zampieri, D., 2017. An extensional syn-sedimentary structure in the Early Jurassic Trento Platform (Southern Alps, Italy) as analogue of potential hydrocarbon reservoirs developing in rifting-affected carbonate platforms. Marine and Petroleum Geology 79, 360–371. https://doi.org/10.1016/j.marpetgeo.2016.11.002

Mauldon, M., 1998. Estimating mean fracture trace length and density from observations in convex windows. Rock Mechanics and Rock Engineering 31, 201–216. https://doi.org/10.1007/s006030050021

Mauldon, M., Dunne, W.M., Rohrbaugh, M.B., 2001. Circular scanlines and circular windows: New tools for characterizing the geometry of fracture traces. Journal of Structural Geology

23, 247–258. https://doi.org/10.1016/S0191-8141(00)00094-8

Mayolle, S., Soliva, R., Caniven, Y., Wibberley, C., Ballas, G., Milesi, G., Dominguez, S., 2019. Scaling of fault damage zones in carbonate rocks. Journal of Structural Geology 124, 35–50. https://doi.org/10.1016/j.jsg.2019.03.007

McCaffrey, K.J.W., Jones, R.R., Holdsworth, R.E., Wilson, R.W., Clegg, P., Imber, J., Holliman, N., Trinks, I., 2005. Unlocking the spatial dimension: Digital technologies and the future of geoscience fieldwork. Journal of the Geological Society 162, 927–938. https://doi.org/10.1144/0016-764905-017

Micarelli, L., Benedicto, A., Wibberley, C.A.J., 2006. Structural evolution and permeability of normal fault zones in highly porous carbonate rocks. Journal of Structural Geology 28, 1214–1227. https://doi.org/10.1016/j.jsg.2006.03.036

Mitchell, T.M., Faulkner, D.R., 2012. Towards quantifying the matrix permeability of fault damage zones in low porosity rocks. Earth and Planetary Science Letters 339–340, 24–31. https://doi.org/10.1016/j.epsl.2012.05.014

Mitchell, T.M., Faulkner, D.R., 2009. The nature and origin of off-fault damage surrounding strike-slip fault zones with a wide range of displacements: A field study from the Atacama fault system, northern Chile. Journal of Structural Geology 31, 802–816. https://doi.org/10.1016/j.jsg.2009.05.002

Müller, C., Siegesmund, S., Blum, P., 2010. Evaluation of the representative elementary volume (REV) of a fractured geothermal sandstone reservoir. Environmental Earth Sciences 61, 1713–1724. https://doi.org/10.1007/s12665-010-0485-7

Murray, J., 1890. The Maltese Islands with special reference to their geological structure. Scott. Geogr. Mag. 449–488.

Oda, M., 1986. An Equivalent Continuum Model for Coupled Stress and Fluid Flow Analysis in Jointed Rock Masses. Water Resources Research 22, 1845–1856.

Pahl, P.J., 1981. Estimating the mean length of discontinuity traces. International Journal of Rock Mechanics and Mining Sciences And 18, 221–228. https://doi.org/10.1016/0148-9062(81)90976-1

Peacock, D.C.P., Sanderson, D.J., Rotevatn, A., 2018. Relationships between fractures. Journal of Structural Geology 106, 41–53. https://doi.org/10.1016/j.jsg.2017.11.010

Pedley, H.M., House, M.R., Waugh, B., 1976. The geology of Malta and Gozo. Proceedings of

the Geologists' Association 87, 325–341. https://doi.org/10.1016/S0016-7878(76)80005-3

Perrin, C., Manighetti, I., Gaudemer, Y., 2016. Off-fault tip splay networks: A genetic and generic property of faults indicative of their long-term propagation. Comptes Rendus - Geoscience 348, 52–60. https://doi.org/10.1016/j.crte.2015.05.002

Priest, S.D., 1993. The collection and analysis of discontinuity orientation data for engineering design, with examples. Rock Testing and Site Characterization. Pergamon. 167–192.

Priest, S.D., Hudson, J.A., 1981. Estimation of discontinuity spacing and trace length using scanline surveys. International Journal of Rock Mechanics and Mining Sciences And 18, 183–197. https://doi.org/10.1016/0148-9062(81)90973-6

Rempe, M., Mitchell, T.M., Renner, J., Smith, S.A.F., Bistacchi, A., Di Toro, G., 2018. The Relationship Between Microfracture Damage and the Physical Properties of Fault-Related Rocks: The Gole Larghe Fault Zone, Italian Southern Alps. Journal of Geophysical Research: Solid Earth 123, 7661–7687. https://doi.org/10.1029/2018JB015900

Reuther, C.D., Eisbacher, G.H., 1985. Pantelleria Rift - crustal extension in a convergent intraplate setting. Geologische Rundschau 74, 585–597. https://doi.org/10.1007/BF01821214

Riley, P.R., Goodwin, L.B., Lewis, C.J., 2010. Controls on fault damage zone width, structure, and symmetry in the Bandelier Tuff, New Mexico. Journal of Structural Geology 32, 766–780. https://doi.org/10.1016/j.jsg.2010.05.005

Rohrbaugh, J.B., Dunne, W.M., Mauldon, M., 2002. Estimating fracture trace intensity, density, and mean length using circular scan lines and windows. AAPG Bulletin 86, 2089–2104. https://doi.org/10.1306/61EEDE0E-173E-11D7-8645000102C1865D

Rong, G., Peng, J., Wang, X., Liu, G., Hou, D., 2013. Permeability tensor and representative elementary volume of fractured rock massesTenseur de perméabilité et volume élémentaire représentatif des massifs de roche fracturéeTensor de permeabilidad y volumen elemental representativo de masas de rocas fractur. Hydrogeology Journal 21, 1655–1671. https://doi.org/10.1007/s10040-013-1040-x

Sævik, P.N., Nixon, C.W., 2017. Inclusion of Topological Measurements into Analytic Estimates of Effective Permeability in Fractured Media. Water Resources Research 53, 9424–9443. https://doi.org/10.1002/2017WR020943

Sanderson, D.J., 2016. Field-based structural studies as analogues to sub-surface reservoirs.

Geological Society Special Publication 436, 207–217. https://doi.org/10.1144/SP436.5

Sanderson, D.J., Nixon, C.W., 2015. The use of topology in fracture network characterization. Journal of Structural Geology 72, 55–66. https://doi.org/10.1016/j.jsg.2015.01.005

Savage, H.M., Brodsky, E.E., 2011. Collateral damage: Evolution with displacement of fracture distribution and secondary fault strands in fault damage zones. Journal of Geophysical Research: Solid Earth 116. https://doi.org/10.1029/2010JB007665

Schulz, S.E., Evans, J.P., 2000. Mesoscopic structure of the Punchbowl Fault, Southern California and the geologic and geophysical structure of active strike-slip faults. Journal of Structural Geology 22, 913–930. https://doi.org/10.1016/S0191-8141(00)00019-5

Schulz, S.E., Evans, J.P., 1998. Spatial variability in microscopic deformation and composition of the Punchbowl fault, southern California: Implications for mechanisms, fluid-rock interaction, and fault morphology. Tectonophysics 295, 223–244. https://doi.org/10.1016/S0040-1951(98)00122-X

Shipton, Z.K., Cowie, P.A., 2001. Damage zone and slip-surface evolution over μm to km scales in high-porosity Navajo sandstone, Utah. Journal of Structural Geology 23, 1825–1844. https://doi.org/10.1016/S0191-8141(01)00035-9

Smith, L., Forster, C.B., Evans, J., 1990. Interaction of fault zones, fluid flow, and heat transfer at the basin scale. In Hydrogeology of Permeability Environments: International Association of Hydrogeologists 2, 41–67.

Smith, D.A., 1980. Sealing and non-sealing faults in Louisiana Gulf Coast basins. Am. Assoc. Pet. Geol. Bull 64, 145–172.

Smith, S.A.F., Bistacchi, A., Mitchell, T.M., Mittempergher, S., Di Toro, G., 2013. The structure of an exhumed intraplate seismogenic fault in crystalline basement. Tectonophysics 599, 29–44. https://doi.org/10.1016/j.tecto.2013.03.031

Tavani, S., Granado, P., Corradetti, A., Girundo, M., Iannace, A., Arbués, P., Muñoz, J.A., Mazzoli, S., 2014. Building a virtual outcrop, extracting geological information from it, and sharing the results in Google Earth via OpenPlot and Photoscan: An example from the Khaviz Anticline (Iran). Computers and Geosciences 63, 44–53. https://doi.org/10.1016/j.cageo.2013.10.013

Taylor, D.J., Dietvorst, J.P.A., 1991. The Cormorant Field, Blocks 211/21a, 211/26a, UK North Sea. Geological Society Memoir 14, 73–82.

https://doi.org/10.1144/GSL.MEM.1991.014.01.09

Terzaghi, R., 1965. Sources of Error in Joint Surveys. Géotechnique 287–304.

Torabi, A., Berg, S.S., 2011. Scaling of fault attributes: A review. Marine and Petroleum Geology 28, 1444–1460. https://doi.org/10.1016/j.marpetgeo.2011.04.003

Twiss, R.J., Moores, E.M., 2006. Structural Geology (2nd Ed.). W. H. Freeman.

Vasuki, Y., Holden, E.J., Kovesi, P., Micklethwaite, S., 2014. Semi-automatic mapping of geological Structures using UAV-based photogrammetric data: An image analysis approach. Computers and Geosciences 69, 22–32. https://doi.org/10.1016/j.cageo.2014.04.012

Vermilye, J.M., Scholz, C.H., 1998. The process zone: A microstructural view of fault growth. Journal of Geophysical Research 103, 12223--12237.

Watkins, H., Bond, C.E., Healy, D., Butler, R.W.H., 2015. Appraisal of fracture sampling methods and a new workflow tocharacterise heterogeneous fracture networks at outcrop. Journal of Structural Geology 72, 67–82. https://doi.org/10.1016/j.jsg.2015.02.001

Wibberley, C.A.J., Shimamoto, T., 2003. <Wibberley and Shimamoto 2003 Internal structure and permeability of major strike-slip fault zones.pdf>. 25. https://doi.org/10.1016/S0191-8141(02)00014-7

Wiprut, D., and Zoback, M.D., 2000. Fault reactivation and fluid flow along a previously dormant normal fault in the Northern North Sea. Geology 28, 595–598. https://doi.org/10.1130/0091-7613(2000)28<595:FRAFFA>2.0.CO;2

Wu, H. and Pollard, D.D., 1995. An experimental study of the relationship between joint spacing and layer thickness. Journal of Structural Geology 17, 887–905.

Yielding, G., Freeman, B., Needham, D.T., 1997. Quantitative fault seal prediction. AAPG Bulletin 81, 897–917.

Zeeb, C., Gomez-Rivas, E., Bons, P.D., Blum, P., 2013. Evaluation of Sampling methods for fracture network characterization using Outcrops. AAPG Bulletin 97, 1545–1566. https://doi.org/10.1306/02131312042

3

Stratigraphic control on damage zone width in faulted platform carbonates: an example from the Gozo Island, Malta

This chapter is presented in the form of a paper that is in preparation to be submitted to the Earth and Planetary Science Letters Journal.

Stratigraphic control on damage zone width in faulted platform carbonates: an example from the Gozo Island, Malta

Mattia Martinelli[1*], Andrea Bistacchi[1], Riccardo Castellanza[1], Fabrizio Balsamo[2]

[1]Dipartimento di Scienze dell'Ambiente e della Terra, Universita' degli Studi di Milano Bicocca, Piazza della Scienza 4, 20126 Milano

[2] NEXT- Natural and Experimental Tectonics research group, Dipartimento Scienze Chimiche, della Vita e della Sostenibilità Ambientale, Università degli Studi di Parma, Padiglione 7 - Scienze della Terra, Campus Universitario, Parco Area delle Scienze 157/A, 43124 Parma, Italy

*corresponding author: m.martinelli34@campus.unimib.it

3.1 Abstract

Fault damage zones (DZ) are fractured volumes of rock that surround the fault core(s), and their structure can have an important impact both on fault mechanics and hydraulic properties, with impact on groundwater flow, ore-deposits, hydrocarbon reservoirs, nuclear waste disposal and contaminant transport in subsurface. It is generally accepted that DZ width is controlled by fault displacement, and increases with increasing offset. However, published data on DZ width in faulted carbonates show a scattering over two orders of magnitude, suggesting that this parameter is controlled also by other factors. Here we present the results of a study performed on two units of the platform carbonates of the Malta and Gozo Islands. These two units, that are cross-cut by normal faults, are characterize by different petrographical, petrophysical and mechanical properties and have completely different Damage Zone width along faults with comparable displacement. More competent and rigid grain-dominated carbonates show DZ thickness of several hundreds of meters, while fracturing in the less competent and more elastic micrite-dominated rocks is developed only very close to the fault core, with a DZ width of a few tens of meters. In order to explain this counterintuitive facies-controlled behavior, we performed petrophysical (porosity, density, permeability) and geo-mechanical (Uniaxial, Brazilian, Triaxial tests) analyses to characterize the mechanical stratigraphy and develop a numerical modelling study. Results highlight the heterogeneous stress distribution in a multilayer with variable elastic parameters subject to horizontal extension. The more elastic unit can more easily expand laterally with respect to the less elastic one with the consequence that σ_3 decrease faster in the last one and these can yield before the more compliant ones even if they are stronger. Also the width of the yielding zone is increased in the stiffer layers, leading to a wider DZ.

3.2 Introduction

A large number of brittle-cataclastic fault zones is composed by a relatively thin fault core, where most displacement is accommodated, characterized by fault rocks (e.g. cataclasites, fault gouges, etc.), surrounded by a wider damage zone, characterized by different types of fault-related structures (e.g. joints, deformation bands, veins, minor faults, etc.) (Caine et al., 1996; Shipton and Cowie, 2001; Berg and Skar, 2005; Bistacchi et al., 2010; Schueller et al., 2013; Choi et al., 2016). Damage zone width is usually defined as a zone where the frequency of minor brittle structures is higher than the regional background, hence the point where the frequency decreases to the background value is considered as the boundary of the damage zone (Beach et al., 1999; Cello et al., 2001; Agosta and Kirschner, 2003; Berg and Skar, 2005; Faulkner et al., 2006; de Joussineau and Aydin, 2007; Mitchell and Faulkner, 2009; Riley et al., 2010; Smith et al., 2013; Balsamo et al., 2019). Several studies suggest that damage zone width is related to the fault displacement through a power-law distribution (Evans, 1990; Knott, 1994; Shipton and Cowie, 2001; Childs et al., 2009; Mitchell and Faulkner, 2009; Mitchell and Faulkner, 2012; Faulkner et al., 2011; Savage and Brodsky, 2011; Torabi and Berg, 2011; Perrin et al., 2016). Some studies also show that damage zone thickness tends to saturate to value of 200-300 m above ~150 meters of displacement. However, datasets used for this correlation, collected by different authors in different rocks and tectonic environments, show a scatter of several orders of magnitude, suggesting that displacement is not the only factor controlling damage zone width (Hull, 1988; Knott, 1994; Shipton et al, 2006; Childs et al., 2009; Choi et al., 2016; Mayolle et al., 2019). Particularly mechanical stratigraphy seems to have a fundamental role in controlling the damage zone width (e.g. Soliva and Schulz, 2008; Roche et al., 2012; Ballas et al., 2014). In this study, we present results obtained in the platform carbonates of the islands of Malta and Gozo. Field analysis performed on two stratigraphic units – the Lower Coralline Limestone Formation and Lower Globigerina Member, show that they are characterized by completely different damage zone thickness along faults with the same tectonic history and displacement. In order to explain these observations, we applied a multidisciplinary approach to characterize the structural, petrophysical (porosity, density, permeability) and geomechanical (Uniaxial, Brazilian, Triaxial tests) properties of the two units. We then used these data as input parameters for a numerical model that allowed us simulating and predicting the role of mechanical stratigraphy in damage zone evolution and width.

3.3 Geological setting

The islands of Malta and Gozo are located in the Pelagian Platform, in the foreland of the Apennine-Sicilian-Maghrebian fold and thrust belt, on the northeast shoulder of the Pantelleria Rift System (Reuther and Eisbacher, 1985; Dart et al., 1993; Pedley et al., 1976; Illies et al., 1981; Martinelli et al., 2019) (Figure 1a). The two Islands are characterized by a Late Oligocene-Late Miocene succession composed by different types of shallow-marine carbonates, organized in five different formations that from the bottom to the top are: i) the Lower Coralline Limestone Formation ii) the Globigerina Limestone Formation iii) the Blue Clay Formation, iv) the Green Sand Formation v) the Upper Coralline Limestone Formation (Figure 1b) (Dart et al., 1993; Felix, 1973; Murray, 1890; Pedley et al., 1976). In this work we focused out attention on the Lower Coralline Limestone and on the Globigerina Limestone Foramtion that we describe here in details.

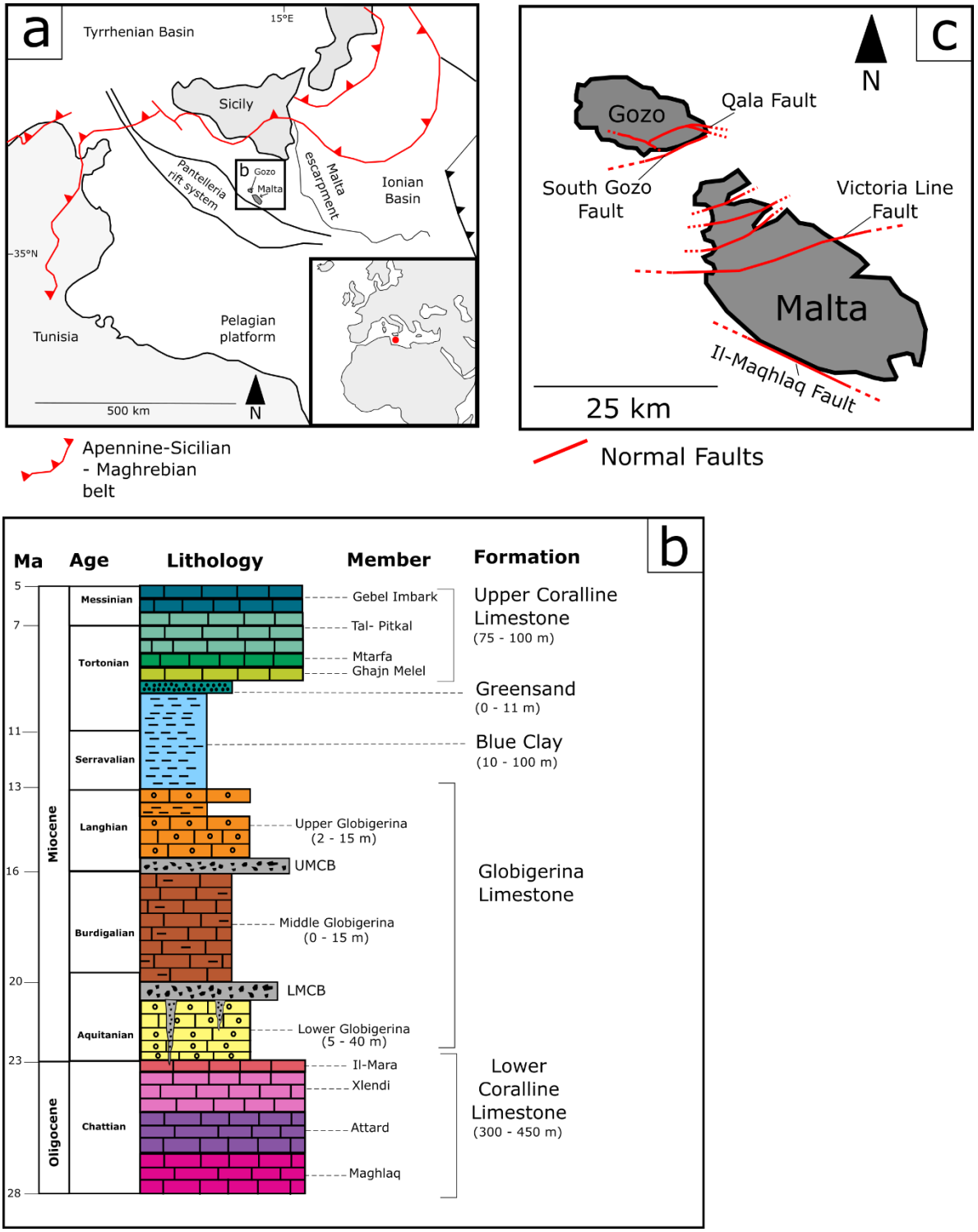

Figure 1: a) Position of the Maltese Islands in the foreland of the Apennine-Sicilian-Maghrebian belt (modified after Dart et al., 1993); b) Stratigraphy of the Maltese islands (stratigraphic column modified after Martinelli et al., 2019 and Dart et al., 1993); c) Main faults of the Maltese islands (modified after Dart et al., 1993;

The Lower Coralline Limestone Formation is Late Oligocene in age (Chattian) with a maximum thickness of 140 meters (Pedley et al., 1976), and it is composed by four members (from bottom to top): the Maghlaq Member, the Attard Member, the Xlendi Member, and the Il Mara Member (Pedley, 1978). All these members are mainly composed by grainstones and packstones with macro-fossils (>250µm) and minor micritic matrix (Michie et al., 2014).

The Globigerina Limestone is divided from the Lower Coralline Limestone by a hardground. It is Miocene in age (Aquitanian-Langhian) and it is subdivided in three members: the Lower Globigerina Member, the Middle Globigerina Member and the Upper Globigerina Member. The Lower Globigerina Member is divided from the Middle Globigerina Member by the Lower Main Conglomerate Bed (LMCB) (Pedley et al., 1976) and the Middle Globigerina Member is dived from the Upper Globigerina Member by the Upper Main Conglomerate Bed (UMCB) (Pedley et al., 1976). All three members are composed mainly by fine-grained biomicritic wackestones and marls, with micro-fossils (<50μm) and a few dispersed large fossils (>250μm) (Pedley et al., 1976; Michie et al., 2014).

Michie et al. 2014 and Michie and Haines, 2016 evidenced a contrast in petrophysical and mechanical properties between the Lower Coralline Limestone Formation and the Lower globigerina Member with field tests carried out with a Schmidt Hammer and porosity/permeability analyses performed in the laboratory. According to these Authors the Lower Coralline Limestone has a Uniaxial Compressive Strength (UCS) of ~80 MPa, a porosity that ranges between 10-15% an average permeability of ~110 mD. In contrast, the Lower Globigerina Member has a UCS of ~40 MPa, a porosity of 30-36% and an average permeability of ~2 mD.

The tectonic evolution of the Maltese Islands (Martinelli et al.,2019, and refs. therein) lead to the development of two sets of normal faults striking WNW-ESE and ENE-WSW (Figure 1c), associated with four sets of joints striking WNW-ESE, ENE-WSW, N-S, and NE-SW. Only in the Lower Globigerina Member and in the upper part of the Lower Coralline Limestone, we observe Neptunian dykes associated with small normal faults (displacement < 5m; Illies et al., 1981; Gatt, 2005; Martinelli et al., 2019).

The main faults outcropping in Malta are the ENE-WSW Victoria Fault that has a vertical displacement of 120 m (Villani et al., 2018) and the WNW-ESE Maghlaq Fault (Bonson et al., 2007; Pedley et al., 1976) located in the SE part of Malta with 210 m of vertical displacement (Bonson et al, 2007). (Figure 1c). On the Gozo island, the two main faults are the ENE-WSW South Gozo Fault with a minimum vertical displacement of 80 meters and the Qala Fault with a vertical displacement of 50 meters (Cooke et al., 2018) (Figure 1c).

Martinelli et al. 2019 demonstrated that this structural framework was developed during two extensional tectonic events:

D1) WNW-ESE extension developed during the Late Aquitanian-Early Burdigalian (20-17 Ma), resulting in the formation of the Neptunian dykes and associated small normal faults;

D2) N-S extension developed from the Late Miocene to the Pliocene (7-1.5 Ma), leading to nucleation and propagation of the large WNW-ESE and ENE-WSW faults (with associated fractures) (e,g. Victoria Fault, Maghlaq Fault, South Gozo Fault, Qala Fault).

During D1 the Lower Globigerina was outcropping at the seabed, as demonstrated by the presence of Neptunian dikes (Martinelli et al., 2019), hence the upper boundary of the Lower Coralline Limestone had an overburden of just 15 m. On the other hand, Bonson et al. (2007) proposed that during D2 (the main extensional event) these units should have an overburden of ~300 meters.

3.4 Damage zone thickness in different stratigraphic units

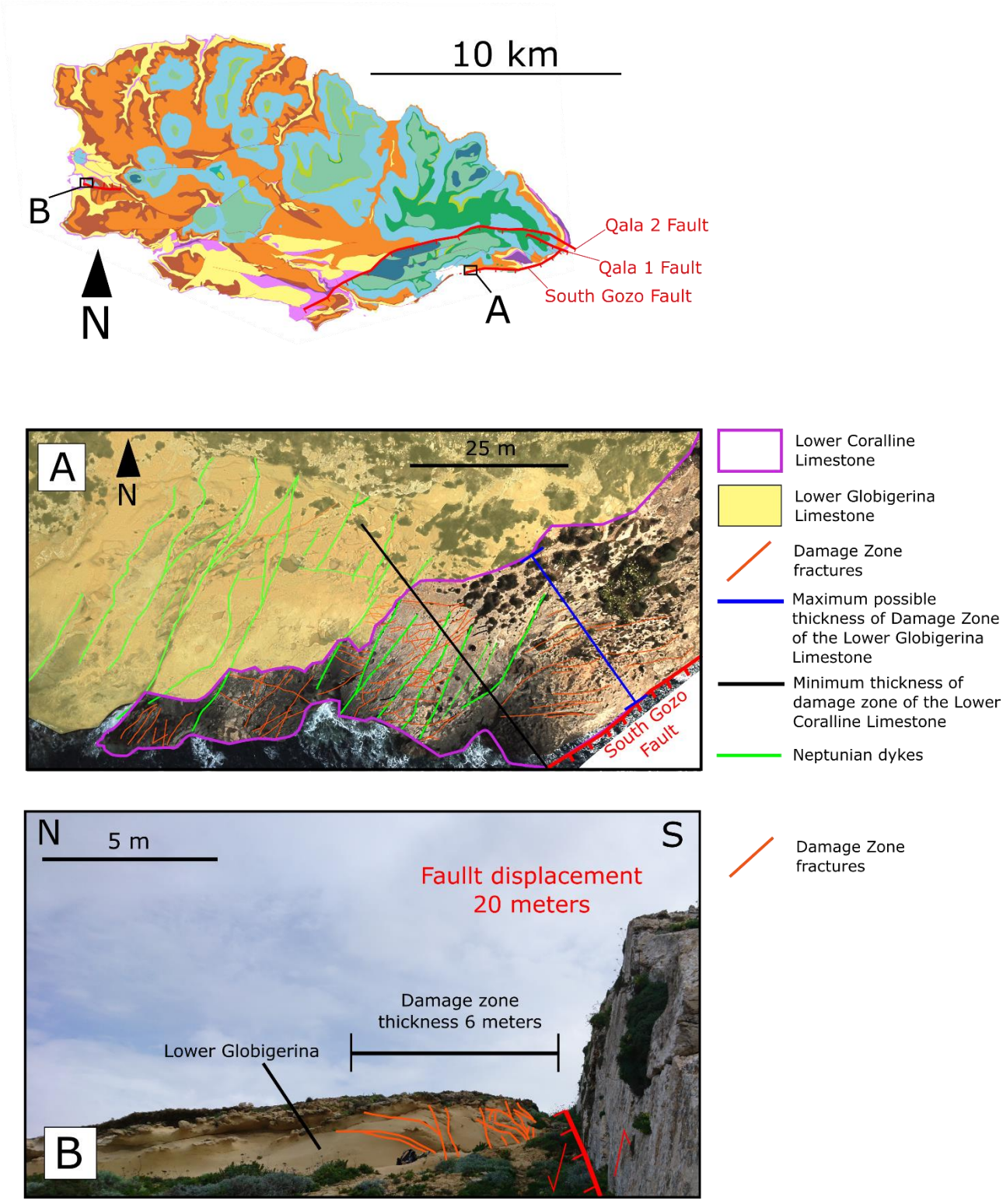

Figure 2: Damage zone thickness in the Lower Coralline Limestone and in the Lower Globigerina Member a) Spectacular outcrop located in the footwall of the South Gozo fault. Here the Lower Coralline Limestone is outcropping from the fault surface up to 50 meters from the fault whereas the Lower Globigerina starts to outcrop from 25 meters from the fault surface onwards. The differences in the fracturation of the two units are clearly visible. While in the Lower Coralline Limestone fractures are developed everywhere in the outcrop indicating that its damage zone should be at least 50 meters thick, the Lower Globigerina is practically non fractured (if we excluded the Neptunian dykes developed during D1 extension) suggesting that its damage zone in this unit could have a maximum thickness of 25 meters; b) another example of the damage zone thickness in the Lower Globigerina Member

Martinelli et al., in preparation (second chapter of this thesis) demonstrated that the footwall damage zone of the Qala 2 Fault (displacement ~30 m) in the Lower Coralline Limestone is more than 500 meters thick. Our field observations performed along several faults both in Gozo and Malta, with displacements comparable to that of the Qala Fault, confirm these values for damage zones in the Lower Coralline Limestone and show that, on the other hand, the Lower Globigerina Member is characterized by a thin damage zone, just a few meters thick (Figure 2a-b). A spectacular example is represented by an outcrop in the footwall of the South Gozo Fault that is characterized by a displacement of 80 meters (Figure 2a). These observations, performed along faults characterized by the same tectonic history and with comparable displacement, suggest that mechanical stratigraphy, and particularly the contrast in geomechanical and petrophysical properties, could have a crucial role in controlling the thickness of damage zones. In order to test this hypothesis, we applied a multidisciplinary approach combining petrographic, petrophysical, and geomechanical analyses, and numerical modelling, that will be explained in detail in the next chapters.

3.5 Petrographic and petrophysical characterization

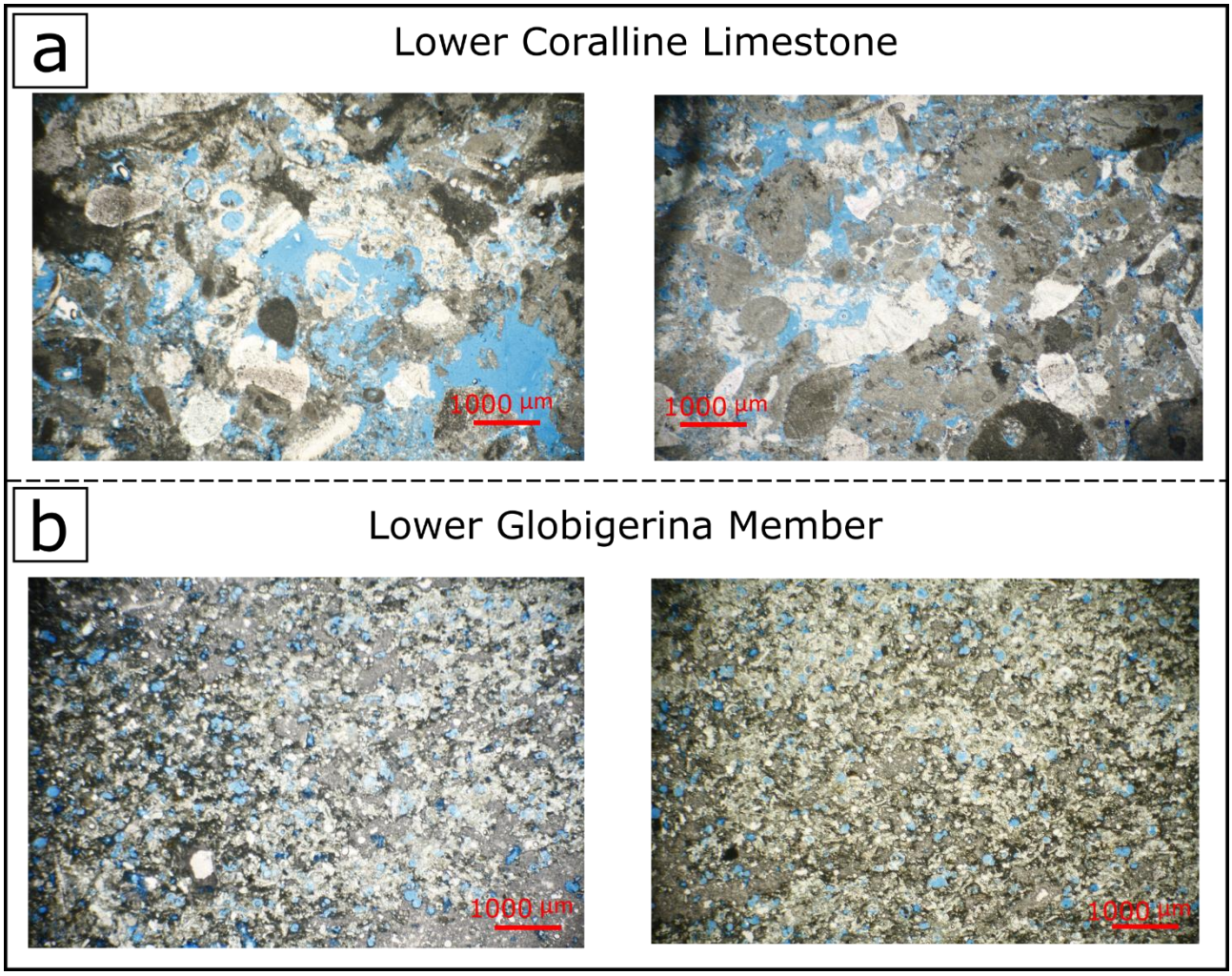

Figure 3: Thin sections impregnated with blue resin of Lower Coralline Limestone (a) and Lower Globigerina Member (b).

We carried out a full set of petrophysical analyses that allowed us measuring density, porosity and permeability. Permeability data were collected directly in the field with a TinyPerm II® portable air

permeameter (manufactured by New England Research). This type of permeameter is equipped

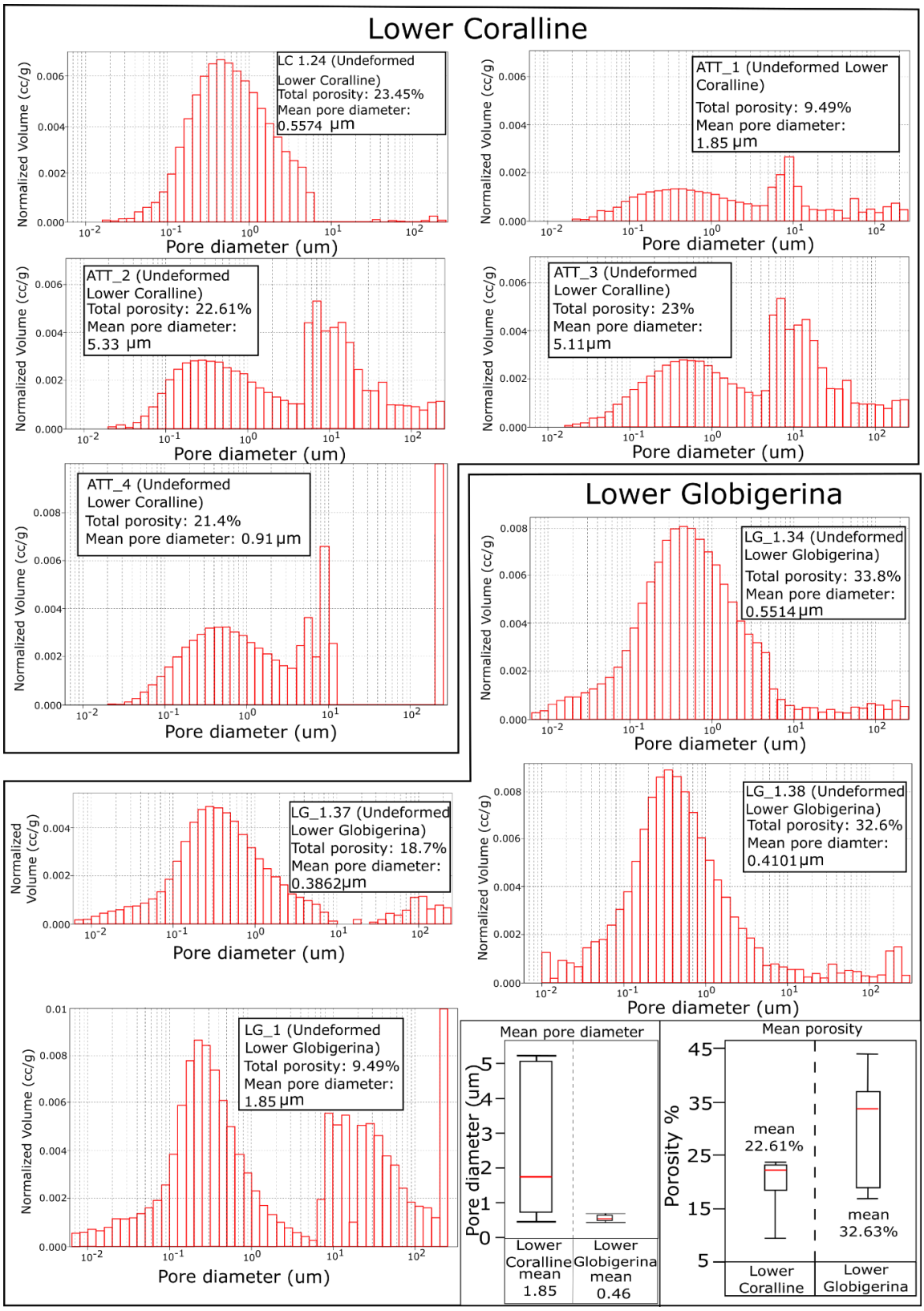

Figure 4: Results of porosity and pore diameter analyses for the Lower Coralline Limestone and the Lower Globigerina Member.

with a 5 mm nozzle and allows characterizing permeability in the range from 10^{-9} to 10^{-15} m^2 (Balsamo et al., 2013, and refs. therein). The slightly lower accuracy of these measurements with

respect to laboratory tests is counterbalanced, in our opinion, by (i) the possibility to test intact materials that are not disturbed by sampling, and by (ii) the possibility to carry out a large number of measurements and have a good statistical coverage of the variability of permeability in a formation outcropping over several km^2.

Density was measured with an Ultrapic 1200e (Quantachrome Instrumensts). Porosity and pore-size distribution characterization was performed using a PoreMaster 33® mercury-injection porosimeter (manufactured by Quantchrome Instruments). This type of porosimeter measures the volume of mercury that penetrates the pores of the samples as a function of the applied hydraulic pressure. The radius R of pores accessible by the pressured mercury is given by the Washburn equation:

$$R = 2\gamma \frac{cos\theta}{P}$$

where γ is the surface tension of mercury, θ is the contact angle of mercury with the sample material, and P is the applied hydraulic pressure (Washburn, 1921; Léon and León, 1998). In this way it is possible to convert the mercury intrusion and extrusion data into pore size distributions.

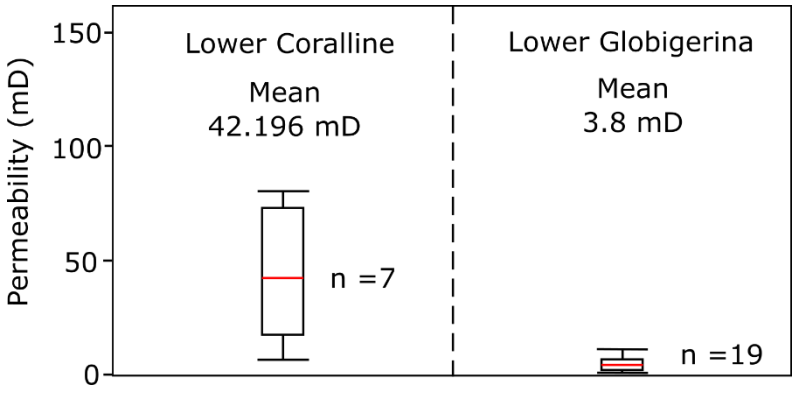

Figure 5: Results of the permeability analysis

Petrographic analyses were performed on thin sections impregnated with resin with a blue stain in order to evidence porosity (Figure 3). Our analyses show that the Lower Coralline Limestone is a packstone/grainstone with grain size around 500 µm (estimated under the optical microscope) with minor matrix content (Figure 3a) and density of 2,106 g/cm^3. Porosity values range between 9% and 24% with a mean of 22.6%. Pore size range between 0.5 and 5.2 µm with a mean of 1.8 µm (Figure 4). Permeability values are very variable and range between 6 mD and 80 mD with a mean around 42.1 mD (Figure 5).

The Lower Globigerina Member is a wackestone with grain size around 10 µm (estimated under the optical microscope) and sparse macro-fossils (Figure 3b) and density 1,755 g/cm^3. Porosity values range between 17% and 44% with a mean of 33% (Figure 4). Pore size range between 0.2 and 0.6 µm with a mean around 0.46 µm. Permeability values are very low and range between 0.7 mD and 11 mD with a mean of 3.8 mD (Figure 5).

3.6 Geomechanical characterization

The geomechanical characterization was performed with Brazilian tests for tensile strength, uniaxial tests for Young modulus E, UCS Uniaxial Compressive Strength) and Poisson Ratio, and triaxial test used to measure additional elastic parameters and reconstruct failure envelopes.

Brazilian and uniaxial test were carried out with a GSDVIS apparatus. We performed 11 Brazilian test, 5 on the Lower Coralline Limestone Formation and 6 on the Lower Globigerina Member, on

samples with a diameter of 38 mm and height of 17 mm, at a rate of shortening of 1 mm every 15 minutes.

Uniaxial tests were performed at a rate of shortening of 1 mm every 10 minutes, on 6 samples of Lower Coralline Limestone and 7 samples of the Lower Globigerina Member, with a diameter of 21 mm and height of 42 mm. The Young modulus E was calculated using the tangent method, that defines E as the slope of the tangent to the stress-strain curve at 50% of the ultimate strength. Two additional uniaxial tests were performed on samples of 38 mm of diameter and 76 mm of height, equipped with strain gauges in order to calculate the Poisson ratio ν and the modulus of rigidity (or shear modulus) defined as $G = E/2(1+\nu)$.

	Stress state for the triaxial tests before decreasing of radial stress (σ3)		
	Sample	σ_1 axial stress	σ_3 radial stress
Lower Coralline Limestone	LC_2.5	61.5 MPa	45 MPa
	LC_1.1	79 MPa	45 MPa
	LC_1.2	118.5 MPa	45 MPa
Lower Globigerina Member	LG_4.4	50.5 MPa	45 MPa
	LG_1.5	37.1 MPa	35 MPa
	LG_1.4	26.5 MPa	25 MPa

Table 1: Values of vertical and radial stress in the triaxial apparatus before the beginning of the decreasing of radial stress

Samples for triaxial tests were prepared with diameter of 38 mm and height of 76 mm, and equipped with strain gauges. Three tests were performed for every unit using a triaxial apparatus equipped with a Hoek cell and manufactured by Controls. In order to simulate the typical stress path for normal faulting, samples were first loaded with an isotropic load ($\sigma_1 = \sigma_2 = \sigma_3$ – isotropic phase) and then the axial load σ_1 was maintained constant while the confining radial stress $\sigma_2 = \sigma_3$ was decreased until failure (deviatoric phase). Both the isotropic and deviatoric phases were carried out at a stress rate of 50N/s. Every test was performed at different values of initial (before the decrease of σ_3) vertical and radial stress (Table 1) Since the used triaxial apparatus can reach a maximum radial stress of 45 MPa for the Lower Coralline Limestone samples (LC_2.5, LC_1.1, LC_1.2, Table 1 and Figure 7) and for sample LG-1.4 (Table 1 and Figure 7) isotropic phase was performed until this value (45 MPa) was reached then vertical stress was increased until the selected value (Table 1). All samples were dried at 50° for almost 18 hours.

Results of Brasilian and Uniaxial tests are summarized in Figure 6. The Attard member has: mean tensile strength of 4.4 MPa (Figure 6a); mean Uniaxial Compressive Strength of 36 MPa (Figure 6c and 6d); Young modulus has a mean of 5.5 GPa (Figure 6e); Poisson ration has value of 0.15 (Figure 6f); Modulus of rigidity (G) is 3.2 GPa. The Lower Globigerina member has a mean tensile strength of 2.26 MPa (Figure 6a); Uniaxial Compressive Strength has a mean value of 13.72 MPa (Figure 6b and 6d); Young modulus has a mean of 2.4 GPa (Figure 6e) Poisson ration has a value of 0.18 (Figure 6f); Modulus of rigidity (G) is 1.5 GPa. As explained above, three triaxial test at different axial and radial stress were performed for every unit. Attard member fails at 118.5 MPa of axial stress and 25 MPa of radial stress; at 79 MPa of axial stress and 3.6 MPa of radial stress; at 61.5 MPa of axial stress and 1 of radial stress. Lower Globigerina fails at 50.5 MPa of axial stress and 11.3 MPa of radial stress; at 37.1 MPa of axial stress and 5 MPa of radial stress; at 26.5 MPa of axial stress and 1.5 of radial stress. Even if the two units have a comparable Poisson ratio, they deform in a complete different way and they have a very different strength. For instance, considering elastic deformation before failure, at the same axial stress the Lower Globigerina Member shows an axial and radial strain ten times higher with respect to the Lower Coralline Limestone (Figure 6f). Combining all the results

of Brazilian, Uniaxial an Triaxial tests, a representative failure envelope of the two units was reconstructed (Figure 7).

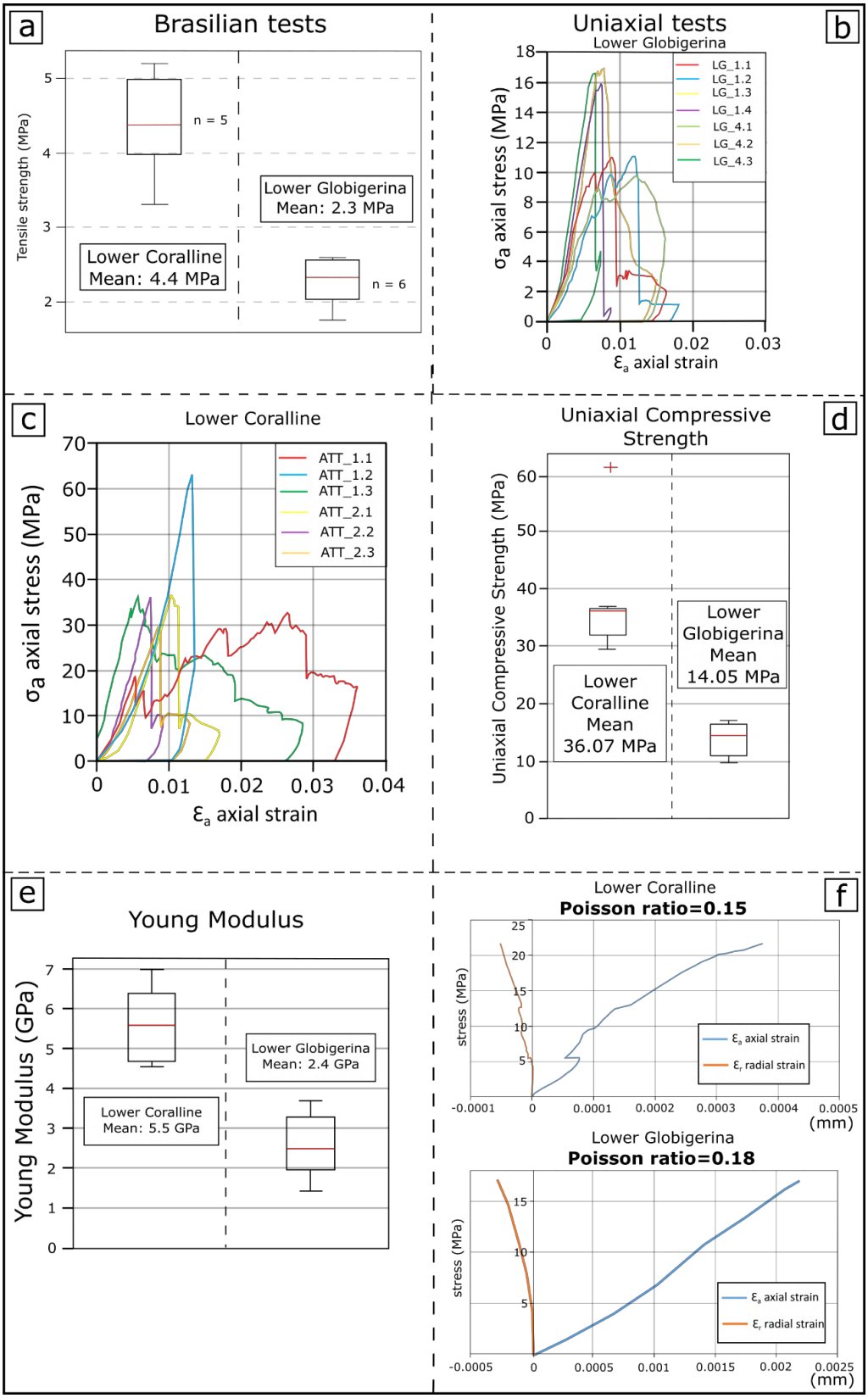

Figure 6: Results of the Brasilian and Uniaxial tests including the Young modulus and the Poisson ratio.

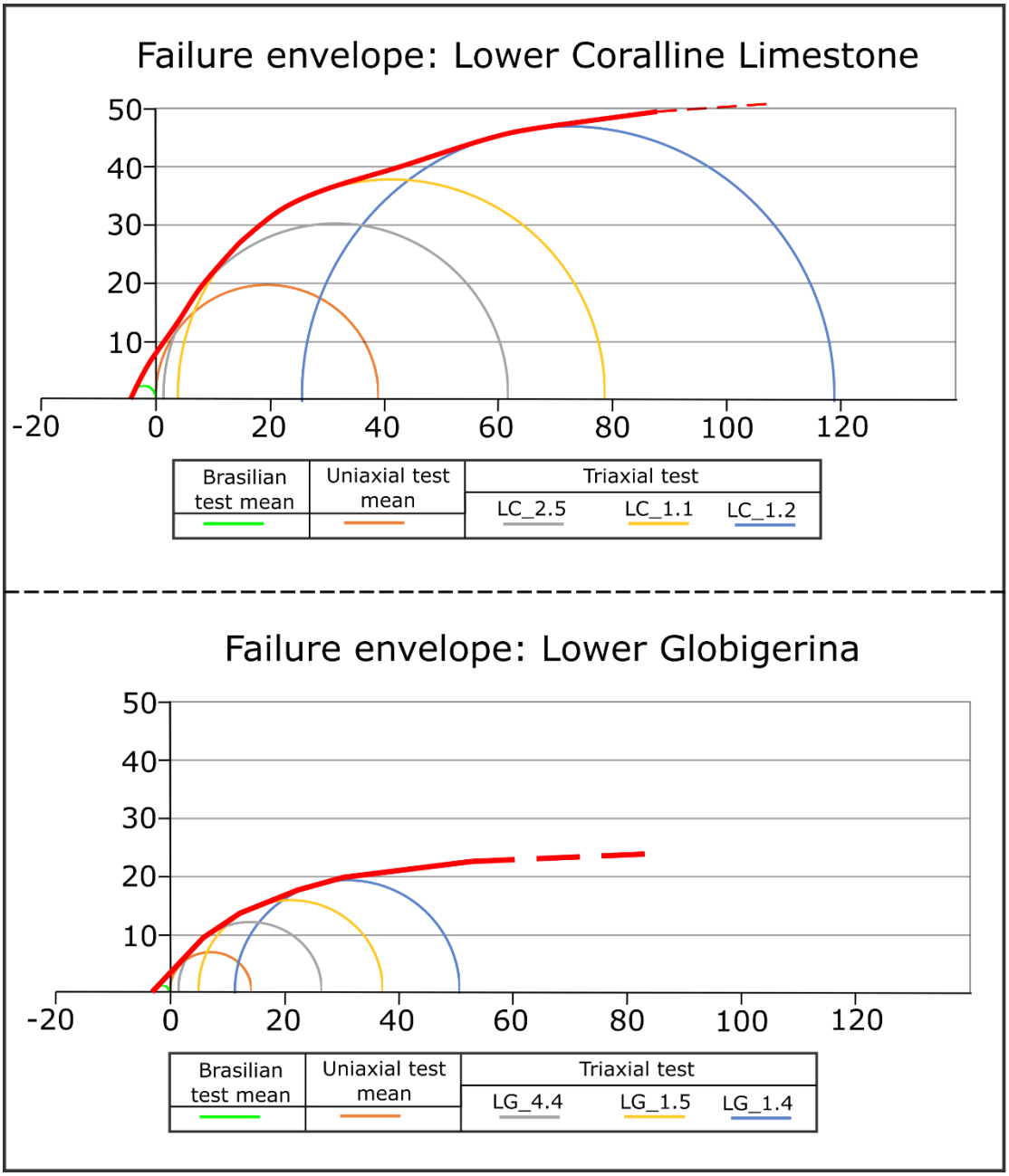

Figure 7: Failure envelope of the Lower Coralline Limestone and of the Lower Globigerina Member extracted from the Brazilian, Uniaxial and Triaxial tests. Codes of the triaxial tests referred to those in Table 1

3.7 Numerical modelling

In order to simulate the normal faulting deformation in a layered stratigraphy with geometry and mechanical stratigraphy representative of the sequence considered in this study, we developed a numerical modelling study using the Finite Element Method in 2D with the code Midas GTS NX® (www.cspfea.net).

All tested setups are 500 m wide and 130 m thick, and include four layers (from bottom to top): (1) weak material 50 m thick; (2) Lower Coralline Limestone 15 m thick; (3) Lower Globigerina Member 15 m thick; (4) weak material 50 m thick (Figure 8). Layers 1 and 4 have a grid resolution of 10x10 meters whereas layers 2 and 3 have grid resolution of 2x2 meters. We used “roller” kinematic boundary conditions at the base and on both sides of the model, hence the displacements are

prescribed perpendicular to the boundaries and free parallel to them. While the vertical position of the bottom boundary is always fixed, the vertical boundaries are fixed along the horizontal axis in the first step of the simulation, and then are progressively displaced to obtain a horizontal extension of 1 cm for each deformation step, up to 20 m of total extension (Figure 8). The top boundary is subject to a normal stress of 10 MPa in order to simulate an overburden of 300 m, as proposed by Bonson et al. 2007.

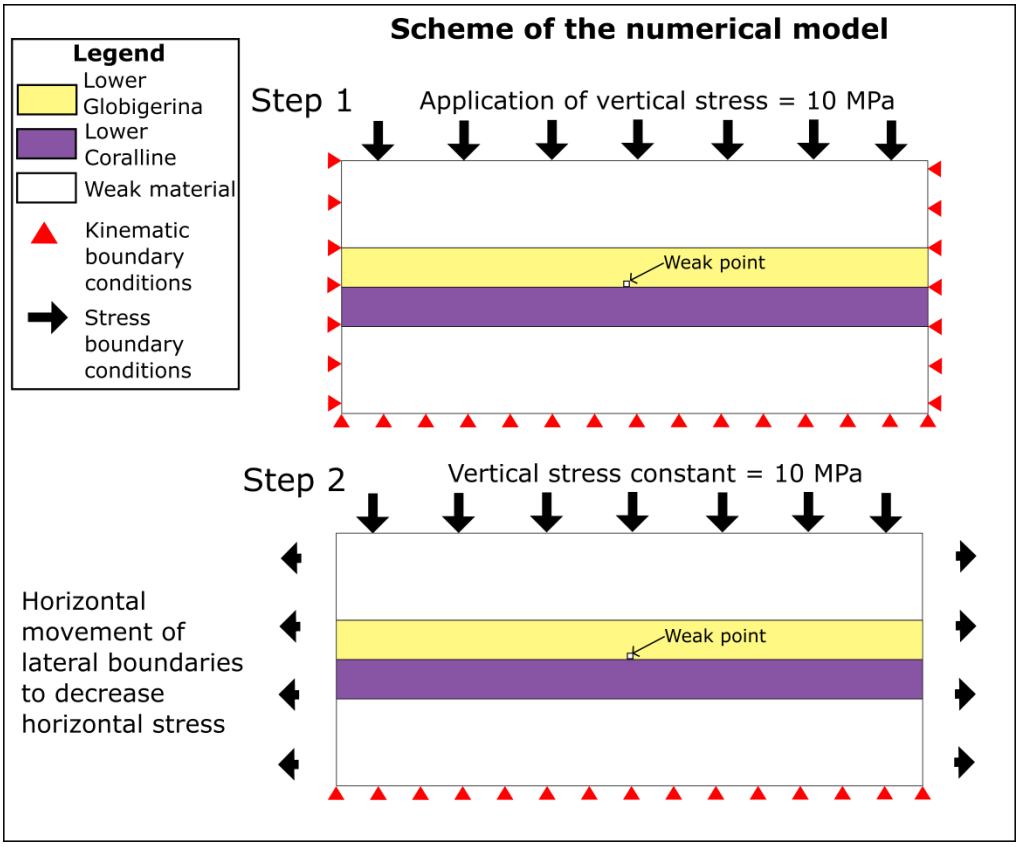

Figure 8: Scheme of the numerical modeling

In order to localize deformation and obtain a fault in the middle of the model, a weak spot 2 m by 2 m was added at the boundary between the Lower Coralline Limestone and the Lower Globigerina Member (Figure 8). Weak layers above and below the Lower Coralline Limestone and Lower Globigerina Member were added in order to allow vertical displacements in the stiffer and stronger layers (Figure 8).

Mechanical parameters for the Lower Coralline Limestone and the Lower Globigerina Member were obtained from the geomechanical analyses, assuming a Mohr-Coulomb failure envelope with a friction angle and cohesion chosen from the experimental failure envelope in the region with normal and tangential stresses considered realistic for our simulations. In particular, we set a cohesion of 5.9 MPa and a friction angle of 32° for the Lower Globigerina Member and a cohesion of 10.5 MPa and a friction angle of 47° for the Lower Coralline Limestone. These parameters were calculated using the Mohr-Coulomb failure envelope of the first and second triaxial tests both for Lower Coralline Limestone (test LC_2.5 and LC_1.1, Figure 7) and Lower Globigerina member (test LG_4.4 and LG_1.5, Figure 7). The tensional strength was obtained from the Brazilian tests. Parameters of the

weak material (1.9 MPa of cohesion and 30° of friction angle) were selected in order to reach failure before the Lower Coralline Limestone and the Lower Globigerina Member.

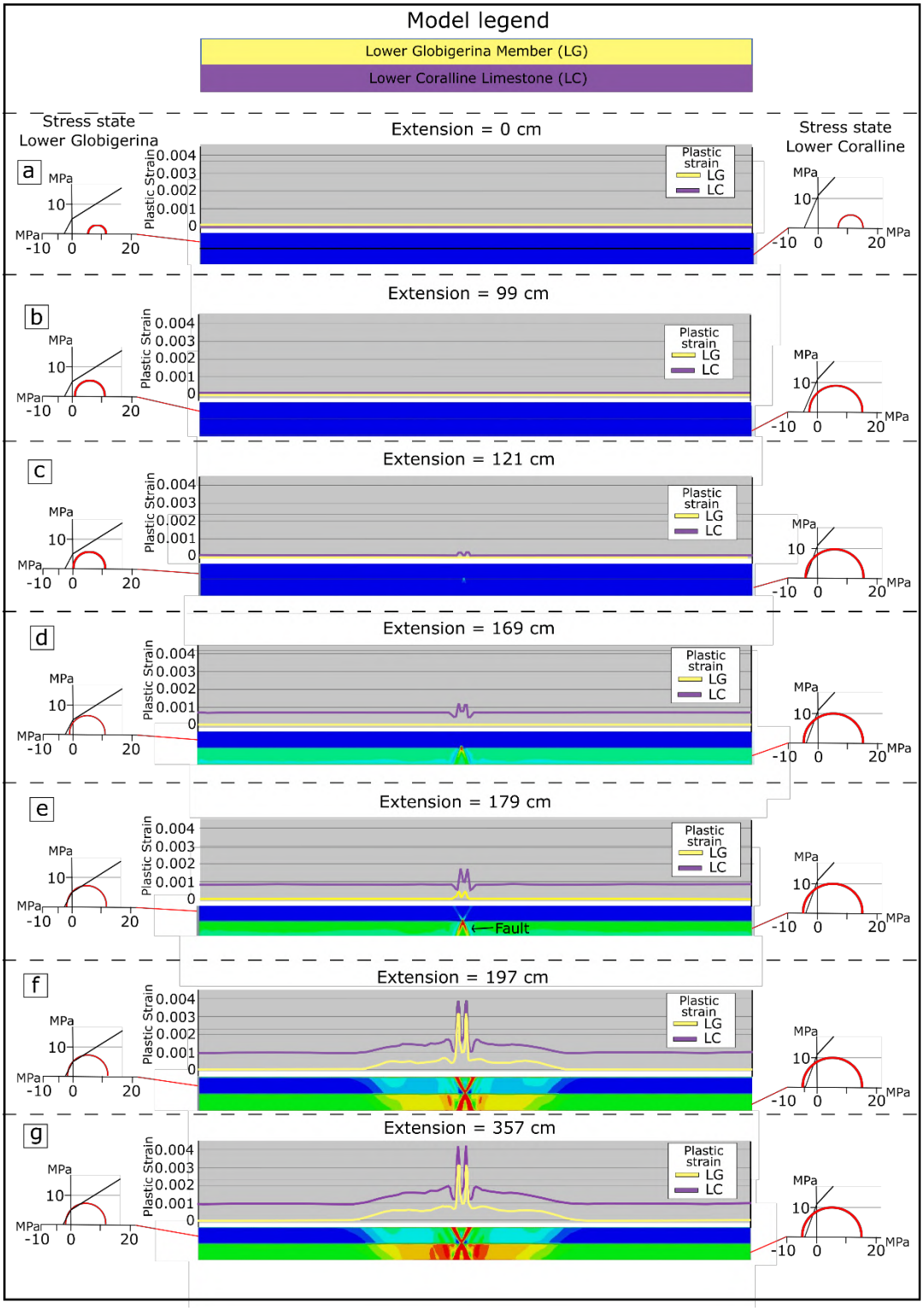

Figure 9: Results of the numerical modeling (see text for a complete explanation). Weak layers at the bottom and at the top of the model are hidden to permit a clear visualization of the results.

As proxy for the damage zone thickness we used the equivalent plastic strain (Figure 9) that is a scalar value used to represent the material's inelastic deformation. If this variable is greater than zero, the material has yielded. (Chen, W.F. and Han, 1988). GTS NX performs continuous numerical models

simulations and for this reason faults are represented by shear zones where strain plasticity is very high. Results of the numerical modeling (Figure 9) study show that, as horizontal extension proceeds, the horizontal stress σ_3 decreases faster in the Lower Coralline Limestone than in the Lower Globigerina Member (Figure 9a,b). For this reason, the Lower Coralline Limestone fails well before the Lower Globigerina Member, even if it is more than two times stronger (Figure 9c). This behavior has the consequence that deformation (plastic strain) continuous to increase in the Lower Coralline Limestone in a distributed manner and fault starts to localize (Figure 9d,e). At the same time the Lower Globigerina doesn't show any evidence of strain plasticity. Only when also the Lower Globigerina Member reaches its failure envelope (Figure 9e), the fault propagates upwards from the Lower Coralline Limestone into the Lower Globigerina Member creating a fault with a damage zone much thinner with respect to the one in the Lower Coralline Limestone (Figure 9f) as testified from the value of the plastic strain that rapidly decrease to zero moving away from the main fault (Figure 9f). After this point, even if the extension continues deformation is localized only close to the slip surface (Figure 9g). It is noteworthy to say that in both the units when the yield point is reach σ_3 does not decrease anymore.

3.8 Discussion

In this work, we analyzed the influence of the mechanical stratigraphy on the damage zone thickness in normal faulted platform carbonates. Combining field data with petrophysical, geomechanical and numerical analysis we demonstrated that units characterized by different elastic and geo-mechanical properties respond to stress in a complete different way. In particular, we observed that strong and stiff unit (Lower Coralline Limestone Formation) are characterized by a wider damage zone with respect to weak and elastic unit (Lower Globigerina Member) and that the first one fails before even if it is stronger. In the next chapters we will explain this counterintuitive behavior and we will also propose a model for the formation of damage zones with variable thickness in units with different mechanic and elastic properties.

3.8.1 Control of the rock elastic properties on the evolution of the stress state

Numerical model shows that σ3 decrease faster in the strong and stiff unit (Lower Coralline Limestone) causing its failure before the weaker and elastic unit (Lower Globigerina member). Our interpretation is that this behavior is caused by the different elastic properties of the two units. Indeed, even if the Poisson ration is similar (0.15 for the Lower Coralline Limestone and 0.18 for the Lower Globigerina member) they have different values of Young and Rigidity modulus and they deform in a complete different way. Indeed, for the same vertical stress the Lower Globigerina Member shows an axial and radial strain ten time higher with respect to the Lower Coralline Limestone. The consequence is that when a vertical stress is applied on the two units the Lower Globigerina Limestone Member can expand laterally ten time mores with respect to the Lower Coralline Limestone. In this way the Lower Globigerina Member create a "pressure" opposite to σ_3 that decrease slower with respect to the Lower Coralline Limestone, with the consequence that it fails before even if it is stronger.

3.8.2 Formation of damage zone of variable thickness in carbonates with different mechanic and elastic properties

Here we propose a general model for the formation of damage zone with different thickness in multilayer carbonates characterized by units with different elastic and mechanical properties affected

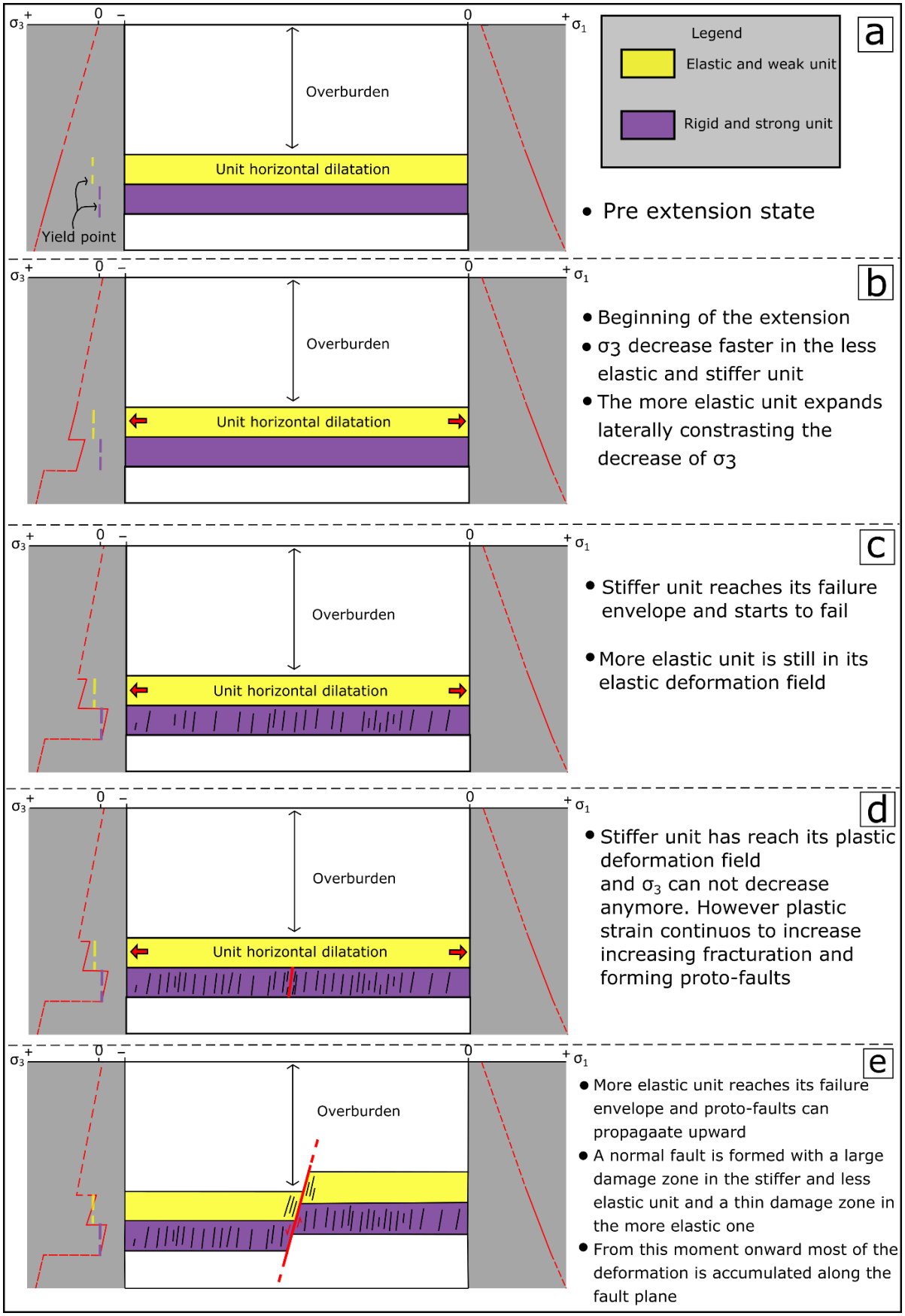

Figure 10: The model proposed for the formation of damage zones with different thickness in multilayer carbonates characterized by units with different elastic and mechanical properties affected by extensional tectonics

by extensional tectonics (Figure 10). Pre extension situation is highlighted in Figure 10a. When the

extension begins the less rigid and weaker unit can more easily expand laterally with respect to the more rigid and stronger one, limiting the decrease of σ_3. The consequence of this behavior is that σ_3 decreases faster in the stiffer unit (Figure 10b) that fails before the less rigid one even if it is stronger (Figure 10c). When the rigid unit reaches its yield point, the less rigid one is still in its elastic domain (Figure 10c). At this point σ_3 cannot decrease anymore in the more rigid unit because it is buffered by plastic yielding, and plastic strain accumulates in this unit. We consider this as a proxy for damage zone development (Figure 10d). When also the less rigid unit yields, the fault propagates upward forming a thoroughgoing normal fault characterized by a much thinner damage zone in the less rigid unit. After this phase, even if the extension continues, most of the deformation is localized along the fault plane due to the strain weakening effect and the thickness of the damage can increase only close to the slip surface (Figure 10e).

3.9 Conclusion

In this work we demonstrated that the elastic properties of rocks play a fundamental role in the control of the damage zone thickness. In a multilayer carbonate stratigraphy composed by units with different elastic properties, in the less rigid units σ_3 decreases at a slower rate with respect to the stiffer units, with the consequence that the latter yield before the former even if they are stronger. This behavior is reflected in the thickness of damage zones that, in a counterintuitive way, are thicker in more rigid and stronger units.

References

Agosta, F., Kirschner, D.L., 2003. Fluid conduits in carbonate-hosted seismogenic normal faults of central Italy. Journal of Geophysical Research: Solid Earth 108, 1–13. https://doi.org/10.1029/2002jb002013

Ballas, G., Soliva, R., Benedicto, A., Sizun, J.P., 2014. Control of tectonic setting and large-scale faults on the basin-scale distribution of deformation bands in porous sandstone (Provence, France). Marine and Petroleum Geology 55, 142–159. https://doi.org/10.1016/j.marpetgeo.2013.12.020

Balsamo, F., Clemenzi, L., Storti, F., Solum, J., Taberner, C., 2019. Tectonic control on vein attributes and deformation intensity in fault damage zones affecting Natih platform carbonates, Jabal Qusaybah, North Oman. Journal of Structural Geology 122, 38–57. https://doi.org/10.1016/j.jsg.2019.02.009

Beach, A., Welbon, A.I., Brockbank, P.J., McCallum, J.E., 1999. Reservoir damage around faults: Outcrop examples from the Suez rift. Petroleum Geoscience 5, 109–116. https://doi.org/10.1144/petgeo.5.2.109

Berg, S.S., Skar, T., 2005. Controls on damage zone asymmetry of a normal fault zone: Outcrop analyses of a segment of the Moab fault, SE Utah. Journal of Structural Geology 27, 1803–1822. https://doi.org/10.1016/j.jsg.2005.04.012

Bistacchi, A., Massironi, M., Menegon, L., 2010. Three-dimensional characterization of a crustal-scale fault zone: The Pusteria and Sprechenstein fault system (Eastern Alps). Journal of Structural Geology 32, 2022–2041. https://doi.org/10.1016/j.jsg.2010.06.003

Bonson, C.G., Childs, C., Walsh, J.J., Schöpfer, M.P.J., Carboni, V., 2007. Geometric and kinematic controls on the internal structure of a large normal fault in massive limestones: The Maghlaq Fault, Malta. Journal of Structural Geology 29, 336–354. https://doi.org/10.1016/j.jsg.2006.06.016

Caine, J.S., Evans, J.P., Forster, C.B., 1996. Fault zone architecture and permeability structure. Geology 24, 1025–1028. https://doi.org/10.1130/0091-7613(1996)024<1025:FZAAPS>2.3.CO;2

Cello, G., Tondi, E., Micarelli, L., Invernizzi, C., 2001. Fault zone fabrics and geofluid properties as indicators of rock deformation modes. Journal of Geodynamics 32, 543–565. https://doi.org/10.1016/S0264-3707(01)00047-3

Chen, W.F. and Han, D.J., 1988. Plasticity for Structural Engineers. Springer-Verlag New York. https://doi.org/10.1016/j.jsg.2018.05.024

Childs, C., Manzocchi, T., Walsh, J.J., Bonson, C.G., Nicol, A., Schöpfer, M.P.J., 2009. A geometric model of fault zone and fault rock thickness variations. Journal of Structural Geology 31, 117–127. https://doi.org/10.1016/j.jsg.2008.08.009

Choi, J.H., Edwards, P., Ko, K., Kim, Y.S., 2016. Definition and classification of fault damage zones: A review and a new methodological approach. Earth-Science Reviews 152, 70–87. https://doi.org/10.1016/j.earscirev.2015.11.006

Cooke, A.P., Fisher, Q.J., Michie, E.A.H., Yielding, G., 2018. Investigating the controls on fault rock distribution in normal faulted shallow burial limestones, Malta, and the implications for fluid flow. Journal of Structural Geology 114, 22–42. https://doi.org/10.1016/j.jsg.2018.05.024

Dart, C.J., Bosence, D.W.J., McClay, K.R., 1993. Stratigraphy and structure of the Maltese Graben system. Journal - Geological Society (London) 150, 1153–1166. https://doi.org/10.1144/gsjgs.150.6.1153

de Joussineau, G., Aydin, A., 2007. The evolution of the damage zone with fault growth in sandstone and its multiscale characteristics. Journal of Geophysical Research: Solid Earth 112, 1–19. https://doi.org/10.1029/2006JB004711

Evans, J.P., 1990. Brevia SHORT NOTES Thickness--displacement relationships for fault zones. Journal of Structural Geology 12, 1061–1065.

Faulkner, D.R., Mitchell, T.M., Healy, D., Heap, M.J., 2006. Slip on "weak" faults by the rotation of regional stress in the fracture damage zone. Nature 444, 922–925. https://doi.org/10.1038/nature05353

Faulkner, D.R., Mitchell, T.M., Jensen, E., Cembrano, J., 2011. Scaling of fault damage zones with displacement and the implications for fault growth processes. Journal of Geophysical Research: Solid Earth 116, 1–11. https://doi.org/10.1029/2010JB007788

Felix, R., 1973. Oligo-Miocene stratigraphy of Malta and Gozo. Mededelingen Landbouwhogeschool Wageningen 73, 1–103.

Gatt, P.A., 2005. Syntectonic Deposition of an Oligo-Miocene Phosphorite Conglomerate Bed in Malta. The Central Mediterranean Naturalist 4, 109–118.

Hull, J., 1988. Thickness-displacement relationships for deformation zones. Journal of Structural Geology 10, 431–435. https://doi.org/10.1016/0191-8141(88)90020-X

Illies, J.H., Institut, G., Karlsruhe, U., Germany, D.K.F.R., 1981. Geological Contributions : Active Rifts GRABEN FORMATION - THE MALTESE ISLANDS - A CASE The Maltese Islands (Malta , GOZO , Comino , and some smaller uninhabited islets) are located in the Strait of Sicily , between Italy and Northern Africa . The archi. 73, 151–168.

Knott, S.D., 1994. Fault zone thickness versus displacement in the Permo-Triassic sandstones of NW

England. Journal - Geological Society (London) 151, 17–25. https://doi.org/10.1144/gsjgs.151.1.0017

Léon Y León, C.A., 1998. New perspectives in mercury porosimetry. Advances in Colloid and Interface Science 76–77, 341–372. https://doi.org/10.1016/S0001-8686(98)00052-9

Martinelli, M., Bistacchi, A., Balsamo, F., & Meda, M., 2019. Late Oligocene to Pliocene Extension in the Maltese Islands and Implications for Geodynamics of the Pantelleria Rift and Pelagian Platform. Tectonics. https://doi.org/10.1029/2019TC005627

Mayolle, S., Soliva, R., Caniven, Y., Wibberley, C., Ballas, G., Milesi, G., Dominguez, S., 2019. Scaling of fault damage zones in carbonate rocks. Journal of Structural Geology 124, 35–50. https://doi.org/10.1016/j.jsg.2019.03.007

Michie, E.A.H., Haines, T.J., 2016. Variability and heterogeneity of the petrophysical properties of extensional carbonate fault rocks, Malta. Petroleum Geoscience 22, 136–152. https://doi.org/10.1144/petgeo2015-027

Michie, E.A.H., Haines, T.J., Healy, D., Neilson, J.E., Timms, N.E., Wibberley, C.A.J., 2014. Influence of carbonate facies on fault zone architecture. Journal of Structural Geology 65, 82–99. https://doi.org/10.1016/j.jsg.2014.04.007

Mitchell, T.M., Faulkner, D.R., 2012. Towards quantifying the matrix permeability of fault damage zones in low porosity rocks. Earth and Planetary Science Letters 339–340, 24–31. https://doi.org/10.1016/j.epsl.2012.05.014

Mitchell, T.M., Faulkner, D.R., 2009. The nature and origin of off-fault damage surrounding strike-slip fault zones with a wide range of displacements: A field study from the Atacama fault system, northern Chile. Journal of Structural Geology 31, 802–816. https://doi.org/10.1016/j.jsg.2009.05.002

Murray, J., 1890. The Maltese Islands with special reference to their geological structure. Scott. Geogr. Mag. 449–488.

Pedley, H.M., House, M.R., Waugh, B., 1976. The geology of Malta and Gozo. Proceedings of the Geologists' Association 87, 325–341. https://doi.org/10.1016/S0016-7878(76)80005-3

Perrin, C., Manighetti, I., Gaudemer, Y., 2016. Off-fault tip splay networks: A genetic and generic property of faults indicative of their long-term propagation. Comptes Rendus - Geoscience 348, 52–60. https://doi.org/10.1016/j.crte.2015.05.002

Reuther, C.D., Eisbacher, G.H., 1985. Pantelleria Rift - crustal extension in a convergent intraplate setting. Geologische Rundschau 74, 585–597. https://doi.org/10.1007/BF01821214

Riley, P.R., Goodwin, L.B., Lewis, C.J., 2010. Controls on fault damage zone width, structure, and symmetry in the Bandelier Tuff, New Mexico. Journal of Structural Geology 32, 766–780. https://doi.org/10.1016/j.jsg.2010.05.005

Roche, V., Homberg, C., Rocher, M., 2012. Architecture and growth of normal fault zones in multilayer systems: A 3D field analysis in the South-Eastern Basin, France. Journal of Structural Geology 37, 19–35. https://doi.org/10.1016/j.jsg.2012.02.005

Savage, H.M., Brodsky, E.E., 2011. Collateral damage: Evolution with displacement of fracture distribution and secondary fault strands in fault damage zones. Journal of Geophysical Research: Solid Earth 116. https://doi.org/10.1029/2010JB007665

Schueller, S., Braathen, A., Fossen, H., Tveranger, J., 2013. Spatial distribution of deformation bands

in damage zones of extensional faults in porous sandstones: Statistical analysis of field data. Journal of Structural Geology 52, 148–162. https://doi.org/10.1016/j.jsg.2013.03.013

Shipton, Z. K., Soden, A. M., Kirkpatrick, J. D., Bright, A. M., & Lunn, R.J., 2006. How Thick is a Fault? Fault Displacement-Thickness Scaling Revisited. Earthquake, 1–13. https://doi.org/10.1017/CBO9781107415324.004

Shipton, Z.K., Cowie, P.A., 2001. Damage zone and slip-surface evolution over μm to km scales in high-porosity Navajo sandstone, Utah. Journal of Structural Geology 23, 1825–1844. https://doi.org/10.1016/S0191-8141(01)00035-9

Smith, S.A.F., Bistacchi, A., Mitchell, T.M., Mittempergher, S., Di Toro, G., 2013. The structure of an exhumed intraplate seismogenic fault in crystalline basement. Tectonophysics 599, 29–44. https://doi.org/10.1016/j.tecto.2013.03.031

Soliva, R., Schulz, R.A., 2008. Distributed and localized faulting in extensional settings: Insight from the north Ethiopian Rift-Afar transition area. Tectonics 27, 1–19. https://doi.org/10.1029/2007TC002148

Torabi, A., Berg, S.S., 2011. Scaling of fault attributes: A review. Marine and Petroleum Geology 28, 1444–1460. https://doi.org/10.1016/j.marpetgeo.2011.04.003

Villani, F., D'Amico, S., Panzera, F., Vassallo, M., Bozionelos, G., Farrugia, D., Galea, P., 2018. Shallow high-resolution geophysical investigation along the western segment of the Victoria Lines Fault (island of Malta). Tectonophysics 724–725, 220–233. https://doi.org/10.1016/j.tecto.2018.01.010

Washburn, E.W., 1921. Note on a method of determining the distribution of pore sizes in a porous material. Proceedings of the National Academy of Sciences, USA. https://doi.org/10.1130/B30686.1

4

Investigating Representative Elementary Volume of a fracture network from outcrop data to drive Discrete Fracture Network modeling

Investigating Representative Elementary Volume of a fracture network from outcrop data to drive Discrete Fracture Network modeling

4.1 Introduction

Fracture networks in the subsurface can be modeled using Discrete Fracture Network (DFN). In DFN models, fractures are usually represented as 2D planar objects (discs or polygons) positioned in a 3D space, even if other type of DFN model have been propose in order to simulate the non-planarity of natural fractures (Lei et al., 2016; Horgan and Young, 2000). Position of fractures are usually simulated using a random distribution (Poisson distribution) (Stoyan and Stoyan, 1994; Lantuejoul, 2002) whereas attitude, size, density and intensity are extrapolated from data derived from outcrop, borehole or seismic observation. Since position and geometry of every fracture is randomly selected the spatial distribution and the connectivity of the fracture network are usually not correct or overestimated. To solve this problem some improvements to the Poisson method have been proposed (Chiles, 1988; Xu and Dowd, 2010) and other authors developed DFN models that take in account the mechanical interaction between fractures to control fracture initiation, growth and arrest (Josnin et al., 2002; Swaby and Rawnsley, 1996; Davy et al., 2013; Cacas et al., 2001; Srivastava et al., 2005; Bonneau et al., 2013; Bonneau et al., 2016). In the last years, geo-mechanically based DFN model have been developed (Lei et al., 2017 and references therein). Using this method fracture network evolution is simulated using the fracture growth physics and applying stress/stress condition extracted from geological data. This type of DFN have the capability to link the fracture geometry with the physical mechanism of their formation, however they required large computational time and the uncertainties in the input data can bring to unprecise results. Apart from the type of DFN method, the realization of a DFN model with a high number of fracture (e.g. reservoir scale) can be very time consuming making impossible to represent all the fractures at every scales. It is therefore necessary to do some simplification representing large scale and midscale fractures explicitly and integrating small scale fracture in the property modeling as implicit fractures. Identify the critical length where fractures can be integrated in the property modeling instead of being considered explicitly is a burning issue that depend on question addressed by the model. In this chapter, we present preliminary results of a work that has the aim to investigate this question by evaluating the size of the Representative Elementary Volume (REV) of a DFN built using the outcrop data of Qala fault zone (Gozo) presented in Chapter 2 of this thesis. We demonstrate that the Representative Elementary Volume evaluated on the DFN model is comparable with the one extracted from the outcrop (second chapter of this thesis). Moreover, we show that in randomly and poorly organized fracture network several DFN at the Representative Elementary Volume scale can be realized to extract histograms of the fracture parameters that can be used to populate the 3D model at the reservoir scale. This allows to represent all the fractures saving computational time and improving the fracture network modeling.

4.2 DFN model and Representative Elementary Volume analysis

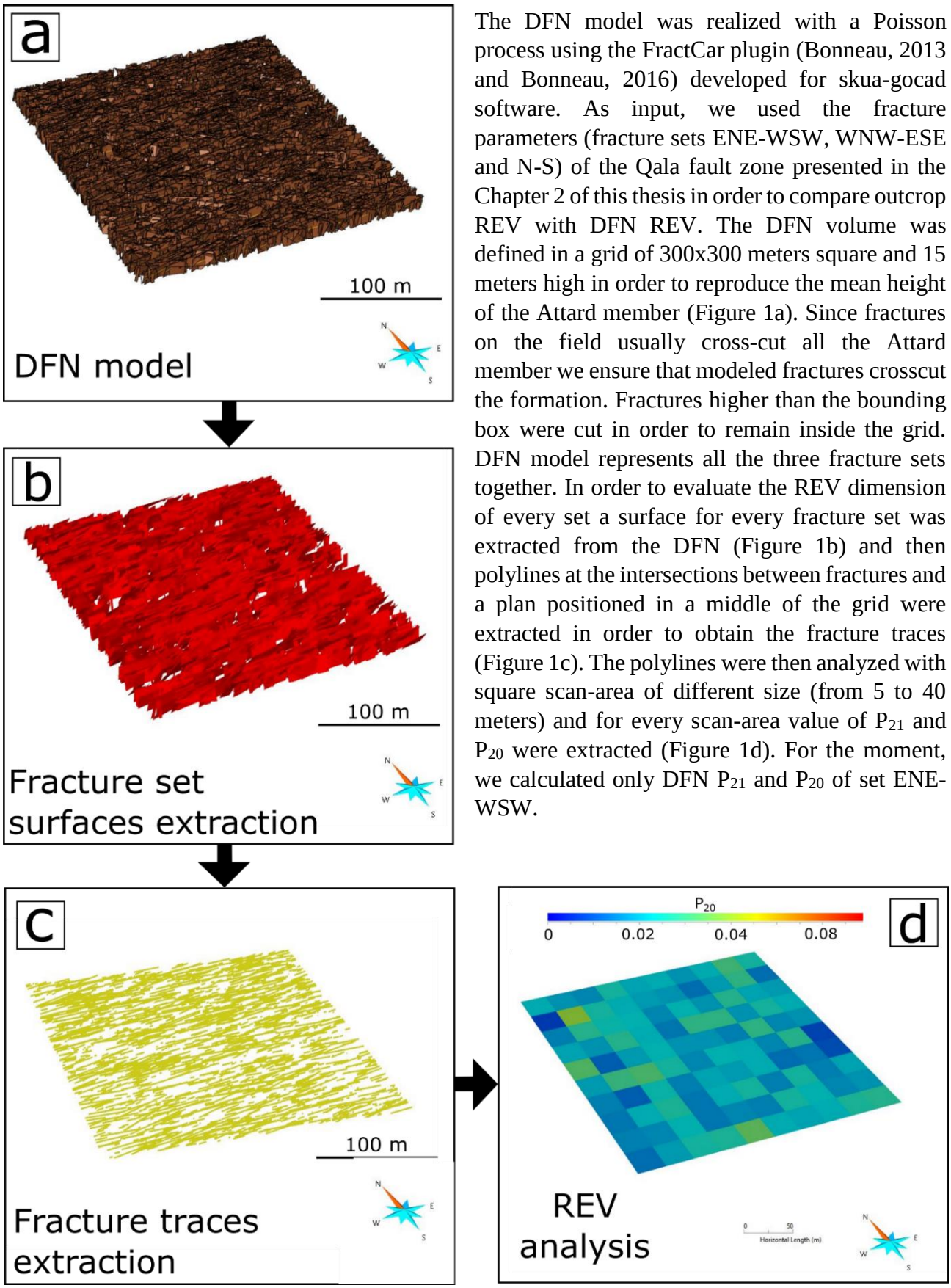

The DFN model was realized with a Poisson process using the FractCar plugin (Bonneau, 2013 and Bonneau, 2016) developed for skua-gocad software. As input, we used the fracture parameters (fracture sets ENE-WSW, WNW-ESE and N-S) of the Qala fault zone presented in the Chapter 2 of this thesis in order to compare outcrop REV with DFN REV. The DFN volume was defined in a grid of 300x300 meters square and 15 meters high in order to reproduce the mean height of the Attard member (Figure 1a). Since fractures on the field usually cross-cut all the Attard member we ensure that modeled fractures crosscut the formation. Fractures higher than the bounding box were cut in order to remain inside the grid. DFN model represents all the three fracture sets together. In order to evaluate the REV dimension of every set a surface for every fracture set was extracted from the DFN (Figure 1b) and then polylines at the intersections between fractures and a plan positioned in a middle of the grid were extracted in order to obtain the fracture traces (Figure 1c). The polylines were then analyzed with square scan-area of different size (from 5 to 40 meters) and for every scan-area value of P_{21} and P_{20} were extracted (Figure 1d). For the moment, we calculated only DFN P_{21} and P_{20} of set ENE-WSW.

Figure 1: The workflow used to extract the Representative Elementary Volume of P_{21} and P_{20} of the DFN

The Representative Elementary Volume dimension was than identified using the method based on T-test and F-test (Esmaieli et., 2010) already explained in Chapter 2 of this thesis. Results show that REV evaluated from DFN is similar to the one extracted from the outcrop data (Figure 2). This indicates that fracture parameters variability is well respected in the DFN model.

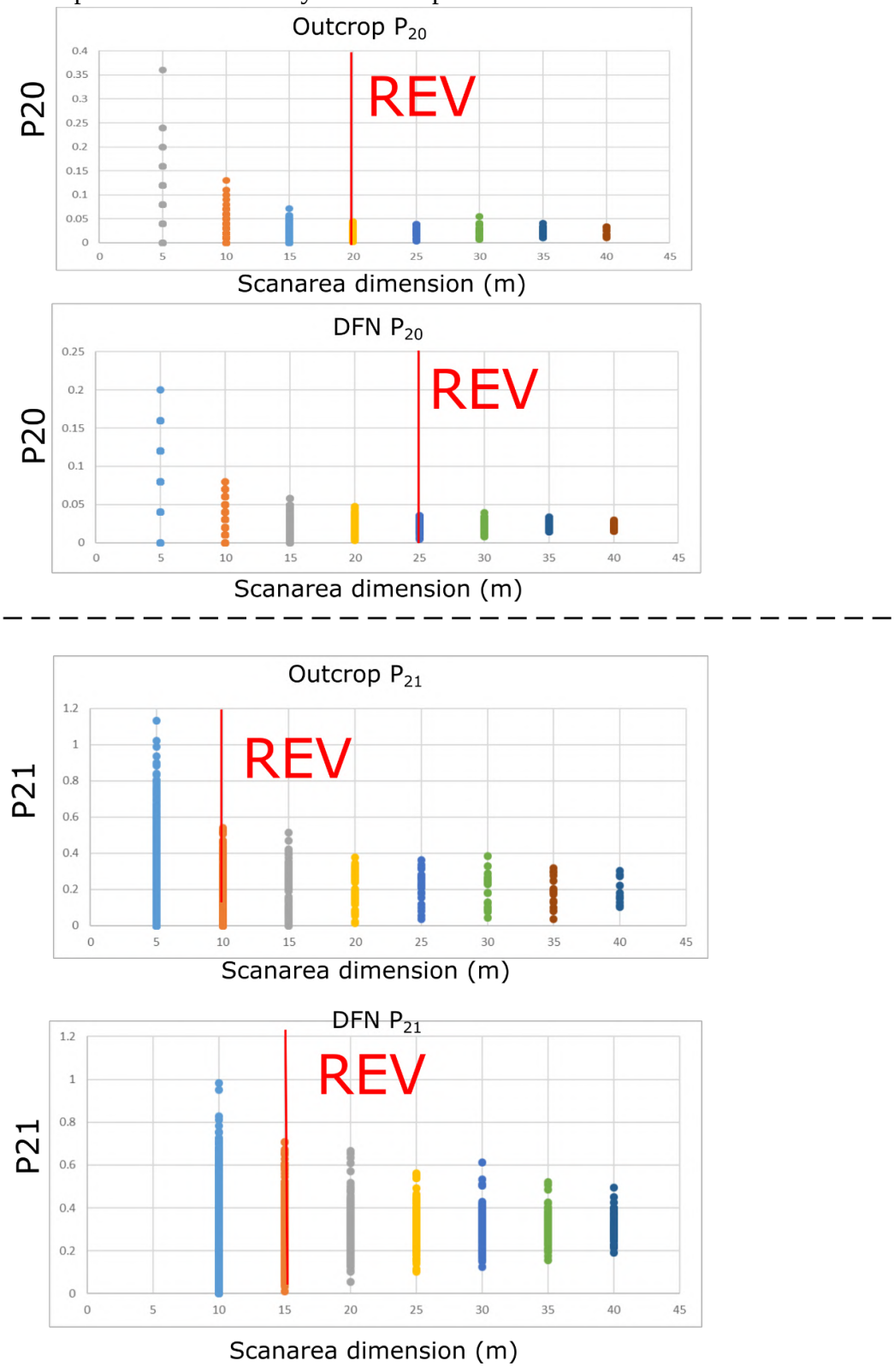

Figure 2: Comparison between outcrop REV and DFN REV. Results show that the two REV have similar dimension indicating the in the DFN model fracture variability of the outcrop is well respected.

4.3 Populate a 3D model using the Representative Elementary Volume

The Representative Elementary Volume previously identified give the cell size in which we can consider that fracture properties are representative of the network of discontinuity. It is then possible to build several DFN at the Representative Elementary Volume scale and compute the equivalent property value for each one. Indeed, stochastic simulations provide a set of equiprobable realizations that generate a variability that can be captured by an histogram (Figure 3). At the end, the histogram of the study property can be used to populate the 3D model (Figure 3). The same result can be obtained realizing a bigger DFN (but small enough to permit

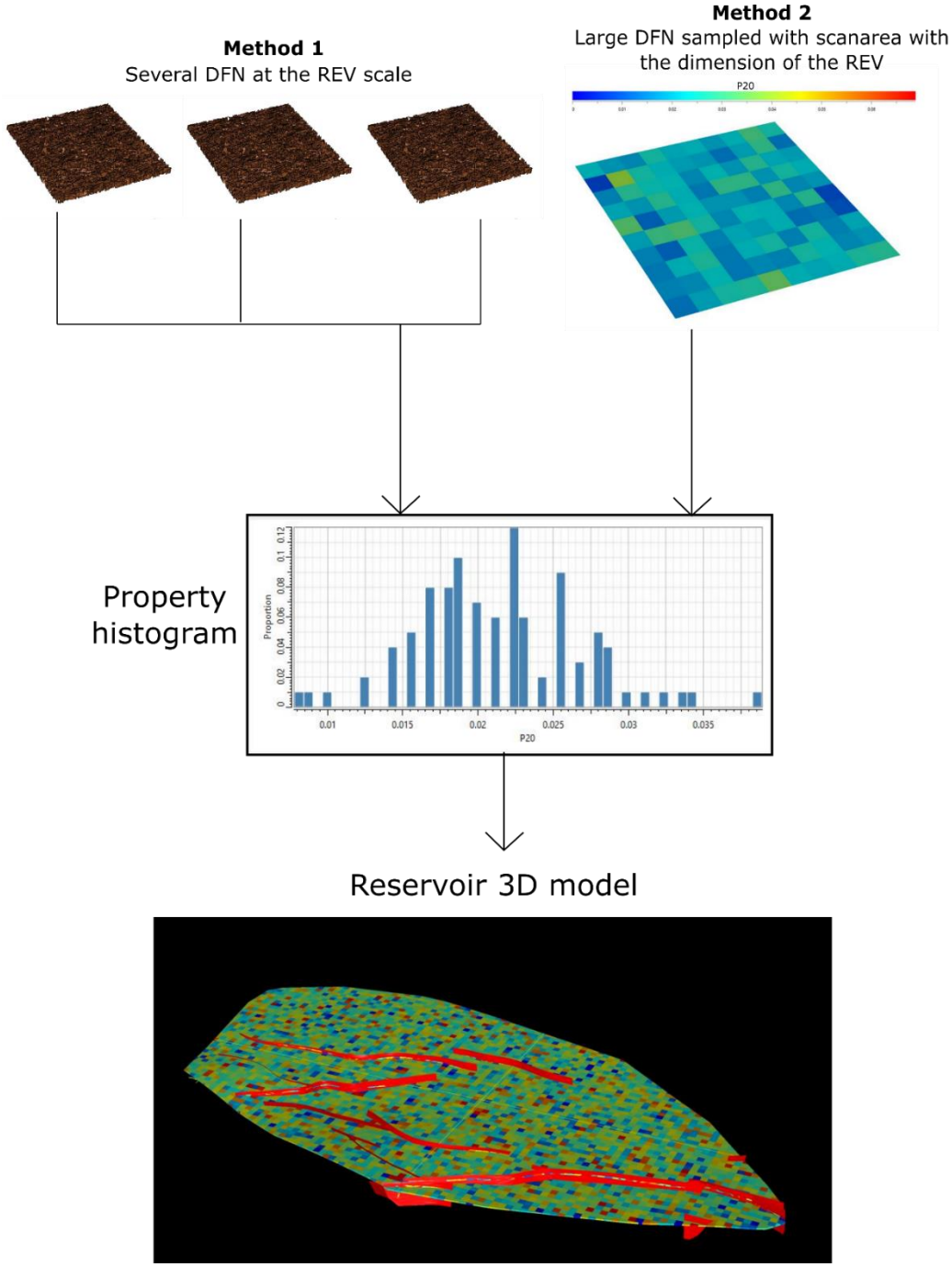

Figure 3: The REV size can be used to build several DFN on a small scale (method 1) or to apply several scan-area with REV dimension on a bigger DFN (method 2) to extract a property histogram that can be used to populate the 3D model

a quick realization) and then extracting the study parameter using scan-area with the same dimension of the Representative Elementary volume (Figure 3).

4.4 Distribute fracture properties in the footwall of the Qala fault

Since in this work, we analyzed the Representative Elementary Volume of the P_{20} and P_{21}fracture network in the damage zone of the Qala fault we realized the 3D geo-model of the Gozo Island in order to distribute P20 and P21 in the area corresponding to the footwall of the Qala fault using the method proposed in the previous chapter. The 3D geo-model of the Gozo Island was built in Skua-Gocad considering both surface and subsurface data. Surface data were derived from the geological map of Malta and Gozo presented in Martinelli et al., 2019 (first chapter of this thesis and available in the supplementary materials). The geological map was digitalized in Arc-map to obtain fault traces and formation boundaries. Moreover, we used the depth maps of the Lower Coralline Limestone and of the Lower and Middle Globigerina Limestone published by Pedley et al., 1976. Depth maps were digitized in Arc-Map in order to obtain curves to use as hard data during the 3D model workflow. As subsurface data more than 120 boreholes with stratigraphic data realized by the Maltese government for water research were digitized to better constrain horizon modeling. All these data were imported in Move were 26 cross-sections were realized. Formations boundaries were projected on the DTM surface and eventually corrected. Fault surfaces were extruded using the information coming from the structural analysis of Martinelli et al., 2019 (first chapter of this thesis) and geological map. As last step data were imported in Skua-Gocad were the 3D geo-model was realized with the structure and stratigraphy workflow (Figure 4). Results explained in Chapter 2 of this thesis, reveal that damage zone in the Lower Coralline Limestone Formation is 520 meters width in the footwall of the Qala fault and for this reason, we extracted a region of 520 meters in the 3D model in the area corresponding to the footwall of the fault. Cells dimension of the model where choose in order to have the same size of the Representative Elementary Volume (25x25 m) (Figure 5c).

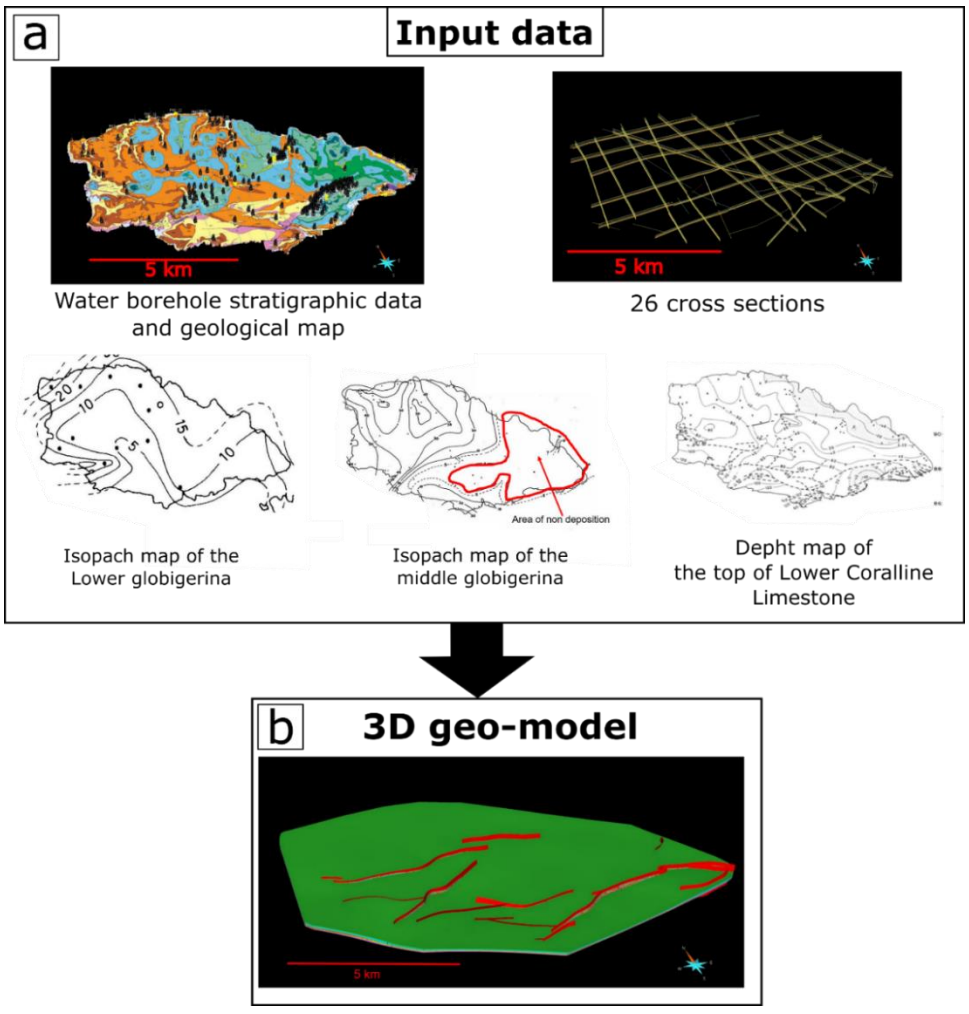

Figure 4: Input data used for the realization of the 3D model of the Gozo Island

To populate the 3D model of the footwall of the Qala fault we covered the DFN realized in the previous chapters with scanarea of the dimension of the REV (25x25 for P20 and 15x15 for P21) and we extracted the property histogram (Figure 5a). Since fracture are randomly distributed and the histogram reveals a normal distribution, we distributed the P_{20} and P_{21} properties using a normal random distribution function fitted on the extracted histogram. The result for P_{20} property is visible in Figure 5b.

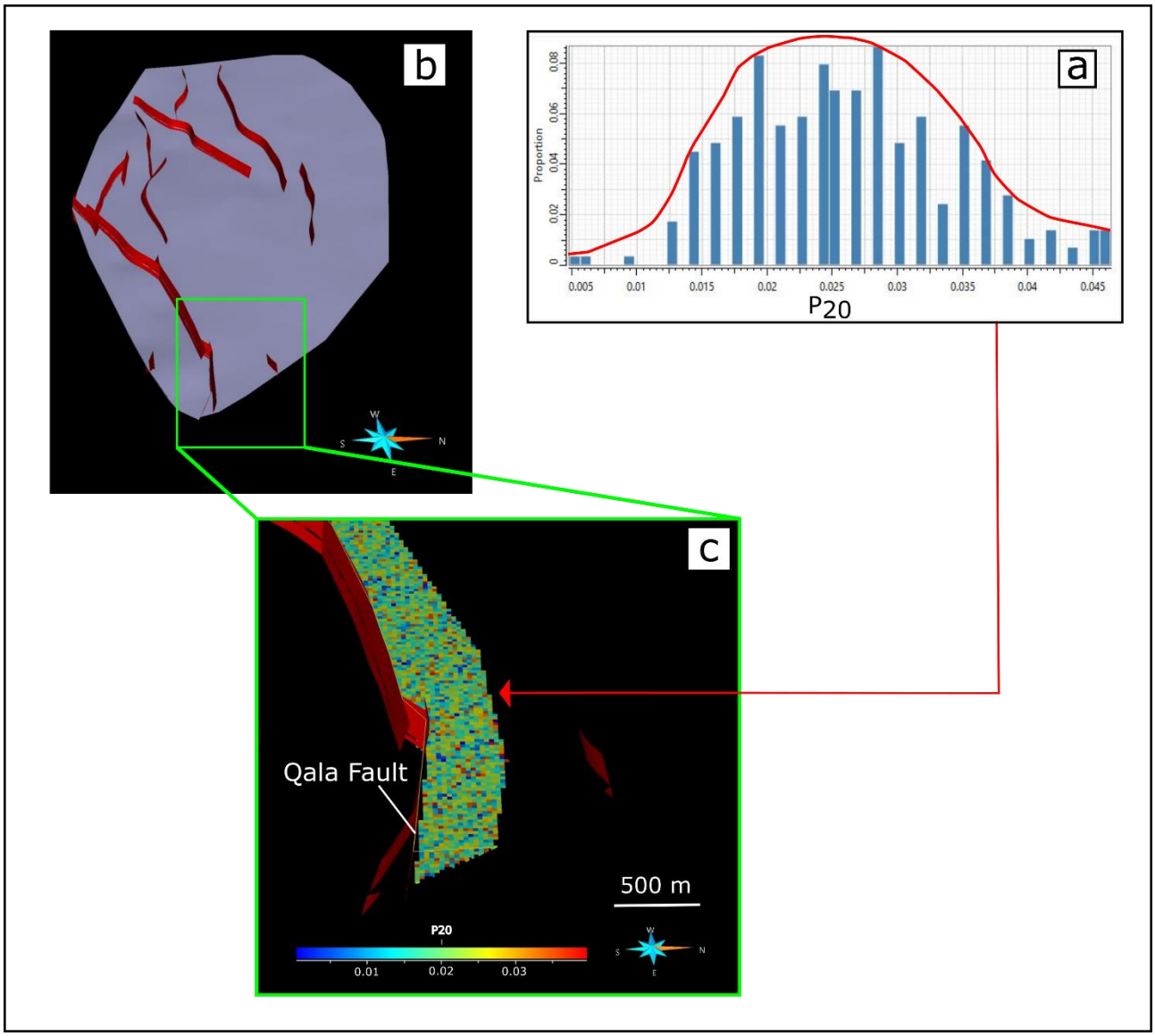

Figure 5: a) The P20 histogram extracted from the outcrop DFN; b) the 3D grid of the Attard member on the Gozo Island; c) P20 property of set ENE-WSW in the footwall of the Qala 2 Fault distributed using a random normal distribution

4.5 Conclusion

In this chapter, we show preliminary results of a study that has the aim to build DFN model on a smaller scale with respect to the reservoir scale in order to solve modeling (try to model all the fracture explicitly) and computational issues (e.g. reduce computational time). We demonstrated that investigating the Representative Elementary Volume of fracture network parameters from outcrop data in homogenous fracture network (randomly or uniformly distributed) can be very useful in order to populate a 3D geo-model. Indeed, using the outcrop data it is possible to realize a DFN model that will have a REV comparable to the one of the outcrop and instead of building a DFN model at the reservoir scale, that can be very time consuming and often requires a simplification of the fracture network, it is possible to evaluate equivalent property by studying DFN realization at the REV scale. With this work, we produce a histogram of the fracture parameters that can be

used to populate the reservoir model. Cells of the grid should correspond to the REV size. A small DFN give the possibility to model all the fractures allowing to fully characterize the fracture network without simplifications. Moreover, it can be used in computational demanding DFN models (e.g. geomechanically based DFN) to reduce computation time and at the same time to perfectly honor fracture connectivity and topology.

4.6 Next steps

The results highlighted in this chapter are only the first step of a work that need to be update and explore with further and deeper analysis. Indeed, the final goal of a DFN model is usually to extract the permeability of the fracture networks. Further analyses have to be done in order to understand if it is possible to reach a REV also for other fracture parameters (e.g. length) and for the permeability tensor.

References

Bonneau, F., Henrion, V., Caumon G., Renard, P., and Sausse J (2013). A methodology for pseudo-genetic stochastic modeling of discrete fracture networks. Computer & Geosciences.

Bonneau, F., Caumon, G., and Renard P. (2016). Impact of stochastic sequential initiation of fractures on spatial correlations and connectivity of discrete fracture networks. Journal of Geophysical Research: Solid Earth.

Cacas, M.-C., J.-M. Daniel, and J. Letouzey (2001), Nested geological modelling of naturally fractured reservoirs, Pet. Geosci., 7, 43–52.

Chilès JP, 1988. Fractal and geostatistical methods for modeling of a fracture network. Math Geol 1988;20:631–54. http://dx.doi.org/10.1007/ BF00890581

Davy P, Le Goc R, Darcel C., 2013 A model of fracture nucleation, growth and arrest, and consequences for fracture density and scaling. J Geophys Res Solid Earth;118:1393–407. http://dx.doi.org/10.1002/jgrb.50120

Esmaieli, K., Hadjigeorgiou, J., and Grenon, M. (2010). Estimating geometrical and mechanical REV based on synthetic rock mass models at Brunswick Mine. International Journal of Rock Mechanics and Mining Sciences. 47(6), 915-926.

Horgan GW, Young IM 2000. An empirical stochastic model for the geometry of two-dimensional crack growth in soil (with Discussion). Geoderma; 96:263–76. http://dx.doi.org/10.1016/S0016-7061(00)00015-X.

Josnin J, Jourde H, Fénart P, Bidaux P, 2002. A three-dimensional model to simulate joint networks in layered rocks. Can J Earth Sci;39:1443–55. http://dx.doi.org/10.1139/e02-043

Lantuéjoul, C., 2002. Geostatistical Simulation: Models and Algorithms, Springer, Berlin, Germany.

Lei, Q., & Wang, X. (2016). Tectonic interpretation of the connectivity of a multiscale fracture system in limestone. Geophysical Research Letters, 43, 1551–1558. https://doi.org/10.1002/2015GL067277

Lei, Q., Latham, J. P., & Tsang, C. F. 2017. The use of discrete fracture networks for modelling coupled geomechanical and hydrological behaviour of fractured rocks. Computers and Geotechnics, 85, 151-176.

Martinelli, M., Bistacchi, A., Balsamo, F., & Meda, M. (2019). Late Oligocene to Pliocene extension in the Maltese Islands and implications for geodynamics of the Pantelleria Rift and Pelagian Platform. Tectonics, 38. https://doi.org/10.1029/2019TC005627

Pedley, H., M., House, M., & Waugh, B. (1976). The Geology of Malta and Gozo. Proc. Geol. Ass. 87 (3), 325-341.

Srivastava, R., P. Frykman, and M. Jensen (2005), Geostatistical simulation of fracture networks, in Geostatistics Banff 2004, Quantitative Geology and Geostatistics, vol. 14–1, edited by R. Srivastava, P. Frykman, and M. Jensen, pp. 295–304, Springer, Netherlands.

Stoyan, D., and H. Stoyan, 1994. Fractals, Random Shapes and Point Fields, Wiley, New York.

Swaby, P. A., and K. D. Rawnsley (1996), An interactive 3D fracture modelling environment, in SPE-36004-MS, pp. 82–87, Society of Petroleum Engineers, Dallas, Tex., doi:10.2118/36004-MS.

Xu C & Dowd P, 2010. A new computer code for discrete fracture network modelling. Comput Geosci; 36:292–301. http://dx.doi.org/10.1016/j.cageo.2009.05.012.

5

General conclusions

General conclusions

In this work, we characterized the fracture network associated with normal faults in carbonates of the Maltese Islands. We demonstrated that the use of outcrop analogues is fundamental to better characterize and model the fracture network parameters and their impact on the fluid flow in the subsurface. Indeed, outcrop analogues allow to investigate the fault and fracture network at different scales and to apply a multidisciplinary approach that allows carrying out different types of analyses, impossible to perform with borehole and seismic data. In particular, thanks to the spectacular and continuous outcrops of the Maltese Islands, in this thesis we were able to characterize:

i) The tectonic evolution of the Maltese Islands and of the Pelagian platform from the Late Oligocene to the Pliocene. This analysis was performed collecting structural and kinematic data that were used to recognize the different sets of joint and faults and to carry out a paleostress modelling, which highlighted the presence of two main extensional tectonic events separated by a period of tectonic quiescence. The first event is a WNW-ESE extension from the Late Aquitanian to the Early Burdigalian that caused the formation of small normal faults associated with Neptunian dykes (D1 extension). The second event is a N-S extension, developed from the Late Miocene to the Pliocene, that lead to the formation of two coeval sets of normal faults striking WNW-ESE and ENE-WSW and four sets of joints striking WNW-ESE, ENE-WSW, N-S and NE-SW (D2 extension). In addition, we were able to correlate this tectonic evolution with the geodynamic evolution of the western and central Mediterranean. Indeed, we demonstrated that both the extensional events took place during periods of slab-retreat and they were caused by the foreland flexure and slab-roll back.

ii) The fracture network parameters in the damage zone of the footwall of Qala fault - a normal fault with ca. 30 m of displacement located in the southeastern part of Gozo. Here we carried out a 3D photogrammetric survey on a spectacular outcrop - 1 km long - that allowed us to obtain a km-scale high resolution Digital Outcrop Model. This allowed digitizing all fractures in the damage zone and background, and extract fracture network parameters with automatic Python scripts that can be used in Skua-Gocad. Moreover, we developed a new workflow for fracture network characterization that combines linear scan-line and scan-area analyses. The linear scan-line analysis is used to characterize the spatial distribution of the fractures and scan-area analysis is used to extract the fracture parameters (length, density, intensity, spacing, topology and Representative Elementary Volume). Thanks to this work we demonstrated the importance of combining field work and Digital Outcrop Models in fracture network characterization. Indeed, this approach allows to collect a huge amount of data, to automatize the process of the extraction of fracture parameters and to obtain highly reliable statistics. From the structural point of view, we show that the footwall of the Qala fault is divided in three distinct zone: i) a thin fault core; ii) a highly fractured Inner Damage Zone (5 meters thick); iii) an Outer Damage Zone (520 meters thick) and that the fracture network of ODZ is connected within 120 meters from the slip surfaces showing that even faults with limited displacement can be surrounded by a large fractured and permeable area that can have an important impact on the fluid flow.

iii) The effect of mechanical stratigraphy on the width of the Damage Zone. Field analysis performed in different units highlighted that, along faults with the same tectonic history and with comparable displacement, damage zone thickness change abruptly in units with different properties. Combining field, geomechanical and petrophysical analyses, we demonstrated that the elastic properties of rocks play a fundamental role in the control of damage zone thickness. In a multilayer carbonate stratigraphy composed by units with different elastic properties and subjected to extensional tectonics, in the less rigid units σ_3 decreases at a slower rate with respect to the stiffer units, with the consequence that the latter yields before the former even if they are stronger. This behavior is reflected in the thickness of damage zones that, in a counterintuitive way, are thicker in more rigid and stronger units. Further analyses are needed to better understand if there is a correlation between the petrophysical and geomechanical parameters of the investigated units.

iv) The Representative Elementary Volume of fracture network parameters extracted from the outcrop, aimed at building statistically-representative DFN models. We demonstrated that using outcrop data it is possible to realize a DFN model that has a REV comparable to the one of the outcrop. This has the consequence that in randomly distributed fracture networks, instead of building a DFN model at the reservoir scale, it is possible to evaluate equivalent properties by studying several DFN realizations at the REV scale. This analysis produces a histogram of the investigated fracture parameter that can be used to populate the reservoir model. Even if further analyses are needed this preliminary results are very encouraging. Indeed, a small DFN give the possibility to model all the fractures allowing to fully characterize the fracture network without simplifications reducing computation time.

Supplementary materials

NOTE FOR THE READER

Supplementary materials contain:

Supplementary materials of chapter 1 and supplementary materials of chapter 2

Supplementary materials of Chapter 1

Geological Map of Malta and Gozo with Fault Slip Data

Mattia Martinelli[1*], Andrea Bistacchi[1], Fabrizio Balsamo[2] and Marco Meda[3]

[1] Dipartimento di Scienze dell'Ambiente e della Terra, Universita' degli Studi di Milano Bicocca, Piazza della Scienza 4, 20126 Milano - Italy

[2] NEXT - Natural and Experimental Tectonics research group, Università di Parma, Dipartimento Scienze Chimiche, della Vita e della Sostenibilità Ambientale, Padiglione, 7 - Scienze della Terra, Campus Universitario, Parco Area delle Scienze 157/A, 43124 Parma - Italy

[3] ENI Spa, Upstream and Technical Services, Via Emilia 1, 20097 San Donato Milanese - Italy

* corresponding author: Mattia Martinelli (m.martinelli34@campus.unimib.it)

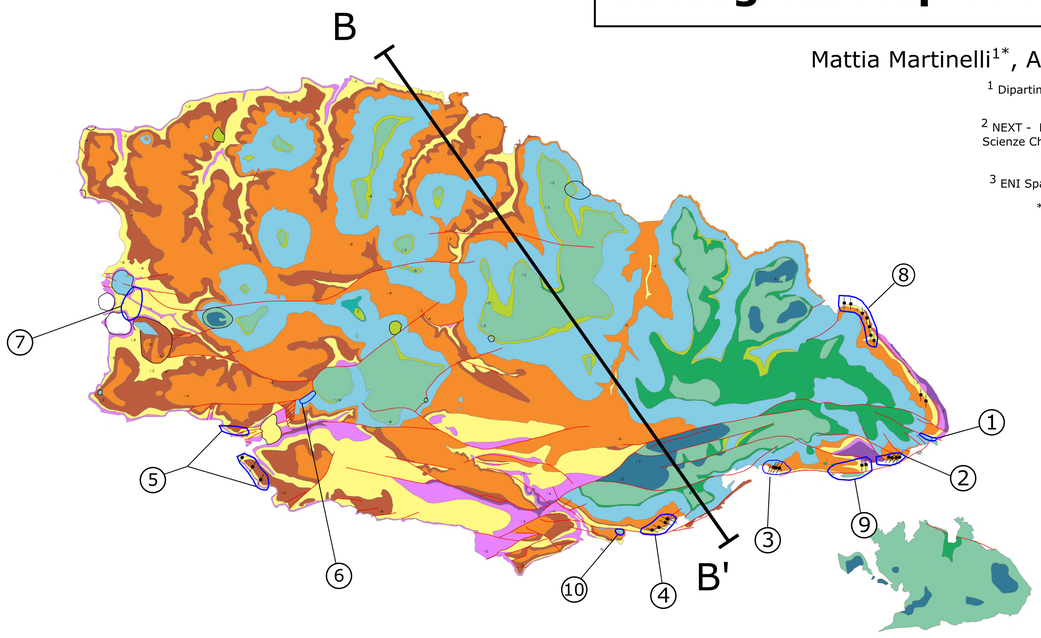

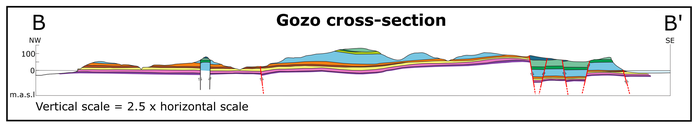

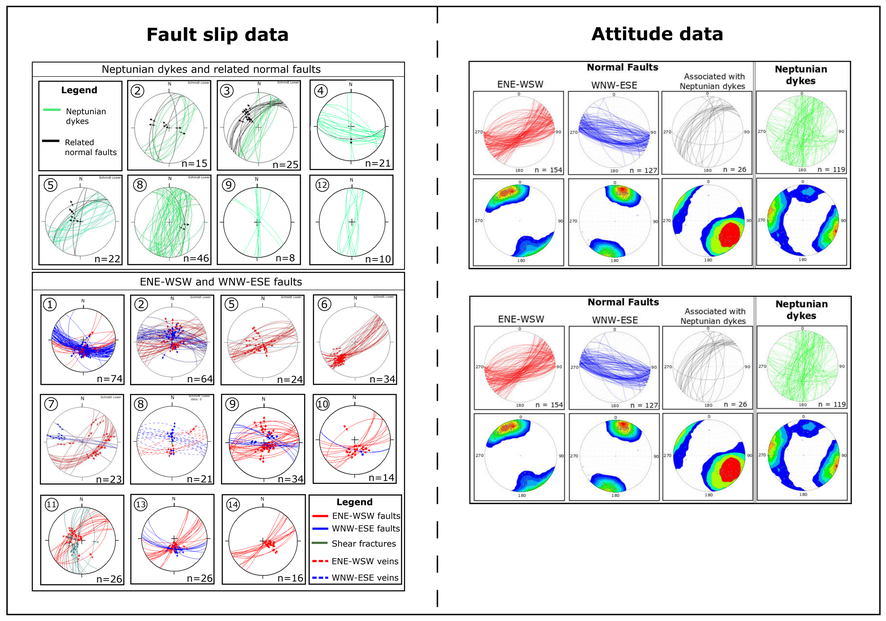

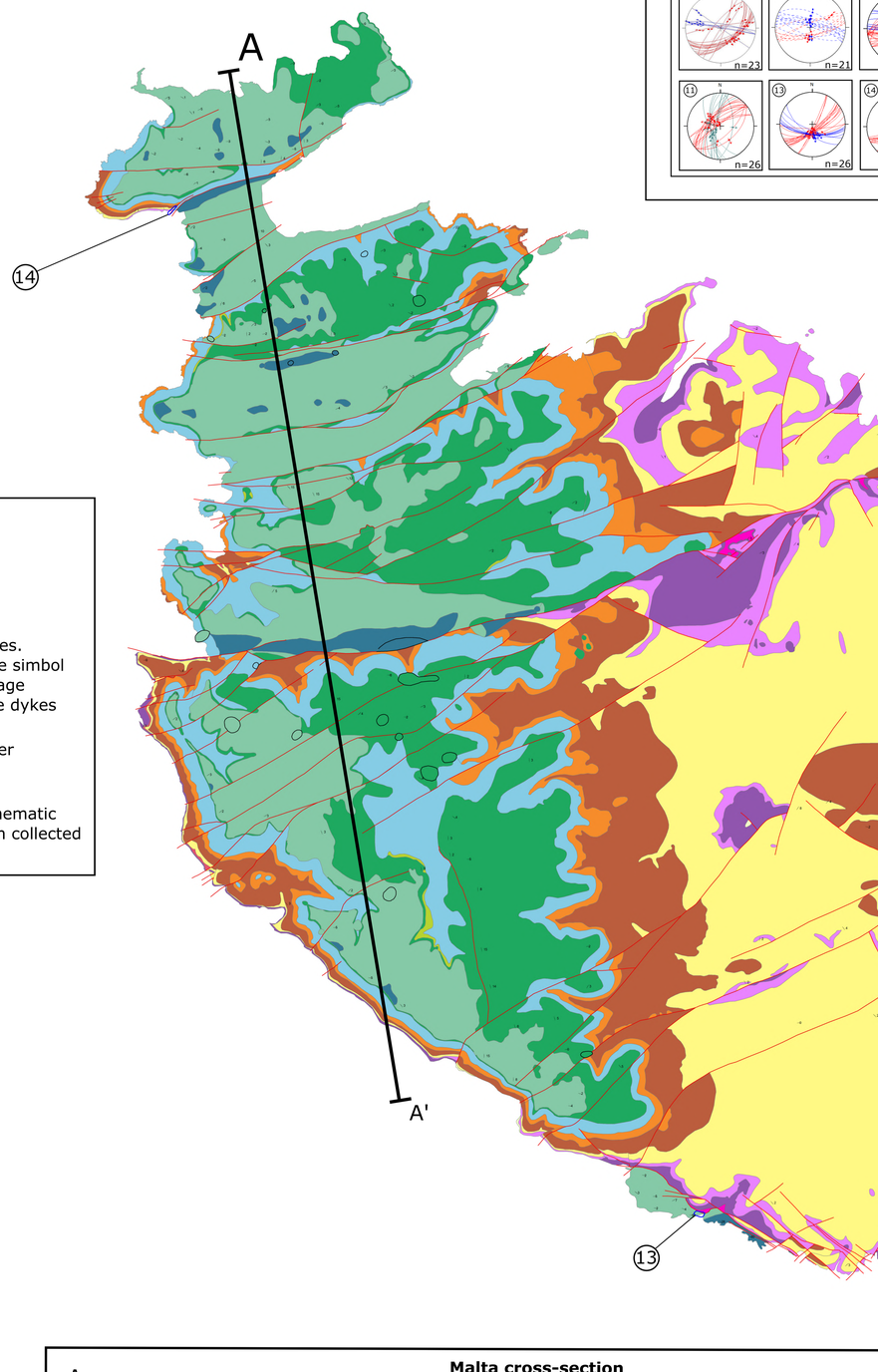

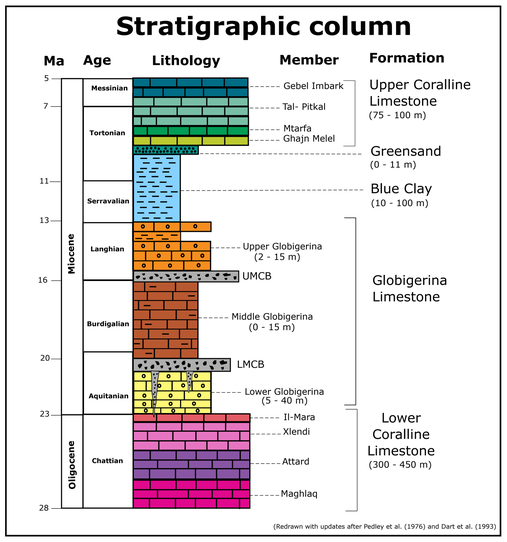

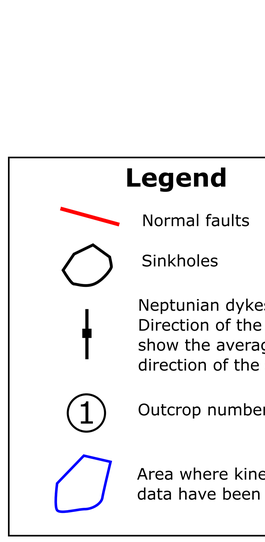

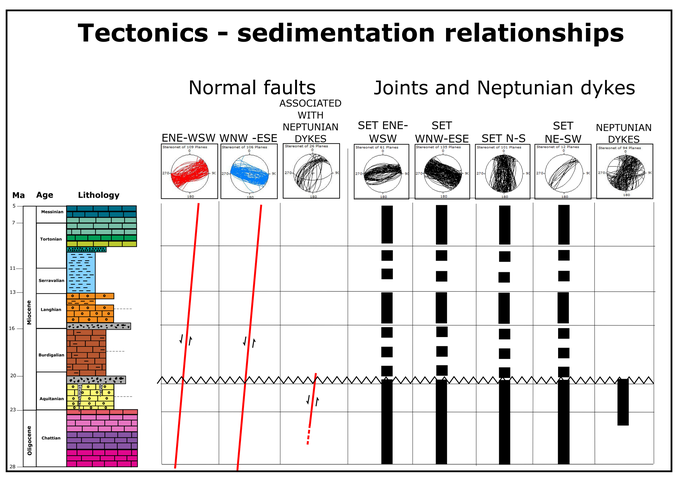

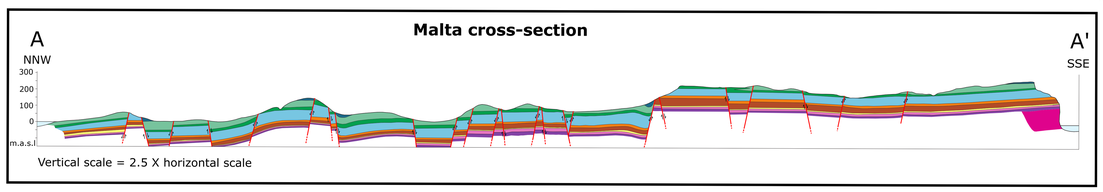

N

10 km

Base Geological Map and cross-sections updated with original geological and structural survey after:
Geological Map of the Maltese Islands, 1993 revision, scale 1:25000. Oil Exploration Directorate, Office of the Prime Minister Malta

Scale 1:25.000

Supporting data Table S1 Chapter 1

Normal Faults						Neptunian Dikes		Joints							
set ENE-WSW		set NW -SE		Associated with Neptunian dikes				set ENE - WSW		set WNW - ESE		set N-S		set NE - SW	
Dip	Dip dir.	Dip	Dip dir.	Dip	Dip dir.	Dip	Dip dir.	Dip	Dip dir.	Dip	Dip dir.	Dip	Dip dir.	Dip	Dip dir.
168	65	80	15	60	115	85	85	60	350	90	190	68	280	85	130
160	70	55	25	55	80	86	90	60	335	72	20	70	285	90	298
340	80	70	200	70	315	86	115	65	150	70	20	65	120	60	310
335	80	69	183	45	325	90	88	75	350	55	205	85	285	73	315
172	72	85	15	50	320	88	88	65	168	90	20	58	275	90	125
172	73	85	5	45	315	85	95	60	354	60	185	75	270	80	315
165	70	88	20	45	320	75	40	65	350	70	185	60	90	88	142
160	80	80	10	52	325	85	45	90	330	60	185	74	75	58	320
355	70	72	20	65	315	85	100	45	358	65	7	68	85	55	125
160	82	80	25	40	335	85	110	62	0	90	30	85	95	67	315
320	68	80	5	65	305	70	295	70	350	55	15	75	80	60	325
355	45	70	10	60	310	70	290	60	345	60	25	85	290		
345	60	90	187	70	312	81	264	60	345	70	30	77	85		
330	85	78	5	65	321	75	264	70	340	82	195	65	65		
345	40	82	2	75	300	75	90	72	355	65	205	73	290		
315	80	80	5	75	277	80	262	55	180	70	40	86	125		
160	70	72	20	90	280	75	85	65	355	75	15	60	310		
165	60	64	10	45	335	80	109	70	345	71	204	88	80		
180	65	70	5	60	320	70	65	75	170	65	215	66	85		
175	66	75	15	60	180	70	130	70	355	52	197	74	85		
180	70	75	15	80	315	85	100	65	170	85	205	74	75		
175	75	60	45	60	110	65	72	78	345	65	215	85	265		
175	60	55	210	50	295	65	90	62	340	90	15	75	110		
180	68	55	15	85	290	65	100	52	150	75	200	73	300		
178	65	85	202	52	280	70	70	68	350	60	45	71	90		
180	55	70	205	72	90	85	112	80	350	60	35	64	270		
180	70	70	200			75	108	87	345	55	25	68	60		
175	60	55	195			70	330	85	350	85	19	80	125		
125	80	65	198			70	125	75	350	80	20	90	270		
115	80	65	220			80	125	62	180	70	20	63	265		
345	80	66	200			80	120	70	162	55	35	73	265		
180	65	65	200			80	90	55	150	75	15	60	50		
165	85	74	205			80	290	65	170	70	15	70	90		
155	80	65	195			50	275	68	170	70	15	70	90		
150	82	54	255			80	275	68	350	55	5	75	70		
154	82	65	185			60	286	75	0	55	15	65	75		
162	80	65	205			80	285	55	345	82	20	70	260		
175	82	75	210			80	260	80	355	85	10	90	85		
180	90	65	192			80	308	50	0	80	25	60	290		
165	84	85	185			60	60	70	350	68	200	85	70		
175	80	66	190			70	285	82	355	80	35	82	80		
155	82	74	190			60	125	75	345	66	185	70	70		
180	84	67	190			70	295	64	165	82	10	74	85		
355	70	70	183			55	60	82	175	90	15	76	90		
346	86	63	190			76	305	78	160	85	5	65	300		
145	80	75	214			55	320	85	165	65	50	72	90		
165	86	64	190			85	100	78	170	70	15	65	270		
345	56	61	210			35	175	88	350	60	15	82	87		
334	80	65	190			50	110	75	175	72	5	85	245		
180	85	75	210			72	105	88	358	50	20	50	260		
340	65	72	195			65	95	55	170	70	200	80	72		
156	80	68	190			58	300	70	180	75	190	65	50		
330	68	65	190			40	110	85	180	76	35	78	270		
145	80	68	185			80	110	67	0	54	20	86	65		
149	68	65	186			80	70	85	355	82	25	58	55		
330	80	78	200			72	90	80	350	85	200	57	245		
155	62	80	198			65	285	86	350	58	195	90	80		
160	68	72	198			74	250	90	160	83	50	75	95		
161	65	78	200			75	280	86	180	67	25	60	95		
145	75	72	210			70	290	62	175	62	25	85	70		
135	72	68	210			60	75	90	340	78	35	62	265		
138	68	66	190			86	295	75	170	75	225	85	70		
140	82	70	185			75	305	65	165	80	205	76	276		
137	80	68	190			82	305	86	0	84	195	40	305		
135	90	60	198			80	305	70	170	74	10	55	115		
160	65	60	200			85	90	82	345	78	195	66	70		
138	75	55	185			85	305	78	355	82	210	68	82		
135	80	60	205			75	110	85	358	52	15	66	260		
155	63	55	204			75	300	84	355	73	195	53	275		
152	70	65	210			70	125	87	345	90	20	50	245		
136	80	62	210			85	125	82	160	85	25	85	70		
137	80	62	190			80	270	70	345	74	188	78	270		
135	85	72	188			85	300	67	343	76	10	68	90		
130	88	80	55			80	110	65	145	85	182	70	75		
130	85	74	200			75	332			75	45	70	120		
131	75	70	197			70	320			78	202				
134	75	72	200			60	305			56	20				
134	75	73	202			70	315			83	20				
310	84	73	204			70	317			85	20				
320	74	74	202			70	120			70	215				
308	80	70	190			80	164			85	20				
165	65	70	195			70	175			80	220				
160	66	85	20			65	145			62	215				
130	90	68	5			64	155			45	190				
175	86	65	2			85	315			70	20				
155	85	80	15			75	310			70	30				
170	88	80	12			65	325			70	245				
154	78	80	0			80	325			68	225				
172	76	80	5			70	145			74	65				
150	85	83	25			85	190			64	40				
150	80	78	10			90	270			68	185				
150	75	85	5			85	264			76	185				
158	85	85	8			85	198			50	210				
174	84	75	18			75	195			85	45				
335	45	75	6			50	195			54	235				
350	50	60	5			74	195			66	210				
347	40	65	8			55	180			75	230				
350	60	80	2			80	185			56	195				
346	60	60	45			70	190			90	45				
355	65	74	185			80	20			74	190				
160	75	85	190			60	195			56	240				
123	74	86	195			90	195			76	192				
125	74	80	30			85	90			70	45				
338	65	85	195			85	95			80	20				
324	58	90	187			55	50			62	45				
160	75	85	180			58	135			64	45				
155	75	88	185			72	125			52	220				
168	75	84	185			60	285			70	5				
143	65	84	182			65	295			70	15				
140	60	75	32			65	115			35	195				
176	75	85	5			60	110			72	15				
180	76	70	25			50	113			66	25				
155	60	70	25			70	140			75	10				
128	80	85	72			80	25			75	20				
174	80	75	15			75	210			56	7				
164	80	75	30			74	40			75	220				
350	70	78	25			60	40			65	235				
350	75	90	188			55	190			75	15				
358	90	90	180			55	190			82	5				
174	55	65	188			65	185			60	220				
174	60	65	183							58	30				
178	75	65	190							54	230				
179	80	65	185							75	210				
140	75	75	204							76	30				
148	80	65	197							90	187				
144	75	65	188							78	5				
140	73	65	218							82	2				
152	74	63	185							80	5				
150	72														
115	80														
115	86														
117	82														
144	82														
136	78														
148	70														
140	78														
155	70														
178	65														
165	64														
160	60														
152	80														
155	60														
135	85														
162	85														
154	85														
128	85														
135	78														
128	85														
120	85														
130	85														
135	80														
160	75														
160	80														
160	78														
158	75														

Supporting data Table S2 Chapter 1

Outcrop 2

	Dip dir.	Dip	Rake
Neptunian dykes	135	58	
	125	72	
	285	60	
	295	65	
	115	65	
	110	60	
	113	50	
	140	70	
Related normal faults	315	80	-90
	110	60	-90
	295	50	-90
	290	85	-90
	280	52	-90
	90	72	-90

Outcrop 3

	Dip dir.	Dip	Rake
Neptunian dykes	295	86	
	305	75	
	305	82	
	305	80	
	90	85	
	305	85	
	110	75	
	300	75	
	125	70	
	125	85	
	270	80	
	300	85	
	110	80	
Related normal faults	315	70	-90
	325	45	-90
	320	50	-90
	315	45	-90
	320	45	-90
	325	52	-90
	315	65	-90
	335	40	-90
	305	65	-90
	310	60	-90
	312	70	-90

Outcrop 4

	Dip dir.	Dip	Rake
Neptunian dykes	190	85	
	198	85	
	195	75	
	195	50	
	195	74	
	180	55	
	185	80	
	190	70	
	20	80	
	195	60	
	195	90	
	270	90	
	264	85	
	20	80	
	195	60	
	195	90	
	25	80	
	210	75	
	40	74	
	40	60	
	190	55	
	190	55	
	185	65	
Releated normal faults	180	60	-90

Outcrop 5

	Dip dir.	Dip	Rake
Neptunian dykes	332	75	
	320	70	
	305	60	
	315	70	
	317	70	
	120	70	
	164	80	
	175	70	
	145	65	
	155	64	
	315	85	
	310	75	
	325	65	
	325	80	
	145	70	
Related normal faults	321	65	-90
	300	75	-90
	277	75	-90
	280	90	-90
	335	45	-90
	320	60	-90

Outcrop 8

	Dip dir.	Dip	Rake
Neptunian dykes	130	70	
	100	85	
	72	65	
	90	65	
	100	65	
	70	70	
	112	85	
	108	75	
	330	70	
	125	70	
	125	80	
	120	80	
	90	80	
	290	80	
	275	50	
	275	80	
	286	60	
	285	80	
	260	80	
	308	80	
	60	60	
	285	70	
	125	60	
	295	70	
	60	55	
	305	76	
	320	55	
	100	85	
	175	35	
	110	50	
	105	72	
	95	65	
	300	58	
	110	40	
	110	80	
	70	80	
	90	72	
	285	65	
	250	74	
	280	75	
	290	70	
	75	60	
Related normal	115	60	-90
	80	55	-100

Outcrop 9

	Dip dir.	Dip
Neptunian dykes	85	85
	90	86
	115	86
	88	90
	88	88
	95	85
	40	75
	45	85

Outcrop 12

	Dip dir.	Dip
Neptunian dykes	100	85
	110	85
	295	70
	290	70
	264	81
	264	75
	90	75
	262	80
	85	75
	109	80

Supporting material Table S3 Chapter 1

Outcrop 1

	Dip-dir	Dip	Rake
set ENE - WSW	160	70	-95
	165	60	-90
	180	65	-90
	175	66	-90
	180	70	-85
	175	75	-85
	175	60	-85
	180	68	-85
	178	65	-90
	180	55	-90
	180	70	-90
	175	60	-90
	125	80	-110
	115	80	-100
	345	80	-110
	180	65	-60
set WNW- ESE	202	85	-90
	205	70	-90
	200	70	-100
	195	55	-85
	198	65	-75
	220	65	-70
	200	66	-100
	200	65	-85
	205	74	-80
	195	65	-80
	255	54	-65
	185	65	-85
	205	65	-75
	210	75	-90
	192	65	-75
	185	85	-85
	190	66	-80
	190	74	-80
	190	67	-90
	183	70	-90
	190	63	-90
	214	75	-80
	190	64	-80
	210	61	-75
	190	65	-75
	210	75	-76
	195	72	-75
	190	68	-70
	190	65	-80
	185	68	-80
	186	65	-75
	200	78	-75
	198	80	-90
	198	72	-75
	200	78	-75
	210	72	-70
	210	68	-70
	190	66	-75
	185	70	-85
	190	68	-83
	198	60	-75
	200	60	-70
	185	55	-90
	205	60	-85
	204	55	-80
	210	65	-85
	210	62	-60
	190	62	-80
	188	72	-88
	55	80	-90
	200	74	-80
	197	70	-74
	200	72	-75
	202	73	-80
	204	73	-80
	202	74	-60
	190	70	-70
	195	70	-62

Outcrop 2

	Dip-dir	Dip	Rake
set ENE - WSW	160	82	-88
	320	68	-80
	355	45	-95
	345	60	-90
	330	85	-90
	345	40	-90
	315	80	-90
	165	85	-85
	155	80	-85
	150	82	-90
	154	82	-90
	162	80	-90
	175	82	-90
	180	90	-70
	165	84	-90
	175	80	-90
	155	82	-90
	180	84	-85
	355	70	-90
	346	86	-80
	145	80	-100
	165	86	-90
	345	56	-110
	334	80	-115
	180	85	-80
	340	65	-115
	156	80	-85
	330	68	-110
set WNW - ESE	187	90	-70
	5	78	-90
	2	82	-82
	5	80	-90
	20	72	-90
	10	64	-95
	5	70	-85
	15	75	-90
	15	75	-80
	45	60	-90
	210	55	-90
	15	55	-90
	20	85	-80
	5	68	-90
	2	65	-90
	15	80	-90
	12	80	-80
	0	80	-90
	5	80	-90
	25	83	-90
	10	78	-90
	5	85	-90
	8	85	-90
	18	75	-90
	6	75	-90
	5	60	-105
	8	65	-100
	2	80	-100
	45	60	-90
	185	74	-80
	190	85	-90
	195	86	-85
	30	80	-70
	195	85	-105
	187	90	-90

Outcrop 5

	Dip-dir	Dip	Rake
set ENE - WSW	355	75	-85
	175	65	-85
	175	65	-85
	155	80	-110
	339	85	-60
	333	78	-80
	350	80	-60
	330	58	-90
	325	58	-90
	165	80	-90
	160	83	-90
	145	82	-100
	155	82	-100
	150	85	-90
	150	80	-90
	155	85	-90
	167	88	-100
	340	65	-85
	155	75	-90
	180	85	-75
set WNW - ESE	185	80	-95

Outcrop 7

	Dip-dir	Dip	Rake
	152	60	-40
	155	55	-55
	160	55	-65
	310	75	-75
	110	80	-70
	152	52	-75
	152	54	-80
	138	55	-70
	135	52	-90
	130	54	-90
	145	50	-90
	10	90	-10
	128	80	-25
	160	65	-20
	120	90	-35
	10	88	-40
	10	80	-40
	5	85	-35
	350	85	-40
	35	90	-25
	260	80	0

Outcrop 6

	Dip-dir	Dip	Rake
set ENE - WSW	145	80	-130
	149	68	-135
	330	80	-45
	155	62	-130
	160	68	-130
	161	65	-140
	145	75	-135
	135	72	-145
	138	68	-150
	140	82	-150
	137	80	-160
	135	90	-165
	160	65	-130
	138	75	-155
	135	80	-155
	155	63	-135
	152	70	-140
	136	80	-140
	137	80	-135
	135	85	-140
	130	88	-145
	130	85	-150
	131	75	-140
	134	75	-145
	134	75	-140
	310	84	-30
	320	74	-35
	308	80	-30
	165	65	-130
	160	66	-130
	130	90	-145

Outcrop 8

	Dip-dir	Dip	Rake
set ENE - WSW veins	168	65	-100
	160	70	-100
	340	80	-140
	335	80	-150
	172	72	-96
	172	73	-101
	165	70	-88
	160	80	-92
	355	70	-64
set WNW - ESE veins	15	80	-80
	25	55	-80
	200	70	-80
	183	69	-90
	15	85	-88
	5	85	-90
	20	88	-90
	10	80	-87
	20	72	-83
	25	80	-85
	5	80	-87
	10	70	-92

Outcrop 9

	Dip-dir	Dip	Rake
set ENE - WSW	175	86	-90
	155	85	-90
	170	88	-90
	154	78	-88
	172	76	-85
	150	85	-80
	150	80	-82
	150	75	-82
	158	85	-88
	174	84	-72
	335	45	-90
	350	50	-90
	347	40	-100
	350	60	-90
	346	60	-100
	355	65	-90
	174	80	-95
	164	80	-95
	350	70	-110
	350	75	-100
	174	55	-95
	174	60	-100
	178	75	-105
set WNW-ESE	180	85	-90
	185	88	-87
	185	84	-75
	182	84	-82
	32	75	-95
	25	70	-90
	25	70	-105
	15	75	-95
	30	75	-95
	188	90	-110
	180	90	-112

Outcrop 10

	Dip-dir	Dip	Rake
set ENE - WSW	123	74	-112
	125	74	-120
	324	58	-90
	160	75	-110
	155	75	-110
	168	75	-90
	143	65	-85
	140	60	-90
	176	75	-80
	180	76	-90
	155	60	-75
	128	80	-120
set WNW-ESE	195	66	-70
	194	66	-70

Outcrop 11

	Dip-dir	Dip	Rake
set ENE - WSW	137	65	-120
	140	50	-95
	320	85	-85
	305	65	-80
	340	80	-90
	325	70	-85
	320	65	-80
	326	60	-65
	320	60	-90
	310	60	-90
	340	75	-80
	295	65	-75
	322	82	-85
	315	55	-90
shear fractures	95	60	-90
	260	65	-85
	240	65	-84
	274	80	-75
	275	80	-80
	285	60	-90
	264	65	-64
	300	65	-70
	285	75	-65
	270	65	-95
	285	80	-80
	280	80	-90

Outcrop 13

	Dip-dir	Dip	Rake
set ENE - WSW	179	80	-92
	140	75	-95
	148	80	-110
	144	75	-110
	140	73	-110
	152	74	-105
	150	72	-100
	115	80	-100
	115	86	-110
	117	82	-100
	144	82	-110
	136	78	-100
	148	70	-110
	140	78	-105
	155	70	-98
	178	65	-90
	165	64	-72
set WNW-ESE	188	65	-85
	183	65	-85
	190	65	-100
	185	65	-78
	204	75	-70
	197	65	-80
	188	65	-70
	218	65	-65
	185	63	-82

Outcrop 14

	Dip-dir	Dip	Rake
set ENE - WSW	160	60	-75
	152	80	-75
	155	60	-75
	135	85	-90
	162	85	-88
	154	85	-85
	128	85	-90
	135	78	-90
	128	85	-90
	120	85	-90
	130	85	-85
	135	80	-90
	160	75	-75
	160	80	-75
	160	78	-77
	158	75	-77

Supplementary materials of Chapter 2

Table S1: This table contains joint attitude data used to build Lower hemisphere equal-area plots and density contour of poles of Figure 7

Joints							
set ENE - WSW		**set WNW - ESE**		**set N-S**		**set NE - SW**	
Dip	Dip dir.	Dip	Dip dir.	Dip	Dip dir.	Dip	Dip dir.
60	350	90	190	68	280	85	130
60	335	72	20	70	285	90	298
65	150	70	20	65	120	60	310
75	350	55	205	85	285	73	315
65	168	90	20	58	275	90	125
60	354	60	185	75	270	80	315
65	350	70	185	60	90	88	142
90	330	60	185	74	75	58	320
45	358	65	7	68	85	55	125
62	0	90	30	85	95	67	315
70	350	55	15	75	80		
60	345	60	25	85	290		
60	345	70	30	77	85		
70	340	82	195	65	65		
72	355	65	205	73	290		
55	180	70	40	86	125		
65	355	75	15	60	310		
70	345	71	204	88	80		
75	170	65	215	66	85		
70	355	52	197	74	85		
65	170	85	205	74	75		
78	345	65	215	85	265		
62	340	90	15	75	110		
52	150	75	200	73	300		
68	350	60	45	71	90		
80	350	60	35	64	270		
87	345	55	25	68	60		
85	350	85	19	80	125		
75	350	80	20	90	270		
62	180	70	20	63	265		
70	162	55	35	73	265		
55	150	75	15	60	50		
65	170	70	15	70	90		
68	170	70	15	70	90		
68	350	55	5	75	70		
75	0	55	15	65	75		
55	345	82	20	70	260		
80	355	85	10	90	85		
50	0	80	25	60	290		
70	350	68	200	85	70		
82	355	80	35	82	80		
75	345	66	185	70	70		
64	165	82	10	74	85		
82	175	90	15	76	90		
78	160	85	5	65	300		
85	165	65	50	72	90		
78	170	70	15	65	270		
88	350	60	15	82	87		
75	175	72	5	85	245		
88	358	50	20	50	260		
55	170	70	200	80	72		
70	180	75	190	65	50		
85	180	76	35	78	270		
67	0	54	20	86	65		
85	355	82	25	58	55		
80	350	85	200	57	245		
86	350	58	195	90	80		
90	160	83	50	75	95		
86	180	67	25	60	95		
62	175	62	25	85	70		
90	340	78	35	62	265		
75	170	75	225	85	70		
65	165	80	205	76	276		
86	0	84	195	40	305		
70	170	74	10	55	115		
82	345	78	195	66	70		
		82	210	68	82		
		52	15				
		73	195				
		90	20				
		85	25				
		74	188				
		76	10				
		85	182				
		75	45				
		78	202				
		56	20				
		83	20				
		85	20				
		70	215				
		85	20				
		80	220				
		62	215				
		45	190				
		70	20				
		70	30				
		70	245				
		68	225				
		74	65				
		64	40				
		68	185				
		76	185				
		50	210				
		85	45				
		54	235				
		66	210				
		75	230				
		56	195				
		90	45				
		74	190				
		56	240				
		76	192				
		70	45				
		80	20				
		62	45				
		64	45				
		52	220				
		70	5				
		70	15				
		35	195				
		72	15				
		66	25				
		75	10				
		75	20				
		56	7				

Table S2: This table contains the position of the fractures along the scanlines used for the linear scanline analysis of Figure 8 and Figure 9

SET ENE-WSW
Fracture position along the scanline (m)
3.113594854
4.600590554
12.83914016
20.61850629
20.67736349
23.50786004
23.91694195
24.89513899
25.85047414
32.04361423
36.63885412
50.40073908
55.29026501
66.82384533
74.37070116
74.61196707
75.49579801
76.98911721
78.12102397
87.66221489
89.40604203
91.58716363
93.1972244
94.76885774
95.50822099
99.65108734
109.5420165
109.7292894
111.8238277
119.2879916
121.0439794
123.7280625
126.6957304
135.8122739
138.7770232
139.0883341
140.1039857
144.8539082
148.5254304
151.2542646
155.2687151
156.3067422
164.3828265
168.9984962
169.7432101
171.4661211
172.159274
174.699376
199.907285
217.3815519
222.3022089
223.1232912
225.0315294
228.4700549
228.5853372
229.2595198
229.4443606
233.1153965
234.7055139
235.1058402
236.4882549
238.5901017
242.878387
248.2957233
274.7733987
279.6614098
289.6183821
294.3912906
303.1255515
332.9294384
340.7357801
342.3892251
344.9512026
355.6015848
356.6664582
370.9534533
376.253297
382.7310351
385.0705797
387.9278229
389.0293575
390.2510844
392.0216383
393.8888473
396.0151503
396.7782042
402.5814099
403.6096419
407.362888
407.9549828
408.3596473
412.1582068
415.7922292
417.4309377
418.7004172
419.7322878
422.2423813
423.5868815
424.4150947
425.730945
425.7320014
427.8491366
429.0321137
430.0074838
432.9538071
434.4882461
434.8938759
435.995982
453.0680298
453.1805152
460.6351467
463.410506
463.4206589
468.2340478
479.1327385
493.4941543
498.762043
503.6244034
505.8945993
507.5998695
508.7687995
517.2986134
520.3874833
521.3759707
523.2196649
527.9672936
530.2335152
533.013845
533.3629138
548.3028037
556.2787122
557.8473757
559.8866145
562.2345164
562.7395394
563.1376945
563.8563345
570.8140887
573.7837996
575.5828804
576.6049719
576.641479
579.1015173
595.7576342
604.5793239
607.0839042
607.3485561
616.3403378
626.5163911
628.8995368
632.0109574
633.2673162
637.9200322
642.1807228
644.3975448
650.4786658
650.9368199
657.0391769
657.2651738
658.4156191
659.9864472
660.6187608
661.7884838
662.9970454
664.5749905
666.1430204
668.3979799
672.3798765
673.389905
674.8598711
677.3115158
683.9557048
688.2225778
691.8795839
696.4997926
697.6400143
698.1724362
699.6242202
707.3141204
709.1547947
710.6390627
720.7390627
723.1270627
723.6753627
727.0715627
733.3790627
734.4301627
734.8470627
736.6755627
744.8697627
748.9574627
752.5740627
783.3740627
791.4340627
799.1140627
825.1440627
827.3807627
829.4169627

SET WNW-ESE
Fracture position along the scanline (m)
0
9.737420536
10.08740255
20.24065246
21.91604559
26.67806348
29.48294425
32.74037369
35.87723516
38.0445288
39.60563357
40.4060712
51.40371561
55.88817572
62.33982013
63.28510699
65.88066813
66.77948607
77.54185532
82.08869241
86.23154313
88.4306535
122.1143424
161.6690244
163.1501691
164.1574144
165.8039212
169.2602041
169.319232
171.1503587
172.0353616
173.4913876
174.3403876
183.7832072
187.5003023
191.6485953
222.0811343
231.2471043
243.2663789
257.445845
257.9072235
259.1307972
276.1954847
280.5132141
284.7023466
300.0465976
302.6799805
306.0614379
309.942538
310.654056
313.6636231
327.0365918
329.40338
334.8082851
336.9468607
346.3131883
349.9887869
353.7369476
365.486846
366.6859339
367.3352309
375.1775267
377.3017653
381.9628796
385.3971991
386.5853712
413.9852558
424.1492142
424.4226258
424.8203907
434.2128992
434.664219
447.2678172
469.9771035
473.5496288
473.9755976
481.5588885
482.0423734
483.0239075
507.3522212
509.8403152
513.1357719
513.6948206
518.3608615

Table 1: The table contains data collected from the CDC database on TB_ cases in Egypt, UK

Country	2000			2001			2002		
	cases	population	rate	cases	population	rate	cases	population	rate
Afghanistan	2666	20595360	12.94	2728	21154031	12.90	2883	21629491	13.33
Albania	104	3173216	3.28	116	3192403	3.63	93	3204284	2.90
Algeria	3913	31287789	12.51	4034	31736053	12.71	4134	32129324	12.87
Andorra	18	66097	27.23	16	68874	23.23	10	71046	14.08
Angola	1294	16394062	7.89	1451	16917497	8.58	1698	17470850	9.72
Anguilla	0	8316	0.00	0	8316	0.00	0	8316	0.00
Antigua and Barbuda	0	66971	0.00	0	67448	0.00	0	67782	0.00
Argentina	1605	36260130	4.43	1600	36636175	4.37	1735	37031802	4.69
Armenia	272	3076200	8.84	249	3076200	8.10	230	3076200	7.48
Aruba	0	69539	0.00	0	70007	0.00	0	70474	0.00
Australia	1250	18886182	6.62	1220	19153394	6.37	1232	19413242	6.35
Austria	1109	8110496	13.67	1093	8169929	13.38	1148	8206524	13.99
Azerbaijan	1405	7798497	18.02	1403	7868385	17.83	1520	7911189	19.21
Bahamas	0	301483	0.00	0	307008	0.00	0	311036	0.00
Bahrain	0	656397	0.00	0	677886	0.00	0	698585	0.00
Bangladesh	58501	129193327	45.28	58501	131581243	44.46	58501	133376684	43.86
Barbados	0	268792	0.00	0	269352	0.00	0	269696	0.00
Belarus	1707	10045237	16.99	1707	10045237	16.99	1707	10045237	16.99
Belgium	1109	10239085	10.83	1093	10296350	10.62	1148	10311970	11.13
Belize	0	232111	0.00	0	239979	0.00	0	247884	0.00
Benin	1294	6394062	20.24	1451	6917497	20.98	1698	7470850	22.73
Bermuda	0	63925	0.00	0	64237	0.00	0	64600	0.00
Bhutan	0	2049412	0.00	0	2090162	0.00	0	2131232	0.00
Bolivia	1294	8394062	15.42	1451	8917497	16.27	1698	9470850	17.93
Bosnia and Herzegovina	104	3973216	2.62	116	3992403	2.91	93	4004284	2.32
Botswana	1294	1394062	92.83	1451	1417497	102.36	1698	1470850	115.45
Brazil	1605	176260130	0.91	1600	176636175	0.91	1735	177031802	0.98
British Virgin Islands	0	21730	0.00	0	22051	0.00	0	22374	0.00
Brunei Darussalam	0	328811	0.00	0	336376	0.00	0	343307	0.00
Bulgaria	1109	8110496	13.67	1093	8169929	13.38	1148	8206524	13.99
Burkina Faso	1294	11394062	11.36	1451	11917497	12.18	1698	12470850	13.62
Burundi	1294	6394062	20.24	1451	6917497	20.98	1698	7470850	22.73
Cambodia	1294	12394062	10.44	1451	12917497	11.23	1698	13470850	12.61
Cameroon	1294	14394062	8.99	1451	14917497	9.73	1698	15470850	10.98
Canada	1250	18886182	6.62	1220	19153394	6.37	1232	19413242	6.35
Cape Verde	0	429474	0.00	0	434625	0.00	0	439801	0.00
Cayman Islands	0	35674	0.00	0	36277	0.00	0	36910	0.00
Central African Republic	1294	3394062	38.13	1451	3917497	37.04	1698	4470850	37.99
Chad	1294	8394062	15.42	1451	8917497	16.27	1698	9470850	17.93
Chile	1605	15260130	10.52	1600	15636175	10.23	1735	16031802	10.82
China	1250	1268182	98.58	1220	1273394	95.82	1232	1277242	96.46
China, Hong Kong SAR	0	6782000	0.00	0	6855000	0.00	0	6928000	0.00
China, Macao SAR	0	441000	0.00	0	449000	0.00	0	457000	0.00
Colombia	1605	41260130	3.89	1600	41636175	3.84	1735	42031802	4.13
Comoros	0	549337	0.00	0	563920	0.00	0	578870	0.00
Congo	1294	3394062	38.13	1451	3917497	37.04	1698	4470850	37.99
Cook Islands	0	18027	0.00	0	18027	0.00	0	18027	0.00
Costa Rica	0	3773057	0.00	0	3834934	0.00	0	3896220	0.00
Croatia	104	4473216	2.33	116	4492403	2.58	93	4504284	2.06
Cuba	1294	11394062	11.36	1451	11917497	12.18	1698	12470850	13.62
Cyprus	0	715000	0.00	0	730000	0.00	0	745000	0.00
Czech Republic	1109	10239085	10.83	1093	10296350	10.62	1148	10311970	11.13
Democratic People's Republic of Korea	1294	22394062	5.78	1451	22917497	6.33	1698	23470850	7.24
Democratic Republic of the Congo	1294	51394062	2.52	1451	52917497	2.74	1698	54470850	3.12
Denmark	1109	5310496	20.88	1093	5369929	20.35	1148	5406524	21.23
Djibouti	1294	794062	162.98	1451	817497	177.50	1698	870850	195.00
Dominica	0	70786	0.00	0	71293	0.00	0	71808	0.00
Dominican Republic	1605	8260130	19.43	1600	8636175	18.53	1735	9031802	19.21
Ecuador	1605	12260130	13.09	1600	12636175	12.66	1735	13031802	13.31
Egypt	1605	68260130	2.35	1600	68636175	2.33	1735	69031802	2.51
El Salvador	1605	6260130	25.64	1600	6636175	24.11	1735	7031802	24.68
Equatorial Guinea	1294	494062	261.96	1451	517497	280.40	1698	570850	297.46
Eritrea	1294	4394062	29.45	1451	4917497	29.51	1698	5470850	31.04
Estonia	1109	1310496	84.64	1093	1369929	79.78	1148	1406524	81.63
Ethiopia	1294	74394062	1.74	1451	74917497	1.94	1698	75470850	2.25
Fiji	0	849000	0.00	0	856000	0.00	0	863000	0.00
Finland	1109	5210496	21.28	1093	5269929	20.74	1148	5306524	21.63
France	1109	60239085	1.84	1093	60296350	1.81	1148	60311970	1.90
French Guiana	0	156000	0.00	0	162000	0.00	0	168000	0.00
French Polynesia	0	235000	0.00	0	240000	0.00	0	245000	0.00
Gabon	1294	1394062	92.83	1451	1417497	102.36	1698	1470850	115.45
Gambia	1294	1394062	92.83	1451	1417497	102.36	1698	1470850	115.45
Georgia	1405	4798497	29.28	1403	4868385	28.82	1520	4911189	30.95
Germany	1109	82239085	1.35	1093	82296350	1.33	1148	82311970	1.39
Ghana	1294	19394062	6.67	1451	19917497	7.29	1698	20470850	8.30
Gibraltar	0	27714	0.00	0	27884	0.00	0	28033	0.00
Greece	1109	10910496	10.17	1093	10969929	9.96	1148	11006524	10.43
Grenada	0	89227	0.00	0	89828	0.00	0	90343	0.00
Guadeloupe	0	422000	0.00	0	426000	0.00	0	430000	0.00
Guam	0	154000	0.00	0	157000	0.00	0	160000	0.00
Guatemala	1605	11260130	14.25	1600	11636175	13.75	1735	12031802	14.42
Guinea	1294	8394062	15.42	1451	8917497	16.27	1698	9470850	17.93
Guinea-Bissau	1294	1394062	92.83	1451	1417497	102.36	1698	1470850	115.45
Guyana	0	765283	0.00	0	767245	0.00	0	769095	0.00
Haiti	1294	8394062	15.42	1451	8917497	16.27	1698	9470850	17.93
Honduras	1605	6260130	25.64	1600	6636175	24.11	1735	7031802	24.68
Hungary	1109	10239085	10.83	1093	10296350	10.62	1148	10311970	11.13
Iceland	1109	5210496	21.28	1093	5269929	20.74	1148	5306524	21.63
India	58501	129193327	45.28	58501	131581243	44.46	58501	133376684	43.86
Indonesia	1605	41260130	3.89	1600	41636175	3.84	1735	42031802	4.13
Iran (Islamic Republic of)	1605	68260130	2.35	1600	68636175	2.33	1735	69031802	2.51
Iraq	1605	24260130	6.62	1600	24636175	6.49	1735	25031802	6.93
Ireland	1109	3910496	28.36	1093	3969929	27.53	1148	4006524	28.66
Israel	1109	6310496	17.57	1093	6369929	17.16	1148	6406524	17.92
Italy	1109	57239085	1.94	1093	57296350	1.91	1148	57311970	2.00
Jamaica	0	2668000	0.00	0	2685000	0.00	0	2702000	0.00
Japan	1250	126886182	0.99	1220	127153394	0.96	1232	127413242	0.97
Jordan	1605	5260130	30.51	1600	5636175	28.39	1735	6031802	28.77
Kazakhstan	1405	14798497	9.49	1403	14868385	9.44	1520	14911189	10.19
Kenya	1294	31394062	4.12	1451	31917497	4.55	1698	32470850	5.23
Kiribati	0	94149	0.00	0	95835	0.00	0	97532	0.00
Kuwait	0	1656397	0.00	0	1677886	0.00	0	1698585	0.00
Kyrgyzstan	1405	4798497	29.28	1403	4868385	28.82	1520	4911189	30.95
Lao People's Democratic Republic	1294	12394062	10.44	1451	12917497	11.23	1698	13470850	12.61
Latvia	1109	1310496	84.64	1093	1369929	79.78	1148	1406524	81.63
Lebanon	1605	4260130	37.68	1600	4636175	34.51	1735	5031802	34.48
Lesotho	1294	1394062	92.83	1451	1417497	102.36	1698	1470850	115.45
Liberia	1294	2394062	54.05	1451	2917497	49.74	1698	3470850	48.93
Libyan Arab Jamahiriya	1605	5260130	30.51	1600	5636175	28.39	1735	6031802	28.77
Liechtenstein	1109	33496	331.08	1093	33929	322.17	1148	34524	332.57
Lithuania	1109	3310496	33.50	1093	3369929	32.44	1148	3406524	33.71
Luxembourg	1109	410496	270.16	1093	419929	260.30	1148	426524	269.17
Madagascar	1294	16394062	7.89	1451	16917497	8.58	1698	17470850	9.72
Malawi	1294	11394062	11.36	1451	11917497	12.18	1698	12470850	13.62
Malaysia	1605	24260130	6.62	1600	24636175	6.49	1735	25031802	6.93
Maldives	0	283000	0.00	0	290000	0.00	0	298000	0.00
Mali	1294	11394062	11.36	1451	11917497	12.18	1698	12470850	13.62
Malta	0	390000	0.00	0	395000	0.00	0	400000	0.00
Martinique	0	381000	0.00	0	385000	0.00	0	389000	0.00
Mauritania	1294	2794062	46.31	1451	3317497	43.74	1698	3870850	43.88
Mauritius	0	1170000	0.00	0	1180000	0.00	0	1190000	0.00
Mayotte	0	149000	0.00	0	155000	0.00	0	161000	0.00
Mexico	1605	98260130	1.63	1600	98636175	1.62	1735	99031802	1.75
Micronesia (Federated States of)	0	108000	0.00	0	109000	0.00	0	110000	0.00
Monaco	0	32000	0.00	0	32500	0.00	0	33000	0.00
Mongolia	1294	2394062	54.05	1451	2917497	49.74	1698	3470850	48.93
Montenegro	104	673216	15.45	116	692403	16.75	93	704284	13.21
Montserrat	0	4500	0.00	0	4500	0.00	0	4500	0.00
Morocco	1605	29260130	5.49	1600	29636175	5.40	1735	30031802	5.78
Mozambique	1294	17394062	7.44	1451	17917497	8.10	1698	18470850	9.19
Myanmar	1294	46394062	2.79	1451	46917497	3.09	1698	47470850	3.58
Namibia	1294	1794062	72.13	1451	1817497	79.83	1698	1870850	90.77
Nauru	0	12000	0.00	0	12000	0.00	0	12000	0.00
Nepal	1294	23394062	5.53	1451	23917497	6.07	1698	24470850	6.94
Netherlands	1109	16239085	6.83	1093	16296350	6.71	1148	16311970	7.04
Netherlands Antilles	0	217000	0.00	0	220000	0.00	0	223000	0.00
New Caledonia	0	215000	0.00	0	220000	0.00	0	225000	0.00
New Zealand	1250	3886182	32.17	1220	3953394	30.86	1232	4013242	30.70
Nicaragua	1605	5260130	30.51	1600	5636175	28.39	1735	6031802	28.77
Niger	1294	11394062	11.36	1451	11917497	12.18	1698	12470850	13.62
Nigeria	1294	123394062	1.05	1451	123917497	1.17	1698	124470850	1.36
Niue	0	2000	0.00	0	2000	0.00	0	2000	0.00
Northern Mariana Islands	0	69000	0.00	0	71000	0.00	0	73000	0.00
Norway	1109	4510496	24.59	1093	4569929	23.92	1148	4606524	24.93
Occupied Palestinian Territory	1605	3260130	49.24	1600	3636175	44.00	1735	4031802	43.05
Oman	0	2256397	0.00	0	2277886	0.00	0	2298585	0.00
Pakistan	1605	141260130	1.14	1600	141636175	1.13	1735	142031802	1.22
Palau	0	19000	0.00	0	19000	0.00	0	19000	0.00
Panama	0	2773057	0.00	0	2834934	0.00	0	2896220	0.00
Papua New Guinea	1294	5394062	23.99	1451	5917497	24.52	1698	6470850	26.24
Paraguay	1605	5260130	30.51	1600	5636175	28.39	1735	6031802	28.77
Peru	1605	27260130	5.89	1600	27636175	5.79	1735	28031802	6.19
Philippines	1605	76260130	2.11	1600	76636175	2.09	1735	77031802	2.25
Pitcairn	0	47	0.00	0	47	0.00	0	47	0.00
Poland	1109	38239085	2.90	1093	38296350	2.85	1148	38311970	2.99
Portugal	1109	10310496	10.76	1093	10369929	10.54	1148	10406524	11.03
Puerto Rico	0	3886000	0.00	0	3897000	0.00	0	3908000	0.00
Qatar	0	556397	0.00	0	577886	0.00	0	598585	0.00
Republic of Korea	1250	47886182	2.61	1220	48153394	2.53	1232	48413242	2.55
Republic of Moldova	1405	4198497	33.46	1403	4268385	32.87	1520	4311189	35.25
Reunion	0	743000	0.00	0	760000	0.00	0	776000	0.00
Romania	1109	22239085	4.99	1093	22296350	4.90	1148	22311970	5.15
Russian Federation	1405	146798497	0.96	1403	146868385	0.96	1520	146911189	1.03
Rwanda	1294	8394062	15.42	1451	8917497	16.27	1698	9470850	17.93
Saint Kitts and Nevis	0	38836	0.00	0	39129	0.00	0	39556	0.00
Saint Lucia	0	156260	0.00	0	157647	0.00	0	158951	0.00
Saint Vincent and the Grenadines	0	116394	0.00	0	117144	0.00	0	117848	0.00
Samoa	0	176908	0.00	0	178173	0.00	0	179316	0.00
San Marino	0	27000	0.00	0	27500	0.00	0	28000	0.00
Sao Tome and Principe	0	149000	0.00	0	155000	0.00	0	161000	0.00
Saudi Arabia	1605	20260130	7.92	1600	20636175	7.75	1735	21031802	8.25
Senegal	1294	10394062	12.45	1451	10917497	13.29	1698	11470850	14.81
Serbia	104	7473216	1.39	116	7492403	1.55	93	7504284	1.24
Seychelles	0	80000	0.00	0	82000	0.00	0	84000	0.00
Sierra Leone	1294	4394062	29.45	1451	4917497	29.51	1698	5470850	31.04
Singapore	1250	4886182	25.58	1220	4953394	24.63	1232	5013242	24.58
Slovakia	1109	5410496	20.50	1093	5469929	19.98	1148	5506524	20.85
Slovenia	1109	1910496	58.04	1093	1969929	55.49	1148	2006524	57.22
Solomon Islands	0	409042	0.00	0	419178	0.00	0	429558	0.00
Somalia	1294	8394062	15.42	1451	8917497	16.27	1698	9470850	17.93
South Africa	1294	44394062	2.92	1451	44917497	3.23	1698	45470850	3.73
Spain	1109	40239085	2.76	1093	40296350	2.71	1148	40311970	2.85
Sri Lanka	1294	19394062	6.67	1451	19917497	7.29	1698	20470850	8.30
Sudan	1294	34394062	3.76	1451	34917497	4.16	1698	35470850	4.79
Suriname	0	415000	0.00	0	417000	0.00	0	419000	0.00
Swaziland	1294	1394062	92.83	1451	1417497	102.36	1698	1470850	115.45
Sweden	1109	8910496	12.44	1093	8969929	12.18	1148	9006524	12.75
Switzerland	1109	7210496	15.38	1093	7269929	15.03	1148	7306524	15.71
Syrian Arab Republic	1605	16260130	9.87	1600	16636175	9.62	1735	17031802	10.19
Tajikistan	1405	6198497	22.67	1403	6268385	22.38	1520	6311189	24.08
Thailand	1605	62260130	2.58	1600	62636175	2.55	1735	63031802	2.75
The former Yugoslav Republic of Macedonia	104	2073216	5.02	116	2092403	5.54	93	2104284	4.42
Timor-Leste	0	849000	0.00	0	856000	0.00	0	863000	0.00
Togo	1294	5394062	23.99	1451	5917497	24.52	1698	6470850	26.24
Tokelau	0	1500	0.00	0	1500	0.00	0	1500	0.00
Tonga	0	98000	0.00	0	99000	0.00	0	100000	0.00
Trinidad and Tobago	0	1268792	0.00	0	1269352	0.00	0	1269696	0.00
Tunisia	1605	9260130	17.33	1600	9636175	16.60	1735	10031802	17.30
Turkey	1605	65260130	2.46	1600	65636175	2.44	1735	66031802	2.63
Turkmenistan	1405	4798497	29.28	1403	4868385	28.82	1520	4911189	30.95
Turks and Caicos Islands	0	18122	0.00	0	18451	0.00	0	18780	0.00
Tuvalu	0	9000	0.00	0	9000	0.00	0	9000	0.00
Uganda	1294	23394062	5.53	1451	23917497	6.07	1698	24470850	6.94
Ukraine	1405	49798497	2.82	1403	49868385	2.81	1520	49911189	3.05
United Arab Emirates	0	3256397	0.00	0	3277886	0.00	0	3298585	0.00
United Kingdom	1109	59910496	1.85	1093	59969929	1.82	1148	60006524	1.91
United Republic of Tanzania	1294	34394062	3.76	1451	34917497	4.16	1698	35470850	4.79
United States of America	1250	282886182	0.44	1220	283153394	0.43	1232	283413242	0.43
United States Virgin Islands	0	108000	0.00	0	109000	0.00	0	110000	0.00
Uruguay	1605	3260130	49.24	1600	3636175	44.00	1735	4031802	43.05
Uzbekistan	1405	25798497	5.45	1403	25868385	5.42	1520	25911189	5.87
Vanuatu	0	189000	0.00	0	196000	0.00	0	203000	0.00
Venezuela (Bolivarian Republic of)	1605	24260130	6.62	1600	24636175	6.49	1735	25031802	6.93
Viet Nam	1605	78260130	2.05	1600	78636175	2.03	1735	79031802	2.19
Wallis and Futuna Islands	0	15000	0.00	0	15000	0.00	0	15000	0.00
Western Sahara	1294	394062	328.45	1451	417497	347.60	1698	470850	360.62
Yemen	1605	19260130	8.33	1600	19636175	8.15	1735	20031802	8.66
Zambia	1294	11394062	11.36	1451	11917497	12.18	1698	12470850	13.62
Zimbabwe	1294	13394062	9.66	1451	13917497	10.43	1698	14470850	11.74

Table S4: This table contains data used for the REV analysis of P_{21} shown in Figure 10

	Set ENE-WSW							
	P21							
scanarea side	5 meters	10 meters	15 meters	20 meters	25 meters	30 meters	35 meters	40 meters
	0.650852025	0.50859499	0.330444992	0.377240002	0.225354001	0.244	0.276438	0.223144
	0.261601001	0.369733989	0.233563006	0.28501001	0.335043013	0.26	0.0997363	0.156449
	0.100536004	0.345090985	0.470111012	0.241647005	0.225612998	0.09	0.247302	0.275252
	0	0.513719976	0.391983002	0.156636998	0.098223798	0.078	0.295237	0.303944
	0	0.517036974	0.240033001	0.158978	0.080035001	0.1818	0.298909	0.11229
	0	0.357849002	0.28698501	0.204823002	0.209395006	0.229	0.0363239	0.104204
	0	0.526067019	0.419834971	0.265009999	0.278724998	0.33	0.0808011	0.16411
	0	0.251641989	0.269612998	0.123976998	0.260096014	0.096	0.187083	0.107045
	0.068650797	0.151077002	0.086070701	0.277727991	0.270211011	0.25	0.135287	0.152235
	0.250247985	0.211270005	0.205694005	0.134675995	0.361990005	0.128	0.130809	0.179739
	0.243146002	0.185651004	0.073337302	0.144452006	0.212371007	0.288	0.20391	0.130785
	0.203984007	0.075133801	0.061477799	0.085420199	0.055617299	0.2665	0.184169	0.282603
	0.266761988	0.463977009	0.278210998	0.175812006	0.036582701	0.0451	0.194394	
	0.260138005	0.333362013	0.324169993	0.250744998	0.252512008	0.124	0.174038	
	0.027925599	0.321700007	0.238731995	0.083354503	0.116623998	0.231	0.317993	
	0	0.420531988	0.228559017	0.118702002	0.156844005	0.1811		
	0	0.422381997	0.316211998	0.184829995	0.184088007	0.2676		
	0.588883996	0.189800993	0.142303005	0.301012009	0.264025986	0.2517		
	0.935104012	0.201243997	0.101152003	0.074045204	0.175456002	0.3838		
	0.652148008	0.238569006	0.317496985	0.054111499	0.321669012	0.1016		
	0.416132003	0.115836002	0.31468299	0.124168999	0.234689996			
	0.53590399	0.0527847	0.200724006	0.146926999	0.315436989			
	0.595203996	0.080333799	0.157529995	0.070479997	0.281098008			
	0.75723201	0.241118997	0.070738703	0.186832994				
	0.605971992	0.200865999	0.078815997	0.244813994				
	0.550167978	0.104262002	0.095866702	0.29183501				
	0.203477994	0.186695993	0.0288237	0.345324993				
	0.203477994	0.135727003	0.191723004	0.254330009				
	0.236149997	0.100749001	0.277139008	0.327093005				
	0.591216028	0.146567002	0.110522993	0.320147991				
	0.076437198	0.0105521	0.142349005	0.178975001				
	0.087474003	0.138732001	0.146863997	0.281695008				
	0.267885	0.249864995	0.110399999	0.32436201				
	0.200798005	0.200950995	0.103817999	0.022127099				
	0	0.217497006	0.216215998	0.080275498				
	0.238912001	0.310488999	0.130899996	0.014009				
	0.988784015	0.283288985	0.229811996	0.164580002				
	0.884404004	0.200845003	0.34709096	0.308993012				
	1.019619942	0.194518998	0.190724999	0.258347005				
	0.561164021	0.173911005	0.218551993	0.148643002				
	0.401547998	0.161241993	0.00713756					
	0.417483985	0.523499012	0.0188438					
	0.567683995	0.38646999	0.025493801					
	0.229912996	0.295006007	0.065882698					
	0.397635013	0.188111007	0.060649797					
	0.186003998	0.233294994	0					
	0.405712008	0.145266995	0.0504147					
	0.798367977	0.090810999	0.251525998					
	0.838919997	0.070006996	0.251935005					
	0.637463987	0.120109998	0.269495994					
	0.213630006	0.174621999	0.282054991					
	0.201223001	0.163301006	0.216554016					
	0.304188997	0.116242997	0.28283					
	0.186934993	0.175336003	0.350701004					
	0.018975999	0.296059996	0.211068004					
	0.216527	0.415600002	0.323478997					
	0.223185003	0.289842993	0.341013968					
	0.280631006	0.200112998	0.268748999					
	0.056596	0.173112005	0.31161201					
	0.154466003	0.232354	0.400005013					
	0.243925005	0.138476998	0.213360995					

Set WNW-ESE							
P21							
5 meters	10 meters	15 meters	20 meters	25 meters	30 meters	35 meters	40 meters
0.26263	0.21802	0.286163	0.328877	0.115636	0.201	0.183149	0.215158
0.22957	0.124018	0.1223	0.085946	0.240133	0.132	0.167428	0.193262
0.140862	0.3972	0.104349	0.385145	0.177325	0.259	0.189044	0.094356
0.638216	0.0851028	0.26379	0.251262	0.20172299	0.1944	0.08343	0.122303
0.183342	0.269842	0.125298	0.336632	0.284771	0.07	0.064611	0.270734
0.0969536	0.369307	0.089376	0.369652	0.272187	0.208	0.321736	0.199622
0	0.0618602	0.366194	0.184541	0.165618	0.142	0.22047	0.118278
0.58278	0.0354017	0.379884	0.223051	0.150007	0.318	0.137491	0.096031
0.485168	0.0061272	0.0976978	0.157343	0.0956013	0.136	0.122685	0.173354
0.224831	0.240391	0.301489	0.0904935	0.0869323	0.0939	0.110909	0.125377
0.277437	0.129349	0.249659	0.0862355	0.0834046	0.372	0.193127	0.264754
5.80E-05	0.0352126	0.384782	0.309827	0.134211	0.124	0.135147	0.119299
0.457556	0.330644	0.409128	0.124569	0.121377	0.214	0.198739	0.106426
0.699864	0.188169	0.373703	0.08742	0.39109099	0.169	0.313808	0.206223
0.158502	0.328983	0.327285	0.0762253	0.14709599	0.156	0.132016	
0.12143	0.589002	0.112365	0.202187	0.076016	0.289	0.129382	
0.0404856	0.306151	0.116613	0.233545	0.166032	0.1	0.105393	
0.047634	0.526999	0.129306	0.0973882	0.222574	0.1	0.200438	
0.188916	0.0705885	0.0757978	0.103401	0.17771	0.0409		
0.050228	0.101286	0.369904	0.0778258	0.13572399	0.131		
0.381274	0.463813	0.165484	0.140374	0.122315	0.08		
0.510504	0.13106	0.265891	0.129949	0.0972806	0.205		
0.238663	0.148419	0.127002	0.125905	0.105254	0.325		
0.120841	0.183132	0.205798	0.127699	0.129535			
0	0.353734	0.0145885	0.0611573	0.138063			
0	0.367346	0.119234	0.153137	0.132514			
0.061698	0.300689	0.0662947	0.052724	0.0325397			
0.341563	0.510605	0.276403	0.0797027	0.13944399			
0.5216	0.229788	0.187677	0.160532	0.237771			
0.642544	0.478853	0.218209	0.152029	0.18753099			
0.347979	0.321404	0.141399	0.110303	0.144517			
0.324781	0.314824	0.359389	0.124403	0.190134			
0.0816784	0.363566	0.145493	0.206534	0.361424			
0.197035	0.21134	0.0794489	0.144833	0.174992			
0	0.256627	0.162606	0.185867	0.0855957			
0.216073	0.264588	0.0533804	0.248818	0.25029901			
0.211263	0.364067	0.0400712	0.0224883	0.103738			
0.275572	0.151082	0.156816	0.0575595				
0.0399227	0.0465911	0.175273	0.234376				
0.139058	0.145792	0.0748773	0.101588				
0.0781872	0.165128	0.140606	0.430575				
0.169151	0.122321	0.132095	0.0224756				
0	0.121217	0.136864	0.153579				
0	0.206319	0.0534729	0.133125				
0	0.139565	0.189662	0.153073				
0	0.121873	0.062972	0.091771				
0	0.0108932	0.177204	0.0659005				
0	0.588699	0.0231813	0.0713293				
0.141607	0.394913	0.156	0.168652				
0.3856	0.226953	0.168926	0.111858				
0	0.106393	0.0683969	0.323577				
0.0245086	0.308914	0.0791156	0.111906				
0.145632	0.308588	0.103051	0.0588585				
0.177697	0.182083	0.158169	0.210308				
0.0150367	0.351335	0.193844	0.298535				
0	0.1529	0.0832964	0.27183				
0	0.0560623	0.138771	0.153618				
0.27815	0.0017416	0.0565813	0.267192				
0.360069	0.154033	0.215356	0.170424				
0.192457	0.268895	0.221126	0.210355				
0.309894	0.0249949	0.214976	0.231444				

Set N-S							
P21							
5 meters	10 meters	15 meters	20 meters	25 meters	30 meters	35 meters	40 meters
0.039987	0.043067	0.019141	0.08692	0.0374	0.031226	0.033472	0.037037
0.113751	0.073412	0.054261	0.120678	0.0175	0.026161	0.044954	0.027176
0	0.071874	0.02928	0.06115	0.0588	0.013714	0.051386	0.092626
0	0.004002	0.162888	0.095169	0.047	0.070486	0.091571	0.070122
0	0.057194	0.031574	0.025281	0.0161	0.008073	0.074574	0.045169
0	0.094794	0.024992	0.05939	0.034	0.06339	0.039025	0.049873
0	0.173589	0.181687	0.070976	0.0793	0.102562	0.069132	0.10477
0	0.170059	0.070913	0.076929	0.114	0.066313	0.065834	0.069906
0	0	0.018341	0.267447	0.051	0.0745	0.081568	0.077079
0.044682	0.004585	0.07487	0.056019	0.112	0.025678	0.090906	0.14339
0	0.021888	0.123056	0.186964	0.0418	0.071039	0.091241	0.038536
0.032757	0.171342	0.038234	0.053845	0.0806	0.097611	0.147199	0.044567
0.043675	0.070188	0	0.13649	0.0592	0.042691	0.159633	0.09472
0.128157	0.137631	0.040098	0.111892	0.056	0.128622	0.056143	0.147355
0.061156	0.079702	0.048617	0.174532	0.14	0.108029	0.056355	
0	0	0.044212	0.14638	0.0383	0.137878	0.102226	
0.127625	0.235973	0.088168	0.163755	0.128	0.138313	0.113741	
0	0	0.077275	0.053448	0.0721	0.070245	0.040926	
0.106389	0.008636	0.308743	0.05596	0.1355	0.079999		
0.110868	0.103504	0.172161	0.079375	0.04	0.070365		
0.066584	0.08546	0.157672	0.032668	0.033	0.064997		
0.031639	0.105282	0.140796	0.090243	0.14	0.105321		
0.076252	0.100263	0.185914	0.095811	0.075	0.147946		
0	0.06935	0.045549	0.106289	0.076	0.165712		
0.069666	0.11822	0.235438	0.057345	0.0091	0.103207		
0	0.159061	0.136499	0.148588	0.12			
0.015967	0.026134	0.091524	0.043261	0.155			
0	0.064775	0.083125	0.047628	0.187			
0	0	0.05966	0.085819	0.111			
0.161067	0.021149	0.203396	0.069837	0.173			
0.099842	0.015197	0.040652	0.082076	0.064			
0.146342	0.015626	0.134662	0.03722	0.119			
0	0.018303	0.13074	0.062866				
0	0.039387	0.261148	0.150426				
0	0.048248	0.135652	0.024846				
0.039584	0.071057	0.158552	0.043235				
0.028053	0.094995	0.127849	0.122231				
0	0.010126	0.069064	0.104557				
0.133024	0.032136	0.057757	0.080737				
0	0.058318	0.088695	0.118331				
0	0.052414	0.030692	0.096417				
0.210889	0.075027	0.025042	0.108209				
0.483352	0.118478	0.103277	0.040955				
0.137545	0.145331	0.003242	0.025305				
0.278924	0.098179	0.038131	0.041155				
0	0.121507	0.147266	0.012618				
0	0.373771	0.161154	0.025688				
0	0.218817	0.062102	0.043333				
0.110784	0.263099	0.077012	0.025563				
0.152895	0.214172	0.095437	0.078206				
0.11377	0.118548	0.052133	0.069558				
0	0.124788	0.023886	0.048987				
0	0.1461	0.119638	0				
0	0.092631	0.069711					
0.018337	0.160453	0.069953					
0.085177	0.123698	0.047115					
0.132165	0	0.041125					
0	0.326307	0.073162					
0	0.215176	0					
0	0.231587	0.143492					
0	0.143656	0.041598					

Table S5: This table contains data used for the REV analysis of the n'_c parameter shown in Figure 10

	n'_c						
scanarea side	10 meters	15 meters	20 meters	25 meters	30 meters	35 meters	40 meters
	1	0.56	0.6206897	0.55384615	0.576471	0.626582	0.533937
	0.5	0.48	0.573913	0.54961832	0.66383	0.704433	0.59366
	0.5454545	0.66666667	0.5287356	0.57142857	0.671329	0.668942	0.625
	0.8571429	0.48	0.5103448	0.56521739	0.723735	0.541667	0.6357
	0.5555556	0.87272727	0.6593407	0.73170732	0.644068	0.60076	0.532751
	0.5333333	0.27272727	0.4861111	0.66666667	0.689076	0.433333	0.512535
	0.2222222	0.6875	0.4642857	0.67045455	0.573248	0.567416	0.395349
	0.7	0.66666667	0.7727273	0.6163522	0.556338	0.593137	0.498915
	0.75	0.44444444	0.6086957	0.55474453	0.454545	0.619718	0.552846
	0.5714286	0.5	0.6666667	0.72619048	0.428571	0.543807	0.558824
	0.8	0.78899083	0.4	0.63803681	0.598837	0.664384	0.467532
	0.6285714	0.66666667	0.5	0.56953642	0.612676	0.494382	
	0.4210526	0.63636364	0.6304348	0.42168675	0.581818		
	0.9142857	0.55882353	0.745098	0.48648649	0.646914		
	0	0.27272727	0.5098039	0.32352941	0.531561		
	0.8	0.82352941	0.7333333	0.59349594			
	0.5	0.72527473	0.5128205	0.64545455			
	0.6486486	0.73469388	0.5967742	0.60606061			
	0.6382979	0.5945946	0.5714286	0.54298643			
	0.8947368	0.64285714	0.7596899	0.64646465			
	0.4444444	0.2962963	0.5849057	0.57324841			
	0	0.70866142	0.5309735	0.44660194			
	0.6285714	0	0.3076923				
	0.4444444	0.72	0.2692308				
	0.5454545	0.62857143	0.3571429				
	0.5714286	0.5625	0.6411483				
	0.5625	0.71232877	0.6900585				
	0.5714286	0.79411765	0.5806452				
	0.875	0.51724138	0.4347826				
	0.75	0.56410256	0.4791667				
	0.9113924	0.21621622					
	0.6111111	0.72131148					
	0.7777778	0.44776119					
	0	0.34782609					
	0.6086957	0.375					
	0.4	0.68181818					
	0.4	0.16666667					
	0.5	0					
	0.9206349	0.35					
	0.7906977	0.42857143					
	0.6666667	0.65116279					
	0.8181818	0.61904762					
	0.8235294	0.36923077					
	0.4166667	0.68571429					
	0.8947368	0.60344828					
	0.25	0.5					
	0.4	0.52525253					
	0.4545455	0.57894737					
	0.4444444	0.47761194					
	0.2	0.62135922					
	0.8253968	0.66666667					
	0	0.62222222					
	0.5294118	0.53097345					
	0.7111111	0.55555556					
	0.75	0.67924528					
	0.4375	0.19354839					
	0.7755102	0.83333333					
	0.9090909						
	0.744186						
	0.8888889						
	0.48						
	0.5714286						
	0.7083333						
	0.3076923						
	0.6923077						
	0.6315789						
	0.6875						
	0.2727273						
	0						
	0.4						
	0.7						
	0.8717949						
	0.125						
	0.6341463						
	0.5454545						
	0.3243243						
	0.6428571						
	0.4705882						
	0.3846154						
	0.6666667						
	0.25						
	0.7272727						
	0.2142857						
	0.1578947						
	0.1176471						
	0.125						
	0.75						
	0						
	0.4444444						
	0.7586207						
	0						
	1						
	0.4705882						
	0.7142857						
	0						
	0.7317073						
	0						
	0.5						
	0.3703704						
	0						
	0.4242424						
	0.6666667						
	0.6956522						
	0.5416667						
	0.6153846						
	0.4390244						
	0.4516129						
	0.3076923						
	0.625						
	0.6382979						
	0.6666667						
	0.6440678						
	0.8085106						
	0.48						
	0.2142857						
	0.6101695						
	0.5882353						
	0.6666667						
	0.6037736						
	0.25						
	0.4137931						
	0.5238095						
	0.4285714						
	0.8076923						
	0.6086957						
	0.5517241						
	0.5416667						
	0.8125						
	0.3703704						
	0.6436782						
	0.5						
	0						
	0.5263158						
	0.490566						
	0.5806452						
	0.5581395						
	0.5789474						
	0.6428571						
	0.4						
	0.1290323						

Table S6: In these tables we reported the fracture length used to build the boxplots of Figure 11. Fracture length are in meters and scanarea number start from the fault zone.

Set ENE-WSW

scanarea 1

Length	Truncated
68.68845	1
2.359654	0
26.61939	1
10.01018	1
30.04795	0
35.71066	0
29.57146	0
7.319311	0
23.85279	0
23.85279	0
26.35063	1
1.862724	0
2.383388	0
3.389925	0
6.398585	0
3.444379	0
2.286709	0
4.921636	1
1.484159	0
9.957717	0
11.50436	0
5.202213	0
3.109535	1
4.289603	1
3.82503	1
6.975873	0
1.884137	0
3.852342	0
3.762737	0
11.22982	0
14.48075	0
2.583812	0
11.41458	0
3.984467	0
10.9209	0
2.589361	0
4.415741	0
21.88211	0
4.143307	0
62.46406	2
23.30275	1
8.097726	0
2.709192	0
1.93352	0
2.036588	0
2.96351	0
1.206174	0
2.800991	0
0.50888	0
5.789699	0
0.763489	0
3.407532	0
3.631219	0
2.21348	0
3.929439	0
5.305558	0
2.7287	0
3.832628	0
4.02926	0
2.345185	1
1.559377	0
7.541129	0
8.35002	0
11.51901	0
26.60572	0
21.21036	0
6.586286	0
2.520684	0
1.261427	0
1.497049	0
7.824903	0
4.596868	0
5.112464	1
9.100798	0
12.08421	0
2.971311	0
25.89694	1
9.588758	1
0.061211	2
0.061211	0
11.24867	0
7.749007	0
1.626141	0
5.497095	0
5.179945	1
68.68845	1
2.359638	1
26.61939	0
10.01018	1
30.04795	0
35.71066	0
29.57146	0
7.319311	0
23.85278	0
23.85278	1
26.35063	0
1.862724	0
2.383388	0
3.389925	0
6.398585	0
3.444365	0
2.286709	1
4.921636	0
3.984467	0
10.9209	0
2.589361	0
4.415741	0
21.88211	0
4.143307	1
62.46406	1
23.30275	0
8.349869	0
11.51901	0
26.60572	0
21.21036	0
6.586286	0
2.520684	0
1.261427	0
1.497049	0
7.824903	0
4.596868	0
5.112449	1
9.100798	0
12.08421	0
2.971311	0
25.89694	1
9.588743	1
0.061211	1
11.24867	0
7.749007	0
1.626141	0
5.497095	0
5.179945	1

scanarea 2

Length	Truncated
9.019599	1
0.213353	0
24.30509	0
0.045411	0
26.7137	1
44.86748	1
52.52038	1
19.21315	0
40.29272	1
50.44839	1
13.09938	1
13.09938	1
0.064935	0
25.19893	1
17.77224	1
17.75383	0
2.710521	0
9.621907	1
22.43728	1
7.134308	1
7.455781	1
7.455781	0
8.271771	0
11.3776	1
0.101757	1
2.480057	0
3.057356	0
7.162775	0
6.816155	1
3.190052	1
1.290923	0
16.04009	0
2.108749	0
1.852573	0
1.779624	0
11.18177	0
14.78991	1
3.621717	1
1.944832	0
1.211511	0
1.196985	0
2.116361	0
17.63449	0
11.38047	0
3.069627	0
1.457188	0
6.290433	0
17.25455	1
5.050296	0
9.725751	0
4.379523	0
3.092638	0
2.58452	0
10.95233	0
19.46032	1
6.488626	0
5.862912	0
8.18867	0
10.42881	0
6.74931	1
3.102924	0
4.393527	1
3.038323	0
6.320692	0
3.09413	1
20.44101	1
37.36462	0

scanarea 3

Length	Truncated
24.91015	1
1.063468	0
2.321189	1
30.67439	1
4.377189	1
10.89212	1
2.019053	1
24.45302	1
4.0566	1
6.878119	1
8.894842	1
11.36892	0
8.250616	1
32.91722	1
2.882947	1
1.558816	1
32.87788	1
10.51757	0
17.36992	1
4.123537	0
17.48698	0
20.05813	1
4.385436	0
17.80075	1
5.594864	0
5.594864	0
18.53632	0
9.017538	0
3.972942	0
17.5801	1
4.767124	0
6.861715	0
0.407562	1
3.129755	0
1.557572	0
2.029627	1
3.058193	0
3.303937	0
2.238452	0
1.554035	0
3.766922	1
0.061213	0
6.709044	0
3.71284	0
3.235329	0
2.035225	1
1.220882	0
3.315615	1
1.203608	1
10.54065	0
4.006303	1
0.162087	1
0.162087	0
5.479706	1
1.064086	0
1.933613	0
0.943058	1
33.08389	1
4.89726	0
1.661621	1
33.14854	1
7.301929	0
0.320348	0
12.71687	0
11.59899	0
5.179296	1
8.879621	0
2.007349	1
0.562764	1
2.614329	0
2.27174	0
4.61469	0
10.15199	0
1.420823	0
3.826498	0
1.657352	1
4.211525	1
0.931015	1
3.410519	0
7.277092	0
4.319892	0
4.308657	0
33.01384	1

scanarea 4

Length	Truncated
43.29798	1
17.17327	1
0.015137	0
16.53199	0
0.014649	0
16.60486	1
18.33828	1
0.030274	0
0.972828	0
0.044924	0
0.551255	0
0.019379	0
12.35952	0
35.16679	1
14.24129	0
7.4528	0
5.070184	0
0.366623	0
3.414206	0
13.65695	1
12.58593	0
12.58593	0
1.891162	0
7.963822	0
3.476243	0
5.489562	0
16.08264	0
7.423223	1
0.380115	0
6.860189	0
2.25602	0
1.246392	0
2.865545	0
2.079233	0
3.109893	0
1.818133	0
4.93	0
8.976192	0
2.0117	0
5.166923	0
3.600997	0
15.20741	0
8.255052	0
5.260056	0
2.871954	0
5.54258	0
5.384761	0
2.509519	0
6.137926	0
1.041485	1
11.52602	1
4.993428	1
3.341572	0
0.636738	0
0.513584	0
0.30428	0
6.376986	0
1.487454	0
33.29741	0
10.13706	0
7.678254	0
16.60299	0

scanarea 5

Length	Truncated
0.015137	0
31.54034	1
3.553671	0
35.90786	1
32.85954	1
0.352484	1
0.01214	0
2.634832	0
0.06006	0
5.525694	0
0.25455	0
29.86788	1
16.30015	1
8.644498	0
2.999187	1
4.964177	1
5.415226	1
0.031022	0
9.067513	0
21.45377	1
8.212896	1
14.61988	1
41.88841	1
1.025569	1
17.86702	0
2.444901	1
0.027344	0
1.748008	0
0.124135	1
36.35832	1
14.04645	1
29.17512	1
0.970533	1
2.944273	0
8.749088	1
16.78737	1
2.115022	0
0.463247	0
0.691493	0
7.204717	0
0.984299	0
1.151378	0
1.854899	0
1.515491	0
3.276421	0
1.330087	0
0.610884	0
0.309752	0
0.756796	0
2.705822	0
8.466862	0
27.36747	1
9.738033	1
1.183347	0
2.806594	0
4.720779	0
1.852162	0
1.378974	0
1.129477	0
1.406721	0
0.904209	1
1.029545	1
1.081128	0
1.625269	0
0.532029	0
0.841441	0
1.816526	0
2.626806	0
1.444559	1
2.099224	0
1.738019	0
0.95965	0
1.971588	0
2.002969	0
4.65083	0
0.549354	0
1.112373	0
1.283312	0
3.43734	0
2.375145	1
3.331014	0
7.75605	0
0.435775	1
5.737905	0
4.092851	1
1.31918	0
0.160067	1
0.160067	1
2.00321	0
5.042971	0
2.071543	0
7.256377	0
3.471459	0
3.07675	0
5.346697	0
1.166579	0
1.129152	1
6.725016	0
4.289543	0
6.903096	1
1.316736	0
2.927962	1
2.044934	0
4.714535	0
1.813526	0
5.511706	1
0.232279	1
1.732932	0
0.651199	0
1.379914	1
6.997402	0
30.83049	1

scanarea 6

Length	Truncated
7.472686	0
10.70748	0
0.038654	0
7.660476	0
3.534513	0
33.51147	1
1.611964	0
9.556608	0
7.309284	0
17.34367	0
5.076882	0
9.327743	1
25.62319	0
1.165509	0
38.25115	1
1.755961	1
14.20643	1
23.07708	0
5.301819	0
20.95042	1
3.62222	0
3.695855	0
0.71705	0
0.013672	0
14.10793	0
8.659118	0
11.45199	0
11.45199	0
21.50607	0
5.127411	0
1.537247	0
9.965776	0
1.537247	0
9.339186	0
1.326468	0
0.915691	0
7.5838	1
10.48101	1
6.147752	0
3.523641	0
8.859332	0
24.96669	1
9.225361	0
0.153218	0
3.549846	1
24.84026	1
12.58968	1
1.013105	0
4.181328	0
4.132477	0
5.481864	0
25.34916	0
0.620864	1
5.973414	0
14.41491	0
2.568341	0
7.667059	0
11.83233	1
2.601304	1
7.946873	0
0.182519	1
2.706923	0
3.779874	0
4.843383	0
2.681722	0
1.295947	0
5.827408	0
0.642203	0
0.664548	0
3.332592	0
2.180306	0
2.153783	0
1.338203	0
3.88332	0
3.373213	0
3.373213	0
4.115921	0
4.353429	0
1.092893	0
2.944087	0
2.731946	0
1.106712	0
3.014721	0
0.958419	0
0.952542	0
1.136458	0
1.124203	0
12.88501	1
3.971221	0
7.454096	0
2.97439	0
1.105537	0
1.952442	0
1.629143	0
2.915524	1
4.385385	1
1.855518	1
0.890006	0
4.51159	0
2.737061	0
4.143821	0
2.741173	0
0.784929	0
3.08909	0
1.491949	0
4.479033	0
3.469283	0
1.337282	1
6.19708	0
2.18981	0
2.31269	0
13.86506	1
3.096578	1
9.962926	0
1.660423	0
4.031789	0
7.287734	0
1.091752	0
3.162993	0
0.655632	0
1.729307	0
1.49993	0
2.246308	0
0.746916	0
2.780609	0
3.188322	0
5.893033	0
1.205111	0
0.731639	0
0.724425	0
0.741781	0
0.844083	0
1.566638	0
0.572919	0
0.555829	0
2.833769	0
0.513264	0
0.754086	0
1.159743	0
0.613779	0
1.778161	0
1.166321	0
1.861746	0
1.776668	0
3.926673	0
0.609957	0
1.206576	0
2.083991	0
0.927406	0
0.805999	0
0.651852	1
0.562651	1
11.92817	0
5.19457	0
29.58745	2
8.44027	0
4.866586	0
3.929494	1
4.94299	0
8.845691	0
9.706781	1
1.695848	1
9.442894	0
32.7043	1
4.626957	0
4.235967	0
3.413547	0
1.952312	0
4.007772	0
2.070987	0
4.038117	0
9.828453	0

scanarea 7

Length	Truncated
26.86237	1
1.5875498	1
6.4286118	0
20.671041	0
29.787802	1
30.563057	1
1.9581305	1
29.176666	1
1.8772211	1
25.750858	1
3.0789595	0
2.5410361	0
23.532656	0
13.883476	1
9.4211197	1
3.4682024	0
2.9450932	0
1.3496457	0
3.8539035	0
2.7180114	0
1.4539126	0
9.080224	1
18.572151	1
23.208042	1
12.529237	0
4.6918154	1
4.3383656	0
5.2266941	0
7.554894	0
7.5219207	0
15.827941	1
17.706392	1
2.7518082	0
3.0478432	0
15.899121	0
4.8536716	0
2.8769119	0
3.3103151	1
2.7144456	0
0.5245478	1
3.0430434	0
1.3683981	1
1.1125481	0
0.6278331	1
0.6278331	1
19.04644	0
3.8099511	1
4.7153168	1
1.1520882	0
5.1979465	0
3.5756865	0
13.749146	2
2.4255264	0
1.3820961	0
2.0038314	0
4.9614615	0
4.1046138	0
3.1625097	1
1.6344465	0
2.2045014	0
4.1282687	0
2.5755579	0
0.7569316	0
2.2363698	0
0.5376992	0
1.4862999	0
3.5454128	1
0.4958727	1
0.9952908	0
2.879142	1
0.8980186	1
1.3223118	0
3.5581486	0
3.1157954	0
2.923142	0
3.7858698	0
1.3663939	0
0.5960112	1
0.3243117	2
1.0088476	0
2.6444297	0
28.192562	2
2.809552	1
2.809552	1
6.0078092	1
23.824371	0
7.6624446	0
0.4604329	0
8.4161015	0
3.8485937	0
0.7438661	1
3.0274231	1
4.5818882	0
1.2215371	1

scanarea 8

Length	Truncated
37.65811	1
3.792063	1
12.57646	0
3.246313	1
7.714334	1
2.503273	0
13.56421	0
5.828031	0
26.2711	0
3.349881	1
2.335433	0
36.70352	1
6.914924	1
32.81811	1
6.055614	0
4.246912	0
14.83768	1
7.005206	0
7.623263	0
8.097327	0
24.61744	1
25.93617	0
7.276371	0
25.43253	1
25.43253	1
19.5631	0
11.58394	1
2.388889	0
15.4417	0
12.62877	0
5.513752	0
18.45028	0
3.261599	0
0.559663	0
1.479607	0
7.163896	0
7.415922	0
4.615691	0
2.368427	0
5.866286	0
4.309541	1
2.235392	0
1.816383	0
1.585732	0
0.932822	0
3.287401	0
6.594926	1
10.26692	0
3.230022	0
2.817634	0
4.945636	0
0.639909	0
1.315779	0
0.874302	0
1.924396	0
2.889034	0
2.159353	0
2.645058	0
6.708623	0
1.690447	0
4.531367	0
3.652071	0
3.261662	0
6.574564	0
2.687968	0
3.283934	0
1.098373	1

scanarea 9

Length	Truncated
29.29825	1
33.52603	1
23.42993	1
15.29735	0
17.40086	1
12.21228	0
14.58367	0
17.74512	1
5.205379	1
20.38135	1
35.02671	1
35.02671	1
13.5477	1
29.77213	0
2.117128	0
3.452782	1
2.418359	1
1.76377	1
1.647304	1
1.558218	1
4.514019	1
0.203767	1
2.346013	0
0.207521	0
6.463988	0
6.63783	0
3.551876	0
2.012968	0
0.648607	0
6.141118	0
12.70313	1
1.031657	0
4.838223	0
5.155268	0
1.715059	0
1.202345	0
9.169662	1
8.233178	1
0.297971	1
4.367073	0
1.1663	0
6.077454	0
3.567869	0
14.47175	0
2.896479	0
3.637683	0
1.640777	0

scanarea 10

Length	Truncated
1.48415947	0
9.957716942	0
11.50431919	0
11.99287128	1
5.202213287	0
32.63777542	1
4.773123264	1
9.601661682	1
0.203929171	2
0.203929171	1
5.901135921	1
0.01643605	1
3.825029612	1
6.975864887	0
1.884136558	0
3.852342367	0
3.762744427	0
11.22981739	0
26.42120743	1
11.9453001	1
10.14925861	1
14.48074532	0
2.583804607	0
11.41458321	0
9.942541122	1
8.097725868	0
2.709154129	0
1.933520079	0
2.036587954	0
0.357682407	1
2.963494539	0
1.206174016	0
2.80099082	0
0.508917809	0
2.637931347	1
5.789698601	0
0.763488829	0
3.407553673	0
3.631218672	0
2.213479996	0
3.929438829	0
5.305588245	0
2.728699684	0
1.111490011	1
3.832658768	0
4.029259682	0
2.345185041	1
1.559376597	0
1.159772396	1
7.84157753	1
3.620105505	1
7.541128635	0

scanarea 11

Length	Truncated
28.46522	1
6.852649	1
2.153799	0
30.97382	1
9.803061	1
34.05992	1
14.03744	0
15.35996	0
3.638213	0
2.077276	0
6.432709	0
13.56931	0
11.73444	0
0.104522	0
1.647512	0
14.33848	1
3.704245	0
9.255983	0
25.57344	0
27.88524	1
34.47102	1
17.46523	1
5.302972	0
0.085319	1
0.085319	1
8.671863	0
4.319609	0
10.00685	0
5.758178	0
12.18217	0
4.924994	0
3.683027	0
4.980807	1
3.954615	0
1.895077	0
8.729032	0
2.941133	0
1.696297	0
2.272254	1
3.236512	1
0.323921	1
6.656871	0
1.738544	0
9.044249	0
2.637131	0
4.119219	0
0.53143	0
1.414572	0
8.009264	0
6.12516	0
2.588409	0
3.070225	0
7.220653	0
7.058918	0
3.679313	0
2.937175	0
8.172575	0
2.271441	0
2.078909	0
2.556275	0
3.202071	1
0.012665	1
1.897686	1
3.604797	0
4.05674	0
1.562999	0
1.050637	0
3.010659	1
17.32285	0
5.178447	0
19.65837	1
4.903883	0
4.001313	0
2.105985	0

scanarea 12

Length	Truncated
32.11673	1
36.10595	1
29.78098	1
14.87565	0
6.199941	0
5.516726	0
17.98345	1
3.963898	1
10.16333	1
8.637326	1

SET WNW-ESE

scanarea 1

Length	Truncated
8.792112	0
0.069549	0
6.162006	0
7.591674	0
9.938755	0
0.038207	0
3.819563	0
2.491601	0
3.419864	0
5.166209	0
11.91171	0
12.8399	0
6.758317	0
3.615602	1
9.756687	1
14.21053	0
12.05861	0
10.36976	0
14.63752	1
14.63752	1
7.584311	0
6.655538	1
4.427661	1
3.103307	0
0.038573	0
11.44345	0
14.3014	0
7.962891	0
0.409476	1
7.296034	0
2.782	0
2.656691	0
2.282793	1
28.67367	0
2.052598	0
1.148282	0
4.21867	0
6.590392	0
8.062913	0
2.748409	0
12.39388	0
9.629546	0
2.935836	1
19.97602	1
12.09759	1
3.156254	1
9.665839	0
28.04562	1
6.198816	1
4.666401	1
9.526249	1
2.318696	1
1.340248	0
33.86243	1
8.692638	0
4.855676	0
4.859824	0
1.497286	0
2.453818	0
0.769288	1
12.23178	1
8.179642	0
4.797503	0
5.654645	0
13.66695	0
1.768791	1
0.544994	0
0.809579	1
12.23689	1
7.605682	0
4.927779	0
5.166488	0
3.20254	0
3.017185	0
7.294237	2
6.588541	1
6.621614	0
7.253973	1
7.902308	0
1.310289	1
3.070496	0
7.717614	0
3.88318	0
32.47221	1
5.265869	0
4.623346	0
4.113001	0
6.427948	0
3.936299	0
4.757701	1
12.13733	1
11.85872	1
9.244102	0
20.12712	0
4.275975	0
7.127579	0
12.32475	0
8.90196	0
5.836856	0
3.088517	0
4.710252	0
3.462948	0
7.226504	0
2.563569	0
1.426008	0
3.402089	0
3.773073	0
2.914142	0
1.386819	0
6.77516	0
5.884434	0
3.141437	0
7.556546	0
6.103742	0
7.845351	1
11.8391	0
8.019414	0
7.905347	1
19.5335	0
3.482799	0
4.444751	0
3.558438	0
9.116588	0
0.922347	0
8.058967	0
6.679187	0
11.17241	1
9.105017	1
2.190476	0
20.53105	1
1.07448	1

scanarea 2

Length	Truncated
19.25374	0
33.49406	1
23.98617	0
4.565962	0
0.019281	0
7.619142	0
8.405786	1
0.7372	0
4.633112	0
4.471744	0
4.471744	0
14.68049	0
29.00224	1
14.23855	0
9.786727	0
16.36856	0
16.11978	0
13.80745	0
4.847216	0
1.251179	0
5.427059	0
2.998393	0
12.08844	0
14.93071	0
8.222153	0
8.222153	0
1.91172	0
6.175271	0
5.433746	0
3.457239	0
7.481819	1
4.485044	0
5.765285	0
2.283802	1
3.361814	1
5.39009	1
4.751106	0
8.920021	1
9.312725	1
1.817921	1
1.228672	1
3.959982	1
0.630406	0
0.070264	1
0.558852	1
1.303016	1
0.128638	1
0.986602	1
0.986602	1
26.88607	1
7.221132	0
1.446853	0
2.246117	0
5.7784	0
2.837788	0
10.20108	1
4.972262	0
2.730657	0
3.668649	0
2.884658	0
0.805725	0
9.522107	0
3.246284	1
7.037548	0
1.319312	0
3.168651	0
2.092585	0
7.200148	1
34.61573	1
30.61225	0
2.500862	0
5.135704	0
1.396352	0
4.883886	0
2.634284	0
1.868088	0
5.28249	0
1.654711	0
2.34369	1
8.810468	1
6.561438	0
25.0153	0
1.352106	0
0.749025	0
3.968472	0
1.339687	0
1.483914	0
2.174106	0
7.97928	0
1.097661	0
3.293304	0
2.540711	0
7.792343	1
0.709156	0
1.552076	0
9.36015	0
2.403699	0
1.113703	1
7.867354	0
5.566962	0
2.487214	0
2.846596	1
7.107081	0
2.126143	0
5.338621	0
8.116825	0
0.911989	0
1.317757	0
2.01149	0
2.592808	0
5.511776	0
1.723746	0
3.212055	0
11.45849	0
1.124223	0
0.628702	1
1.950162	0
3.166587	0
4.835098	1
3.414145	1
1.238808	0
6.966836	0
3.075151	0
0.913033	0
4.374417	0
0.977243	0
0.718809	0
19.86175	0
2.295426	0
2.68319	0
1.552895	0
1.554038	0
1.554533	0
8.271564	0
2.798661	0
2.957885	0
5.918923	1
0.544994	1
1.419802	0
2.716528	1

scanarea 3

Length	Truncated
3.208621	0
6.68722	0
5.523471	1
8.256237	0
2.928624	0
6.364209	0
20.58441	0
3.300884	1
0.027832	0
8.351149	0
5.864972	0
15.93183	0
1.834419	1
2.361202	1
0.672407	1
8.995281	0
3.11291	0
3.224941	0
1.116599	0
2.798479	0
9.747773	0
1.806472	0
0.468723	1
0.468723	0
4.907228	0
1.097417	0
2.527382	0
4.963867	0
5.388916	0
17.36721	1
17.36721	1
4.359174	0
7.439565	0
5.569107	0
5.569107	0
30.14641	0
9.29771	0
35.40577	0
3.150946	0
3.691618	0
6.273499	1
1.285922	1
2.455302	0
11.79088	0
1.012354	0
2.570817	0
0.719751	0
3.190191	0
0.135543	0
4.27335	0
1.51604	0
3.171385	0
2.512979	0
1.312369	0
1.929775	0
1.753671	1
1.941718	1
1.064301	0
1.671069	0
0.723223	1
3.468737	1
5.656159	0
1.189574	0
15.2231	1
3.059101	0
2.025615	1
3.046	0
1.84655	0
2.426231	0
6.032088	0
2.109475	0
3.106375	0
1.12842	0
1.509565	0
5.592309	0
2.096283	0
2.98493	0
2.132385	0
1.83473	0
2.742082	1
0.43807	1
0.080557	1
3.657283	0
4.343112	0
6.81775	0
1.349105	0
7.617467	0
0.748866	0
0.706301	0
1.762233	0
1.613392	0
2.911299	0
4.043059	0
0.93489	0
1.76004	0
0.843936	0
1.758217	0
1.139849	0
3.570277	0
2.89904	0
3.235785	0
1.585494	0
2.971059	0
1.343908	0
1.289033	0
0.665871	0
0.603911	0
1.812978	0
2.599625	0
3.222306	1
1.984705	0
3.465011	0
1.944713	0
0.487027	0
1.490969	0
2.858207	0
5.603451	0
4.098241	0
5.335377	0
3.596298	1
0.130921	1
11.68021	1
2.171232	1
0.709869	1
6.869672	0
11.61335	0
2.234677	0
1.924599	0
2.098049	0
0.741763	0
2.043304	0
1.775673	0
1.723823	0
5.210419	0
1.123637	0
0.687137	0
15.62959	0
1.88636	0
1.820411	0
1.278047	0
2.488989	0
4.720526	0
3.568999	0
2.948849	0
0.864556	0
0.667538	0
1.23473	0
5.895662	0
8.777905	0
1.461609	0
2.03234	0
2.170331	0
5.890375	0
3.099077	0
12.4695	0
0.766826	0
2.497336	0
1.975135	0
5.612925	0

scanarea 4

Length	Truncated
32.89405	1
9.543534	0
8.339399	1
4.70576	0
4.70576	0
0.069622	1
1.967231	0
9.475698	0
1.450924	0
1.56666	0
0.986094	0
1.226499	0
0.47729	1
1.259424	0
0.911367	0
1.061423	0
14.0421	0
2.794347	0
0.892796	0
0.967522	0
3.258942	0
2.515418	0
3.830574	0
3.005689	0
1.472713	0
1.79131	0
3.665962	0
2.669246	0
0.752847	1
2.158115	0
1.816948	0
3.627119	1
2.897731	1
7.018579	1
2.027891	0
2.369006	0
0.217276	1
1.19172	0
0.933665	0
1.685007	0
3.1905	0
1.922815	0
5.868674	0
2.321212	0
3.640729	0
0.942603	0
0.33146	0
0.704783	0
0.864998	0
0.868372	0
18.35299	0
1.886248	0
1.651575	1
2.151373	0
1.311874	0
2.548671	1
0.189758	1
0.189758	0
0.939425	0
2.060281	0
2.324982	0
1.899753	0
2.609571	0
1.016003	0
1.77337	0
2.938914	0
4.263544	0
8.307984	0
0.332246	0
0.590875	0
0.415385	0
0.347227	0
6.446472	0
2.164062	0
1.534251	0
4.892302	0
1.438907	1
5.121048	0
2.396095	0
5.765756	0
0.943056	0
1.580635	0
2.384371	0
3.107588	0
2.299024	0
2.306899	0
2.588791	0
6.312634	0
2.36837	0
0.652161	0
0.943171	0
1.150164	0
3.18767	0
1.549497	0
0.347079	0
0.926005	0
1.031459	0
1.160742	0
0.615722	0
0.668191	0
1.315385	0
2.038328	0
1.4377	0
1.231864	0
1.861489	0
1.680818	0
1.747406	0
0.464363	0
2.61839	0
1.573043	0
2.954862	0
0.745014	0
1.093827	0
4.525052	0
1.075976	0
1.006057	0
6.161376	0
3.529907	0
1.109811	0
5.169764	0
2.087155	0
2.234901	0
1.933508	0
5.264429	0
4.123743	0
1.411776	0
5.698101	0
0.829676	0
3.228483	0
3.687143	1
2.489913	0
2.561517	0
18.49599	0

scanarea 5

Length	Truncated
0.679628	1
2.234288	0
2.368641	1
0.615072	1
0.745398	0
0.397223	0
20.11777	0
1.524811	0
6.476577	0
1.299462	0
3.929477	0
0.819576	0
1.213462	0
2.59424	0
7.673736	0
12.08069	0
7.141245	1
1.658928	1
18.08757	1
11.5235	0
3.121433	0
1.356187	0
2.139161	1
2.74514	0
4.769953	0
7.977269	0
3.327296	0
12.18363	0
4.2659	0
13.79076	0
37.27803	1
4.485817	0
5.171404	0
6.382779	1
8.343081	0
0.225357	0
1.603298	1
3.08656	0
5.370183	1
33.98615	1
9.811725	1
6.940268	1
6.940268	1
3.121667	0
0.71322	0
2.115492	0
2.981083	0
4.503152	0
13.5085	0
5.678717	0
4.989805	0
2.80722	0
2.188545	0
16.89195	0
2.18006	0
3.912267	0
0.862194	0
2.368728	0
1.753359	1
0.113954	1
5.261134	0
2.039115	0
7.72441	0
2.603462	0
3.504759	0
4.82115	0
2.049786	0
1.751723	0
2.196024	0
2.92624	0
4.819523	0
1.882672	0
2.119704	0
1.679909	0
0.617515	0
0.722668	0
1.162207	0
2.817933	0
1.858535	0
3.940544	0
1.451935	0
2.556055	0
4.156538	0
1.683323	0
0.681992	0
0.715242	0
2.517361	0
1.939664	0
0.579184	1
0.99656	1
0.597756	1
1.873309	0
1.854083	0
0.960504	0
1.862012	0
1.754284	0
3.160328	0
2.059213	0
2.881836	0
2.574855	0
1.0462	0
0.93172	0
3.776123	0
3.53723	0
1.590556	0
1.885171	0
5.868226	0
3.255487	0
3.460994	0

scanarea 6

Length	Truncated
32.05779	1
6.797707	1
13.20767	0
6.05207	0
10.20383	0
1.414316	0
2.013101	0
0.443995	0
3.168564	0
1.999185	0
3.464228	0
3.081731	0
3.277222	0
2.209563	1
0.517722	1
2.593397	0
9.161985	0
4.704887	0
5.461358	0
7.770772	1
11.26946	0
10.53812	0
4.43296	0
6.520469	0
7.970366	0
5.877421	0
1.414882	0
2.115336	0
1.251394	0
3.138214	0
3.313547	0
5.669998	0
2.856234	1
0.280629	1
9.872477	0
0.143731	1
1.239006	0
0.238335	0
1.466866	0
1.408273	0
4.070693	0
0.982831	0
12.46258	0
1.352399	0
1.114603	0
1.755155	0
2.098916	0
2.601045	0
0.613464	0
8.440355	0
10.08877	1
2.030149	0
3.494023	0
1.997503	0
1.619515	0
0.488173	0
7.089528	0
4.5929	0
0.186321	1
0.186321	0
5.579687	0
0.785828	1
0.091462	1
1.620869	1
5.294256	1
1.875676	1
1.546208	1
1.048021	0
5.381495	1
11.94353	0
3.724292	1
2.159043	0
3.756322	1
3.758106	0
2.021163	0
2.428778	0
4.286716	0
2.51372	0
1.881825	0
8.778296	0
1.310415	0
1.004864	0
6.366942	0
4.280766	0
5.193818	0
0.82204	0
1.164074	0
1.735951	0
1.578725	0
2.576184	0
2.705068	0
1.269138	0
1.790313	0
1.196971	1
8.611633	0
11.88247	1
5.253088	0
1.570274	1
0.448379	1
0.820801	1
1.524356	0
3.203998	0
1.789839	0
1.725531	1
1.725531	1
4.029226	0
2.288945	0
2.96378	0
6.182083	0
1.397122	0
1.489328	0
7.537865	1
1.734855	0
7.956248	0
6.175395	1
2.546508	0
3.662462	0
1.95674	0
1.698923	0
3.978895	1
1.9474	1
1.262062	0
1.4074	0
1.479917	1
0.166652	1
0.22959	1
1.506091	0
4.000839	0
1.0546	0
1.220545	0
5.873983	0
5.157946	0
2.078704	0
2.846995	0
1.843099	0
0.951696	0
1.982918	0
2.018701	0
1.032149	0
2.598844	0
0.997212	0
5.78823	0
1.230825	1
1.316919	1
0.712496	0
2.115649	0
2.106251	0
2.549729	0
6.474374	0
2.035503	0
0.925626	0
2.306353	0
7.216327	0
3.177186	0
1.331987	0
3.2284	0
1.140862	0
8.248849	0
2.077961	0
5.114414	0
1.880945	0
2.507258	0
7.701643	0
3.863129	0
2.074487	0
6.228187	0
3.50263	0
1.35688	0
5.100842	0
4.699714	0
2.737228	0
8.59338	0
2.503903	0
1.224467	0
8.543243	0
1.778662	0
2.278697	0
2.717682	0

scanarea 7

Length	Truncated
10.48394	1
3.898941	0
3.6114	0
4.421872	0
1.992361	0
4.137311	0
3.588256	0
3.076215	0
2.145846	0
14.73608	0
17.49285	1
1.263981	0
10.67407	0
8.958831	1
13.7515	0
4.127744	1
5.552766	1
13.05035	1
1.402233	0
0.644541	1
1.036531	1
0.88215	0
4.967097	1
4.967097	1
0.517398	1
1.279556	1
4.912847	0
1.075752	0
7.016801	1
4.39258	0
1.816736	1
0.565077	1
1.956329	1
3.238719	1
3.853009	0
8.082073	0
1.539721	0
3.823153	0
1.440633	0
0.864952	0
14.65382	0
6.260679	0
3.603595	0
0.41048	0
1.071743	0
3.080428	0
1.188925	0
2.277709	0
0.748038	0
2.235023	0
0.918345	0
2.141685	0
8.567985	0
1.325491	0
1.474068	0
1.820946	0
0.651417	0
6.034369	0
1.436743	0
4.272635	0
2.014718	0
8.37473	0
19.1611	1
4.492609	0
3.647959	0
2.242366	0
0.517726	1
0.517726	0
6.465861	0
2.455193	0
1.145427	0
0.620024	0
2.331523	0
1.654092	0
1.723688	0
0.711992	0
2.136543	0
7.18947	0
8.405154	0
3.658394	0
2.087029	0
3.587375	0
3.446424	0
0.855795	0
3.085391	0
1.000411	0
0.999724	0
5.597491	0
2.430953	0
2.770923	0
3.82593	0
4.516298	0
1.094983	0
0.725309	0
1.943653	1
2.968286	0
1.043456	1
1.354816	1
8.811207	0
3.929249	0
1.94253	0
3.900281	0
3.404096	0
1.591846	0
1.677855	0
1.557802	0
7.058295	0
3.243328	0
2.8255	0
3.394504	0
2.097332	0
2.503251	1
7.991742	0
3.681783	0
3.274216	0
4.570385	0
2.5215	0
1.434867	0
1.512778	0
12.67073	0
17.21718	1
1.229244	0
3.5416	0
0.695858	0
2.158028	0
10.43467	0
2.394715	0
1.231457	0
3.567527	0
2.885893	0
3.750005	0
1.916646	0
1.446284	1
3.933595	1
1.786558	0
5.431778	0
7.853837	0
1.153223	0
5.665862	0
0.17296	0
9.673889	0
1.32546	0
1.309116	0
5.998909	1
8.561734	1
0.298213	1
1.958938	1
0.264726	1
3.291887	1
4.122716	1
6.030886	0
3.702032	1
3.752552	1
3.752552	1
1.891629	1
2.42837	0
1.628027	0
2.958302	0

scanarea 8

Length	Truncated
3.988015	1
0.194305	1
1.369156	1
0.194193	1
0.194193	0
2.651623	1
0.921156	0
2.674445	0
8.23124	1
0.807623	0
5.803857	0
13.57896	0
5.913758	1
3.758605	1
0.302934	1
4.344316	1
2.104769	0
1.608059	1
4.37774	1
4.327055	1
0.811507	0
3.626312	0
3.604873	0
1.877839	1
1.023742	1
0.067048	1
0.067048	0
1.775244	0
0.461537	0
2.559767	0
2.048829	1
1.257458	0
3.728034	0
4.624352	0
8.966417	0
1.461221	0
3.464702	0
4.930381	1
1.219081	1
0.664408	1
0.833924	1
1.888215	0
1.548132	0
3.476435	0
1.954666	0
3.239618	1
0.170879	1
0.170879	0
4.501023	0
5.178762	0
1.212582	1
0.167426	1
2.445897	0
1.867658	0
2.803139	1
2.102861	1
0.527037	1
0.215421	1
0.22158	1
3.273206	0
0.992844	1
0.283683	1
8.97171	0
0.96093	0
3.015979	0
1.395917	0
1.56227	0
7.64864	0
4.432409	0
7.094267	0
4.634675	0
2.951173	1
2.799208	1

SET N-S

scanarea 1

Length	Truncated
3.37509	0
1.675899	0
1.259285	0
2.519164	0
0.855841	0
2.225312	0
2.845592	0
0.855734	0
2.632802	0
10.82983	0
5.077083	0
0.866563	1
1.033924	0
1.46924	0
1.621024	0
0.588954	0
6.073873	0
5.87359	0
5.07181	0
3.099002	0
4.891554	0
0.077813	1
0.077813	0
2.033222	0
1.395791	0
2.11741	0
5.473816	0
0.575703	0
4.682917	0
2.260277	0
8.095334	1
2.615619	0
2.250976	0
2.99262	0
2.104804	0
1.59302	0
8.048801	0
1.879985	0
2.356452	0
2.057578	0
2.261342	0
0.947603	0
4.687009	0
5.449176	0
5.345206	0
3.466032	1

scanarea 2

Length	Truncated
2.211388	1
3.013072	0
2.23106	1
2.23106	1
4.502506	0
5.170061	1
0.491814	1
3.156513	0
3.31871	0
3.033771	1
0.191287	1
1.867565	0
9.983842	0
4.05179	0
2.953874	0
1.84691	0
5.04038	0
2.107667	0
3.216743	0
2.340985	0
1.795179	0
2.862341	0
0.879553	0
1.387526	0
3.729088	0
2.494177	0
3.469972	0
2.265956	0
6.127951	0
0.642012	0
0.366248	0
0.838926	0
0.810357	0
1.675903	0
2.206007	0
1.146742	0
0.611655	0
3.562327	0
1.749969	0
1.211794	0
6.35186	0
8.115273	0
6.544725	0
2.501449	0
4.347134	0
3.924654	0
4.85662	0
1.593508	0
3.329619	0
3.334705	0
3.538353	0
2.088825	0
2.232178	0
1.765494	0
1.764408	0
2.773848	0
2.163156	0
1.366064	0
2.765075	0
3.347873	0
3.356443	0
1.267171	0
8.054009	0
6.414586	0
2.584005	0
1.455348	0
1.890512	0
1.438787	0
3.107983	0
3.787289	0
3.013511	0
2.835891	0
1.003986	0
4.216835	0
4.129709	0
4.722131	0
5.127563	0
2.393918	0
4.985476	0
6.220531	0
1.985901	0
5.459834	0
3.822757	0
2.268049	0
4.859756	0
7.051467	0
1.008534	0
6.85768	0
2.42312	0
2.533739	0
2.229457	0
7.36741	0
2.976411	0
4.941426	0
5.44778	0
2.464012	0
1.479122	0
3.0476	0
1.724802	0
1.739928	0
0.935467	0
2.397524	0
0.786601	0
3.410569	0
3.001979	0
1.873655	0
4.552769	0
2.319761	0
5.922779	0
1.578327	0
2.168038	0
2.40723	0

scanarea 3

Length	Truncated
3.567366	0
1.445301	1
11.28503	0
3.640309	0
8.841815	0
6.365991	0
7.541258	0
4.250574	0
2.673429	0
28.28438	0
6.376282	0
4.081562	0
4.676979	0
5.365361	0
3.606409	1
3.606409	1
10.32721	0
11.9008	0
4.77012	0
2.130054	0
1.410567	0
1.678422	0
2.087726	0
3.351098	0
4.249078	0
1.941652	0
6.385857	0
8.487191	0
2.719651	0
2.523997	0
1.530763	0
5.00686	0
8.429488	0
1.688762	0
3.159515	0
2.087582	0
3.167472	0
0.596776	0
0.753146	0
0.486312	0
1.076952	0
1.853601	0
2.473579	0
2.229058	0
1.105425	0
1.395993	0
0.87271	0
1.778382	0
1.363525	0
5.303676	0
3.316604	0
1.693536	0
2.416279	0
0.678669	0
3.447494	0
2.353668	0
6.240876	1
1.403341	0
2.198343	0
3.092287	0
6.531257	0
2.184212	0
4.77378	0
1.993994	0
3.242215	0
4.254679	0
2.473853	0
1.313403	0
3.561424	0
1.625546	0
11.04717	0
4.431609	0
0.628754	0
2.178721	0
2.839474	0
1.651911	0
3.341916	0
1.987159	0
2.318135	0
2.491143	1
2.48053	0
3.984992	0
0.715578	0
3.996205	0
4.63044	0
3.697875	0
3.940998	0
2.45084	0
2.465939	0
2.105532	0
1.553933	0
1.386635	0
1.109723	0
2.485219	0
1.867426	0
1.647502	0
1.629923	0
5.496249	0
7.653396	0
2.885677	0
0.942141	0
3.142344	0
3.388707	0
2.474578	0
3.123851	0

scanarea 4

Length	Truncated
7.830268	0
7.571118	0
7.639729	0
2.166234	0
1.873149	0
1.448734	0
0.661356	0
4.368184	0
4.900896	0
5.087684	0
7.254695	0
1.548707	0
1.500125	0
0.941895	0
1.111821	0
1.678163	0
0.623256	0
5.996995	0
2.852922	0
4.322054	0
3.511129	0
6.31744	0
6.116164	0
1.094566	1
7.746621	0
9.660537	0
8.866419	0
10.83582	0
2.364465	0
10.31311	0
2.181345	0
1.975385	1
2.617674	1
0.633155	0
1.747773	0
4.054847	0
2.907722	0
2.38789	0
2.855842	0
0.839153	0
0.695447	0
6.216493	0
2.932131	0
0.714299	0
4.321184	0
6.917259	0
6.002507	0
1.355374	0
2.938105	0
2.802039	0
0.62495	1
0.982549	1
1.258407	0
2.678564	0
0.743269	0
1.148917	0
3.280191	0
1.754681	0
1.481787	0
0.691435	0
1.547508	0
1.269407	1
6.298193	0
1.208165	0
1.527483	0
6.162097	0
1.412043	0
1.194512	0
3.057482	0
1.603575	0
1.060297	0
2.194021	0
1.191092	0
4.540032	0
0.871468	0
1.99982	0
1.604534	0
0.926473	0
0.906377	0
1.591095	0
2.632847	0
0.952446	0
10.09043	0
3.149083	0
2.700395	0
1.469094	0
2.653772	0
2.021099	0
1.711111	0
2.764996	1
0.411747	1
2.49426	0
0.778582	0
0.851612	0
3.176351	0
1.225942	0
1.725409	0
0.303267	0
0.380397	0
0.26621	0
1.041037	0
0.455202	0
2.155887	0
2.607811	0
1.628145	0
1.984401	0
1.70012	0
0.976486	0
0.584398	0
0.837482	0
1.523019	0
1.186337	0
0.629109	0
1.171246	0
0.770381	0
1.453945	0
3.195383	0
1.083435	0
0.678066	0
0.470697	0
1.783478	0
1.221902	0
1.208992	0
3.885693	0
3.408125	0
3.497504	0
1.704066	0

scanarea 5

Length	Truncated
1.677776	0
1.677776	0
1.694481	1
1.2512	0
0.102744	1
0.405013	1
0.735779	1
0.666203	1
1.183407	0
8.58692	0
3.133264	0
5.28497	0
1.858836	0
7.929321	0
3.226563	0
0.15093	1
0.15093	0
4.376925	0
2.601965	0
3.550214	0
4.169136	0
0.884731	0
2.427614	0
3.783345	0
2.071058	0
5.088652	0
6.71083	0
2.903261	0
8.393024	0
2.431412	0
0.392116	0
3.637988	0
3.399243	0
8.614997	1
0.963891	0
4.734411	0
1.917301	0
5.445597	0
5.63371	0
1.898243	1
2.275391	0
1.323512	0
1.281129	0
9.506042	1
6.817092	1
0.925787	0
2.143905	0
8.09343	0
16.31084	1
1.802671	1
9.002266	1
3.034606	1
5.211679	0
1.698538	0
3.822549	0
3.568355	0
4.291893	0
3.54394	0
1.861471	0
2.024752	0
12.48229	0
4.028825	0
1.205231	0
2.449673	0
0.740922	0
4.897318	1
0.511398	1
8.693444	0
2.685777	0
0.519089	0
0.598606	0
2.024222	0
0.995117	0
1.206241	0
2.577582	0

scanarea 6

Length	Truncated
0.027512	1
0.050798	1
0.049775	1
1.060371	1
4.317382	1
3.064355	1
3.144999	0
4.354495	0
1.651892	0
1.917488	0
0.997442	0
0.770107	0
1.534951	0
10.13826	0
0.413288	0
2.296551	0
2.409503	0
2.41695	0
0.6436	0
2.116377	0
0.063708	1
0.063708	0
3.906101	0
8.814849	0
1.270029	0
1.676393	0
4.193644	1
0.903773	0
5.420341	0
2.078612	0
1.647748	0
1.954355	0
5.24808	0
0.714027	0
0.714493	0
3.821571	0
1.558186	1
4.425907	0
6.522704	0
4.493392	0
3.257963	0
9.753926	0
11.26437	0
2.860761	0
4.406497	0
1.327935	0
1.52405	1
2.960705	0
2.375612	0
5.768967	0
3.63465	0
3.563618	0
8.419086	0
7.041513	0
1.613688	0
1.865842	0
3.468709	0
2.022361	1
1.967257	0
1.829601	0
2.39859	0
1.589874	0
0.862506	0
1.903249	0
2.044229	0
2.091825	1
1.070336	0
2.356122	0
0.585427	0
1.604495	0
1.385286	0
1.012561	0
0.847277	0
1.21209	0
1.069371	0
1.378581	0
3.428386	0
0.757946	0
2.433214	0
1.596732	0
1.304266	0
0.697282	0
2.160385	0
2.391176	0
1.580616	0
1.314722	0
0.899529	0
1.919798	0
2.290391	0
1.818964	0
1.241429	0
1.128704	0
4.378986	0
2.19503	0
2.118222	0
3.008242	0
3.128866	0
1.275044	0
3.368387	0
5.612345	1
2.508104	0
2.894453	0
3.003657	0
2.634929	0
1.787805	0
1.426697	0
2.572809	0
1.558356	0
5.747702	0
6.141213	0
4.281596	0
5.94946	0
1.683898	0
2.449376	0
2.475821	0
2.006916	0
3.283212	0
4.014084	0
2.639067	0
5.883699	0
1.280213	0
2.01606	0
0.856948	0
2.196235	0

scanarea 7

Length	Truncated
4.936684	0
7.690042	0
5.823775	0
7.450139	0
2.960004	0
1.986582	0
0.916249	0
2.466557	0
1.423864	1
1.423864	1
0.909267	1
1.072399	0
2.179036	1
0.692305	0
0.58545	0
5.946683	0
0.818305	0
0.945404	0
1.656961	0
2.301301	0
1.247303	0
1.002387	0
1.423345	0
5.019946	0
2.206887	0
1.212311	0
6.608935	0
1.815424	0
5.416198	0
1.556029	0
2.232294	0
1.705284	0
3.295459	0
3.636274	0
1.227882	0
1.964174	0
3.557545	0
2.567588	1
1.033281	0
1.095871	0
1.700546	0
5.106546	0
3.360437	0
1.091584	0
1.244607	0
1.49026	0
1.513651	0
1.724374	0
0.939624	0
6.205772	1
0.053364	1
3.072098	1
5.61625	0
6.477539	0

scanarea 8

Length	Truncated
3.017487	0
1.253108	1
1.528895	0
5.272219	0
8.679032	0
1.378099	0
2.496042	0
6.409542	1
6.409542	1
2.650382	0
0.991414	0
2.970549	0
1.724135	0
1.428516	0
1.545725	0
1.477928	0
1.694005	0
1.751588	1
0.142592	1
0.087133	1
2.188798	0
0.768141	0
4.573517	0
3.058872	0
3.849046	0
2.480987	0
2.629793	0
4.6815	0
3.43954	0
0.916402	0
4.390515	0
3.188234	0
0.988537	0
2.587538	0
0.103421	1

Table 76: In these tables we reported the fracture spacing data used to build the boxplots of Figure 11. Fracture spacings are in meters and scanarea number start from the fault zone.

SET N-S

scanarea_1	scanarea_2	scanarea_3	scanarea_4	scanarea_5	scanarea_6	scanarea_7	scanarea_8
spacing (m)	spacing (m)	spacing (m)	spacing (m)	spacing (m)	spacing (m)	spacing (m)	spacing (m)
1.820877075	10.28440857	3.54133606	5.748954773	5.001800537	10.50980949	6.587955475	4.70905304
1.735992432	11.75991821	10.30551147	1.519744873	1.024120331	21.03404999	0.203525543	7.41835022
17.67391968	19.42481995	8.377456665	2.685005188	8.143547058	21.00332451	7.976787567	14.03062439
2.345947266	2.14553833	8.060134888	8.29158783	5.175804138	7.107352257	1.53547287	7.041847229
17.16949463	0.896133423	1.971099854	0.71660614	9.008647919	11.33536339	1.78842926	14.82484436
16.72653198	11.50952148	13.06217194	5.688354492	5.670871735	14.82686329	0.401836395	6.665351868
16.70037842	2.730377197	4.669769287	1.606201172	3.309183121	4.757558823	2.998908997	15.04683685
9.898971558	5.837661743	6.111465454	2.502723694	5.349925995	5.925445557	8.242580414	3.519798279
9.373321533	0.511581421	5.276733398	7.959083557	8.849514008	13.8350296	3.449352264	3.694335938
8.847824097	1.903015137	2.173294067	9.926620483	6.073261261	10.52269268	3.185245514	14.46382141
14.81204224	6.101989746	2.997650146	5.627754211	2.924062729	4.072490692	5.038711548	10.31278992
20.69258118	0.721038818	0.024017334	1.6926651	5.523929596	1.288650036	7.537212372	3.298225403
21.43019104	1.658157349	4.670013428	2.320426941	8.69049263	14.71156502	6.803207397	25.20581055
31.30345154	1.636657715	2.195388794	3.024108887	3.452037811	2.850184441	4.730304718	1.06804657
8.396347046	8.622406006	5.302032471	0.611984253	3.023347855	7.894546509	14.67364502	5.41778183
6.571594238	1.544219971	1.284286499	3.990486145	2.5391922	9.402640343	2.736602783	1.852706909
14.97644043	7.178924561	1.189819336	10.21265411	5.698047638	2.052455425	17.16769791	0.929218292
7.832717896	15.51335144	2.446609497	1.779121399	8.531364441	3.213296652	16.90055084	5.131069183
6.654403687	8.450790405	6.865646362	2.138137817	3.404003143	2.319901705	19.5234642	1.332946777
21.16120911	4.148178101	6.839828491	7.294075012	3.473770142	8.474464417	17.39029694	0.579612732
6.737182617	4.325866699	3.120559692	1.321479797	2.154071808	1.627864838	1.129516602	3.147079468
8.947250366	7.003387451	2.770019531	8.508361816	5.87216568	2.312748909	1.537010193	3.762947083
1.101608276	2.136932373	1.194244385	1.271430969	8.372236252	4.279260635	1.41027832	5.371536255
9.735153198	1.923324585	0.923080444	0.465187073	3.355966568	1.712748528	0.380886078	2.235626221
9.14515686	0.924926758	0.400695801	8.497947693	3.924196243	2.473781586	1.088176727	3.378005981
1.814712524	1.003601074	10.29441833	0.317123413	1.701190948	1.681013584	16.35813522	3.670333862
0.695907593	0.944229126	0.276641846	2.245140076	14.23614883	0.792974949	2.108818054	7.543598175
2.418640137	0.42590332	1.211196899	8.916900635	3.331195831	2.531287432	2.147880554	3.608940125
1.361938477	25.75236511	26.09300232	2.660942078	4.374326706	0.715538979	2.551353455	3.577705383
4.353500366	1.50553894	1.499298096	8.686286926	1.400022507	0.725981951	0.362716675	7.804122925
1.399307251	12.62353516	26.96618652	1.996513367	17.53429985	7.516811371	2.746778488	7.324951172
1.60256958	5.44090271	7.610900879	1.499786377	1.31464386	4.494722843	2.16979599	8.06464386
2.67414856	2.191055298	4.148376465	7.100074768	2.132177353	0.407032967	18.36064911	8.99552536
1.66255188	8.601364136	5.386047363	2.283676147	0.784955978	8.440403938	12.93793869	0.536880493
31.8959198	1.966888428	12.29705811	4.694137573	18.78264236	2.351971626	4.709823608	0.553844452
2.156799316	5.060241699	18.74015808	0.378326416	2.171882629	5.608739376	5.509384155	0.852996826
4.729904175	1.873016357	0.584197998	1.569778442	2.562229156	0.245988846	7.374824524	0.504890442
31.63124084	1.878555298	4.57711792	3.783744812	15.08408737	4.321634293	4.568397522	2.203834534
1.84387207	1.542236328	4.381439209	2.973617554	4.24414444	0.622857094	1.030872345	3.512584686
5.508972168	1.722991943	3.00982666	0.939888	1.929965973	8.508935928	7.25806427	2.710170746
7.818832397	4.036376953	19.0035553	1.281196594	4.2296772	2.851179838	5.222373962	3.790664673
27.93486023	2.566711426	1.173461914	1.048278809	1.688207626	4.978782654	0.556594849	
11.26107788	2.780700684	27.57756042	6.18396759	4.215200424	1.005455017	1.025154114	
5.779571533	1.027984619	5.123550415	1.524864197	1.446292877	5.667254448	5.999485016	
5.253189087	4.400405884	2.736419678	1.045974731	9.211021423	2.399227142	3.023773193	
37.03620911	9.821105957	5.550964355	4.09487915	0.404756546	1.719058037	5.559328079	
36.93544006	3.910827637	24.95629883	0.843444824	0.746965408	6.563217163	3.211753845	
	7.714294434	6.492889404	1.390640259	9.621519089	5.566056252	10.04059982	
	1.751785278	15.94522095	3.572929382	0.423700333	6.838814735	3.380847931	
	1.944580078	9.903366089	4.890213013	2.05242157	9.653207779	9.90007019	
	7.898452759	6.137908936	1.903030396	18.63245773	7.503805161	13.30950737	
	8.702362061	3.630203247	7.316818237	3.310829163	3.790083885		
	2.629455566	11.85466003	1.211502075	3.394426346	0.32004261		
	6.221618652	9.045593262	3.860710144	2.14397049	2.232896805		
	14.24234009	9.09552002	4.016120911	17.82775879	1.59930706		
	14.27284241	10.5684967	5.948387146	0.209747314	14.87543106		
	17.81268311	10.63658142	3.72064209	3.307373047	4.253918648		
	12.94064331	13.09214783	8.809555054	2.235584259	14.15619183		
	2.413513184	10.7046814	2.082550049	3.980712891	2.867256165		
	9.456863403	8.71446228	8.522651672	7.155292511			
	0.553955078	8.597396851	7.893806458	2.162811279			
	1.778884888	10.8964386	3.901130676	3.830879211			
	4.643951416	14.6678772	3.721801758	0.312461853			
	0.486221313	12.18441772	6.26776886	8.467863083			
	2.616439819	2.287445068	1.538085938	6.0884552			
	0.248733521	1.580825806	0.904067993	2.477420807			
	7.524597168	1.831436157	3.394996643	3.718292236			
		1.583145142	5.409812927	9.259830475			
		0.498855591	2.215057373	10.05231857			
		2.508010864	7.64931488	7.118301392			
		2.332580566	3.114524841	16.07948685			
		0.532562256	12.27370453	6.694213867			
		1.442077637	1.532447815	16.09660721			
		7.711380005	9.818107605	16.11371613			
		4.882873535	2.872024536	0.052875519			
		3.356643677	17.3466568	6.506580353			
		2.417709351	2.76374054	5.881969452			
		0.690933228	2.383468628	5.130123138			
		1.089935303	3.042121887	6.87670517			
		0.854034424	8.917999268	5.939849854			
		1.492279053	2.413925171	3.467048645			
		1.497558594	2.475013733	1.3797189			
		5.822601318	5.216545105	6.732719421			
		0.512039185	9.168083191	5.763965607			
		1.080001831	1.737213135	2.282035828			
		3.046051025	2.193557739	0.470993042			
		2.363677979	5.00743866	1.557373047			
		6.049972534	9.418251038	6.841758728			
		6.659179688	1.195602417	7.740936279			
		4.093658447	1.68157959	1.926776886			
		5.854248047	7.0963974	7.927211761			
		4.615371704	10.20037079	0.811546326			
		12.00289917	4.268325806	4.993404388			
			21.55478668	10.54858398			
			11.30322266	5.491744995			
			4.65133667	1.873321533			
			12.95096588	5.990085602			
			15.46927643	1.311878204			
			1.5	8.088047028			
			4.389953613	7.238864899			
			4.477935791	8.334030151			
			6.283996582	3.798271179			
			11.86791229	7.175769806			
			3.294670105	2.692222595			
			6.571121216	7.553695679			
			11.85157776	3.966587067			
			15.03565216	7.112667084			
			6.85824585	2.770671844			
			11.83524323	7.603988647			
			15.67763519	4.134902954			
			7.145362854	11.95750809			
			11.81890869	5.688430786			
			7.092216492	0.761230469			
			7.432571411	10.4537735			
			11.80256653	3.727050781			
			8.43888855	3.928123474			
			0.969566345	2.193771362			
			0.945587158	2.022621155			
			15.3420105	1.017944336			
			7.252037048	1.957237244			
			7.950149536				
			1.105209351				
			9.63407135				
			11.40407562				
			3.652862549				
			4.211418152				
			11.47613525				
			16.14139557				
			19.72872162				
			15.97721863				
			7.994796753				
			3.950744629				
			7.751106262				
			4.515548706				
			3.431930542				
			3.59172821				
			8.125358582				
			7.12374115				
			11.73230743				
			7.466743469				
			7.991622925				
			7.183349609				
			24.93800354				
			0.815101624				
			0.25415802				
			1.098243713				

Figure S1: This figure contains the results of the t-test and f-test performed for the REV analysis of P_{20}, P_{21} and n'_c parameters

P_20 Set ENE-WSW				
Size	T-test		F test	
	P-valeu	Result	P-value	Result
5	0.0327	rejected	2.18E-06	rejected
10	0.7177	accepted	8.15E-04	rejected
15	0.5809	accepted	0.0159	rejected
20	0.9775	accepted	0.1775	accepted
25	0.5969	accepted	0.4161	accepted
30	0.8481	accepted	0.1578	accepted
35	0.4282	accepted	0.7918	accepted

P_21 ENE-WSW				
Size	T-test		F test	
	P-valeu	Result	P-value	Result
5	0.7823	accepted	5.84E-04	rejected
10	0.635	accepted	0.0213	rejected
15	0.6052	accepted	0.0529	accepted
20	0.6886	accepted	0.288	accepted
25	0.2868	accepted	0.4247	accepted
30	0.5536	accepted	0.3835	accepted
35	0.7922	accepted	0.5787	accepted

P_20 WNW-ESE				
Size	T-test		F test	
	P-valeu	Result	P-value	Result
5	0.8529	accepted	1.79E-07	rejected
10	0.7507	accepted	7.34E-05	rejected
15	0.7154	accepted	9.41E-04	rejected
20	0.691	accepted	0.0024	rejected
25	0.4895	accepted	0.0093	rejected
30	0.5983	accepted	0.0087	accepted
35	0.5338	accepted	0.4444	accepted

P_21 WNW-ESE				
Size	T-test		F test	
	P-valeu	Result	P-value	Result
5	0.9356	accepted	7.52E-05	rejected
10	0.834	accepted	0.0038	rejected
15	0.7885	accepted	0.0306	rejected
20	0.9399	accepted	0.0911	accepted
25	0.9868	accepted	0.3657	accepted
30	0.6612	accepted	0.1684	accepted
35	0.9158	accepted	0.6272	accepted

P_20 N-S				
Size	T-test		F test	
	P-valeu	Result	P-value	Result
5				
10	0.7428	accepted	0.0025	rejected
15	0.7346	accepted	0.0237	rejected
20	0.5566	accepted	0.0967	accepted
25	0.2711	accepted	0.0401	accepted
30	0.561	accepted	0.3846	accepted
35	0.6523	accepted	0.9085	accepted

P_21 N-S				
Size	T-test		F test	
	P-valeu	Result	P-value	Result
5	0.9368	accepted	2.28E-04	rejected
10	0.884	accepted	0.0095	rejected
15	0.9121	accepted	0.0523	accepted
20	0.644	accepted	0.2773	accepted

n'_c				
Size	T-test		F test	
	P-valeu	Result	P-value	Result
5				
10	0.9320	accepted	1.3012e-04	rejected
15	0.8981	accepted	0.0013	rejected
20	0.6103	accepted	0.00477	rejected
25	0.2242	accepted	0.2856	accepted
30	0.0616	accepted	0.5958	accepted
35	0.1087	accepted	0.07456	accepted

SCRIPT 1

Python script developed for the Gocad plugin GoPy to create linear scanlines on a DOM or scanarea surface

```
#INPUT
#DOM or scanarea border
Dom_border = XXX
#DOM or scanarea surface
Dom_surface = XXX
#number of scanline to create
Nx = XXX
#Linear scanline azimuth
scanline_azimuth = XXX
#END INPUT
Ny = 5
Nz = 5
Nc = Nx/2
#create voxet from medium plane of DOM or scanarea
GocadCmd.VoxetBoxCreate(
   name=  "vox"
   ,gobjs=  Dom_border
   ,Scale_X_dimension_by=    "1"
   ,Scale_Y_dimension_by=    "1"
   ,Scale_Z_dimension_by=    "1"
   ,number_cells_along_X= Nx
   ,number_cells_along_Y=  Ny
   ,number_cells_along_Z=  Nz
   ,first_axis_is_time_or_depth= "false"
)
#create a surface from the central section of voxet
GocadCmd.TSurfCreateFromVoxetPlane(
   name=    "section_surf"
   ,voxet=    "vox"
   ,axis=    "U"
   ,plane=  Nc
   ,copy_properties=    "true"
   ,property=    "all_properties"
)
# select central point of center section surface
Xlist = list(i.property("X").get() for i in GObj("section_surf"))
Ylist = list(i.property("Y").get() for i in GObj("section_surf"))
Zlist = list(i.property("Z").get() for i in GObj("section_surf"))
a = Xlist[0]
b = Xlist[Nx-1]
c = a + b
Xmed = c/2
d = Ylist[0]
e = Ylist[Nx-1]
f= d + e
Ymed = f/2
g = Zlist[0]
h = Zlist[Nx-1]
i= g + h
Zmed = i/2
# create scanline surface
for i in range (Nx):
   GocadCmd.TSurfCreateFromVoxetPlane(
      name=    "scan_%i"%i
      ,voxet=    "vox"
      ,axis=    "U"
      ,plane=    i
      ,copy_properties=    "true"
      ,property=    "all properties"
   )
   scan = "scan_%i"%i
   GocadCmd.TSurfCreateFromPlane(
      name=    "scan_m%i"%i
      ,points=    scan
      ,Clip_with_XYZ=    "true"
      ,Clip_with_voxet=    "false"
      ,Do_not_clip_Z=    "false"
      ,voxet=    "none"
      ,scale=    "2.0"
   )
   GocadCmd.GObjsMove(
      objects=  "scan_m%i"%i
      ,rotate=    "true"
      ,origin=  ( str(Xmed),  str(Ymed),  str(Zmed) )
      ,axis=    ("0",  "0",  "1")
      ,angle=   scanline_azimuth
      ,translate= "false"
      , translation=    ("0.0",  "0.0",  "0.0")
   )
   scanli = "scan_m%i"%i
   surfs =  scanli, Dom_surface
   GocadCmd.PLineCreateFromTSurfIntersection(
      name=   "scan_line_%i"%i
      ,tsurfs=   surfs
   )
   runStrg2 = "GObjDestroy objects",  scan,  "1"
   run (runStrg2)
   runStrg3 = "GObjDestroy objects",  scanli,  "1"
   run (runStrg3)
run("GObjDestroy objects section_surf 1")
```

SCRIPT 2

Python script developed for the Gocad plugin GoPy to calculate fracture spacing along scanlines created with script number 1

```
# INPUT
#number of scanline
Sn = XXX
#trace (curve) of fractures
Fracture_trace = XXX
#END_INPUT
#extract vertical surface from fracture traces
GocadCmd.TSurfCreateFromTube(
   name= "fracture_surface"
   ,curves=    Fracture_trace
   ,expansion=    ( "0",  "0",  "3" )
   ,select_number_of_levels=    "false"
   ,number_of_levels=    "1"
   ,seal_ends=    "false"
   ,two_ways=    "true"
   ,dissociate_vertices=    "true"
)
for i in range (Sn):
   scan = "scan_line_%i"%i
   #create intersection point between scanline and fracture
surfaces
      GocadCmd.VSetCreateFromPLineAndTSurfIntersection(
       name=    "pointset_%i"%i
       ,lines= scan
       ,surfaces=    "fracture_surface"
       ,copy_surfaces_properties=    "false"
       ,store_normal=    "false"
       ,normal_property_name=  "None"
       ,copy_lines_properties=   "false"
   )
   # list of point (intersection between fracture and scanline)
for every scanline
   tempTrace = "pointset_%i"%i
   pts = list ((i.X,i.Y,i.Z) for i in GObj(tempTrace))
   c = len(pts)
  punti_totali = "scan_line_spacing_%i"%i
   # calculate distance between point (fracture spacing)
   for i in range (c-1):
      punti = "point_%i"%i
      P = pts[i]
      Q = pts[i+1]
      dist = distance(P, Q)
      #create a point in the middle between two fractures
and transfer spacing properties to this point
      Xlist = list(i.property("X").get() for i in GObj(tempTrace))
      Ylist = list(i.property("Y").get() for i in GObj(tempTrace))
      Zlist = list(i.property("Z").get() for i in GObj(tempTrace))
      a = Xlist[i]
      b = Xlist[i+1]
      c = a + b
      Xmed = c/2
      d = Ylist[i]
      e = Ylist[i+1]
      f= d + e
      Ymed = f/2
      g = Zlist[i]
      h = Zlist[i+1]
      i= g + h
      Zmed = i/2
      points = ( str(Xmed),  str(Ymed),  str(Zmed))
      vset_create_from_point_list(punti, points)
      #create properties on pointset
      GocadCmd.PropertyCreate(
         gobj= punti
         ,property_name= "lenght"
      )
#set spacing value to the property
      GocadCmd.PropertySetValue(
            punti
         ,property=    "lenght"
         ,value=  dist
         ,region=    "everywhere"
      )
      #create poinset for every scanline
      GocadCmd.VSetCreateFromAtomicGroup(
         name=    punti_totali
         ,points=    punti
         ,region=    "everywhere"
         ,copy_properties=    "true"
         ,dissociate_vertices=    "false"
         ,merge_parts=    "false"
      )
                        #create a pointset containing all the
point of all scanline
      GocadCmd.VSetCreateFromAtomicGroup(
         name=   "all_scanline_spacing"
         ,points=  punti_totali
         ,region=    "everywhere"
         ,copy_properties=    "true"
         ,dissociate_vertices=    "false"
         ,merge_parts=    "false"
      )


      runStrg2 = "GObjDestroy objects", punti,  "1"

      run (runStrg2)
```

SCRIPT 3

Python script developed for the Gocad plugin GoPy to calculate length, trend and plunge of the fracture sets

The script stating from fracture trace interpretation calculates lenght, trend and plunge of the fracture set inside a convex scanline

For the Input data the user needs: a curve representig the scanline; the fracture traces; azimuth and dip of the strata and a surface representig the medium plane of the outcrop or the surface of the scanarea

```
#INPUT
#scanarea_border_curve
scanline = XXX
#medium plane of the outcrop or scanarea surface
medium_plane = XXX
# Fracture trace curve
Fracture_trace = XXX
#azimuth_dip of the bessing or of the scanrea
bedAzi =XXX
#dip of the bedding or of the scanarea
bedDip = XXX
#END INPUT
heightRibbon = 2
bedAzi = float(bedAzi)
bedDip = float(bedDip)
heightRibbon = float(heightRibbon)

Dip = 0
# default values (needed if input as string)
if not(bedAzi):
   bedAzi = 0.0
if not(bedDip):
   bedDip = 0.0
if not(heightRibbon):
   heightRibbon = 20.0
trendPrj =  math.radians(bedAzi-180)
plungePrj = math.radians(90-bedDip)
extrX =
math.sin(trendPrj)*math.cos(plungePrj)*heightRibbon
extrY =
math.cos(trendPrj)*math.cos(plungePrj)*heightRibbon
extrZ = -math.sin(plungePrj)*heightRibbon
trendPrjcircle =  math.radians(bedAzi-90)
plungePrjcircle = math.radians(bedDip)
dirX = math.sin(trendPrjcircle)*math.sin(plungePrjcircle)
dirY = math.cos(trendPrjcircle)*math.sin(plungePrjcircle)
dirZ = -math.cos(plungePrjcircle)
#copy fracure trace
GocadCmd.PLineCreateFromPLines(
   name=    "Fracture_trace_copy"
   ,curves=  Fracture_trace
   ,copy_points=    "true"
   ,merge=    "false"
   ,copy_properties=    "true"
)
# copia scanarea border
GocadCmd.PLineCreateFromPLines(
   name=    "scanline_copy"
   ,curves=    scanline
   ,copy_points=    "true"
   ,merge=    "false"
   ,copy_properties=    "fasles"
)
# project fracture traces on DOM surface or on the scanarea
GocadCmd.PLineFitCthCommand(
      "Fracture_trace_copy"
   ,target=    medium_plane
   ,constant_thickness=    "true"
   ,thickness_value=    "0"
   ,thickness_property=    "1"
   ,dir_shoot= (str(dirY) , str(-dirX),  str(-dirZ))
)
# simplify fracture traces in order to avoid computational
issues
GocadCmd.PLineFilterSize(
    "Fracture_trace_copy"
   ,minimum_size=   1e+009
   ,length_unit=    "m"
)
# project scanarea border on DOM or scanarea surface
GocadCmd.PLineFitCthCommand(
      scanline
   ,target=    medium_plane
   ,constant_thickness=    "true"
   ,thickness_value=    "0"
   ,thickness_property=    "1"
   ,dir_shoot= (str(dirY) , str(-dirX),  str(-dirZ))
)
# create border surface from scanarea border
GocadCmd.TSurfCreateFromTube(
   name=    "scanline_surface_border"
   ,curves=    scanline
   ,expansion=    ( str(extrX),  str(extrY),  str(extrZ) )
   ,select_number_of_levels=    "false"
   ,number_of_levels=    "1"
   ,seal_ends=    "false"
   ,two_ways=    "true"
   ,dissociate_vertices=    "true"
)
# add a point at the intersection between fracture traces
and scanarea border
GocadCmd.PLineBreakAtSurfaceIntersection(
      "Fracture_trace_copy"
   ,surface=    "scanline_surface_border"
   ,split=    "false"
)
# create another DOM or scanarea surface
GocadCmd.TSurfCreateFromPatch(
   name=    "scanline_area"
   ,curve=    scanline
   ,densification_type=    "homogeneous triangles"
   ,densification_factor=    "1.0"
   ,use_normal=    "false"
   ,dissociate_vertices=    "true"
)
# copy the created surface
GocadCmd.TSurfCreateFromTSurfs(
   name=    "scanline_area_copy"
   ,surfaces=    "scanline_area"
   ,dissociate_vertices=    "true"
   ,merge=    "false"
   ,exactly=    "true"
   ,copy_constraints=    "false"
)
# translate the copied surface

GocadCmd.GObjsMove(
```

```
   objects=  "scanline_area_copy"
   ,translate=    "true"
   ,translation=    ( str(extrX),  str(extrY),  str(extrZ) )
)
#assigne geological feature to the surface
GocadCmd.GeoBoundarySetGeologicalInformation(
       "scanline_area_copy"
   ,geologic_feature=    "scanline_area_feature"
   ,geologic_type=    "Horizon"
   ,stratigraphic_age=    "undefined"
   ,stratigraphic_time=    "0"
)
# create a region (Region 1) in the fracture traces from
geological feature
GocadCmd.BitRegionManagerGeologicFeatureRegion(
        "Fracture_trace_copy"
   ,region=   "Region_1"
   ,use_top_feature=    "false"
   ,top_feature=    "none"
   ,use_bottom_feature=   "true"
   ,bottom_feature=  "scanline_area_feature"
   ,stype=    "or"
   ,dynamic=   "false"
)
# create a property call distance in the fracture traces curve
GocadCmd.ComputeDistanceProperty(
       "Fracture_trace_copy"
   ,property_name=    distance
   ,region_name=   "everywhere"
   ,triangulated_surfaces=  "scanline_surface_border"
)
#create a region (Region 2) that contains points of the
fracture traces that are located within 0.3 meters from the
scanarea border
GocadCmd.BitRegionManagerRangeRegion(
         "Fracture_trace_copy"
   ,region=   "Region_2"
   ,property=    distance
   ,use_max=    "true"
   ,max=    "0.3"
   ,stype=   "or"
   ,dynamic=    "false"
)
# merge the two regions
GocadCmd.BitRegionManagerOrRegion(
       "Fracture_trace_copy"
   ,region=    "Region_1"
   ,with_=  "Region_2"
)
# create new curves from the region
GocadCmd.PLineCreateFromPLineRegion(
   name=    "fracture"
   ,curve=   "Fracture_trace_copy"
   ,region=  "Region_1"
   ,dissociate_vertices=    "true"
   ,copy_properties=    "false"
)
# calculate fracture length
# split fracture traces into parts in order to calculate length
of every part
tic = clock()
GocadCmd.PLinesCreateFromEachPLinePart(
   curves= "fracture"
)
# initialize i
i = 1
surfs = "" # DON'T CHANGE THIS
# process all parts
while 1:
   temp = "fracture_part%i"%i
   testObj = GObj(temp)

   if not testObj.is_valid():
      break
   else:
     # create a list of points with coordinates of the two
nodes at the end of the fractrure trace
      pts = list((i.X,i.Y,i.Z) for i in GObj(temp))
      #calculate the length of the fracture
      length = distance(pts[0],  pts[1])
      # calculate direction cosines of the fracture
      cosX = pts[0][0] - pts[1][0]
      cosY = pts[0][1] - pts[1][1]
      cosZ = pts[0][2] - pts[1][2]
      # calculate trend/plunge of line
      trend = math.degrees(math.atan2(cosX,cosY))
      #plunge = -math.degrees(math.asin(cosZ/length))
      # create length property
      GocadCmd.PropertyCreate(
        gobj= temp
        ,property_name= "length"
        )
      # copy length value in length property
      GocadCmd.PropertySetValue(
        temp
        ,property= "length"
        ,value= length
        ,region= "everywhere"
        )
      # create trend property
      GocadCmd.PropertyCreate(
        gobj= temp
        ,property_name= "trend"
        )
      # copy trend value in trend property
      GocadCmd.PropertySetValue(
           temp
        ,property= "trend"
        ,value= trend
        ,region= "everywhere"
        )
      # create plunge property
      #GocadCmd.PropertyCreate(
        #gobj= temp
        #,property_name= "plunge"
        #)
      # copy plunge value in plunge property
      #GocadCmd.PropertySetValue(
            # temp
        # ,property= "plunge"
        #,value= plunge
        #,region= "everywhere"
        #)
      # create single curve from curve part
      GocadCmd.PLineCreateFromPLines(
          name=    "Fracture_truncated"
        ,curves=    temp
        ,copy_points=    "true"
        ,merge=    "false"
        ,copy_properties=    "true"
```

```
        )
      runStrg12 = "GObjDestroy objects",  temp,  "1"
      run (runStrg12)
      i = i +1
# create pointset from intersection between fracture and
scanline_border
# in order to recognize which fractures are truncated from
the scanrea border
#this allows to apply corrections during the characterization
of the length distribtution in oder software (e.g. Matlab)

GocadCmd.VSetCreateFromRegion(
   Name=  "Pointset_truncated"
   ,object=  "Fracture_trace_copy"
   ,Region=     "Region_2"
   ,Copy_Property=     "false"
   ,Property=     "all_properties"
)
# set property to pointset
GocadCmd.PropertyCreate(
   gobj= "Pointset_truncated"
   ,property_name= "truncated"
)
# copy trend value in trend property
GocadCmd.PropertySetValue(
  "Pointset_truncated"
   ,property= "truncated"
   ,value= "1"
   ,region= "everywhere"
)
# set property to pointset
GocadCmd.PropertyCreate(
   gobj=  "Fracture_truncated"
   ,property_name= "truncated"
)
# copy trend value in trend property
GocadCmd.PropertySetValue(
  "Fracture_truncated"
   ,property= "truncated"
   ,value= "0"
   ,region= "everywhere"
)
GocadCmd.AtomicGroupPropagateProperties(
   client=  "Fracture_truncated"
   ,server=  "Pointset_truncated"
   ,all_properties=     "false"
   ,property=  "truncated"
)
run("GObjDestroy objects fracture 1")
```

SCRIPT 4

Python script developed for the Gocad plugin GoPy to calculate fracture termination (I, Y, X termination) of a fracture network inside a scanarea. The script extracts the number of I, Y and X terminations.

```
#INPUT
#fracture trace
Fracture_trace= "test_2"
#Fracture_surfaces
outSurf= "frac"
#Scanarea_surface
scan_surf= "si"
#maximum distance of a fracture tip from another fracture
#to consider it a Y termination
T_fracture_distance = "0.1"
#END_INPUT
#extract borders from test_surfaces
GocadCmd.PLineCreateFromTSurfBorders(
   name=     "scan_border"
   ,tsurf=     scan_surf
   ,dissociate_vertices=     "true"
   )
# copy input multi-polyline
GocadCmd.PLineCreateFromPLines(
   name= "smoothLine"
   ,curves= Fracture_trace
   ,copy_points= "true"
   ,merge= "true"
   ,copy_properties= "false"
   )
# split smooth multi-polyline into parts
GocadCmd.PLinesCreateFromEachPLinePart(
   curves= "smoothLine"
   )
# initialize i
i = 1
surfs = "" # DON'T CHANGE THIS
# process all parts
while 1:
   print ''
   print 'i: ', i
      tempRibbon = "fracture_s%i"%i
   surfs = surfs, tempRibbon
   tempTrace = "smoothLine_part%i" %i
   testObj = GObj(tempTrace)
      if not testObj.is_valid():
       break
   else:
 # copy the original curve in a temporary curve file
       GocadCmd.PLineCreateFromPLines(
          name= "tempTraceSimply"
          ,curves= tempTrace
          ,copy_points= "true"
          ,merge= "true"
          ,copy_properties= "false"
          )
 # create surface extrusion from line fracture interpretation
       GocadCmd.TSurfCreateFromTube(
          name=     tempRibbon
```

```
        ,curves=   tempTrace
        ,expansion=    ( 0,  0,  1)
        ,select_number_of_levels=    False
        ,number_of_levels=    1
        ,seal_ends=    "false"
        ,two_ways=    "true"
        ,dissociate_vertices=    "true"
      )
  i = i +1
 #extract borders from outSurf
GocadCmd.PLineCreateFromTSurfBorders(
  name=    "bordersall"
  ,tsurf=    outSurf
  ,dissociate_vertices=    "true"
)
# create lines from surfaces intersection
GocadCmd.PLineCreateFromTSurfIntersection(
  name=    "intersections"
,tsurfs=    surfs
)
#copy intersections curve
GocadCmd.PLineCreateFromPLines(
  name=    "simplyintersection"
  ,curves=  "intersections"
  ,copy_points=    "true"
  ,merge=    "true"
  ,copy_properties=    "false"
)
# simplify lenght of simplyintersection (reduce the curves to
only two vertex)
GocadCmd.PLineFilterSize(
   "simplyintersection"
  ,minimum_size=   1e+009
  ,length_unit=    "m"
)
# extrude small surfaces from simplyintersection curves
testObj = GObj("simplyintersection")

if not testObj.is_valid():
  pass
else:
  GocadCmd.TSurfCreateFromTube(
       name=    "simplyintersectionsurfs"
     ,curves=   "simplyintersection"
     ,expansion=    ( "0.1",  "0.1",  "0" )
     ,select_number_of_levels=    False
     ,number_of_levels=    1
     ,seal_ends=    "false"
     ,two_ways=    "true"
     ,dissociate_vertices=    "true"
  )


for i in range (1):
  scan_intersection = "scanline_intersections%i"%i
  surf_intersection = "surfaces_intersections%i"%i
  fracture_termin = "termination_fracture%i"%i
  scan_border = "border_scan_%i"%i
  T_termination = "T_term%i"%i
   # create point from intersections between scanline and S0
ribbon surfaces
  GocadCmd.VSetCreateFromPLineAndTSurfIntersection(
    name=    scan_intersection
    ,lines=    scan_border
    ,surfaces=    outSurf
    ,copy_surfaces_properties=    "true"
    ,store_normal=    "false"
    ,normal_property_name=    "None"
    ,copy_lines_properties=    "false"
  )
  # create point from intersections between scanline the
intersecrions line and scanline surfaces
  GocadCmd.VSetCreateFromPLineAndTSurfIntersection(
    name=  surf_intersection
    ,lines=    "intersections"
    ,surfaces=    scan_surf
    ,copy_surfaces_properties=    "false"
    ,store_normal=    "false"
    ,normal_property_name=   "None"
    ,copy_lines_properties=    "false"
  )
  # create point from intersections between scanline
surfaces and test surfaces or S0 ribbon borders
  GocadCmd.VSetCreateFromPLineAndTSurfIntersection(
    name=    fracture_termin
    ,lines=    "bordersall"
    ,surfaces=    scan_surf
    ,copy_surfaces_properties=    "true"
    ,store_normal=    "false"
    ,normal_property_name=    "None"
    ,copy_lines_properties=    "false"
  )
  # merge all the parts in the pointsets to avoid the
presence of parts
  GocadCmd.VSetMergeAllSubVSets(
     scan_intersection
  )
  GocadCmd.VSetMergeAllSubVSets(
      surf_intersection
  )
  GocadCmd.VSetMergeAllSubVSets(
      fracture_termin
  )
  num_sui= len(list(i for i in GObj(surf_intersection))) #
number of fracture mutual intersection inside the scanline
area (X&T)
  num_tf= len(list(i for i in GObj(fracture_termin))) #
number of fracture termination (E&T)
  # NOW THE SCRIPTS CREATE A POINTSET FOR T, X, AND E
TERMINATION AND CALCULATE THE TERMINATION
STATISTIC (FRACMAN)
  # compute distance between fracture termination points
and simplyintersectionsurfs
  testObj = GObj("simplyintersectionsurfs")
  if not testObj.is_valid():
    pass
  else:
    GocadCmd.ComputeDistanceProperty(
```

```
        fracture_termin
    ,property_name=    "distanceprop"
    ,region_name=    "everywhere"
    ,triangulated_surfaces=    "simplyintersectionsurfs"
          )
  # create region from propery distance in fracture
termination
    GocadCmd.BitRegionManagerRangeRegion(
      fracture_termin
    ,region=    "distanceprop_region"
    ,property=    "distanceprop"
    ,use_min=    "false"
    ,min=    "0"
    ,use_max=    "true"
    ,max=    T_fracture_distance
    ,stype=    "or"
    ,dynamic=    "false"
          )
    #create pointset from distanceprop_region
    GocadCmd.VSetCreateFromRegion(
      Name=    T_termination
    ,object=    fracture_termin
    ,Region=  "distanceprop_region"
    ,Copy_Property=    "false"
    ,Property=    "all_properties"
    )
    # calculate number of T_termination in every scanline
  testObj2 = GObj(T_termination)
  if not testObj2.is_valid():
    T_term = 0
  else:
    T_term = float(len(list(i for i in GObj(T_termination))))
  print T_term
  X_term =float(len(list(i for i in GObj(surf_intersection))))
  ET = float(len(list(i for i in GObj(fracture_termin))))
  E_term = ET - T_term
# create a single surface from the scanline surf
  GocadCmd.TSurfCreateFromTSurfs(
    name=    "scan_line_surf_tot"
    ,surfaces=  scan_surf
    ,dissociate_vertices=    "true"
    ,merge=    "false"
    ,exactly=    "true"
    ,copy_constraints=    "true"
  )
  #create a single pointset from termination_fracture
  GocadCmd.VSetCreateFromAtomicGroup(
    name=    "fracture_termination_tot"
    ,points=    fracture_termin
    ,region=    "everywhere"
    ,copy_properties=    "true"
    ,dissociate_vertices=    "true"
    ,merge_parts=    "true"
  )
  #create a single pointset from scanline_intersection
  GocadCmd.VSetCreateFromAtomicGroup(
    name=    "surfaces_intersections_tot"
    ,points=    surf_intersection
    ,region=    "everywhere"
    ,copy_properties=    "true"
    ,dissociate_vertices=    "true"
    ,merge_parts=    "true"
  )
  # create a single pointset from T_term
  GocadCmd.VSetCreateFromAtomicGroup(
    name=    "T_termination_tot"
    ,points=    T_termination
    ,region=    "everywhere"
    ,copy_properties=    "true"
    ,dissociate_vertices=    "true"
    ,merge_parts=    "true"
  )
  GocadCmd.PLineCreateFromPLines(
    name=  "scan_border_tot"
    ,curves=  scan_border
    ,copy_points=    "true"
    ,merge=    "false"
    ,copy_properties=    "true"
  )
  runStrg3 = "GObjDestroy objects",  fracture_termin,  "1"
  run (runStrg3)
  runStrg4 = "GObjDestroy objects",  surf_intersection,  "1"
  run (runStrg4)
  runStrg7 = "GObjDestroy objects",  scan_surf,  "1"
  run (runStrg7)
  runStrg8 = "GObjDestroy objects",  scan_border,  "1"
  run (runStrg8)
  runStrg11 = "GObjDestroy objects",  T_termination,  "1"
  run (runStrg11)
# CREATE X_TERMINATION AND E_TERMINATION POINTSET
# Create T property on T_termination_tot(T=1), fracture
termination tot (T = 0) and surfaces_intersections_tot (T =
0).
GocadCmd.PropertyCreate(
    gobj= "T_termination_tot"
    ,property_name= "T"
)
#GocadCmd.PropertyCreate(
    gobj= "fracture_termination_tot"
    ,property_name= "T"
)
GocadCmd.PropertyCreate(
    gobj= "surfaces_intersections_tot"
    ,property_name= "T"
)
# set property value.
GocadCmd.PropertySetValue(
    "T_termination_tot"
    ,property=    "T"
    ,value=  "1"
    ,region=    "everywhere"
)
GocadCmd.PropertySetValue(
    "fracture_termination_tot"
    ,property=    "T"
    ,value=  "0"
    ,region=    "everywhere"
)
```

```
GocadCmd.PropertySetValue(
      "surfaces_intersections_tot"
      ,property=    "T"
      ,value=   "0"
      ,region=    "everywhere"
 )
# tranfer properties T from T termination tot to
fracture_termination_tot and surfaces_intersections_tot
GocadCmd.AtomicGroupPropagateProperties(
   client=    "fracture_termination_tot"
   ,server=    "T_termination_tot"
   ,all_properties=    "false"
   ,property=    "T"
)
GocadCmd.AtomicGroupPropagateProperties(
   client=    "surfaces_intersections_tot"
   ,server=    "T_termination_tot"
   ,all_properties=    "false"
   ,property=    "T"
)
# create region T region from property range in
fracture_termination_tot and
surfaces_intersections_tot_intersections_tot
# The region will be composed from the points with T
property value = 0
GocadCmd.BitRegionManagerRangeRegion(
      "fracture_termination_tot"
   ,region=    "T_region"
   ,property=    "T"
   ,use_min=    "false"
   ,min=    "0.1"
   ,use_max=    "true"
   ,max=    "0.1"
   ,stype=    "or"
   ,dynamic=    "false"
)
GocadCmd.BitRegionManagerRangeRegion(
      "surfaces_intersections_tot"
   ,region=    "T_region"
   ,property=    "T"
   ,use_min=    "false"
   ,min=    "0.1"
   ,use_max=    "true"
   ,max=    "0.1"
   ,stype=    "or"
   ,dynamic=    "false"
)
# create new pointset from pointset region
GocadCmd.VSetCreateFromRegion(
   Name=   "E_termination_tot"
   ,object=    "fracture_termination_tot"
   ,Region=    "T_region"
   ,Copy_Property=    "false"
   ,Property=    "all_properties"
)
GocadCmd.VSetCreateFromRegion(
   Name=   "X_termination_tot"
   ,object=    "surfaces_intersections_tot"
   ,Region=    "T_region"
   ,Copy_Property=    "false"
   ,Property=    "all_properties"
)
run("GObjDestroy objects ")
run("GObjDestroy objects simplyintersection 1")
run("GObjDestroy objects simplyintersectionsurfs 1")
run("GObjDestroy objects bordersall 1")
run("GObjDestroy objects intersections 1")
```

SCRIPT 5

Python script developed for the Gocad plugin GoPy to perform P_{21} REV analysis. The script starting from a regular pointset grid create several scanarea of size decided by the user. The script extracts a region for every scanare inside the fracture traces curve and it creates a new fracture trace for every region. Length of every fracture traces is then calculated with a macro of skua-gocad and stored as properties on the fracture trace. P_{21} is then calculated dividing the calculated fracture length for the scanarea dimension.

```
#INPUT
#Fracture trace
Fracture_set= XXX
#regular pointset grid
Grid_pointset= XXX
#number of points in the grid
num_p= XXX
#size dimension of the scanarea (m)
cell_size = XXX
#height of the scanarea (if in 2D put 1)
cell_height = XXX
# END INPUT
cell_volume =  cell_size * cell_size * cell_height
cell_size_true = cell_size +1
for i in range (num_p):
   cube = "c_%i"%i
   c_surf= "s_%i"%i
   c_reg = "r_%i"%i
   scan_area_surf= "scan_s_%i"%i
   scan_area_surf_border= "scan_s_b_%i"%i
   region_curve = "curve_r_%i"%i
   curve_region = "curve_region_new_%i"%i
   scan_border_surface = "scan_border_surface_%i"%i
   pts = list ((i.X,i.Y,i.Z) for i in GObj(Grid_pointset))
   dn = pts[i][0]
   fn = pts[i][1]
   en = pts [i][2]
   GocadCmd.VoxetCreate(
      name=    cube
      ,origin=    (dn,  fn,  en)
      ,step_u=   ("1",  "0",  "0")
      ,step_v=   ("0",  "1",  "0")
      ,step_w=   ("0",  "0",  "1")
      ,nu=   cell_size_true
      ,nv=    cell_size_true
      ,nw=   cell_height
      ,coordinate_system_name=    "Default"
   )
   #create surfaces from cells
     GocadCmd.TSurfCreateFromVoxetPlane(
      name=    scan_area_surf
      ,voxet=    cube
      ,axis=    "W"
      ,plane=    0
      ,copy_properties=    "true"
      ,property=    "all properties"
   )
   GocadCmd.GObjsMove(
      objects=    scan_area_surf
      ,translate=    "true"
      ,translation=   (0, 0,  0.5)
   )
   #extract border
   GocadCmd.PLineCreateFromTSurfBorders(
      name=  scan_area_surf_border
      ,tsurf=  scan_area_surf
      ,dissociate_vertices=    "true"
   )
   GocadCmd.TSurfCreateFromTube(
      name=    scan_border_surface
      ,curves= scan_area_surf_border
      ,expansion=   (0,  0,  3)
      ,select_number_of_levels=    "False"
      ,number_of_levels=   "1"
      ,seal_ends=   "false"
      ,two_ways=    "true"
      ,dissociate_vertices=    "true"
   )
   GocadCmd.PLineBreakAtSurfaceIntersection(
       Fracture_set
      ,surface=    scan_border_surface
      ,split=    "false"
   )
#create a region inside the fracture trace for every scanarea
   GocadCmd.BitRegionManagerInitFromClosedPolygons(
       Fracture_set
      ,region=    region_curve
      ,polygon= scan_area_surf_border
      ,stype=    "or"
      ,dynamic=    "false"
   )
#create a new fracture traces curve from every region
   GocadCmd.PLineCreateFromPLineRegion(
      name=    curve_region
      ,curve=  Fracture_set
      ,region= region_curve
      ,dissociate_vertices=   "true"
      ,copy_properties=   "false"
   )
   # END
```

SCRIPT 6

Python script developed for the Gocad plugin GoPy to perform P_{20} REV analysis. The script creates a point in the center of every fracture creating a pointset of fracture centers, then starting from a regular pointset grid create several scanarea of size decided by the user and extract a region for every scanarea in the pointset following the same procedure of script 5. Then the number of pointset in every scanarea is calculated and stored as a properties

```
#INPUT
#number of fractures in the fracture trace curve
num = XXX
for i in range (num):
#insert the name of the fracture traces curve
   Fracture_trace = GObj("XXX_part%i"%i)
   Fracture_center = "pointset_center_%i"%i
   testObj = GObj("set_1_South_part%i"%i)
   if not testObj.is_valid():
      pass
   else:
      x = (max(i.X for i in Fracture_trace) +min(i.X for i in
Fracture_trace )) /2
      y = (max(i.Y for i in Fracture_trace) +min(i.Y for i in
Fracture_trace)) /2
      z = (max(i.Z for i in Fracture_trace) +min(i.Z for i in
Fracture_trace)) /2
      vset_create_from_point_list(Fracture_center, ((x, y, z),
))
      #run ('VSetCreateFromPoints coordinate_system_name
"Default_depth" name "Fracture_center" points', ((x, y, z), ))
      #tranfer lenth properties from curve to point
#create one poinset containging all the fracture centers
      GocadCmd.VSetCreateFromAtomicGroup(
         name=    "Fracture_center_all"
         ,points=    Fracture_center
         ,region=    "everywhere"
         ,copy_properties=    "true"
         ,dissociate_vertices=  "true"
         ,merge_parts=    "false"
```

SCRIPT 7

Python script developed for the Gocad plugin GoPy to perform P20 REV analysis. This script is a continuation of script 6. The script starting from a regular pointset grid create several scanarea of size decided by the user and extract a region for every scanarea in the pointset containing the fracture centers created with script 6 following the same procedure of script 5. Then the number of pointset in every scanarea is calculated and stored as a properties. P_{20}

```
#INPUT
#regular pointset grid
Grid_pointset= XXX
#number of points in the grid
num_p= XXX
#dimension of the scanarea
cell_size = 20
#scanarea height (if 2D put 1)
cell_height = 1
#END_INPUT
cell_volume =  cell_size * cell_size * cell_height
cell_size_true = cell_size +1
for i in range (num_p):
   cube = "c_%i"%i
   c_surf= "s_%i"%i
   c_reg = "r_%i"%i
   scan_area_surf= "scan_s_%i"%i
   scan_area_surf_border= "scan_s_b_%i"%i
   region_point = "point_r_%i"%i
   point_region = "point_region_new_%i"%i
   scan_border_surface = "scan_border_surface_%i"%i
   pts = list ((i.X,i.Y,i.Z) for i in GObj(Grid_pointset))
   dn = pts[i][0]
   fn = pts[i][1]
   en = pts [i][2]
   GocadCmd.VoxetCreate(
      name=    cube
      ,origin=    (dn,  fn,  en)
      ,step_u=    ("1",  "0",  "0")
      ,step_v=    ("0",  "1",  "0")
      ,step_w=    ("0",  "0",  "1")
      ,nu=    cell_size_true
      ,nv=    cell_size_true
      ,nw=    cell_height
      ,coordinate_system_name=    "Default"
   )
   #create surfaces from cells
   GocadCmd.TSurfCreateFromVoxetPlane(
      name=    scan_area_surf
      ,voxet=    cube
      ,axis=    "W"
      ,plane=    0
      ,copy_properties=    "true"
      ,property=    "all properties"
   )
   GocadCmd.GObjsMove(
      objects=    scan_area_surf
      ,translate=    "true"
```

```
   ,translation=    (0, 0,  0.5)
)
#extract border
GocadCmd.PLineCreateFromTSurfBorders(
   name=  scan_area_surf_border
   ,tsurf=  scan_area_surf
   ,dissociate_vertices=     "true"
)
GocadCmd.BitRegionManagerInitFromClosedPolygons(
        "Fracture_center_all"
   ,region=     region_point
   ,polygon= scan_area_surf_border
   ,stype=     "or"
   ,dynamic=     "false"
)
GocadCmd.VSetCreateFromRegion(
   Name=     point_region
   ,object= "Fracture_center_all"
   ,Region=  region_point
   ,Copy_Property=     "true"
   ,Property=    "all_properties"
)
# END
```